MNRAS 000, 1–68 (2024) Preprint 18 April 2024 Compiled using MNRAS LATEX style file v3.0

Beyond MACS: Physical properties of extremely X-ray luminous clusters at $z > 0.5$

H. Ebeling[1], J. Richard[2], B. Beauchesne[3], Q. Basto[2], A.C. Edge[4]★ & I. Smail[4]

[1] *Institute for Astronomy, University of Hawaii, 640 N. Aohoku Place, Hilo, HI 96720, USA*
[2] *Univ Lyon, Univ Lyon1, Ens de Lyon, CNRS, Centre de Recherche Astrophysique de Lyon UMR5574, F-69230, Saint-Genis-Laval, France*
[3] *Institute of Physics, Laboratory of Astrophysics, École Polytechnique Fédérale de Lausanne, Observatoire de Sauverny, CH-1290 Versoix, Switzerland*
[4] *Centre for Extragalactic Astronomy, Department of Physics, Durham University, South Road, Durham DH1 3LE, UK*

Accepted —. Received —; in original form —

ABSTRACT

We present a sample of over 100 highly X-ray luminous galaxy clusters at $z \approx 0.5$–0.9, discovered by the extended Massive Cluster Survey (eMACS) in *ROSAT* All-Sky Survey (RASS) data. Follow-up observations of a subset at higher resolution and greater depth with the *Chandra X-ray Observatory* are used to map the gaseous intra-cluster medium, while strong-gravitational-lensing features identified in *Hubble Space Telescope* imaging allow us to constrain the total mass distribution. We present evidence of the exceptional gravitational-lensing power of these massive systems, search for substructure along the line of sight by mapping the radial velocities of cluster members obtained through extensive ground-based spectroscopy, and identify dramatic cases of galaxy evolution in high-density cluster environments. The available observations of the eMACS sample presented here provide a wealth of insights into the properties of very massive clusters ($\gtrsim 10^{15}$ M$_\odot$) at $z > 0.5$, which act as powerful lenses to study galaxies in the very distant Universe. We also discuss the evolutionary state, galaxy population, and large-scale environment of eMACS clusters and release to the community all data and science products to further the understanding of the first generation of truly massive clusters to have formed in the Universe.

Key words: gravitational lensing: strong – galaxies: clusters: general

1 INTRODUCTION

Occupying the top spot in the mass-ranked hierarchy of gravitationally collapsed structures in the Universe, massive galaxy clusters play a unique role in numerous areas of astrophysical and cosmological research: they allow us to study the evolution and interaction of baryonic and non-baryonic matter across a wide range of environments and redshifts (e.g., Vikhlinin et al. 2001; Markevitch et al. 2002; Harvey et al. 2015; Ebeling et al. 2017; van Weeren et al. 2019), act as powerful gravitational telescopes that magnify faint background sources out to the very highest redshifts (e.g., Kneib & Natarajan 2011, and references therein), and provide independent constraints on fundamental cosmological parameters (e.g., Vikhlinin et al. 2009; Allen et al. 2011; Planck Collaboration et al. 2014; Mantz et al. 2015; Bocquet et al. 2019). Importantly, they also provide valuable opportunities to observe and understand the evolution of galaxies in high-density environments, from ram-pressure stripping of infalling galaxies (e.g., Gunn & Gott 1972; Vollmer et al. 2001; Cortese et al. 2007; Ebeling et al. 2014; Boselli et al. 2022) to the mechanisms driving the growth of central cluster galaxies (e.g., Oemler 1976; Merritt 1985; Dubinski 1998; De Lucia & Blaizot 2007; McDonald et al. 2016).

The ability to quantify changes in the ensemble properties of the population of massive clusters with lookback time is crucial for many of the aforementioned science applications. However, attempts to constrain the physical properties of massive clusters, primarily their mass and relaxation state, at ever-increasing redshifts face the obvious challenge that the most massive clusters ($M \gtrsim 10^{15}$ M$_\odot$) have not had time to form in significant numbers beyond their typical redshift of formation, commonly thought to be $z \sim 1$. As a result, observational studies of such systems beyond the local Universe have, so far, been limited to extreme clusters at the median redshift of $z \sim 0.45$ probed by the X-ray-based[1] Massive Cluster Survey (MACS; Ebeling et al. 2001, 2007, 2010; Mann & Ebeling 2012; Repp & Ebeling 2018). At significantly higher redshifts, studies frequently use the term "massive cluster" loosely, sampling systems of average mass ($\sim 10^{14}$ M$_\odot$), such as those detected in surveys exploiting the Sunyaev-Zel'dovich (SZ; Sunyaev & Zeldovich 1980) effect (Bleem et al. 2020; Hilton et al. 2021) or in all-sky infrared surveys (Gonzalez et al. 2019), or targeting the precursors of today's massive clusters (in their infancy) at redshifts well beyond unity (e.g., Steidel et al. 1998; Papovich et al. 2010; Gobat et al. 2011; Newman et al. 2014; Wang et al. 2016; Morishita et al. 2023).

The extended Massive Cluster Survey (eMACS; Ebeling et al. 2013), described below, was designed to push X-ray searches for very massive clusters to the highest possible redshifts without lowering

★ E-mail: alastair.edge@durham.ac.uk

[1] An X-ray luminosity of 10^{45} erg s^{-1} (0.1–2.4 keV) corresponds to a cluster mass of 10^{15} M$_\odot$ (e.g. Lovisari et al. 2020, and references therein).

© 2024 The Authors

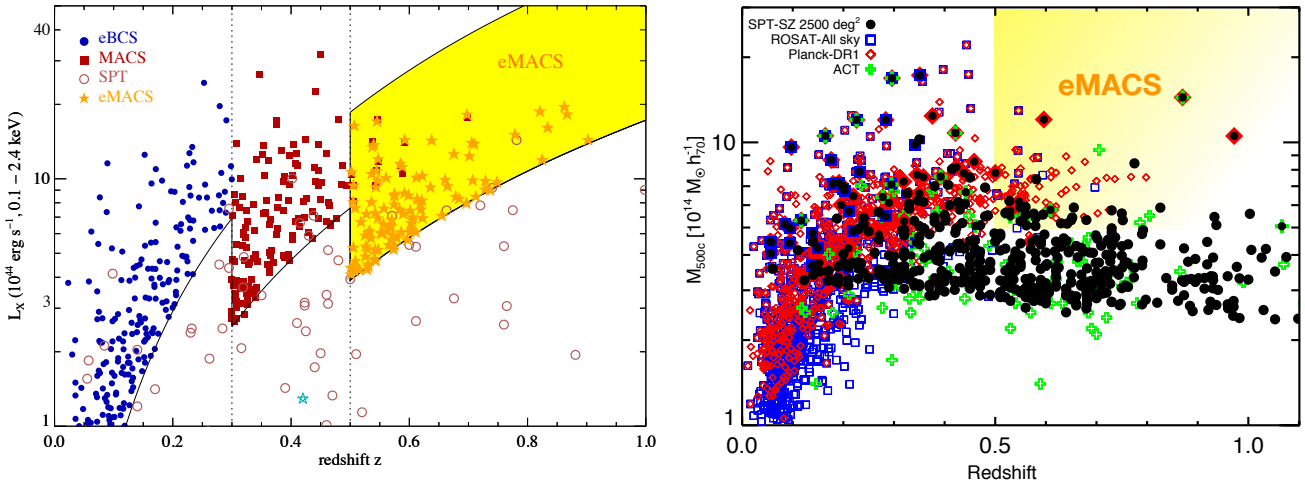

Figure 1. Left: Distribution of X-ray luminosity vs redshift for cluster samples compiled from RASS data, as well as for SZ-selected samples. Right: Mass estimates versus redshift for galaxy clusters from SZ and and X-ray selected samples (adapted from Bleem et al. 2015). eMACS complements existing surveys by focusing on the high-mass, high-redshift regime. Although total masses are not available for all clusters shown in the left-hand plot, the equivalence of an X-ray luminosity of 10^{45} erg s^{-1} (0.1–2.4 keV) and a total mass of 10^{15} $M_\odot$ is well established for galaxy clusters (e.g., Applegate et al. 2014).

the absolute mass threshold of $\sim 10^{15}$ $M_\odot$ set at $z > 0.3$ by MACS (Applegate et al. 2014). We here present the eMACS sample as it stands, including an overview of optical, radio, and X-ray follow-up observations of eMACS clusters performed to date. Based on the available data, we give first assessments of the physical properties (mass, evolutionary state, large-scale environment etc) of all eMACS clusters for which sufficient high-quality data, from both ground- and space-based follow-up observations, are in hand.

This paper is structured as follows. After this brief introduction, we provide an overview of the eMACS project in Section 2, summarize follow-up observations in Section 3, and describe the methods used to analyze the reduced data in Section 4. Section 5 presents the results obtained for the physical properties of eMACS clusters, followed by our conclusions in Section 6. More technical details about the compilation of the eMACS sample from X-ray and optical survey data can be found in Appendix A, while Appendix B serves as a repository for summaries of key observational findings for each cluster.

We assume the ΛCDM concordance cosmology, i.e., $\Omega_m = 0.3$, $\Omega_\Lambda = 0.7$, and $H_0 = 100h$ km s^{-1} Mpc^{-1}, with $h = 0.7$.

2 EMACS

The distant clusters presented and discussed here were all discovered (or, in a few cases, re-discovered) in the course of the extended Massive Cluster Survey, eMACS. An X-ray selected cluster survey based on *ROSAT* All-Sky Survey data (RASS; Voges et al. 1999) within a solid angle of over 20,000 deg^2, defined by $|b| > 20°$, $\delta > -30°$, eMACS extends similar work at lower redshifts (e.g., Ebeling et al. 1997; De Grandi et al. 1999; Ebeling et al. 2000, 2001; Reiprich 2001; Ebeling et al. 2002; Böhringer et al. 2004; Ebeling et al. 2007, 2010, 2013; Böhringer et al. 2013) to $z > 0.5$ in an attempt to find the first generation of truly massive clusters out to redshifts approaching unity.

Fig. 1 shows the X-ray luminosity, mass, and redshift regime explored by eMACS in comparison with other cluster surveys. The RASS flux limits of the eBCS (Ebeling et al. 2000), MACS, and eMACS surveys are 3×10^{-12}, 10^{-12}, and 0.5×10^{-12} erg cm^{-2} s^{-1} (0.1–2.4 keV), respectively. By design, eMACS finds clusters that are as X-ray luminous as the most extreme systems discovered in the eBCS and MACS surveys, but at yet higher redshift. Solid angle is crucial in this context; while the South Pole Telescope (SPT; Carlstrom et al. 2011), a facility designed for the detection of the SZ effect in clusters, is capable of detecting clusters with constant efficiency at all redshifts, the much smaller solid angle covered by the SPT surveys prevents it from finding exceptionally massive clusters in significant numbers. The commonalities and differences between SZ- and X-ray cluster surveys in mass-redshift space are summarized in Fig. 1 which also shows the cluster samples compiled by the SPT, the Atacama Cosmology Telescope (ACT; Swetz et al. 2011), and the Planck satellite. Although Planck covered the entire sky, the mission's limited angular resolution results in a selection that is biased against clusters even at modest redshift (Malte Schäfer & Bartelmann 2007; Bleem et al. 2015), creating a strongly redshift-dependent selection function more similar to that of RASS-based cluster samples at moderate redshifts than those of high-resolution SZ surveys such as those conducted with the SPT and ACT. As illustrated in Fig. 1, eMACS does not compete with, but instead complements, SZ cluster surveys.

In a nutshell, the eMACS sample was compiled as follows. Candidates were selected from the RASS source catalogue[2] based on very few, simple X-ray selection criteria (beyond the mentioned cuts in Galactic and equatorial latitude, cuts in the spectral X-ray hardness ratio and in the RASS flux in the 0.1–2.4 keV band were applied; see Appendix A for details). Next, visual inspection of optical images covering a $5' \times 5'$ area around each source in the publicly available data obtained by the PanSTARRS (PS) facility (Kaiser et al. 2002), specifically the PS1 3π survey (Chambers et al. 2016), was used to identify plausible clusters as either overdensities of faint galaxies of similar colour or fields that appear blank to the depth of the PS 3π data. We refer the reader to Appendix A for more details. As a final step, spectroscopic follow-up observations of this tentative cluster sample were conducted to limit the sample to clusters at a redshift of $z > 0.5$. Results from an eMACS pilot project were presented

[2] Note that eMACS, unlike MACS, draws not only from the RASS Bright Source Catalogue but also from the Faint Source Catalogue.

name	z	n_z	t_{ACIS-I} (ks)	JVLA observed	HST passbands							
eMACSJ0014.9−0056	0.5330	18	30	Y		F606W			F110W		F140W	
MACSJ0018.5+1626	0.5473	-	67	Y	F435W	F606W	F814W	F105W		F125W	F140W	F160W
MACSJ0025.4−1222	0.5848	-	158	Y	F435W		F814W	F105W		F125W	F140W	F160W
eMACSJ0026.2+0120	0.6357	22		Y		F606W	F814W		F110W		F140W	
eMACSJ0027.0+1252	0.6063	22		-					F110W		F140W	
eMACSJ0030.5+2618	0.4970	20	18	Y		F606W	F814W		F110W		F140W	
eMACSJ0031.2+1907	0.5304	20		-		F606W			F110W		F140W	
eMACSJ0042.5−1103	0.5701	13	12	-			F814W		F110W		F140W	
eMACSJ0043.1−1129	0.7282	19		-		F606W	F814W		F110W		F140W	
eMACSJ0045.2−0151	0.5471	15	49	Y					F110W		F140W	
eMACSJ0101.1+1831	0.6533	23		Y		F606W	F814W		F110W		F140W	
eMACSJ0121.4+2143	0.6011	17		-		F606W	F814W		F110W		F140W	
eMACSJ0122.7+1454	0.5469	15		-					F110W		F140W	
eMACSJ0124.0+0430	0.5363	14		-		F606W						
eMACSJ0127.5−0606	0.5055	14		-					F110W		F140W	
eMACSJ0135.2+0847	0.6185	38	12	Y					F110W		F140W	
eMACSJ0153.4+1722	0.5464	21		-		F606W						
eMACSJ0200.3−2454	0.7126	25		-								
eMACSJ0224.5−1615	0.6223	15		-					F110W		F140W	
eMACSJ0241.0+2557	0.5752	22		-		F606W			F110W		F140W	
eMACSJ0248.2+0237	0.5561	19	45	-					F110W		F140W	
eMACSJ0252.4−2100	0.7017	26		-					F110W			
eMACSJ0256.7−1623	0.8621	18	33	Y		F606W	F814W		F110W		F140W	
eMACSJ0256.9−1631	0.8670	17	33	Y		F606W	F814W		F110W		F140W	
MACSJ0257.1−2325	0.5056	-	38	Y	F435W	F606W	F814W	F105W		F125W	F140W	F160W
eMACSJ0324.0+2421	0.9023	26	31	-	F435W	F606W	F814W	F105W		F125W	F140W	F160W
eMACSJ0325.4−0359	0.5721	12		-					F110W		F140W	
eMACSJ0403.6+1544	0.5275	20		-		F606W	F814W		F110W		F140W	
eMACSJ0429.0−1011	0.5418	10		-					F110W		F140W	
MACSJ0454.1−0300	0.5376	-	14	Y			F814W	F105W	F110W	F125W	F140W	F160W
eMACSJ0502.9−2902	0.6028	23	49	-		F606W	F814W		F110W		F140W	
MACSJ0647.7+7015	0.5922	-	39	Y	F435W	F606W	F814W	F105W	F110W	F125W	F140W	F160W
MACSJ0717.5+3745	0.5454	-	243	Y	F435W	F606W	F814W	F105W	F110W	F125W	F140W	F160W
eMACSJ0742.9+5001	0.6013	15		-		F606W	F814W		F110W		F140W	
MACSJ0744.8+3927	0.6976	-	90	Y	F435W	F606W	F814W	F105W	F110W	F125W	F140W	F160W
eMACSJ0747.0+6937	0.5696	13		-		F606W	F814W		F110W		F140W	
eMACSJ0804.6+5325	0.5786	20	4	-		F606W	F814W		F110W		F140W	
eMACSJ0834.2+4524	0.6606	32	33	Y		F606W	F814W		F110W		F140W	
eMACSJ0840.2+4421	0.6377	39	32	Y		F606W	F814W		F110W		F140W	
eMACSJ0841.8−0429	0.5359	11		-		F606W	F814W		F110W		F140W	
eMACSJ0850.2−0611	0.5744	22		-		F606W	F814W		F110W		F140W	
eMACSJ0910.8+3850	0.5618	19		-		F606W	F814W		F110W		F140W	
MACSJ0911.2+1746	0.5051	-	42	Y	F435W		F814W	F105W		F125W	F140W	F160W
eMACSJ0921.6−0621	0.6842	15		Y		F606W	F814W		F110W		F140W	
eMACSJ0934.6+0540	0.5627	15		-		F606W			F110W		F140W	
eMACSJ0935.1+0614	0.7787	21	30	Y		F606W	F814W		F110W		F140W	
eMACSJ0943.3−1842	0.5687	12		Y		F606W	F814W		F110W		F140W	
eMACSJ1025.0−1354	0.6196	13		-		F606W	F814W		F110W		F140W	
eMACSJ1027.2+0345	0.7482	10		Y		F606W	F814W		F110W		F140W	

Table 1. The eMACS sample at the time of publication; we list the cluster redshift, the number of spectroscopic redshifts measured, and the HST passbands in which imaging data were obtained. We also indicate which clusters were observed with the JVLA at 5 GHz to date. The 12 eMACS clusters released earlier as part of the MACS sample (Ebeling et al. 2007) are listed for completeness' sake (n_z entries are deliberately omitted for these 12 clusters).

in Ebeling et al. (2013), and an assessment of the lensing power of eMACS clusters is provided by Zalesky & Ebeling (2020).

References to the "current" eMACS sample are motivated by the sample's incompleteness, both with regard to the optical screening of all cluster candidates identified in the X-ray selection process described in Appendix A and with regard to the spectroscopic confirmation of these candidates. However, in light of the progress made in the compilation of cluster samples from the RASS' successor, the next-generation X-ray all-sky survey *eROSITA* (e.g., Chiu et al. 2023), we opt for releasing the current eMACS sample (together with all supporting follow-up data) to prevent unnecessary investments of observing time into the confirmation and characterization of *eROSITA* detections that merely duplicate prior eMACS discoveries and results.

Table 1 lists all 111 entries in the current eMACS sample and provides an overview of selected follow-up observations performed to date (see Sections 3.2 and 3.4 for details). Fig. 2 shows the location of all clusters on the sky and demonstrates that the incompleteness of the sample presented here is not a strong function of celestial position, either in Galactic or equatorial coordinates.

3 OBSERVATIONS AND DATA REDUCTION

3.1 Groundbased imaging

By design, all eMACS clusters are covered in five optical passbands ($g'r'i'z'y'$) in the PS1 3π survey (Chambers et al. 2016). Although crucial for the identification of clusters among the many faint X-ray sources in the RASS, the PS1 3π imaging data are too shallow to serve more ambitious purposes.

Consequently, we obtained short (~300s) observations of all eMACS clusters to a limiting magnitude of approximately 23 (AB) through the g', r', and i' filters[3] with the GMOS imaging spectro-

[3] For a small number of clusters, imaging with GMOS was also obtained in the z' passband.

name	z	n_z	t_{ACIS-I} (ks)	JVLA observed	HST passbands							
eMACSJ1030.5+5132	0.5182	23	20	Y		F606W	F814W		F110W		F140W	
eMACSJ1050.6+3548	0.5077	39		Y		F606W	F814W					
eMACSJ1057.5+5759	0.6027	12		-		F606W	F814W		F110W		F140W	
eMACSJ1131.1+3553	0.5159	12		Y		F606W	F814W		F110W		F140W	
eMACSJ1136.8+0005	0.5968	26	4	Y		F606W	F814W		F110W		F140W	
eMACSJ1144.2−2836	0.5070	30	31	Y		F606W	F814W		F110W		F140W	
eMACSJ1148.0+5116	0.5834	28		Y		F606W	F814W		F110W		F140W	
MACSJ1149.5+2223	0.5445	-	366	Y	F435W	F606W	F814W	F105W	F110W	F125W	F140W	F160W
eMACSJ1157.9−1046	0.5570	25	156	-	F435W		F814W		F110W		F140W	
eMACSJ1209.4+2640	0.5553	22	16	Y				F105W	F110W		F140W	F160W
eMACSJ1212.5−1216	0.6786	28		Y			F814W		F110W		F140W	
eMACSJ1222.3+2418	0.5085	14		Y		F606W			F110W		F140W	
eMACSJ1248.2+0743	0.5733	15		-		F606W	F814W		F110W		F140W	
eMACSJ1251.3+3131	0.5069	16		-		F606W	F814W		F110W		F140W	
eMACSJ1257.3+3654	0.5253	14		-		F606W			F110W		F140W	
eMACSJ1341.9−2442	0.8339	26	34	Y		F606W	F814W	F105W	F110W	F125W	F140W	F160W
eMACSJ1350.7−1055	0.8247	12	33	Y								
eMACSJ1353.7+4329	0.7364	31	40	Y	F435W	F606W	F814W	F105W		F125W	F140W	F160W
eMACSJ1407.0−0015	0.5520	14	4	Y		F606W	F814W					
eMACSJ1414.7+5446	0.6121	26	33	-		F606W	F814W		F110W	F125W	F140W	F160W
eMACSJ1419.1−0624	0.5432	22		Y			F814W		F110W		F140W	
eMACSJ1419.2+5326	0.6384	32		-			F814W		F110W		F140W	
MACSJ1423.8+2404	0.5434	-	19	Y	F435W	F606W	F814W	F105W	F110W	F125W	F140W	F160W
eMACSJ1430.0+4127	0.6646	13		Y		F606W	F814W		F110W		F140W	
eMACSJ1437.8+0616	0.5350	19		-		F606W			F110W		F140W	
eMACSJ1443.2+0102	0.5284	23		Y		F606W	F814W		F110W		F140W	
eMACSJ1508.1+5755	0.5421	48	49	Y		F606W	F814W		F110W		F140W	
eMACSJ1518.3+2927	0.6050	33		Y		F606W	F814W		F110W		F140W	
eMACSJ1523.1+1329	0.5010	18		-		F606W	F814W		F110W		F140W	
eMACSJ1527.6+2044	0.6967	28	25	Y	F435W	F606W	F814W	F105W	F110W	F125W	F140W	F160W
eMACSJ1621.2−0231	0.5014	9		Y		F606W	F814W		F110W		F140W	
eMACSJ1621.4+7232	0.5863	34		Y		F606W	F814W		F110W		F140W	
eMACSJ1631.1+1528	0.5087	11		Y		F606W	F814W		F110W		F140W	
eMACSJ1709.5+4731	0.5527	40		Y		F606W	F814W		F110W		F140W	
eMACSJ1732.4+1934	0.5406	41		Y		F606W	F814W		F110W		F140W	
eMACSJ1756.8+4008	0.5743	117	89	Y	F435W	F606W	F814W	F105W	F110W	F125W	F140W	F160W
eMACSJ1757.5+3045	0.6105	32		Y		F606W	F814W		F110W		F140W	
eMACSJ1823.1+7822	0.6754	20	22	Y	F435W	F606W	F814W	F105W	F110W	F125W	F140W	F160W
eMACSJ1831.1+6214	0.8207	25	23	Y		F606W	F814W		F110W		F140W	
eMACSJ1831.9+5746	0.7072	15		Y		F606W	F814W		F110W		F140W	
eMACSJ1852.0+4900	0.6035	32	20	Y		F606W	F814W		F110W		F140W	
eMACSJ2018.3−2242	0.5302	20		Y		F606W	F814W		F110W		F140W	
eMACSJ2020.1−1432	0.5653	22		-		F606W	F814W		F110W		F140W	
eMACSJ2025.5−2313	0.7098	19		Y		F606W	F814W		F110W		F140W	
eMACSJ2026.7−1920	0.6219	40	32	Y		F606W	F814W		F110W		F140W	
eMACSJ2037.1−2534	0.5263	36		Y		F606W	F814W		F110W		F140W	
eMACSJ2045.8−2438	0.5917	20		-			F814W		F110W		F140W	
eMACSJ2100.4+0724	0.5742	13		-		F606W	F814W		F110W		F140W	
eMACSJ2114.4+0427	0.5898	20		Y		F606W	F814W		F110W		F140W	
MACSJ2129.4−0741	0.5879	-	40	Y	F435W	F606W	F814W	F105W	F110W	F125W	F140W	F160W
eMACSJ2137.2−2232	0.6131	23		Y		F606W	F814W		F110W		F140W	
eMACSJ2201.9+0711	0.5633	11		-		F606W	F814W		F110W		F140W	
eMACSJ2207.5−0302	0.5304	21		Y		F606W	F814W		F110W		F140W	
MACSJ2214.9−1359	0.5022	-	38	Y			F814W	F105W		F125W		F160W
eMACSJ2220.3−1211	0.5292	35	12	-		F606W	F814W		F110W		F140W	
eMACSJ2229.9−0808	0.6214	65		Y		F606W	F814W		F110W		F140W	
eMACSJ2236.0+3451	0.7287	25		-		F606W	F814W		F110W		F140W	
eMACSJ2315.3−2128	0.5400	43	31	-		F606W	F814W		F110W		F140W	
eMACSJ2316.6+1246	0.5258	32		Y		F606W	F814W		F110W		F140W	
eMACSJ2320.9+2912	0.4960	45	10	-			F814W		F110W		F140W	
eMACSJ2327.4−0204	0.7055	24	146	Y	F435W	F606W	F814W			F125W		F160W
eMACSJ2351.6−2818	0.5679	18		-		F606W			F110W		F140W	

Table 1. continued.

graph on the 8m Gemini-North telescope on Maunakea. Extending to over 1 Mpc in radius from the centre of a cluster at $z > 0.5$, the 5.5′ field of view of GMOS offers a comprehensive view of the projected spatial distribution of likely cluster galaxies (as identified from their characteristic red-sequence colours) and allowed the efficient selection of targets for the spectroscopic follow-up observations described in Section 3.3. A more detailed description of the GMOS imaging survey of eMACS clusters, as well as of the associated data reduction techniques, is provided in the context of the mass-traces-light algorithm AStroLens that provided a first assessment of the gravitational-lensing strength of eMACS clusters (Zalesky & Ebeling 2020).

3.2 *HST* imaging

Optical and near-infrared imaging with high angular resolution and low sky background is critical for several key science goals of the eMACS project, most notably the detection of strong-gravitational-lensing features, as well as dust and star formation in brightest cluster galaxies (BCGs), and ram-pressure stripping of "jellyfish" galaxies.

To achieve these objectives, eMACS clusters were observed with

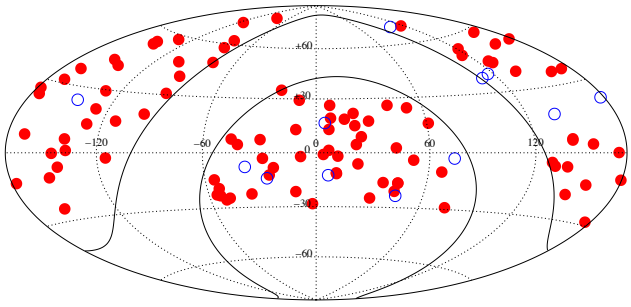

Figure 2. The distribution of eMACS clusters in the equatorial sky. The 12 clusters also included in the MACS sample and presented previously in Ebeling et al. (2007) are shown as open symbols. Solid lines delineate the 40-deg wide exclusion zone around the Galactic plane. While the statistical completeness of eMACS has not been quantified, the distribution of clusters across the surveyed solid angle is approximately isotropic.

the Advanced Camera for Surveys (ACS) and the Wide-Field Camera 3 (WFC3) aboard the *Hubble Space Telescope* (*HST*) in four SNAPshot programs (GO-13671, GO-14098, GO-15132, and GO-15843). In addition, eMACS clusters of special interest were targeted by us in dedicated *HST* imaging campaigns (GO-15466, GO-15608, GO-15844, GO-16428) that added either depth or area on the sky to existing SNAPshot data. A number of eMACS clusters were also observed independently by other teams.

The listed SNAPshot programmes requested imaging observations in four passbands: F606W and F814W (ACS; 1200s each), as well as F110W and F140W (WFC3; 700s each), although the random nature of SNAPshot surveys meant that not all clusters were observed in all passbands. Imaging was also performed in the F435W passband of ACS, as well as the WFC3 near-infrared filters F105W, F125W, and F160W, in targeted GO observation awarded to us or other teams. An overview of the available *HST* data in these eight passbands is provided in Table 1. Except for eMACSJ0200.3 which has no *HST* imaging, all eMACS clusters were observed in at least one passband[4],

All *HST* data were reduced using standard procedures. Specifically, all available *HST* images for a given field were corrected for geometric distortions and mapped to a common coordinate frame tied to the Gaia astrometric reference frame, using the TweakReg and AstroDrizzle packages (Fruchter & et al. 2010). False-colour RGB images[5] were then created using the same colour table, scaling, and limits for all fields. We used SExtractor (Bertin & Arnouts 1996) to generate source catalogues and to obtain photometry in the three chosen passbands. Cluster members were tentatively identified as members of the red sequence (e.g., Visvanathan & Sandage 1977; Bower et al. 1992) based on colour-magnitude diagrams. We refer the reader to Basto et al. (in preparation) for additional details.

We note that, since the vast majority of the *HST* images were obtained in randomly selected SNAPshot observations, the resulting *HST* imaging dataset can be considered unbiased and representative of the eMACS sample as a whole. A mild bias is introduced, however, by our efforts to secure multi-passband coverage (or greater observational depth) for clusters showing exceptional strong-lensing features in the SNAPshot observations.

[4] Scheduled *HST* observations of eMACSJ1350.7 were canceled by the proposers after *CXO* observations of the field failed to detect diffuse X-ray emission, thereby ruling out the presence of a galaxy cluster (see Section 5.1.2).
[5] Whenever possible (see Table 1), we use the F606W, F814W, and F110W images to populate the B, G, and R channels, respectively.

3.3 Optical and near-infrared spectroscopy

Extensive spectroscopic follow-up observations were conducted to target presumed cluster members, potential strong-lensing features, and likely counterparts of X-ray point sources (detected in the *CXO* observations described in Section 3.4) in the eMACS cluster fields. These observations were performed with the DEep Imaging Multi-Object Spectrograph (DEIMOS; Faber et al. 2003), the Low-Resolution Imaging Spectrometer (LRIS; Oke et al. 1995), and the Multi-Object Spectrometer For Infra-Red Exploration (MOSFIRE; McLean et al. 2010, 2012) on the Keck-1 and -2 10m telescopes on Maunakea, Hawai'i. The individual multi-object spectroscopy targets were selected from *HST*, GMOS, PS1/3π, and *CXO* observations. Whenever possible (i.e., depending on the availability and quality of *HST* and *CXO* data), priority was given to redshifts measurements of likely strong-lensing features and X-ray point sources, with the remainder of the mask being used to target probable cluster members (selected by their colours). In the following we briefly summarize the instrumental setup for the three spectrographs used.

DEIMOS: 1″ slit width; 600 line mm^{-1} grating; GG455 order-blocking filter; central wavelength 6300Å; 1.2Å pixel^{-1} sampling;
LRIS: 1″ slit width; D680 dichroic; 300/5000 grism (8.8Å FWHM resolution, red arm); 600/7500 grating and central wavelength 8100Å (4.7Å resolution, blue arm);
MOSFIRE: 0.7″ slit width; *I*, *J*, *K*, and / or *H* band, depending on the expected wavelength of emission-line features; ABBA dither pattern with (typically) 1.5″ offset; 2.8Å pixel^{-1} sampling.

Exposure times ranged from approximately 1800s to several hours, depending on atmospheric conditions, airmass, and the faintness of the primary targets on a given MOS mask. We typically observed all targets first in the optical window and then added near-infrared spectroscopy with MOSFIRE only for strong-lensing features for which no identifiable features were detected in prior observations with LRIS or DEIMOS.

Most of the DEIMOS spectra were reduced using a modified version of the DEEP2 pipeline (Cooper et al. 2012; Newman et al. 2013), with more recently acquired data having been processed with the PypeIt package (Prochaska et al. 2020). An early version of PypeIt was also used to reduce the LRIS data, while the MOSFIRE data reduction was mostly performed with the pipeline designed by the MOSFIRE commissioning team and written by Nick Konidaris with extensive checking and feedback from Chuck Steidel and other MOSFIRE team members (Steidel et al. 2014) .

Although we aimed at obtaining, for each eMACS cluster, at least 20 spectroscopic redshifts of cluster members as well as spectroscopic confirmation of at least one gravitational-lensing feature, weather patterns on Maunakea and the vagaries of the telescope-time allocation process introduced seasonal biases. We also deliberately devoted extra resources to the spectroscopic follow up of eMACS clusters of particular interest, e.g., the most distant ones, the most obvious and most spectacular gravitational lenses, or the most extreme mergers. As a result, the spectroscopic coverage of the sample presented here is uneven, as is apparent from the number of redshifts obtained for each cluster listed in Table 1.

3.4 X-ray imaging spectroscopy

We searched the public archive CHASER[6] for data collected for eMACS clusters with the Advanced CCD Imaging Spectrometer

[6] https://cda.harvard.edu/chaser/

(ACIS) aboard the *Chandra X-ray Observatory* (*CXO*); for consistency, we retrieved and analyzed only observations performed with the instrument's ACIS-I array in VFAINT mode. Of the resulting list of 47 eMACS clusters observed (see Table 1), the majority were targeted by the eMACS team (PI Ebeling), with most of the remainder having been selected as part of follow-up observations of detections of the Sunyaev-Zeldovich effect. Excluding the 12 systems at $z > 0.5$ discovered previously by the MACS project (Ebeling et al. 2007) and discussed extensively in the literature (e.g., LaRoque et al. 2003; Ebeling et al. 2007; Bradač et al. 2008; Zitrin et al. 2011; Limousin et al. 2012; Ogrean et al. 2016; Wilber et al. 2018; Jauzac et al. 2018), we are left with 35 new systems. For each cluster we reduce and then merge all available observational datasets.

We emphasize that the resulting subset of eMACS clusters with *CXO*/ACIS-I data is not representative of the full sample but reflects the scientific interests and target selection criteria put forward by the authors of the underlying *CXO* proposals. As a result, biases in favour of the most X-ray luminous, the most distant, and the most disturbed clusters are introduced; additional biases may be present but remain unknown to us.

Our data reduction extensively uses routines from the CIAO software environment (Fruscione et al. 2006) and largely follows established procedures, beginning with the reprocessing and reprojecting of the archival data, before removing time intervals affected by background flares (we first examine the high-energy 9–12 keV band, then the entire ACIS-I passband). We subsequently identify X-ray point sources as detected by the WAVDETECT source-detection algorithm (Freeman et al. 2002) but employ a visual check to ensure the validity of all point sources in the automatically generated source list.

Since our analysis is similar to the process described in detail in the literature (e.g., Mahler et al. 2023; Beauchesne et al. 2024); we here provide only a brief summary. For each observation, we retrieve the associated ACIS-I blank-sky background from the public archive and compute the response of the instruments within a circle of radius 1 Mpc, initially centred on the cluster position in the RASS source catalogue. To model the background emission (both instrumental and sky backgrounds), we use an empirical model consisting of B-spline functions. For each observation, we build this model by first fitting the blank-sky spectrum for each CCD in the 0.1–13 keV band. We then use a linear combination of these models to define a background model per observation as a linear combination of the CCD models. This linear combination is optimised on the blank-sky spectrum of the chosen cluster region by keeping all coefficients frozen for the spectral fit of the cluster and optimizing only one global amplitude per observation. This procedure allows us to estimate the scaling between the science and the blank-sky observations without relying on the observing time or the particle background. More details about the background estimation can be found in Appendix A of Beauchesne et al. (2024).

3.5 Radio observations

The majority of the clusters presented here (see Table 1) were observed with the Jansky VLA in B-array at 5 GHz in 2016 as part of a larger campaign to observe MACS and eMACS clusters to search for activity in the BCG and other cluster members (PI Edge, 16A-167). All targets were observed in two visits of 300s each, separated by 60–80 mins, with an associated, nearby phase calibrator. These observations reach a consistent noise level of $\sim 30\ \mu$Jy per beam and a resolution of $\sim 2.0''$ that depends weakly on declination.

4 ANALYSIS

4.1 Galaxy spectroscopy

Redshifts were measured and corrected to the heliocentric frame using an adaptation of the SPECPRO package (Masters & Capak 2011). We determined cluster velocity dispersions with the ROSTAT software developed by Beers et al. (1990).

4.2 X-ray imaging spectroscopy

To determine fundamental physical parameters of the ICM emission recorded with *CXO*, we proceed as follows. The overall spectral model is the combination of the previously defined empirical background with a physical model of the cluster emission; we adopt a single-temperature plasma, represented by a single APEC model (Astrophysical Plasma Emission Code, XSAPEC) with solar abundance ratios from Asplund et al. (2009) and photoelectric absorption parameterized by the column density of neutral hydrogen ($n_{\rm H}$) along the line of sight (XSPHABS). We fit the combined spectrum to the data in the 0.5–7 keV range using the nested-sampling algorithm provided in the MULTINEST package (Feroz et al. 2019) through its Python wrapper (Buchner et al. 2014). During this fit, the density, temperature (kT), and metallicity (Z) of the intracluster medium (ICM) are allowed to vary, in addition to the background normalisation. Since $n_{\rm H}$ is poorly constrained for most clusters, we set it to the Galactic value provided by the HI4PI project (HI4PI Collaboration et al. 2016).

We perform the spectral fitting within a circular area that is determined iteratively. We start by fitting the data within a circle of radius 1 Mpc around the RASS position of each eMACS cluster. From the posterior distribution of the ICM temperature and the cluster redshift, we derive the distributions of r_{1000} and M_{1000} using the relation provided in Arnaud et al. (2002). We also compute the centroid of the X-ray emission within the initial fitting area of 1 Mpc with the python package PYPROFFIT (Eckert et al. 2020) and then define a new extraction region around this centroid position, with a radius given by the median of the r_{1000} distribution. We repeat this process until the new r_{1000} median is included in the median-centred interval of 68 per cent of the previous distribution, and the associated emission centroids are similar. We do not quantitatively monitor the convergence of the centre position, but require the previous centre position to be within 6 arcsec of the new one. In most cases, the differences in the location of the centroid between fits are of the order of 1 arcsec or less. The resulting values of r_{1000} range approximately from 500 to 1000 kpc for our sample.

The spatial distribution of the X-ray emission from eMACS clusters observed with *CXO* is, in all figures in this paper, represented by the isointensity contours of the X-ray surface brightness after adaptive smoothing to 3σ significance with the ASMOOTH algorithm (Ebeling et al. 2006).

4.3 Strong gravitational lensing

We use the multi-band high-resolution images obtained with *HST* (all but four eMACS clusters were observed with *HST* in at least two passbands; see Section 3.2 and Table 1) to identify potential strongly lensed images based on their similarity in colours and morphologies. The corresponding sources were given high priority for the spectroscopic follow-up observations described in Section 3.3. For the strong-lensing analysis described below we consider the subset of 25

eMACS clusters with at least one multiple-image system confirmed by spectroscopic redshifts.

We use the Lenstool software (Jullo et al. 2007) to create lens models by parameterising the mass distribution of each cluster as a combination of double Pseudo Isothermal Elliptical (dPIE) mass profiles at both large (cluster) and small (galaxy) scales. Following similar work on large cluster samples (e.g., Richard et al. 2010, 2021), we optimise the set of parameters of large-scale dPIE components to best reproduce the locations of the confirmed multiple-image systems in each cluster. To account for the mass in small-scale components, we include each cluster member (selected from the red sequence) as a galaxy-scale perturber of the overall mass distribution. We fix these galaxies' geometric parameters (centre, ellipticity, position angle) at the values in the *HST* photometric catalogue, while the remaining parameters of these small-scale dPIEs (velocity dispersion, cut and core radii) are assumed to follow a light-traces-mass relation with their luminosity.

5 RESULTS AND DISCUSSION

In the following we present our findings on the gravitational-lensing strength (as estimated from our strong-lensing analysis), the properties of the ICM, and the galaxy population of eMACS clusters.

We stress again that the eMACS sample presented here is not statistically complete; in addition, the sample's coverage in follow-up observations (be it galaxy spectroscopy, *HST* imaging, or X-ray imaging spectroscopy with *CXO*) is currently inhomogeneous. Given these limitations, the goal of this paper is not a comprehensive characterization of the population of X-ray luminous clusters at $z > 0.5$. Rather, we aim to highlight subsets of the sample as well as individual systems that were found to be exceptional, warrant further study, or yield insights into the selection biases of cluster samples compiled at different wavelengths and using different survey techniques.

The statistical completeness (or lack thereof) of eMACS and any eMACS subsample is strongly affected by both statistical and systematic uncertainties in the RASS data from which cluster candidates were selected (see Section 2 and Appendix A for details). The most important contributors are shot noise (some RASS detections of eMACS clusters are comprised of a dozen or fewer net X-ray photons) and contamination by X-ray point sources, a systematic issue that we describe and assess in the following section.

5.1 *CXO* versus RASS

Since *ROSAT*'s effective point-spread function (PSF) is significantly broadened during the RASS compared to the on-axis PSF of the system (and can not be easily modeled, De Grandi et al. 1997), the standard source-detection algorithms used in the RASS reliably recognize only relatively nearby and X-ray bright clusters as intrinsically extended sources (Ebeling et al. 1996). Moreover, the RASS X-ray fluxes and luminosities of clusters even at $z < 0.3$ are prone to contamination from unresolved X-ray point sources, be they embedded in the cluster or physically unrelated fore- or background sources. At the far higher redshifts and dramatically poorer photon statistics probed by eMACS, the impact of X-ray point sources on our RASS-selected sample is *a priori* unquantifiable but can be measured through follow-up observations with *CXO* that allow point sources to be resolved and removed.

Fig. 3 demonstrates that eMACS delivers on the promise of Fig. 1 by showing a comparison of the cluster luminosities as observed in the RASS and in the dedicated follow-up observations performed with *CXO* of selected eMACS clusters. Here, we have removed all point sources from the *CXO* data prior to measuring the luminosity of the diffuse ICM emission, whereas (by necessity) no such correction was applied to the RASS luminosities. We find that, in general, contamination from X-ray point sources is a minor effect[7], as no significant offset from the identity relation (shown as a dotted line in Fig. 3) is seen in the correlation, and the scatter about it is largely consistent with the statistical uncertainties in the RASS-based measurements, with the exception of the four systems labeled in Fig. 3 and discussed below.

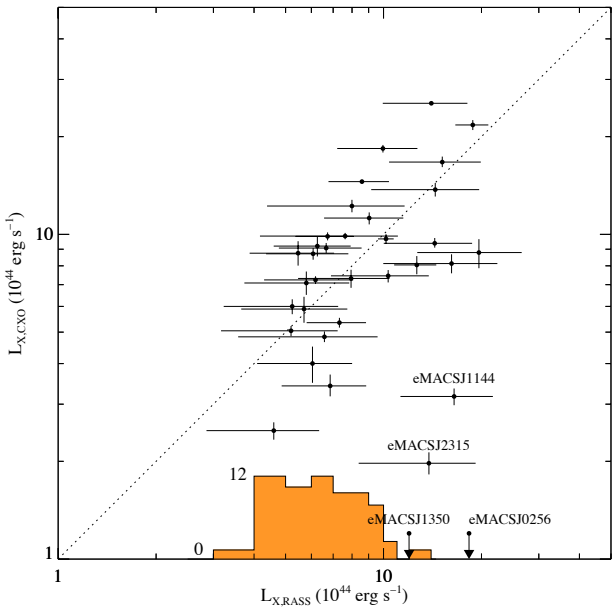

Figure 3. Comparison of eMACS cluster luminosities in the 0.1–2.4 keV band, as derived from RASS and *CXO* observations. The most extreme outliers are labelled and discussed in Section 5.1.1. Two *CXO* non-detections (see Section 5.1.2) are plotted as upper limits at fiducial *CXO* luminosities of 1.2×10^{44} erg s^{-1}. The distribution in RASS X-ray luminosity of the eMACS clusters without *CXO*/ACIS-I data is shown as a histogram. Note that X-ray point sources were removed before measuring cluster luminosities in the high-resolution *CXO* data, whereas the luminosities observed in the RASS include X-ray point sources (where present).

5.1.1 *Flux contamination*

We highlight in Fig. 3 two clusters (eMACSJ1144.2 and eMACSJ2315.3) for which the point-source corrected X-ray luminosity as measured from *CXO* observations falls below the RASS estimate by over a factor of five. Even for such outliers, however, the cause of the discrepancy is not always readily apparent. As shown in Figs. B23 and B46, several X-ray point sources contribute to the X-ray flux measured for these two clusters at the low angular resolution of the RASS; however, the total flux from all X-ray point sources out to 2′ radius from the peak of the ICM emission amounts to less than 10% of the reported RASS fluxes in Fig. 3. Then again, since many types of X-ray point sources are time variable, any of the point sources apparent in Figs. B23 and B46 could have been substantially brighter in the early 1990s when the RASS was conducted.

[7] For the sample presented here, the median flux from point sources within the RASS detect cell is less than 5×10^{-15} erg cm^{-2} s^{-1} (0.1–2.4 keV).

The degree of point-source contamination in X-ray selected cluster surveys may also depend on the mass and evolutionary state of the systems under study. Low-mass clusters and groups of galaxies are less dense and dynamically younger; as a result, late-type galaxies tend to be more prevalent and nuclear activity (in cluster members as well as in galaxies in the cluster environment) may be stronger and more common. Anecdotally, the point source contamination appears indeed to be more pronounced in the RASS-selected MACS and BCS cluster samples which, probing lower redshifts, sample a broader range of cluster masses than eMACS (e.g., Ebeling et al. 2010).

5.1.2 Misidentifications

While the relative flux contributions from the diffuse ICM and from related or unrelated point sources can be difficult to disentangle for individual clusters (but does not invalidate the presence and discovery of the respective cluster), a total absence of ICM emission renders the respective entry in our catalogue a plain misidentification.

Based on the current *CXO* follow-up observations, we are aware of two such cases: as noted in Fig. 3, eMACSJ0256.9 ($z = 0.8670$) and eMACSJ1350.7 ($z = 0.8247$) show no significant extended X-ray emission in 33ks observations with *CXO*. We show the *HST* image of the former (an already awarded *HST* observation of the latter was cancelled by us after the *CXO* observation failed to detect ICM emission) as well as the histogram of radial velocities of galaxies in this region in Fig. B9. Note the absence of ICM emission from eMACSJ0256.9 (Fig. B9) in spite of an obvious overdensity of galaxies at the catalogued RASS source position and the high velocity dispersion of 1170^{+140}_{-240} km s^{-1} measured for the structure (based on 17 concordant redshifts). eMACSJ0256.9 thus underlines the critical importance of moderately deep follow-up observations with a high-resolution X-ray facility like *CXO* to identify non-clusters: as is apparent from Fig. B9, the X-ray flux detected in the RASS is in fact generated by several X-ray point sources, the brightest of which was spectroscopically identified by us as a QSO at $z = 0.8562$, i.e., at the same redshift of the purported cluster. We discuss eMACSJ0256.9 further in Section 5.5.2 in the context of large-scale structure.

5.2 Strong lensing

Given the size of the eMACS sample (and the wealth of strong-lensing features present), a comprehensive strong-lensing study of all eMACS clusters not only requires significant observational and analytical resources but also faces systematic challenges. Although compelling signs of strong gravitational lensing are found in the majority of eMACS clusters for which the prerequisite *HST* imaging is available (Fig. 6), the limitations of the data available for some clusters (e.g., no colour information; no spectroscopic redshifts; clipping of the strong-lensing area by the WFC3 aperture) hampers the secure identification of the most powerful lensing constraints: multiple-image systems. Nevertheless, for clusters with at least one spectroscopically confirmed multiple-image system, we are able to create tentative lens models as described in Section 4.3.

5.2.1 Lensed sources

Strong lensing by massive galaxy clusters offers unique insights into the properties of background galaxies in two complementary ways: by probing the background population in a statistical manner, thereby providing valuable constraints on, for instance, the galaxy luminosity function at redshifts that are not observationally accessible in other ways (e.g., Bouwens et al. 2022), and by enabling detailed studies of the physical properties of individual, intrinsically faint background objects at more modest redshifts (e.g., Alavi et al. 2014). If quantitative insights are aimed for, both of these avenues of research require credible models of the mass distribution within the cluster lenses, and hence the identification of unambiguous strong-lensing features to constrain these lens models (see Sect. 4.3). While exploiting the former, statistical goal requires much deeper follow-up observations (such as those of the Frontier Fields project Lotz et al. 2017, or the JWST UNCOVER program Bezanson et al. 2022) than have been performed for eMACS to date, first steps toward the latter goal can be taken with the data at hand.

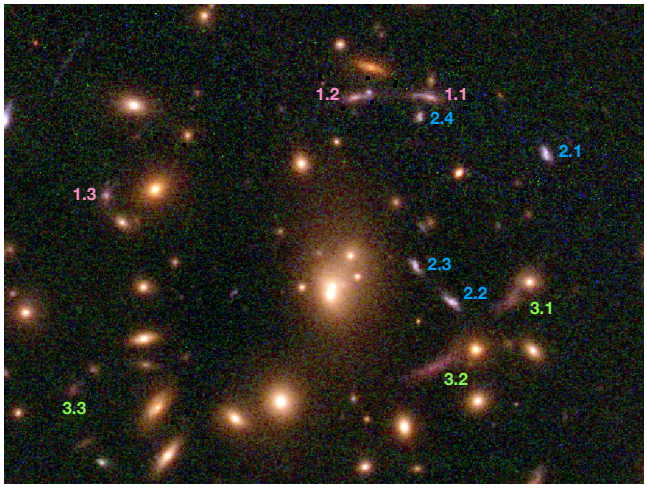

Figure 4. *HST* image of the core of eMACSJ1248.2 at $z = 0.573$ ($40'' \times 30''$, see also Fig. B28). The components of three multiple-image systems are marked, among them a rare hyperbolic-umbilical configuration (System 2, with four images: 2.1–2.4), although unfortunately this currently lacks a spectroscopic redshift.

For 106 eMACS clusters existing multi-band *HST* imaging enables us to visually survey the core regions of the clusters for potential strongly lensed background sources, identifiable as highly sheared images (arcs and giant arcs) and multiply imaged sources. Many of these systems are cusp arcs, producing three images, the brightest two of which display mirror symmetry (e.g., eMACSJ0121.4 and eMACSJ1222.3 in Fig. 6). However, higher multiplicity and more complex configurations are seen, such as quads (e.g., eMACSJ1027.2 in Fig. 6) or rare hyperbolic umbilical lensing events as in eMACSJ1248.2 (System 2 in Fig.4; see also Fig. B28). The significance of such exotic lenses is discussed, e.g., by Lagattuta et al. (2023).

The colours and morphologies of the strongly lensed features showcase the diversity of high-redshift sources seen through the cores of massive clusters at $z > 0.5$ and, in rare cases, can even reveal extended background structures, such as the galaxy group at $z = 2.55$ lensed by eMACSJ1437.8 (Figs. 5 and B33). For background sources at modest redshifts, typically at $z \leq 2$, the larger apparent sizes and in general brighter magnitudes allow complex internal structures of the sources to be readily apparent through the mirror symmetry and image shear that result from strong gravitational lensing; examples are the spiral galaxy at $z = 1.195$ behind eMACSJ1212.5 (Figs. 6 and B26), or the quiescent galaxy at $z = 1.594$ behind eMACSJ1341.9

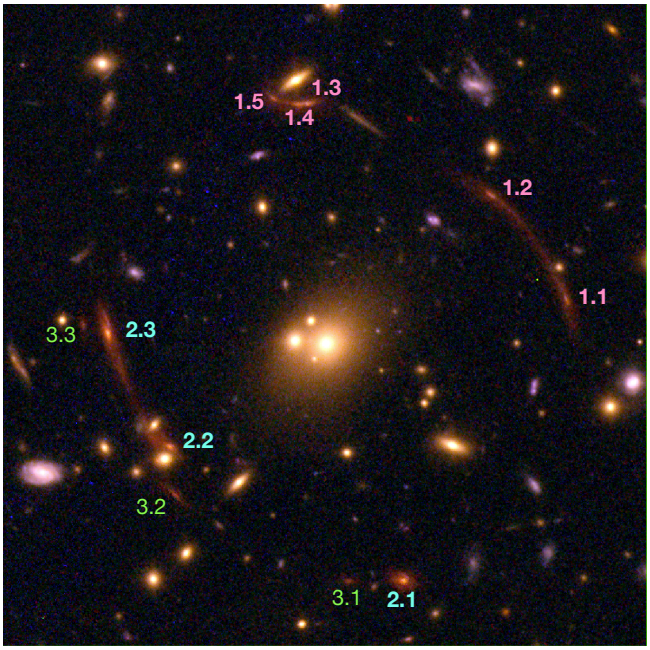

Figure 5. *HST* image of the core of eMACSJ1437.8 at $z = 0.535$ ($50'' \times 50''$, see also Fig. B33), revealing a group of background galaxies at $z = 2.55$ gravitationally lensed by the foreground cluster. The components of three multiple-image systems (two of them, Systems 1 and 2, spectroscopically confirmed at $z = 2.546$ and $z = 2.556$) are marked.

(discussed in Ebeling et al. 2018; see also Figs. 6 and B29), although resolved galaxy features can be seen out to higher redshifts (e.g., The Scream at $z = 3.375$ behind eMACSJ222.9, Figs. 6 and B45). At higher redshifts, the combination of strong image shear and increasingly compact sources sizes (particularly in the restframe UV at $z \gtrsim 2$), as well as surface-brightness dimming, contribute to the apparent narrowness of some lensed features, such as the complex "straight arc" at $z = 2.03$ in eMACSJ1756.8 (Figs. 6 and B38), or highly sheared examples like the giant arc in eMACSJ2327.4 at $z = 2.983$ (Sharon et al. 2015, see also Figs. 6 and B48).

5.2.2 *Einstein radii and systematic effects*

As a first indicator of central lensing strength, we list in Table 2 the Einstein radius, R_E[8], of the 25 eMACS clusters modeled to date with Lenstool, estimated for a fiducial source at $z = 2$; in addition, we also list the total projected gravitational mass within that radius. Both quantities exhibit a large spread for reasons that include true diversity in the clusters' physical characteristics[9] as well as uncertainties in the model assumptions for cluster lenses currently constrained by only a single multiple-image system.

The impact of modeling uncertainties (specifically fixing the core radius of cluster-scale mass components) on the Einstein radii derived for eMACS clusters with few strong-lensing constraints is particularly strong for models based on a single multiple-image system with a redshift much lower or higher than our fiducial redshift of $z = 2$.

That both real physical cluster characteristics and the lens-modeling methodology affect the derived Einstein radii becomes apparent also when the Einstein radii from our Lenstool analysis are compared to those obtained in a previous strong-lensing analysis of almost the entire eMACS cluster sample with the AStroLens package (Zalesky & Ebeling 2020). Unlike Lenstool, AStroLens uses a light-traces-mass approach that, although calibrated using a small number of clusters with spectroscopically confirmed strong-lensing features, relies entirely on the spatial distribution of light from the cluster galaxies (as measured from ground-based imaging) to derive mass models for eMACS clusters. As such, AStroLens provides an estimate of the global lensing power on scales determined by the extent of the distribution of cluster galaxies. Lenstool, by contrast, models the mass distribution in much greater detail from actual strong-lensing features – but only within the strong-lensing regime, i.e., the cluster core.

Comparing the Einstein radii estimated by the two methods for the eMACS subsample listed in Table 2, we find a systematic offset between the results from the two methods, in the sense that AStroLens on average overestimates the Einstein radius by a fac-

Name	$R_{E,PM}$ (arcsec)	$M(r < R_{E,PM})$ (10^{12} $M_\odot$)	N_{mi}	$N_{mi,z}$
eMACSJ0030.5+2618	9 ± 2	16	4	4
eMACSJ0121.4+2143	12 ± 1	40	3	3
eMACSJ0252.4−2100	15 ± 2	72	12	12
eMACSJ0256.7−1623	11 ± 1	49	12	12
eMACSJ0324.0+2421	11 ± 2	51	3	3
eMACSJ0502.9−2902	25 ± 3	164	20	9
eMACSJ0834.2+4524	32 ± 4	324	9	9
eMACSJ0840.2+4421	14 ± 1	58	8	8
eNACSJ0934.6+0540	16 ± 2	60	10	7
eMACSJ0943.3−1842	> 12	> 37	3	3
eMACSJ1057.5+5759	20 ± 10	119	4	2
eMACSJ1157.9−1046	> 15	> 44	9	3
eMACSJ1209.4+2640	22 ± 2	131	19	7
eMACSJ1212.5−1216	40 ± 4	542	3	3
eMACSJ1248.2+0743	17 ± 2	69	11	3
eMACSJ1341.9−2442	16 ± 2	79	5	5
eMACSJ1353.7+4329	38 ± 5	525	13	4
eMACSJ1437.8+0616	14 ± 1	47	11	8
eMACSJ1527.6+2044	21 ± 2	136	7	2
eMACSJ1756.8+4008	> 19	> 79	7	7
eMACSJ1831.1+6214	> 18	> 133	5	5
eMACSJ1852.0+4900	15 ± 2	54	5	5
eMACSJ2229.9−0808	> 11	> 27	9	6
eMACSJ2316.6+1246	22 ± 3	114	9	9
eMACSJ2327.4−0204	35 ± 4	420	12	12

Table 2. Einstein radii at $z_{source} = 2$ and enclosed masses from our strong-lensing analysis of all eMACS clusters with spectroscopically confirmed multiple-image systems (PM = Parametric Model). We show entries as lower limits where an obviously present second mass component is not included in our lens model due to a lack of strong-lensing constraints. Also listed is N_{mi}, the number of multiple images used to constrain each model, and $N_{mi,z}$, the number of such images belonging to spectroscopically confirmed multiple-image systems.

[8] Following, e.g., Meneghetti et al. (2023), we compute the equivalent Einstein radius R_E as the radius of the circular aperture enclosing the same area as the tangential critical line at this redshift.

[9] Including the cluster environment, as strong lensing is sensitive to the total projected mass along the line of sight.

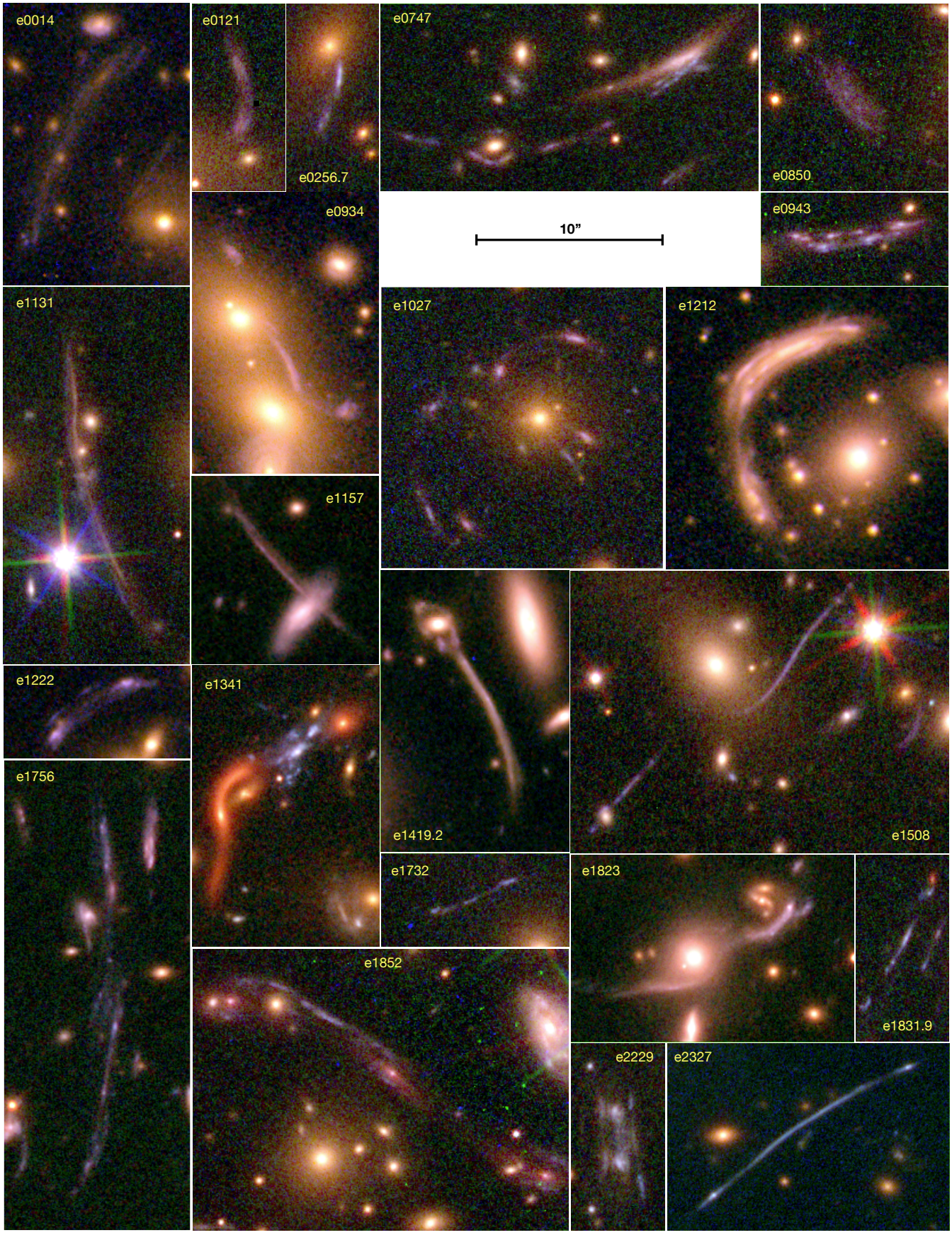

Figure 6. Examples of strong-lensing features in *HST* images of eMACS clusters. We use a shorthand notation for the cluster names.

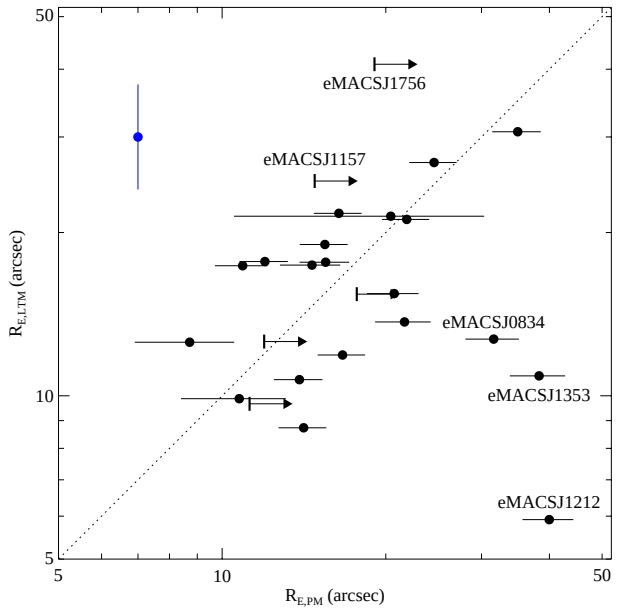

Figure 7. Comparison of Einstein radii estimated for a fiducial background source at $z = 2$ for 25 eMACS cluster using the parametric-modeling software Lenstool ($R_{E,PM}$) and the light-traces-mass package AStroLens ($R_{E,LTM}$). The dotted line marks the identity relation; the five most extreme outliers, labelled in this graph, are discussed in Section 5.2. The blue error bar in the upper left indicates the approximate statistical uncertainty of 25% of the $R_{E,LTM}$ values. Note that all AStroLens measurements shown in this graph were scaled by a factor of 0.8 to remove a systematic bias relative to the Lenstool results.

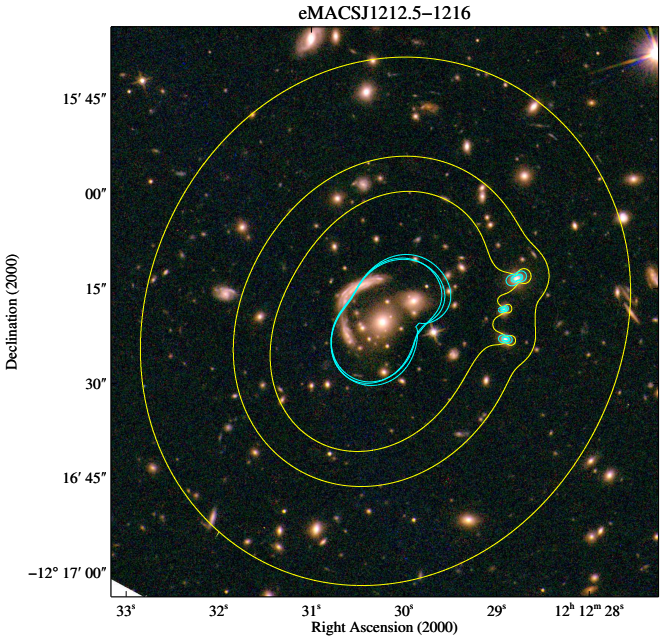

Figure 8. The core of eMACSJ1212.5 (cf. Fig. B26) with tangential critical lines for strong gravitational lensing of a background source at $z = 1.195$ (the redshift of the observed multiple-image system) and $z = 2$ overlaid in cyan and yellow, respectively. For each source redshift, the critical line is shown for cluster core radii of 60, 100, and 200 kpc. By design, the critical lines for $z_{src} = 1.195$ satisfy the strong-lensing constraints for any core radius.

tor of 1.26±0.12. Once this bias is removed[10], the results show an overall correlation that is reassuring, given the differences in the methodologies of the two analyses and in the underlying observational data (Fig. 7). The scatter about the identity line (characterized by $R_{E,LTM}/R_{E,PM} = 1.00\pm0.28$, where $R_{E,LTM}$ denotes the rescaled Einstein radii obtained with AStroLens) is substantial though and indicative of small-scale structure in the majority of eMACS clusters, as expected for a population of clusters that are actively growing through mergers and accretion (see Sections 5.3 and 5.4). The comparison of AStroLens and Lenstool results also highlights dramatically different Einstein radii measured by the two algorithms for three clusters, labelled in Fig. 7 and reviewed in more detail below. The more sophisticated strong-lensing analysis of eMACS clusters presented in Basto et al. (in preparation) will improve upon the lens models used here and allow a more robust investigation of systematic effects.

While the Einstein radii determined by the two methods are in good agreement once the mentioned systematic bias is removed, Fig. 7 reveals a handful of extreme outliers that warrant discussion. The most extreme one is eMACSJ1212.5, the cause being mostly the Lenstool assumption of a core radius of 200 kpc and the significant extrapolation from the measured redshift of $z = 1.2$ of the multiple-image system to the fiducial value of $z = 2$, as illustrated in Fig. 8. In addition, for compact clusters whose light distribution is dominated by only one or two galaxies with little contribution from other cluster members, the Einstein radius obtained with AStroLens depends sensitively on the assumed scaling relations for the BCG. Hence, while Lenstool likely overestimates the lensing strength of eMACSJ1212.5, the same quantity is likely to have been underestimated by AStroLens.

A different systematic effect is likely responsible for two slightly less extreme outliers in Fig. 7, eMACSJ0834.2 (Fig. B13) and eMACSJ1353.7 (Fig. B30). Both systems are small-separation double clusters and active mergers with very high velocity dispersions of 1590^{+140}_{-200} km s^{-1} and 1600^{+110}_{-160} km s^{-1}, respectively; both are also extremely X-ray luminous (see Section 5.4). In addition, the lens models of both clusters are constrained by robust strong-lensing constraints at 100-200 kpc, i.e., at much larger radial distances than eMACSJ1212.5, and the redshifts of the lensed sources are closer to our fiducial value of $z = 2$ than in the case of eMACSJ1212.5. As a result, the required extrapolations are much more modest, and the large Einstein radii presented in Table 2 and Fig. 7 are not only less uncertain but also consistent with all other known physical properties of these clusters. The outlier status of eMACSJ0834.2 and eMACSJ1353.7 in Fig. 7 is thus likely to be due to AStroLens underestimating the lensing power of line-of-sight mergers whose galaxy distribution (and hence light distribution) is by necessity much less extended than that of similarly massive systems colliding along an axis that is closer to the plane of the sky.

The cause of the discrepancy in the R_E values of the remaining two clusters labeled in Fig. 7, eMACSJ1157.9 (Fig B24) and eMACSJ1756.8 (Fig. B38) is less speculative and already hinted at by them being flagged as lower limits in Table 2. The reason for the small Einstein radius of eMACSJ1157.9, a system that is included in the list of the ten most powerful cluster lenses in the analysis by Za-

[10] We note that the subsample of Table 2 includes nine of the ten eMACS clusters that were used in the calibration of AStroLens (the tenth one being eMACSJ0850.2, Fig. B15), and that discrepancies for this subset were, in part, apparent and acknowledged in Zalesky & Ebeling (2020).

lesky & Ebeling (2020), is simply the lack of spectroscopic redshifts for several multiple-image systems readily identified in the *HST* images, which cause the western cluster component to be completely absent from the current, tentative Lenstool model (Fig. B24). Future spectroscopic follow-up observations are bound to secure additional redshifts for strong-lensing features in this area and help recover the full extent of the cluster mass distribution. An even more dramatic outlier (in the same sense as eMACSJ1157.9) is eMACSJ1756.8, shown in Fig. B38. Again at least half of the mass distribution of this highly elongated system is missing from the parametric lens model. However, in this case the reason is not a lack of redshifts but an actual lack of strong-lensing features in the eastern half of the cluster. The cause of this cluster's outlier status in Fig. 7 thus appears to be a physical property of the system, namely an unusually flat mass profile that dramatically reduces the probability for strong gravitational lensing around the eastern cluster core. A weak-lensing analysis is needed to test this hypothesis and establish a robust total mass for this extreme merger. Weak-lensing follow-up studies might also benefit other eMACS clusters that appear to contain additional cluster-scale components that lack suitable strong-lensing features, such as eMACSJ0943.3 (Fig. B18), eMACSJ1831.1 (Fig. B41), or eMACSJ2229.9 (Fig. B45).

While the short list of eMACS clusters with Lenstool models presented here contains several exceptional gravitational lenses, many other eMACS clusters exhibit strong-lensing features that make them promising candidates for in-depth follow-up studies. Among the systems with existing *HST* images, such noteworthy clusters are eMACSJ0014.9 (Fig. B1), eMACSJ0031.2 (Fig. B5), eMACSJ0121.4 (Fig. B7), eMACSJ0747.0 (Fig. B12), eMACSJ0850.2 (Fig. B15), eMACSJ0934.6 (Fig. B16), eMACSJ1027.2 (Fig. B19), eMACSJ1131.1 (Fig. B22), eMACSJ1144.2 (Fig. B23) eMACSJ1222.3 (Fig. B27), eMACSJ1414.7 (Fig. B31), eMACSJ1419.2 (Fig. B32), eMACSJ1508.1 (Fig. B34), eMACSJ1732.4 (Fig. B37), and eMACSJ1823.1 (Fig. B40).

5.3 ICM properties and relaxation state

An overview of the key cluster properties derived from the X-ray follow-up observations described in Section 3.4 is given in Table 3. Since most of the underlying *CXO* observations were obtained with the explicit (and modest) goal of establishing point-source-subtracted cluster luminosities and assessing the large-scale morphology of the ICM, the chosen ACIS-I exposure times are relatively short for such faint targets.

5.3.1 ICM temperature and luminosity; cluster mass

Although the global cluster luminosities and ICM temperatures presented here should be considered tentative (our analysis is unable to account for low-surface-brightness emission from the cluster outskirts, or for cool cores, shock-heated gas, and any other temperature variations), the results are in good agreement with the L_X-kT relation established for other X-ray selected cluster samples. As shown in Fig. 9, eMACS extends the L_X-kT relation for galaxy clusters to higher luminosities and higher ICM temperatures than probed by existing X-ray selected cluster samples at $z > 0.5$.

The results of our X-ray analysis summarized in Table 3 also unambiguously confirm that eMACS achieved its goal of probing both the redshift-X-ray luminosity and the redshift-mass regime highlighted in Fig. 1. As shown in Figs. 3 and 9, the point-source corrected X-ray luminosities of eMACS clusters are of the order of 10^{45} erg

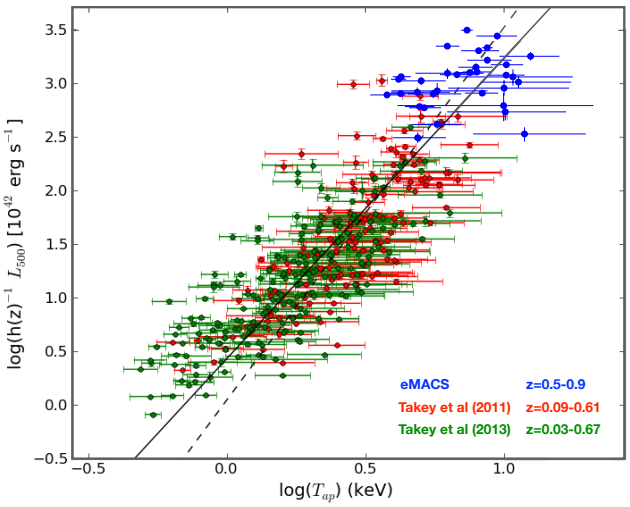

Figure 9. Bolometric luminosities and global ICM temperatures measured by us for the subsample of 35 eMACS clusters observed with *CXO*, overlaid on the L_X–kT relation determined by Takey et al. (2013) for a sample of 345 clusters detected with *XMM-Newton* (reproduced from Takey et al. 2013). Note that, unlike Takey and collaborators, we measured both quantities within r_{1000}.

s^{-1}, consistent with the eMACS target range shown in Fig. 1 (left). The same holds for the cluster masses. Although the existing *CXO* observations allow direct measurements of the cluster mass (under the assumption of hydrostatic equilibrium) only to a radius of r_{1000}, M_{200} can be estimated through extrapolation of the universal cluster mass profile to r_{200} which approximately doubles these values (e.g., Pointecouteau et al. 2005; Ettori et al. 2019), yielding total masses in excess of 10^{15} M$_\odot$ for over one third of the subset for which *CXO* data are currently available (Fig 10). We note that this extrapolation assumes the NFW profile found to describe the mass distribution in relaxed clusters (Navarro et al. 1997); for disturbed systems (of which eMACS found many; see below), the increase in the enclosed mass from r_{1000} to r_{200} would be even higher. Since our follow-up observations with *CXO* targeted preferentially the most distant and most X-ray luminous clusters, the mass distribution shown in Fig 10 should, however, not be taken as representative of the eMACS sample as a whole.

5.3.2 Relaxation state

We show in Fig. 11 the X-ray surface brightness for all eMACS clusters with *CXO*/ACIS-I data. Note the wide range of morphologies, from almost perfectly circular and strongly peaked (e.g., eMACSJ1030.5, eMACSJ2026.7) to extremely disturbed (e.g., eMACSJ1157.9, eMACSJ1508.1, eMACSJ1756.8). Also noteworthy are two fields which show no diffuse ICM emission at all, eMACSJ0256.9 and eMACSJ1350.7; we discussed these eMACS misidentification earlier in Section 5.1.2 within the larger context of contamination from X-ray point sources.

Recognizing the futility of a sophisticated ICM substructure analysis based on (typically) a few thousand photons, we adopt the simple but robust visual classification scheme of Ebeling et al. (2007) and assign each cluster a morphological classification from 1 (fully relaxed) through 4 (highly disturbed), based on X-ray and optical appearance, as well as X-ray/optical alignment. The resulting classification is indicated both in Fig. 11 and in Table 3.

The low fraction of fully relaxed systems (morphological class 1)

Name	z	n_H (10^{20} cm^{-2})	$L_{X,RASS}$ [0.1–2.4 keV]	t_{ACIS-I} (ks)	r_{1000} (kpc)	$f_{X,CXO}$ [0.5–7 keV]	$L_{X,CXO}$ [0.5–7 keV]	$kT_{X,CXO}$ (keV)	$M_{X,CXO}(< r_{1000})$ (10^{14} M$_\odot$)	Morph. class
eMACSJ0014.9−0056	0.5330	2.95	6.2±1.9	29.3	884^{+77}_{-60}	$11.6^{+0.6}_{-0.5}$	$13.0^{+0.6}_{-0.6}$	$10.2^{+1.7}_{-1.4}$	$7.0^{+2.0}_{-1.4}$	2
eMACSJ0030.5+2618	0.4970	3.47	4.6±1.7	15.6	626^{+78}_{-61}	$3.7^{+0.4}_{-0.4}$	$3.5^{+0.4}_{-0.4}$	$4.9^{+1.3}_{-0.9}$	$2.4^{+1.0}_{-0.6}$	2
eMACSJ0042.5−1103	0.5701	2.54	6.9±2.0	11.9	865^{+248}_{-193}	$4.6^{+0.6}_{-0.6}$	$6.0^{+0.8}_{-0.8}$	$10.1^{+6.7}_{-3.9}$	$6.9^{+7.8}_{-3.7}$	4
eMACSJ0045.2−0151	0.5471	2.71	5.2±2.0	49.4	613^{+38}_{-35}	$5.9^{+0.3}_{-0.3}$	$7.1^{+0.3}_{-0.4}$	$5.0^{+0.6}_{-0.6}$	$2.4^{+0.5}_{-0.4}$	3
eMACSJ0135.2+0847	0.6185	4.87	7.9±2.5	11.5	582^{+82}_{-60}	$6.3^{+0.6}_{-0.5}$	$10.1^{+0.9}_{-0.9}$	$4.9^{+1.5}_{-1.0}$	$2.2^{+1.1}_{-0.6}$	4
eMACSJ0248.2+0237	0.5561	5.09	6.6±3.0	44.5	621^{+45}_{-38}	$5.6^{+0.3}_{-0.3}$	$6.9^{+0.4}_{-0.3}$	$5.2^{+0.8}_{-0.6}$	$2.5^{+0.6}_{-0.4}$	4
eMACSJ0256.7−1623	0.8621	4.29	19.6±6.9	32.2	546^{+127}_{-94}	$3.3^{+0.5}_{-0.4}$	$11.9^{+1.9}_{-1.5}$	$5.7^{+3.0}_{-1.8}$	$2.5^{+2.1}_{-1.1}$	3
eMACSJ0256.9−1631	0.8670	4.32	18.3±6.6	32.1	56^{+13}_{-16}	$0.0^{+0.0}_{-0.0}$	$0.0^{+0.1}_{-0.0}$	$0.1^{+0.0}_{-0.0}$	$0.0^{+0.0}_{-0.0}$	–
eMACSJ0324.0+2421	0.9023	8.48	14.4±5.3	30.8	787^{+99}_{-94}	$6.0^{+0.4}_{-0.4}$	$24.3^{+1.8}_{-1.6}$	$12.5^{+3.4}_{-2.9}$	$7.7^{+3.3}_{-2.4}$	3
eMACSJ0502.9−2902	0.6028	1.25	6.7±1.9	47.5	753^{+46}_{-43}	$9.9^{+0.4}_{-0.4}$	$14.9^{+0.6}_{-0.6}$	$8.0^{+1.0}_{-0.9}$	$4.7^{+0.9}_{-0.8}$	3
eMACSJ0804.6+5325	0.5786	3.81	5.8±2.1	3.9	888^{+256}_{-174}	$9.3^{+1.2}_{-1.2}$	$12.7^{+1.6}_{-1.7}$	$10.8^{+7.0}_{-3.8}$	$7.5^{+8.6}_{-3.6}$	4
eMACSJ0834.2+4524	0.6606	2.80	10.0±2.8	32.6	643^{+32}_{-30}	$14.6^{+0.5}_{-0.5}$	$27.5^{+0.9}_{-1.0}$	$6.2^{+0.7}_{-0.6}$	$3.2^{+0.5}_{-0.4}$	4
eMACSJ0840.2+4421	0.6377	2.42	14.4±4.3	31.4	715^{+28}_{-30}	$8.8^{+0.4}_{-0.3}$	$15.2^{+0.7}_{-0.5}$	$7.5^{+0.7}_{-0.6}$	$4.2^{+0.5}_{-0.5}$	2
eMACSJ0935.1+0614	0.7787	3.55	15.2±4.8	29.9	681^{+59}_{-47}	$9.3^{+0.5}_{-0.5}$	$26.3^{+1.3}_{-1.4}$	$8.1^{+1.5}_{-1.1}$	$4.3^{+1.2}_{-0.8}$	3
eMACSJ1030.5+5132	0.5182	1.28	6.7±1.4	19.7	578^{+22}_{-21}	$12.7^{+0.4}_{-0.4}$	$13.3^{+0.5}_{-0.5}$	$4.3^{+0.4}_{-0.3}$	$1.9^{+0.2}_{-0.2}$	1
eMACSJ1136.8+0005	0.5968	2.10	5.7±2.0	3.9	844^{+261}_{-174}	$7.0^{+0.9}_{-0.8}$	$10.3^{+1.4}_{-1.2}$	$10.0^{+7.2}_{-3.7}$	$6.6^{+8.2}_{-3.3}$	4
eMACSJ1144.2−2836	0.5070	5.52	16.5±5.2	30.8	675^{+75}_{-63}	$4.7^{+0.4}_{-0.4}$	$4.6^{+0.4}_{-0.4}$	$5.7^{+1.3}_{-1.1}$	$3.0^{+1.1}_{-0.8}$	4
eMACSJ1157.9−1046	0.5570	2.91	7.6±3.4	125.3	558^{+17}_{-17}	$10.3^{+0.3}_{-0.3}$	$12.9^{+0.3}_{-0.4}$	$4.2^{+0.3}_{-0.3}$	$1.8^{+0.2}_{-0.2}$	4
eMACSJ1209.4+2640	0.5553	1.48	6.1±1.7	15.9	712^{+67}_{-50}	$11.2^{+0.7}_{-0.6}$	$13.9^{+0.8}_{-0.8}$	$6.8^{+1.3}_{-0.9}$	$3.8^{+1.2}_{-0.7}$	3
eMACSJ1341.9−2442	0.8339	6.01	16.2±6.2	32.8	546^{+69}_{-53}	$3.3^{+0.3}_{-0.3}$	$11.0^{+0.9}_{-0.9}$	$5.6^{+1.5}_{-1.1}$	$2.4^{+1.0}_{-0.6}$	4
eMACSJ1350.7−1055	0.8247	3.42	12.0±4.7	31.9	62^{+10}_{-18}	$0.0^{+0.1}_{-0.0}$	$0.0^{+0.3}_{-0.0}$	$0.1^{+0.0}_{-0.0}$	$0.0^{+0.0}_{-0.0}$	–
eMACSJ1353.7+4329	0.7364	1.14	9.0±2.5	40.1	694^{+51}_{-51}	$7.3^{+0.4}_{-0.4}$	$18.0^{+0.9}_{-0.9}$	$7.9^{+1.2}_{-1.1}$	$4.3^{+1.0}_{-0.9}$	4
eMACSJ1407.0−0015	0.5520	3.57	6.0±2.0	3.9	849^{+409}_{-291}	$5.6^{+1.2}_{-1.4}$	$6.8^{+1.5}_{-1.7}$	$10.0^{+11.1}_{-5.8}$	$6.4^{+14.4}_{-4.6}$	3
eMACSJ1414.7+5446	0.6121	1.41	10.2±0.6	32.6	846^{+60}_{-52}	$10.9^{+0.5}_{-0.5}$	$17.1^{+0.8}_{-0.7}$	$10.2^{+1.5}_{-1.2}$	$6.8^{+1.5}_{-1.2}$	3
eMACSJ1508.1+5755	0.5421	1.60	7.3±1.5	47.3	797^{+52}_{-55}	$7.7^{+0.3}_{-0.3}$	$9.0^{+0.4}_{-0.4}$	$8.3^{+1.2}_{-1.1}$	$5.2^{+1.1}_{-1.0}$	4
eMACSJ1527.6+2044	0.6967	4.55	8.0±3.6	24.5	741^{+78}_{-59}	$9.4^{+0.6}_{-0.5}$	$20.2^{+1.3}_{-1.1}$	$8.7^{+1.9}_{-1.3}$	$5.0^{+1.8}_{-1.1}$	3
eMACSJ1756.8+4008	0.5743	3.28	8.6±1.8	126.1	799^{+18}_{-17}	$18.2^{+0.2}_{-0.2}$	$24.4^{+0.3}_{-0.2}$	$8.7^{+0.4}_{-0.4}$	$5.4^{+0.4}_{-0.3}$	4
eMACSJ1823.1+7822-NE	0.6803	3.02	†12.7±1.9	22.1	496^{+41}_{-33}	$5.0^{+0.3}_{-0.3}$	$9.9^{+0.7}_{-0.6}$	$3.8^{+0.6}_{-0.5}$	$1.5^{+0.4}_{-0.3}$	1
eMACSJ1823.1+7822-SW	0.6784	3.02	†12.7±1.9	22.1	534^{+62}_{-50}	$2.4^{+0.2}_{-0.3}$	$4.8^{+0.5}_{-0.5}$	$4.2^{+1.0}_{-0.7}$	$1.8^{+0.7}_{-0.5}$	3
eMACSJ1831.1+6214	0.8207	4.15	18.8±2.2	22.0	718^{+61}_{-59}	$11.4^{+0.6}_{-0.6}$	$36.7^{+1.9}_{-2.1}$	$9.5^{+1.7}_{-1.5}$	$5.3^{+1.5}_{-1.2}$	4
eMACSJ1852.0+4900	0.6035	3.90	6.3±1.7	19.8	596^{+64}_{-59}	$8.4^{+0.6}_{-0.7}$	$12.7^{+1.0}_{-1.1}$	$5.0^{+1.1}_{-0.9}$	$2.3^{+0.8}_{-0.6}$	4
eMACSJ2026.7−1920	0.6219	4.14	10.3±3.4	31.8	541^{+31}_{-27}	$6.1^{+0.3}_{-0.3}$	$9.9^{+0.5}_{-0.5}$	$4.2^{+0.5}_{-0.4}$	$1.8^{+0.3}_{-0.3}$	1
eMACSJ2220.3−1211	0.5292	3.78	5.2±2.0	12.4	934^{+228}_{-136}	$10.0^{+1.0}_{-0.9}$	$11.0^{+1.1}_{-1.0}$	$11.3^{+6.2}_{-3.1}$	$8.2^{+7.7}_{-3.1}$	2
eMACSJ2315.3−2128	0.5400	1.72	13.8±5.4	30.8	952^{+276}_{-183}	$3.1^{+0.4}_{-0.4}$	$3.6^{+0.4}_{-0.4}$	$11.9^{+7.9}_{-4.1}$	$8.9^{+10.2}_{-4.2}$	3
eMACSJ2320.9+2912	0.4960	7.35	5.5±1.6	9.6	709^{+115}_{-88}	$14.6^{+1.3}_{-1.5}$	$13.8^{+1.3}_{-1.4}$	$6.2^{+2.2}_{-1.5}$	$3.5^{+2.0}_{-1.1}$	3
eMACSJ2327.4−0204	0.7055	4.62	14.0±4.1	138.9	679^{+16}_{-16}	$17.8^{+0.3}_{-0.4}$	$39.4^{+0.8}_{-0.8}$	$7.3^{+0.4}_{-0.4}$	$3.9^{+0.3}_{-0.3}$	2

Table 3. Global physical characteristics of eMACS clusters from *CXO*/ACIS-I data available at the time of publication; n_H values represent the Galactic neutral-hydrogen column density (HI4PI Collaboration et al. 2016); all X-ray fluxes (unabsorbed) and luminosities are listed in units of 10^{-13} erg s^{-1} cm^{-2} and 10^{44} erg s^{-1}, respectively. Errors correspond to 1σ confidence. We list the properties of the two components of the double cluster eMACSJ1823 separately; note, however, that the listed RASS flux (marged with a †symbol) is the same and duplicated for both entries, since this source is not resolved in the RASS. See Ebeling et al. (2007) for a description of the morphological classification listed in the final column. An estimate of the total cluster mass within r_{200} can be obtained by doubling $M_{1000} = M(< r_{1000})$ (see Section 5.3).

is immediately apparent, indicating that massive clusters at $z > 0.5$ are undergoing vigorous growth through the accretion of surrounding structures. At face value, the dominance of disturbed systems seems to contradict claims that X-ray selected clusters samples suffer from a strong "cool-core bias" in favor of relaxed clusters at higher redshift (Rossetti et al. 2017; Andrade-Santos et al. 2017). This claim is disputed though, as it may attribute erroneously to X-ray selection what is in fact caused by Malmquist bias: indeed, volume-complete (as opposed to flux limited) samples of X-ray selected clusters were found to be dominated not by cool-core clusters but by dynamically

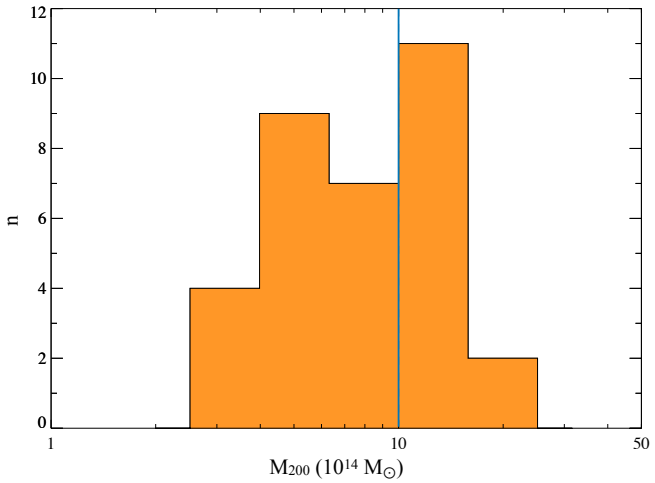

Figure 10. Distribution of total cluster masses (M_{200}) for the 33 eMACS clusters observed with *CXO*/ACIS-I to date (see Table 1). M_{200} is estimated from M_{1000} (Table 3) by extrapolating the universal cluster mass profile (e.g., Pointecouteau et al. 2005; Ettori et al. 2019) from r_{1000} to r_{1000}. The vertical line marks the mass of 10^{15} $M_\odot$ referred to in Section 1 and highlighted as characteristic for the eMACS target regime in mass-redshift space (Fig. 1, right).

active, disturbed systems (Chon & Böhringer 2017). As is, the data shown in Fig. 11 cannot be used to assess the validity of either claim, since eMACS is not volume complete and since the subset of eMACS clusters with existing *CXO* data is biased in favour of disturbed systems simply as a result of the scientific goals of the underlying *CXO* proposals. A subset with (almost) complete *CXO* coverage can, however, be defined by considering only the most X-ray luminous eMACS clusters. As shown in Fig. 12, only one of the 12 clusters in the almost volume-complete subsample of eMACS clusters with $L_{X,RASS} > 1.1 \times 10^{45}$ erg s^{-1} is classified as fully relaxed (morphological class 1). Of the two systems without *CXO* data (both visible at $z \sim 0.7$ in Fig. 12), one (eMACSJ0252.4, shown in Fig. 13) can be safely assumed to be highly relaxed (morphology class 1 or, at most, 2), based on the analysis of Ebeling et al. (2021) and the strong optical emission lines from its BCG, while the other (eMACSJ2025.5) is a very improbable candidate for the same classification, based on its optical appearance (see Fig. B44).

A conservative conclusion is thus that the fraction of cool-core clusters does not significantly exceed 10% among the most X-ray luminous clusters at $z > 0.5$ (2 of 19), in agreement with the findings of Mann & Ebeling (2012). A decrease in the fraction of relaxed systems as we approach the redshift of formation for massive clusters is not only plausible on evolutionary grounds, but also firmly expected from the impact of mergers in the rapidly evolving exponential tail of the most massive clusters. Such events boost, temporarily but dramatically, both the X-ray luminosity and the ICM temperature of the respective systems (Randall et al. 2002), thereby creating the opposite of a "cool-core bias" (Fedeli & Bartelmann 2007).

5.4 The most X-ray luminous eMACS clusters

We here provide a brief overview highlighting the ten most X-ray luminous systems[11] with $L_{X,CXO} \geq 1.5 \times 10^{45}$ erg s^{-1}, several of which were previously highlighted in Zalesky & Ebeling (2020), but note that an eleventh cluster, the massive merger eMACSJ0502.9 (Fig. B11), makes the same luminosity cut, too. A visual summary of this subsample is shown in Fig. 14; additional details for each cluster can be found in Appendix B. A more comprehensive analysis and discussion of the properties of the most X-ray luminous eMACS clusters[12] is given by Basto et al. (in preparation).

5.4.1 eMACSJ0324.0+2421

eMACSJ0324.0 deserves special mention for being the only galaxy cluster at $z > 0.9$ not merely detected, but in fact discovered in the RASS. Fig. B10 summarizes the observational evidence for this system (see also Fig. 14). Two almost equally luminous BCG candidates, a disturbed ICM morphology that nonetheless features only a single X-ray peak, a very high global gas temperature of (13 ± 3) keV, a very large Einstein radius and very high enclosed mass of $M(< 240\,\mathrm{kpc}) = 4.6 \times 10^{14}$ $M_\odot$ derived from a lens model constrained by two spectroscopically confirmed multiple-image systems (see Section 5.2), and an exceptionally high velocity dispersion of 1520^{+150}_{-220} km s^{-1} all suggest that eMACSJ0324.0 is an actively growing, massive cluster, observed in the post-collision phase (but still close to core passage) of a merger that proceeds largely along our line of sight.

5.4.2 eMACSJ0834.2+4524

The appearance of eMACSJ0834.2 (Fig. B13, see also Fig. 14 and Section 5.2) provides ample and unambiguous evidence of an ongoing collision of two components of comparable mass. Although our strong-lensing mass model is unable to resolve multiple cluster-scale components, two well separated peaks are observed in the X-ray surface brightness. The offsets of these peaks in the ICM density from the BCGs of the two subclusters are indicative of a collision axis that lies at least partly in the plane of the sky. A line-of-sight component of the merger-induced peculiar velocities is, however, also likely, given the very high velocity dispersion of 1590^{+140}_{-200} km s^{-1}. We note the quite modest ICM gas temperature of (6.2 ± 0.7) keV; such a low global temperature could be indicative of the presence of cool cores (the eastern component of e0834 exhibits a noticeably compact X-ray peak) and points to the absence of large amounts of shock-heated gas. We thus speculate that we either observe the merger well before first core passage or that the collision involves a large impact parameter, thereby leaving the cluster cores relatively unperturbed, even after several core passages.

[11] These systems fall precisely into the extreme regime of the L_X-z parameter space targeted by the eMACS project and highlighted in Fig. 1.

[12] Note that the subset of the most X-ray luminous eMACS clusters selected from RASS data and highlighted in Fig. 12 differs from the one drawn from the *CXO*-based X-ray luminosities listed in Table 3 and considered here and by Basto and collaborators. Although the X-ray fluxes recorded in the RASS and those derived from follow-up *CXO* observations are correlated, both photon noise and contamination from (possibly time variable) X-ray point sources introduce substantial scatter, as shown in Fig. 3. Interestingly, the subset of the most X-ray luminous eMACS clusters drawn from RASS data (Fig. 12) includes not only both of the eMACS misidentifications but also both of the most dramatic outliers from the mentioned correlation (see Fig. 3).

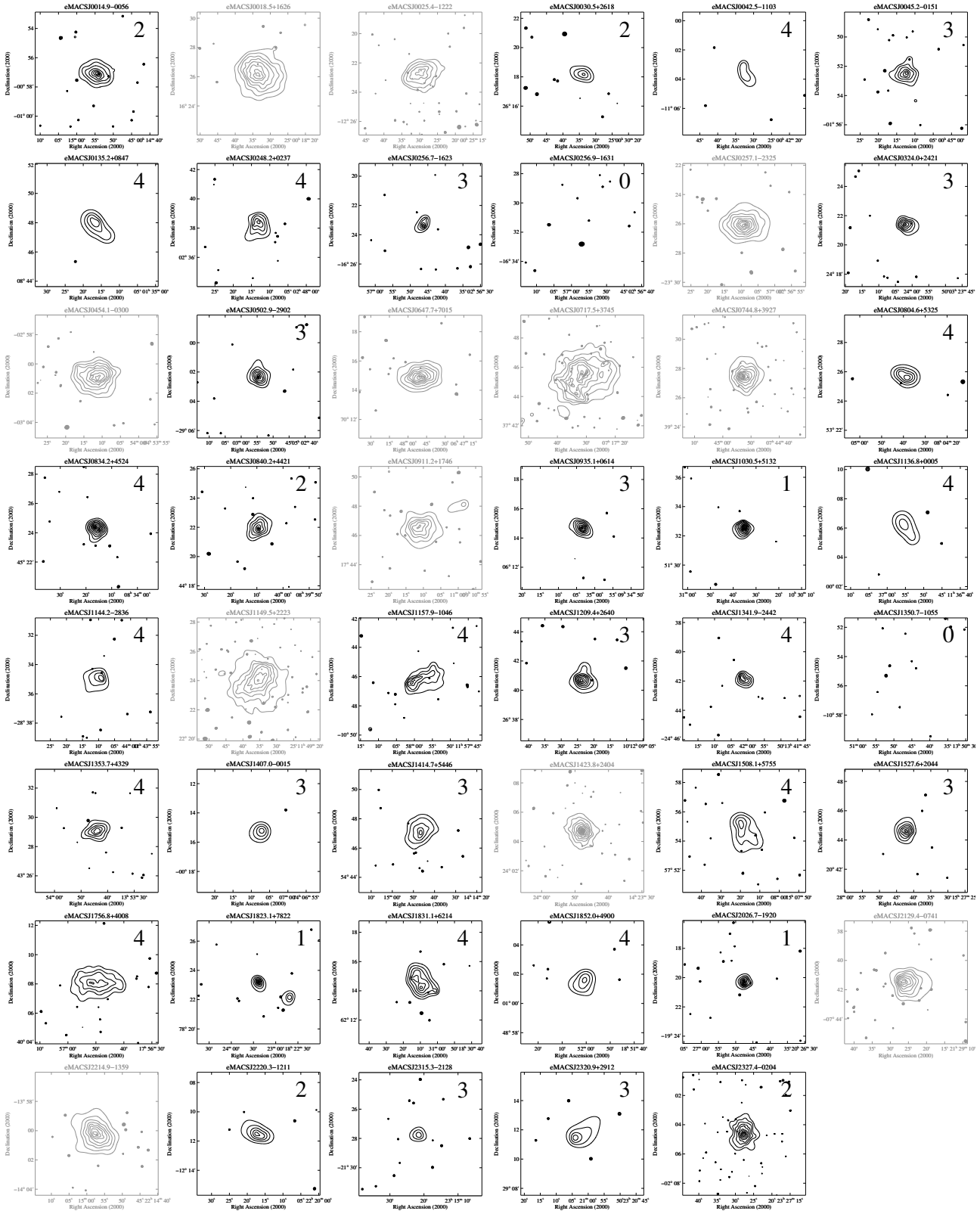

Figure 11. Contours of the adaptively smoothed X-ray surface brightness in the 0.5–7 keV band from the *CXO* observations described in Section 3.4. Contours in this and all subsequent figures are logarithmically spaced by factors of 1.2, starting at three times the background level. The 12 clusters previously discovered in the MACS project (Ebeling et al. 2007) are included only for completeness' sake and shown in gray. The morphological class assigned to each cluster is shown in the upper right corner of each panel. (Note that we again exclude the 12 MACS clusters that, by design, are also part of the eMACS sample.)

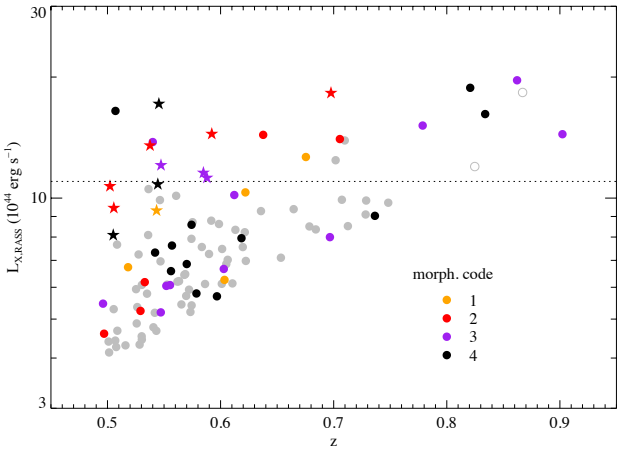

Figure 12. As Fig, 1 (left) but focusing solely on eMACS and highlighting the subset of eMACS clusters observed with *CXO*/ACIS-I (coloured symbols). The 19 clusters with $L_{X,RASS} > 1.1 \times 10^{45}$ erg s^{-1} (an additional two, shown as open circles, are the misidentifications discussed in Section 5.1.2), form an almost complete subsample of which only two are lacking *CXO* data. The 12 MACS clusters at $z > 0.5$ are shown as stars. Very few of the most X-ray luminous eMACS clusters exhibit a relaxed X-ray morphology.

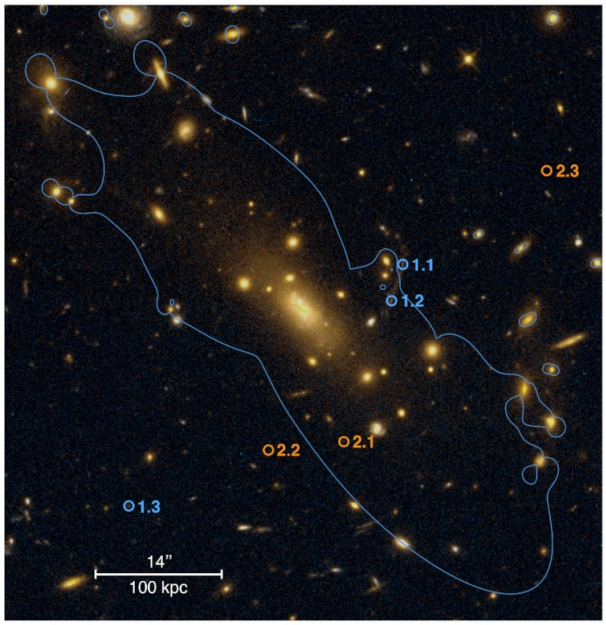

Figure 13. The core of eMACSJ0252.4−2100, as viewed with *HST*; overlaid is the critical line (for a source at $z = 3.46$) from a lens model constrained by the two marked multiple-image systems (figure reproduced from Ebeling et al. 2021). Although no *CXO* data are available for eMACSJ0252 at present, the optical appearance and extreme dominance of the BCG suggest this system is very likely to have a morphological class of 1.

Owing to the system's highly disturbed morphology, our best-fitting lens model is characterized by a large Einstein radius and a high enclosed mass of $M(< 220\,\mathrm{kpc}) = 3.2 \times 10^{14}$ M$_\odot$.

5.4.3 *eMACSJ0840.2+4421*

While not fully relaxed (note the absence of a pronounced X-ray peak and the non-circular geometry apparent in Fig. B14 and Fig. 14), eMACSJ0840.2 is one of the least disturbed clusters in this subset of the most X-ray luminous eMACS clusters. Both the excellent X-ray/optical alignment and the substantial but (for a cluster of this size) modest ICM temperature of (7.5 ± 0.7) keV suggest that eMACSJ0840.2 is observed well past its most recent merger event. Two spectroscopically confirmed multiple-image systems constrain the mass in the cluster core to $M(< 80\,\mathrm{kpc}) = 4 \times 10^{13}$ M$_\odot$. Since the velocity dispersion of (1320 ± 120) km s^{-1} (based on 39 redshifts) of eMACSJ0840.2 is unlikely to be inflated by ongoing merging activity along the line of sight, we can use the virial scaling relation to compute an estimate of the dynamical mass of the system (Evrard et al. 2008; Saro et al. 2013). The result, $M_{\mathrm{dyn}} = (2.6 \pm 0.1) \times 10^{15}$ M$_\odot$, places eMACSJ0840.2 in the top tier of massive clusters at any redshift (see Fig 1).

5.4.4 *eMACSJ0935.1+0614*

Exceptionally X-ray luminous, in particular given its high redshift of $z = 0.78$, eMACSJ0935.1 is one of two eMACS clusters in our Top Ten list that do not currently have a lens model. The *CXO* data for this system show neither a compact core nor pronounced substructure in the ICM (Fig. 14); however, markedly elliptical X-ray surface-brightness contours, as well as a clear offset of the X-ray peak from the BCG, still identify eMACSJ0935.1 as a dynamically disturbed cluster (Fig. B17). The cluster core features neither an extremely luminous BCG nor signs of strong gravitational lensing, suggesting a shallow mass profile that may be the result of mergers of several clusters of moderate mass.

5.4.5 *eMACSJ1353.7+4329*

eMACSJ1353.7, previously discussed in Section 5.2, has one of the highest velocity dispersions of any eMACS cluster (see Section 5.5.1); however, closer inspection of all available data (Fig. B30) suggests that the measured value of 1600^{+110}_{-160} km s^{-1} is inflated by an infalling group. The cluster exhibits the textbook signature (a single X-ray peak between two BCGs, Fig. 14) of what is probably a late-stage merger close to the plane of the sky. The two BCGs are at essentially the same redshift ($z = 0.736$ and $z = 0.739$); the looser group of galaxies to the East, however, features redshifts close to $z = 0.75$, adding a pronounced and narrow peak to the radial-velocity histogram that we interpret as evidence of infall of a foreground group of galaxies. The lens model for eMACSJ1353.7, well constrained by three multiple-image systems, one of which is spectroscopically confirmed, yields a very high enclosed mass of $M(< 250\,\mathrm{kpc}) = 4.3 \times 10^{14}$ M$_\odot$ for this powerful gravitational lens. The not exceptionally high ICM temperature of (7.9 ± 1.2) kev measured by us suggests that this ongoing merger is observed well after the temporary temperature boost triggered by the initial collision.

5.4.6 *eMACSJ1414.7+5446*

Like for eMACSJ1353.7, the extreme velocity dispersion measured for eMACSJ1414.7 (1700^{+180}_{-210} km s^{-1}) is likely inflated by peculiar velocities from an ongoing merger proceeding along an axis that lies close to our line of sight. Although strong-lensing features are clearly discernible near the cluster core (Fig. B31), we currently have no spectroscopically confirmed multiple-image system that could

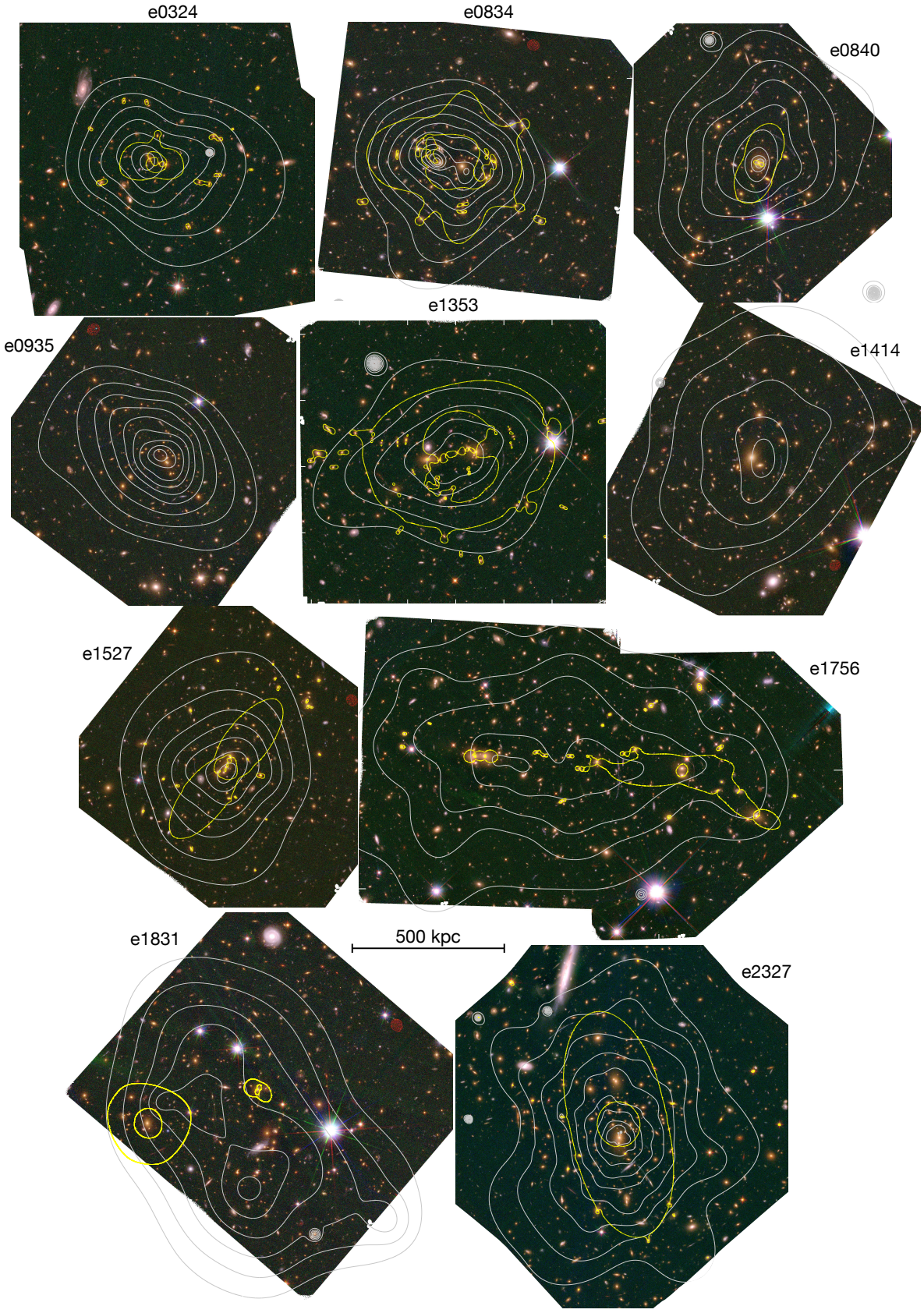

Figure 14. *HST* images of the ten most X-ray luminous eMACS clusters (based on point-source corrected fluxes measured from *CXO* observations). Overlaid in gray and yellow are isointensity contours of the adaptively smoothed X-ray emission and the critical line for gravitational lensing of a source at a fiducial redshift of $z = 2$, respectively.

anchor a lens model for eMACSJ1414.7 The fact that the X-ray peak of eMACSJ1414.7 is offset to the West of the BCG (Fig. 14), with no obvious second cluster core apparent in this direction in the galaxy distribution, might indicate a collision at a significant impact parameter. The gap in the radial-velocity histogram and the high global ICM temperature of 10 keV suggest that the eMACSJ1414.7 merger is either observed shortly after the first core passage or prior to a second collision with an infalling group of galaxies.

5.4.7 eMACSJ1527.6+2044

eMACSJ1527.6 is another eMACS cluster with an exceptionally high velocity dispersion, 1580^{+190}_{-230} km s^{-1}, but, in contrast to eMACSJ1353.7 and eMACSJ1414.7, without clear signs of line-of-sight substructure in the radial-velocity histogram (Fig. B35). Since the ICM temperature of $(8.7^{+1.9}_{-1.3})$ keV is above average, even for massive clusters, we tentatively conclude that eMACSJ1527.6 is an active merger observed during or shortly after first core passage. Although we cannot rule out that the absence of multiple peaks in the X-ray surface brightness distribution (Fig. 14) is primarily the result of the very short *CXO*/ACIS-I exposure time of only 25 ks, the presence of several BCG candidates in close proximity in the cluster core suggests, in conjunction with the very velocity dispersion, that the merging clusters are on trajectories that would make them difficult to separate even in a much deeper X-ray observation. Strong-lensing constraints from three multiple-image systems (one of them spectroscopically confirmed) yield a lens model of eMACSJ1527.6 that is markedly more elongated than the ICM distribution (Fig. B35). A discrepancy between the collisonal and collisionless mass components of this kind is a textbook characteristic of ongoing merger activity.

5.4.8 eMACSJ1756.8+4008

eMACSJ1756.8 is an obvious large-separation merger and the most powerful cluster lens in the eMACS sample according to AStroLens. Although we invested substantial resources into spectroscopic follow-up observations of the strong-lensing features identified in this system (Figs. 6 and B38), the lack of multiple-image systems near the eastern cluster core prevents us from constraining the mass in the presumably dominant part of this highly extended system (see also Section 5.2. As a result, the Einstein radius and enclosed mass listed for eMACSJ1756.8 in Table 2 should be considered firm lower limits. A very high total mass is expected also from the X-ray estimate of 5.4×10^{14} M$_\odot$ for the total cluster mass (Table 3) and the very high velocity dispersion of 1400^{+80}_{-90} km s^{-1}, which is based on 117 spectroscopic redshifts, the largest number available for any eMACS cluster. The wide (optical) separation of the three cluster cores in the plane of the sky (800 kpc altogether), the location of the X-ray peak between two of them, and the high ICM temperature of (8.7 ± 0.4) keV identify eMACSJ1756.8 unambiguously as a linear, post-collision merger of as many as three galaxy clusters.

5.4.9 eMACSJ1831.1+6214

Although narrowly beaten to the title of "most X-ray luminous eMACS cluster" by eMACSJ2327.4 (see below), eMACSJ1831.1 ($L_{\rm X,CXO} = (3.7 \pm 0.2) \times 10^{45}$ erg s^{-1}) stands out as one of only a handful exceptionally massive clusters known at $z > 0.8$. As is apparent from Fig. B41, eMACSJ1831.1 (not to be confused with eMACSJ1831.9, Fig. B42) is a highly complex system that consists of at least two components, as evinced by its very disturbed X-ray morphology and the presence of several optical cluster cores (Fig. 14). Both X-ray peaks are shallow and far from the closest BCG candidate, indicative of a pronounced segregation of collisional and non-collisional matter that is only observed in active mergers. Like eMACSJ1756.8 (Sections 5.2 and 5.4.8), eMACSJ1831.1 lacks prominent strong-lensing features near two of its apparent optical cores, causing the associated cluster-scale mass concentrations to be missing from the Lenstool model (the respective Lenstool results are marked as lower limits in Table 2). Spectroscopic confirmation of a faint straight arc that appears to mark a saddle point in the potential close to the NE X-ray peak (cf. Fig. B41) would greatly improve the current, incomplete lens model of this exceptional system. The complexity of eMACSJ1831.1 ($z = 0.8207$) is reflected also in redshift space, where the discovery of a superimposed background cluster at $z = 0.858$ suggests that the system is part of an even more extended large-scale structure.

5.4.10 eMACSJ2327.4−0204

The most X-ray luminous eMACS cluster, eMACSJ2327.4 (Fig. B48), was known previously and published as RCS2 J2327 by Gilbank et al. (2011). For completeness' sake we show in Fig. 14 (and in Fig. B48) the archival *CXO* data and a simple lens model based on the multiple-image systems at $z = 1.42$ and $z = 2.98$ (Fig. 6) identified by Sharon et al. (2015). Since RCS2 J2327 is a well known powerful gravitational lens, we refer the reader to the literature for details of its physical properties.

5.5 Cluster galaxy properties

The spectroscopic follow-up observations of galaxies in the fields of eMACS (candidate) clusters (see Section 3.3) served multiple purposes, the most fundamental of which was the confirmation of the cluster ID and the establishment of a cluster redshift above the $z = 0.5$ threshold set for eMACS. Subsequent spectroscopic observations targeted not only the clusters' galaxy population in general (to measure velocity dispersions and search for substructure along the line of sight) but also specific galaxies of interest, such as the brightest cluster galaxies (BCGs); possible cases of ongoing ram-pressure stripping of infalling galaxies; potential AGN within (or superimposed onto) the cluster flagged as X-ray point sources; and of course strong-lensing features (i.e., highly amplified background galaxies) whose redshifts are crucial to constrain the cluster mass distribution (Section 4.3)

Although an exhaustive discussion of the findings of all these studies is beyond the scope of this paper, we present brief summaries and highlights in the following sections.

5.5.1 Velocity dispersion and line-of-sight substructure

While a robust systemic cluster redshift can be derived from a handful of concordant redshifts, a credible velocity dispersion requires much better statistics and should ideally also be computed from a stellar-mass-limited and spatially complete sample, in order to avoid biases introduced by an over-representation of galaxies near the cluster core or, conversely, the cluster outskirts. Since our selection of galaxies for spectroscopic follow-up was largely driven by technical constraints (spectrograph characteristics) and our desire to maximize efficiency by simultaneously advancing all science goals served by

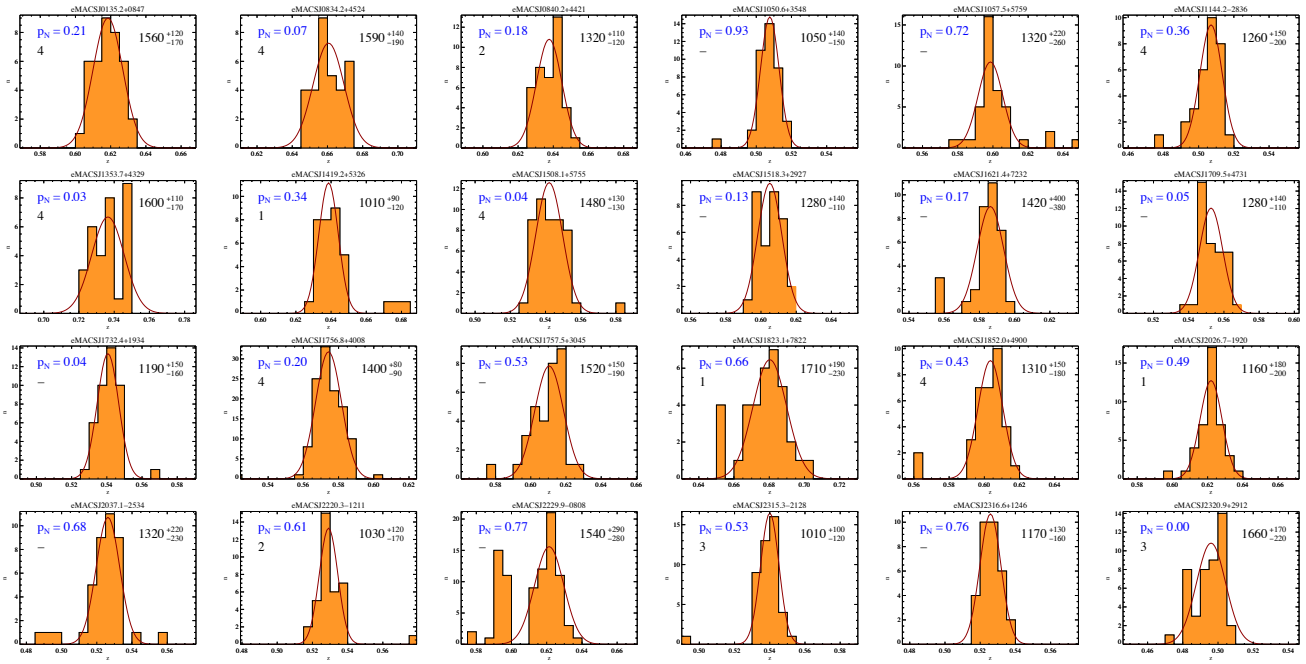

Figure 15. Histograms of the radial velocities for eMACS clusters with at least 30 spectroscopic redshifts. We list for each cluster the velocity dispersion in units of km s^{-1} and, in the upper left corner of each panel, the probability of the redshift histogram within $\delta z = \pm 0.02$ of the systemic cluster redshift being drawn from a Gaussian distribution, as well as the morphological class of each cluster from Fig. 11, where available.

these observations, the set of cluster galaxies with spectroscopic redshifts is statistically not well defined. Specifically, in clusters with few spectroscopic redshifts (fewer than 20) the dense cluster cores are likely to be undersampled, leading to potentially systematically low velocity dispersions.

We show in Fig. 15 the radial-velocity histograms of the 24 eMACS clusters for which at least 30 spectroscopic redshifts have been secured. At present eMACSJ2229.9 is the only eMACS cluster for which multiple components along the line of sight can be clearly resolved with the radial-velocity data in hand. Fig. B45 summarizes our knowledge of this system, a superposition of two clusters at $z = 0.595$ and $z = 0.625$. No *CXO* data have been obtained for this system to date; however, the presence of RASS 6135 (Villforth et al. 2017), a luminous QSO that is in fact a member of the $z = 0.625$ component of this double cluster, suggests a significant point-source contribution to the X-ray luminosity recorded in the RASS. A prominent fold arc at $z = 3.375$ (dubbed "The Scream" by us, in homage to Edvard Munch's famous painting) with an obvious counterimage to the north, together with a second triple image at $z = 5.166$, constrain a highly elongated Lenstool model[13] that, however, does not fully reflect the mass distribution of both cluster components acting in projection along our line of sight (Section 5.2 and Table 2).

While the statistics of the radial-velocity data shown in Fig. 15 are too poor to clearly reveal line-of-sight substructure in any other eMACS cluster, the probability (as estimated by the Shapiro-Wilk statistic; Shapiro & Wilk 1965) of the observed set of redshifts having been drawn from a normal distribution is a useful diagnostic to complement the morphological classification based on a cluster's optical and X-ray appearance in projection on the sky (Section 5.3 and Fig. 11). As can be seen in Fig. 15, a disturbed morphology in the plane of the sky is not strongly correlated with significant substructure also along the line of sight: of the nine eMACS clusters in morphological class 3 or 4, only three have radial-velocity distributions that fail the Shapiro-Wilk normality test at greater than 95% confidence ($p_N < 0.05$). Conversely, however, *all* eMACS clusters that fail the test and have been observed with *CXO* (eMACSJ1353.7, eMACSJ1508.1, and eMACSJ2320.9) are classified as heavily disturbed based on the X-ray / optical apperance, and the remaining two with $p_N < 0.05$ that have no *CXO* data as of yet (eMACSJ1709.5, Fig. B36, and eMACSJ1732.4, Fig. B37) show the same highly complex galaxy distribution associated with a morphological classification of 3 or 4. We tentatively conclude that the collisions in progress in these systems proceed along axes that are oblique with respect to both our line of sight and the plane of the sky. For the remaining eMACS clusters in morphology class 3 and 4, the good statistical agreement of the observed radial-velocity distributions with a Gaussian suggests that the respective merger activity occurs predominantly in the plane of the sky. These numbers are roughly consistent with isotropy in the orientation of the merger axis. Interestingly, the complementary (if small) subsample of the five eMACS clusters with at least 30 spectroscopically confirmed cluster members and a relaxed or only mildly disturbed morphology (morphology class 1 or 2) passes the Shapiro-Wilk normality test without exception.

Although encouraging, our insights into line-of-sight substructure remain qualitative even for the small subset of eMACS clusters targeted most heavily in our spectroscopic follow-up observations. Much more extensive redshift surveys of almost all eMACS clusters and their surroundings will be required to map the environment in which eMACS clusters are embedded and the pathways along which they accrete the matter that fuels their growth.

[13] Our strong-lensing analysis supersedes the one presented by Griffiths et al. (2021) which is based on an erroneous redshift for The Scream.

Figure 16. Close-up view (100 kpc on a side) of notable eMACS BCGs, as seen with *HST*. Evidence of dust obscuration is found in the majority of these galaxies. eMACSJ1057.5 and eMACSJ1148.0 show extended blue filaments to the north-east and south of the BCG, respectively, comparable to systems at lower redshift (O'Dea et al. 2010). All are detected in either our JVLA radio observations or VLASS data.

5.5.2 Large-scale structure

On much larger scales than typically probed by our spectroscopic follow-up observations of individual clusters (see Section 3.3), a glimpse of the cosmic web (Bond et al. 1996) is ironically provided with assistance from one of the non-clusters in the eMACS sample, eMACSJ0256.9. Although no diffuse X-ray emission is detected from eMACSJ0256.9 in our *CXO* follow-up observation (see Section 5.1.2), an overdensity of galaxies is clearly discernible both in our *HST* images and in the histogram of radial velocities of galaxies in this field (Fig. B9). We conclude that eMACSJ0256.9 is likely a filamentary structure aligned with our line of sight that masquerades as a three-dimensional overdensity only in this projection. Although eMACSJ0256.9 is thus not a three-dimensionally collapsed mass concentration, it appears to be a cluster in the process of formation, as indicated by the high velocity dispersion of 1170^{+140}_{-240} km s^{-1} measured for galaxies in this structure. The presence of an actively evolving filament is of interest in the context of interconnected large-scale structure since eMACSJ0256.9−1631 ($z = 0.867$) is only 6 Mpc (13′) away in projection from eMACSJ0256.7−1623 ($z = 0.862$), an intrinsically massive cluster (Fig. B8). This separation amounts to only about three times the virial radius of eMACSJ0256.7, rendering matter overdensities within the putative massive filament candidates for accretion onto the node of the cosmic web marked by eMACSJ0256.7 within the next few Gyr.

While (after evaluation of the *CXO* data) eMACSJ0256.9−1631 and eMACSJ0256.7−1623 remain a pair in the eMACS catalogue only by virtue of the commonality of a high velocity dispersion, eMACSJ1823.1 ($z = 0.680$, Fig. B40) is a true cluster pair, and the only obvious pre-collision double cluster in our sample. Separated by 865 kpc in projection, both components appear dynamically relaxed, with the dominant north-eastern cluster exhibiting evidence of a cool core. Although the radial-velocity histograms show no sign of substructure along the line of sight (Fig. B40), the very high velocity dispersion of the NE component ($\sigma > 1500$ km s^{-1}) suggests peculiar velocities (bulk motions) along the line of sight, a notion that is supported by the presence of a nearby foreground structure at $z = 0.65$. eMACSJ1823.1 thus marks a node of the cosmic web that might be actively accreting matter from orthogonal directions.

5.5.3 Brightest Cluster Galaxies

All X-ray selected samples of galaxy clusters contain clusters dominated by a BCG, these frequently display strong optical emission lines, star formation, and an associated reservoir of cold molecular gas (e.g., Crawford et al. 1999; Green et al. 2016). As demonstrated in the MUSE study of eMACSJ0252.4 (Ebeling et al. 2021, Fig. 13), such "active" BCGs are seen out to $z \sim 0.7$ and stand out in the optical regime as bluer than the expected colour of an evolved stellar population.

Our spectroscopic follow-up covers all BCGs in eMACS apart from those in eMACSJ0934.6, which has a published SDSS spectrum, and eMACSJ1852.0 which at present has no publicly available spectrum. For 17 of the 110 BCGs in the sample these spectra show significant [Oii]λ3727 line emission, indicating star formation comparable to that seen in the most active BCGs at lower redshifts (Green et al. 2016), where Hα line emission is typically used to gauge this activity. If we take the presence of an active BCG as an indicator of cluster relaxation, this spectroscopic estimate of the fraction of cool-core clusters of (15±4)% is consistent with the percentage estimated from X-ray imaging (approximately 10%) in Section 5.3. While the fraction of cool-core clusters is often found to be higher at lower redshifts, these more local studies benefit from both the accessibility of the Hα line and more extensive X-ray observations.

Radio emission from 28 BCGs in our sample is detected at $> 5\sigma$ or 150μJy in the JVLA observations at 5 GHz. With 66 systems having been observed, this number corresponds to a detection rate of (42±8)%, comparable to the detection rate at the same observed frequency reported by Hogan et al. (2015a) for the most X-ray luminous clusters at $z < 0.3$. The range in radio spectral index and the mean radio spectral index of $\alpha = -0.95$, computed using available RACS, VLASS, TGSS, and LOFAR data for the detected sources, are also comparable to those found in previous studies. Of the remaining 45 clusters without a JVLA observation, 11 (i.e., 24%) have a VLASS detection at 3 GHz at the higher flux density limit of 0.5 mJy reached in that all-sky survey, suggesting a comparable radio-power distribution for the sample as a whole.

Several BCGs in the eMACS sample in addition to eMACSJ0252.4 (Ebeling et al. 2021, Fig. 13) are notable in their optical morphol-

ogy. Specifically, eMACS1030.5 (Figs. 16, B20) harbors a spectacular case of an active BCG and is the brightest radio source in the eMACS sample, with properties comparable to those of compact, core-dominated sources such as 4C+55.16 (Hogan et al. 2015b; Rose et al. 2022; Timmerman et al. 2022) and MACSJ0242.5 (Allingham et al. 2023). Signs of active star formation, dust or multiple cores are discernible in the *HST* images of other eMACS BCGs, demonstrating that "active" BCGs are common at $z > 0.5$; Fig. 16 shows 100 kpc × 100 kpc cutouts from our *HST* images for several examples.

5.5.4 *Ram-pressure Stripping*

In addition to being prime targets for investigations of phenomena and physics operating on scales of hundreds of kpc, massive galaxy clusters provide a high-density environment that shapes the evolution of the constituent galaxies on kpc scales. Two areas of galaxy evolution that are of particular interest are the interactions of BCGs and their active nuclei with the surrounding ICM (see Section 5.5.3) and the potential rapid morphological transformation of late-type field galaxies into early-type cluster members through ram-pressure stripping by the ICM (Gunn & Gott 1972).

While the textbook "jellyfish" appearance of galaxies undergoing ram-pressure stripping (e.g., Cortese et al. 2007; Owers et al. 2012; Ebeling et al. 2014) is less readily discernible at the high redshifts of eMACS clusters, the superb angular resolution of *HST* reveals many promising cases in the eMACS sample. We show in Fig. 17 examples of spectroscopically confirmed cluster members likely experiencing ram-pressure stripping. Note that we include spirals with an almost undisturbed morphology since, in the environment encountered within massive clusters, essentially all late-type galaxies are expected to be undergoing ram-pressure stripping to some degree and will ultimately be stripped of the majority of their atomic and molecular gas. Many other late-type galaxies with similarly intriguing morphology are found in *HST* images of eMACS clusters and await spectroscopic follow-up observations to establish cluster membership.

Although their faintness and small angular size renders these galaxies challenging targets for in-depth follow-up studies of their internal dynamics, the excitation state of the intragalactic medium, or the effects of ram-pressure stripping on central black holes (all topics at the focus of "jellyfish" studies in the more nearby Universe out to about $z = 0.3$: Kalita & Ebeling 2019, and references therein), the mere detection of debris trails or ICM-induced deformations of the galactic disk can provide valuable constraints on the direction of motion in the plane of the sky. The potential of ram-pressure stripping as a diagnostic of peculiar motions perpendicular to our line of sight was pointed out by Ebeling & Kalita (2019) and, in the eMACS sample, is exemplified by eMACSJ1757.5 (Fig. B39) which illustrates that the tell-tale morphology of "jellyfish" galaxies can indeed reveal dominant axes of galaxy infall even at $z > 0.5$.

6 CONCLUSIONS

Based on RASS detections comprising as few as 6 photons, the extended Massive Cluster Survey (eMACS) has compiled a sample of over 100 very X-ray luminous galaxy clusters after searching over 20,000 square degrees of extragalactic sky. Limited to clusters at $z > 0.5$, eMACS probes a population that was hitherto barely explored: the first generation of truly massive clusters ($M \gtrsim 10^{15}$ M$_\odot$). Extensive follow-up observations of eMACS cluster candidates with ground- and space-based observatories, crucial to overcome the poor photon statistics of the underlying RASS detections, confirmed the presence of clusters in the vast majority of the targeted systems but, so far, have also shown two to be non-clusters. As importantly, follow-up work from radio to X-ray wavelengths yielded valuable insights into the physical properties of many of these systems and allowed us to constrain their gravitational-lensing strength, evolutionary state, and ICM gas temperature. In addition, these observations revealed examples of highly active BCGs, powerful QSOs, and late-type galaxies undergoing ram-pressure stripping during their high-velocity passage through the dense ICM.

The sample presented here includes the most distant galaxy cluster ever discovered in the RASS (eMACSJ0324.0 at $z = 0.90$, Fig. B10), extremely powerful gravitational lenses (e.g., eMACSJ1212.5, Fig. B26; eMACSJ1341.9, Fig. B29 and Ebeling et al. 2018; or eMACSJ1353.7, Fig. B30), a newly discovered "exotic" hyperbolic umbilical lens (eMACSJ1248.2, Fig. 5), exceptionally X-ray luminous cluster collisions in various phases of the merging process (e.g., eMACSJ1756.8, Fig. B38; eMACSJ1831.1, Fig. B41), extraordinarily "active" BCGs, e.g., in eMACSJ0252.4 (Ebeling et al. 2021, Fig. 13) and eMACSJ1030.5 (Fig. 16), and numerous systems whose potentially remarkable physical properties are only hinted at by the existing data (e.g., eMACSJ1144.2, eMACSJ1508.1, eMACSJ1757.5).

We highlight in particular the potential importance of the massive clusters at $z > 0.5$ presented in this work as powerful gravitational telescopes to study faint sources in the very distant Universe (as already demonstrated, for example with the lensed sources at $z = 3.375$ and $z = 5.166$ in eMACSJ2229.9). The main benefits of selected eMACS clusters as probes for *James Webb Space Telescope* (*JWST*) surveys of the very distant Universe, $z \gg 10$, are their high masses and high redshifts, which also yield a corresponding reduction in contamination from intracluster light, allowing faint lensed features to be more easily identified in the high-amplification regions near the cluster centres. We anticipate that *JWST* surveys of these clusters will be as productive as the current exploitation of the MACS sample for studying faint galaxies and individual stars in the high-redshift Universe (e.g., Abdurro'uf et al. 2023; Atek et al. 2023; Diego et al. 2023; Asada et al. 2024; Fujimoto et al. 2024).

While the current eMACS sample is not statistically complete, tentative conclusions about the physical properties of the population of very massive clusters at $z > 0.5$ can be drawn from better defined subsets. Specifically, the morphology of the ICM of eMACS clusters in high-resolution imaging X-ray observations and the optical properties of eMACS BCGS from both imaging and spectroscopic follow-up work suggest that the cool-core fraction lies at or below ~15%, consistent with the findings of Mann & Ebeling (2012) and expectations for a sample that approaches the redshift of cluster formation at $z \sim 1$. The analysis of all existing *CXO*/ACIS-I data for eMACS clusters shows that the power-law model of the L_X–kT relation established for less massive clusters at lower redshifts (e.g., Takey et al. 2013) extends to the regime probed by eMACS (Fig. 9). For the majority of eMACS clusters, velocity dispersions are very high, reaching and exceeding 1500 km s^{-1} for several systems (Fig. 15). While clear signs of line-of-sight substructure are not detectable at the current statistics, the highest velocity dispersions exceed reasonable virial estimates and suggest that inflation from peculiar (bulk) velocities from ongoing cluster growth is common in this cluster population.

As, over three decades after its completion, the RASS is being succeeded by eRASS1 (Merloni et al. 2024), the second all-sky survey ever conducted with an imaging X-ray telescope, the samples of the most X-ray luminous clusters at $z > 0.3$ compiled by the

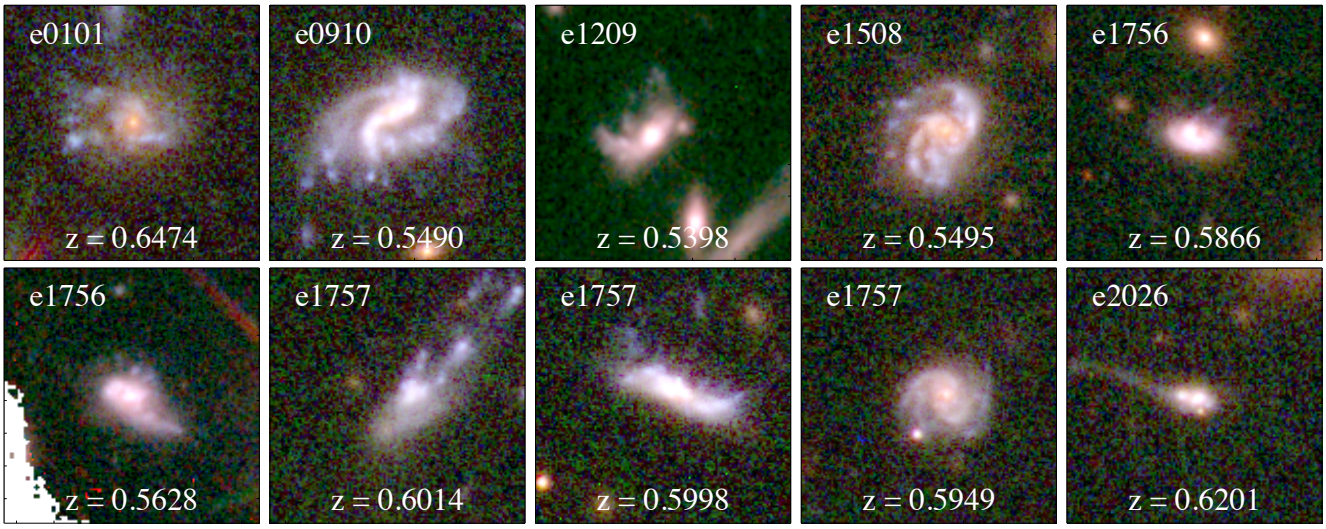

Figure 17. *HST* images (50 kpc on the side) of spectroscopically confirmed cluster members showing evidence of ram-pressure stripping by the ICM. Shortened names in the upper left corner of each panel indicate the respective host cluster.

MACS and eMACS projects are being complemented by a wealth of discoveries down the mass and luminosity scale, all the way to groups of galaxies, protoclusters, and dense filaments. In addition, *eROSITA*'s much greater sensitivity will yield vastly better photon statistics, and at least estimated ICM temperatures, for all eMACS clusters that, as of yet, have not been targeted in dedicated follow-up observations with *CXO*.

Although neither the compilation of the eMACS sample nor the analysis of the physical properties of all eMACS clusters are complete at this point, we here release all data and data products obtained and derived by us in the course of this program to avoid duplication and unnecessary investments of precious observing resources by the extragalactic community (Zaznobin et al. 2023).

ACKNOWLEDGEMENTS

We thank Lukas Zalesky for permission to use unpublished AStroLens results in Section 5.2.2. of this paper. HE gratefully acknowledges financial support from grants administered by STScI and CXC. Specifically, support for programs GO-13671, -14098, -15132, -15466, -15608, -15843, -15844, and -16428 was provided by NASA through a grant from the Space Telescope Science Institute, which is operated by the Associations of Universities for Research in Astronomy, Incorporated, under NASA contract NAS5-26555. Support for this work was also provided by the National Aeronautics and Space Administration through *CXO* Award Number GO9-20120X, GO0-21125X, GO1-22119X, and GO2-23119X, issued by the *Chandra* X-ray Center, which is operated by the Smithsonian Astrophysical Observatory for and on behalf of the National Aeronautics Space Administration under contract NAS8-03060. Durham authors acknowledge support from STFC (ST/T000244/1, ST/X001075/1). This research has made use of data obtained from the *Chandra* Data Archive and the *Chandra* Source Catalogue, and software provided by the *Chandra* X-ray Center (CXC) in the application packages CIAO and Sherpa.

DATA AVAILABILITY

The data underlying this article are available in the MAST, *CXO*, and Keck data archives.

REFERENCES

Abdurro'uf et al., 2023, ApJ, 945, 117
Alavi A., et al., 2014, ApJ, 780, 143
Allen S. W., Evrard A. E., Mantz A. B., 2011, ARA&A, 49, 409
Allingham J. F. V., et al., 2023, MNRAS, 522, 1118
Andrade-Santos F., et al., 2017, ApJ, 843, 76
Applegate D. E., et al., 2014, MNRAS, 439, 48
Arnaud M., Aghanim N., Neumann D. M., 2002, A&A, 389, 1
Asada Y., et al., 2024, MNRAS, 527, 11372
Asplund M., Grevesse N., Sauval A. J., Scott P., 2009, ARA&A, 47, 481
Atek H., et al., 2023, MNRAS, 519, 1201
Bayliss M. B., Hennawi J. F., Gladders M. D., Koester B. P., Sharon K., Dahle H., Oguri M., 2011, ApJS, 193, 8
Beauchesne B., et al., 2024, MNRAS, 527, 3246
Beers T. C., Flynn K., Gebhardt K., 1990, AJ, 100, 32
Bertin E., Arnouts S., 1996, A&AS, 117, 393
Bezanson R., et al., 2022, arXiv e-prints, p. arXiv:2212.04026
Bleem L. E., et al., 2015, ApJS, 216, 27
Bleem L. E., et al., 2020, ApJS, 247, 25
Bocquet S., et al., 2019, ApJ, 878, 55
Böhringer H., et al., 2004, A&A, 425, 367
Böhringer H., Chon G., Collins C. A., Guzzo L., Nowak N., Bobrovskyi S., 2013, A&A, 555, A30
Bond J. R., Kofman L., Pogosyan D., 1996, Nature, 380, 603
Boselli A., Fossati M., Sun M., 2022, A&ARv, 30, 3
Bouwens R. J., Illingworth G., Ellis R. S., Oesch P., Stefanon M., 2022, ApJ, 940, 55
Bower R. G., Lucey J. R., Ellis R. S., 1992, MNRAS, 254, 601
Bradač M., Allen S. W., Treu T., Ebeling H., Massey R., Morris R. G., von der Linden A., Applegate D., 2008, ApJ, 687, 959
Buchner J., et al., 2014, A&A, 564, A125
Carlstrom J. E., et al., 2011, PASP, 123, 568
Chambers K. C., et al., 2016, arXiv e-prints, p. arXiv:1612.05560
Chiu I. N., Klein M., Mohr J., Bocquet S., 2023, MNRAS, 522, 1601
Chon G., Böhringer H., 2017, A&A, 606, L4

Cooper M. C., Newman J. A., Davis M., Finkbeiner D. P., Gerke B. F., 2012, spec2d: DEEP2 DEIMOS Spectral Pipeline, Astrophysics Source Code Library, record ascl:1203.003 (ascl:1203.003)
Cortese L., et al., 2007, MNRAS, 376, 157
Crawford C. S., Allen S. W., Ebeling H., Edge A. C., Fabian A. C., 1999, MNRAS, 306, 857
De Grandi S., Molendi S., Böhringer H., Chincarini G., Voges W., 1997, ApJ, 486, 738
De Grandi S., et al., 1999, ApJ, 514, 148
De Lucia G., Blaizot J., 2007, MNRAS, 375, 2
Diego J. M., et al., 2023, A&A, 679, A31
Dubinski J., 1998, ApJ, 502, 141
Ebeling H., Kalita B. S., 2019, ApJ, 882, 127
Ebeling H., Voges W., Bohringer H., Edge A. C., Huchra J. P., Briel U. G., 1996, MNRAS, 281, 799
Ebeling H., Edge A. C., Fabian A. C., Allen S. W., Crawford C. S., Böhringer H., 1997, ApJ, 479, L101
Ebeling H., Edge A. C., Bohringer H., Allen S. W., Crawford C. S., Fabian A. C., Voges W., Huchra J. P., 1998, MNRAS, 301, 881
Ebeling H., Edge A. C., Allen S. W., Crawford C. S., Fabian A. C., Huchra J. P., 2000, MNRAS, 318, 333
Ebeling H., Edge A. C., Henry J. P., 2001, ApJ, 553, 668
Ebeling H., Mullis C. R., Tully R. B., 2002, ApJ, 580, 774
Ebeling H., White D. A., Rangarajan F. V. N., 2006, MNRAS, 368, 65
Ebeling H., Barrett E., Donovan D., Ma C. J., Edge A. C., van Speybroeck L., 2007, ApJ, 661, L33
Ebeling H., Edge A. C., Mantz A., Barrett E., Henry J. P., Ma C. J., van Speybroeck L., 2010, MNRAS, 407, 83
Ebeling H., et al., 2013, MNRAS, 432, 62
Ebeling H., Stephenson L. N., Edge A. C., 2014, ApJ, 781, L40
Ebeling H., Qi J., Richard J., 2017, MNRAS, 471, 3305
Ebeling H., Stockmann M., Richard J., Zabl J., Brammer G., Toft S., Man A., 2018, ApJ, 852, L7
Ebeling H., Richard J., Smail I., Edge A. C., Koekemoer A. M., Zalesky L., 2021, MNRAS, 508, 3663
Eckert D., Finoguenov A., Ghirardini V., Grandis S., Kaefer F., Sanders J., Ramos-Ceja M., 2020, The Open Journal of Astrophysics, 3, 12
Ettori S., et al., 2019, A&A, 621, A39
Evrard A. E., et al., 2008, ApJ, 672, 122
Faber S. M., et al., 2003, in Iye M., Moorwood A. F. M., eds, Society of Photo-Optical Instrumentation Engineers (SPIE) Conference Series Vol. 4841, Instrument Design and Performance for Optical/Infrared Ground-based Telescopes. pp 1657–1669, doi:10.1117/12.460346
Fedeli C., Bartelmann M., 2007, A&A, 474, 355
Feroz F., Hobson M. P., Cameron E., Pettitt A. N., 2019, The Open Journal of Astrophysics, 2, 10
Freeman P. E., Kashyap V., Rosner R., Lamb D. Q., 2002, ApJS, 138, 185
Fruchter A. S., et al. 2010, in 2010 Space Telescope Science Institute Calibration Workshop. pp 382–387
Fruscione A., et al., 2006, in Silva D. R., Doxsey R. E., eds, Society of Photo-Optical Instrumentation Engineers (SPIE) Conference Series Vol. 6270, Society of Photo-Optical Instrumentation Engineers (SPIE) Conference Series. p. 62701V, doi:10.1117/12.671760
Fujimoto S., et al., 2024, ApJ, 964, 146
Gilbank D. G., Gladders M. D., Yee H. K. C., Hsieh B. C., 2011, AJ, 141, 94
Gobat R., et al., 2011, A&A, 526, A133
Gonzalez A. H., et al., 2019, ApJS, 240, 33
Green T. S., et al., 2016, MNRAS, 461, 560
Griffiths R. E., Rudisel M., Wagner J., Hamilton T., Huang P.-C., Villforth C., 2021, MNRAS, 506, 1595
Gunn J. E., Gott J. Richard I., 1972, ApJ, 176, 1
HI4PI Collaboration et al., 2016, A&A, 594, A116
Harvey D., Massey R., Kitching T., Taylor A., Tittley E., 2015, Science, 347, 1462
Hilton M., et al., 2021, ApJS, 253, 3
Hogan M. T., et al., 2015a, MNRAS, 453, 1201
Hogan M. T., et al., 2015b, MNRAS, 453, 1223
Jauzac M., et al., 2018, MNRAS, 481, 2901
Jullo E., Kneib J. P., Limousin M., Elíasdóttir Á., Marshall P. J., Verdugo T., 2007, New Journal of Physics, 9, 447
Kaiser N., et al., 2002, in Tyson J. A., Wolff S., eds, Society of Photo-Optical Instrumentation Engineers (SPIE) Conference Series Vol. 4836, Survey and Other Telescope Technologies and Discoveries. pp 154–164, doi:10.1117/12.457365
Kalita B. S., Ebeling H., 2019, ApJ, 887, 158
Kneib J.-P., Natarajan P., 2011, A&ARv, 19, 47
LaRoque S. J., et al., 2003, ApJ, 583, 559
Lagattuta D. J., et al., 2023, MNRAS, 522, 1091
Limousin M., et al., 2012, A&A, 544, A71
Lotz J. M., et al., 2017, ApJ, 837, 97
Lovisari L., et al., 2020, ApJ, 892, 102
Mahler G., et al., 2023, ApJ, 945, 49
Malte Schäfer B., Bartelmann M., 2007, MNRAS, 377, 253
Mann A. W., Ebeling H., 2012, MNRAS, 420, 2120
Mantz A. B., et al., 2015, MNRAS, 446, 2205
Markevitch M., Gonzalez A. H., David L., Vikhlinin A., Murray S., Forman W., Jones C., Tucker W., 2002, ApJ, 567, L27
Masters D., Capak P., 2011, PASP, 123, 638
McDonald M., et al., 2016, ApJ, 817, 86
McLean I. S., et al., 2010, in McLean I. S., Ramsay S. K., Takami H., eds, Society of Photo-Optical Instrumentation Engineers (SPIE) Conference Series Vol. 7735, Ground-based and Airborne Instrumentation for Astronomy III. p. 77351E, doi:10.1117/12.856715
McLean I. S., et al., 2012, in McLean I. S., Ramsay S. K., Takami H., eds, Society of Photo-Optical Instrumentation Engineers (SPIE) Conference Series Vol. 8446, Ground-based and Airborne Instrumentation for Astronomy IV. p. 84460J, doi:10.1117/12.924794
Meneghetti M., et al., 2023, A&A, 678, L2
Merloni A., et al., 2024, A&A, 682, A34
Merritt D., 1985, ApJ, 289, 18
Morishita T., et al., 2023, ApJ, 947, L24
Navarro J. F., Frenk C. S., White S. D. M., 1997, ApJ, 490, 493
Newman A. B., Treu T., Ellis R. S., Sand D. J., 2013, ApJ, 765, 25
Newman A. B., Ellis R. S., Andreon S., Treu T., Raichoor A., Trinchieri G., 2014, ApJ, 788, 51
O'Dea K. P., et al., 2010, ApJ, 719, 1619
Oemler A. J., 1976, ApJ, 209, 693
Ofek E. O., Seitz S., Klein F., 2008, MNRAS, 389, 311
Ogrean G. A., et al., 2016, ApJ, 819, 113
Oke J. B., et al., 1995, PASP, 107, 375
Owers M. S., Couch W. J., Nulsen P. E. J., Randall S. W., 2012, ApJ, 750, L23
Papovich C., et al., 2010, ApJ, 716, 1503
Planck Collaboration et al., 2014, A&A, 571, A20
Pointecouteau E., Arnaud M., Pratt G. W., 2005, A&A, 435, 1
Prochaska J. X., et al., 2020, Journal of Open Source Software, 5, 2308
Randall S. W., Sarazin C. L., Ricker P. M., 2002, ApJ, 577, 579
Reiprich T. H., 2001, PhD thesis, Max-Planck-Institute for Extraterrestrial Physics, Garching
Repp A., Ebeling H., 2018, MNRAS, 479, 844
Richard J., et al., 2010, MNRAS, 404, 325
Richard J., et al., 2021, A&A, 646, A83
Rose T., et al., 2022, MNRAS, 509, 2869
Rossetti M., Gastaldello F., Eckert D., Della Torre M., Pantiri G., Cazzoletti P., Molendi S., 2017, MNRAS, 468, 1917
Saro A., Mohr J. J., Bazin G., Dolag K., 2013, ApJ, 772, 47
Shapiro S. S., Wilk M. B., 1965, Biometrika, 52, 591
Sharon K., et al., 2015, ApJ, 814, 21
Sharon K., et al., 2020, ApJS, 247, 12
Steidel C. C., Adelberger K. L., Dickinson M., Giavalisco M., Pettini M., Kellogg M., 1998, ApJ, 492, 428
Steidel C. C., et al., 2014, ApJ, 795, 165
Sunyaev R. A., Zeldovich I. B., 1980, ARA&A, 18, 537
Swetz D. S., et al., 2011, ApJS, 194, 41
Takey A., Schwope A., Lamer G., 2013, A&A, 558, A75

Timmerman R., van Weeren R. J., Botteon A., Röttgering H. J. A., McNamara B. R., Sweijen F., Bîrzan L., Morabito L. K., 2022, A&A, 668, A65
Vikhlinin A., Markevitch M., Murray S. S., 2001, ApJ, 551, 160
Vikhlinin A., et al., 2009, ApJ, 692, 1060
Villforth C., et al., 2017, MNRAS, 466, 812
Visvanathan N., Sandage A., 1977, ApJ, 216, 214
Voges W., et al., 1999, A&A, 349, 389
Voges W., Henry J. P., Briel U. G., Böhringer H., Mullis C. R., Gioia I. M., Huchra J. P., 2001, ApJ, 553, L119
Vollmer B., Cayatte V., Balkowski C., Duschl W. J., 2001, ApJ, 561, 708
Wang T., et al., 2016, ApJ, 828, 56
Wilber A., et al., 2018, MNRAS, 476, 3415
Zalesky L., Ebeling H., 2020, MNRAS, 498, 1121
Zaznobin I. A., et al., 2023, Astronomy Letters, 49, 599
Zitrin A., Broadhurst T., Barkana R., Rephaeli Y., Benítez N., 2011, MNRAS, 410, 1939
van Weeren R. J., de Gasperin F., Akamatsu H., Brüggen M., Feretti L., Kang H., Stroe A., Zandanel F., 2019, Space Sci. Rev., 215, 16

APPENDIX A: THE COMPILATION OF CLUSTER CANDIDATES FROM THE RASS

The eMACS project was launched in 2010, almost a decade before the launch of *eROSITA*, and was motivated by the realization that the RASS, the only existing all-sky survey with an imaging X-ray telescope, had not been fully exploited in search for massive clusters. In fact, there are thousands of X-ray sources below the MACS flux limit that can be examined in an even more ambitious cluster survey, and yet have never been tapped systematically. Our approach to using this valuable resource is detailed in the following.

A1 The RASS Faint-Source Catalogue

Conducted in great circles through the ecliptic poles that result in a median exposure time of 370s, the RASS was, until 2020, the only existing all-sky survey conducted in soft X-rays (0.1–2.4 keV) and a powerful resource for X-ray studies that require extremely large areal coverage. Two official source catalogues (the Bright Source Catalogue, BSC, and the Faint Source Catalogue, FSC) as well as images and photon event tables for the entire survey are publicly available. The BSC contains only sources comprising at least 15 net photons, and featuring count rates in excess of 0.05 ct s^{-1}; its defining criterion, however, is the maximum likelihood value assigned to all RASS sources by the official RASS source detection algorithm. The BSC comprises 18,802 sources above this preset detection-likelihood threshold. *MACS is based on sources selected from the BSC.*

The much larger FSC, which lists over 100,000 additional sources comprising as few as 6 net photons, has seen very little use in scientific studies, due to its poorly known statistical properties. The enormous potential of the FSC becomes, however, immediately obvious when the distributions of net counts and count rate of FSC and BSC sources are inspected and compared. Following the approach taking for MACS (for details, see Ebeling et al. 2001), we limit both data sets to the extragalactic sky ($|b| \geq 20°$) and the equatorial sky observable from Mauna Kea ($-40° < \delta - 80°$) but apply no other cuts. The resulting histograms (proxies for the respective differential logN-logS distributions) for the BSC and FSC are plotted in Fig. A1 and demonstrate that

(i) in spite of its suggestive minimal source count value of 15, the BSC is not complete above this limit: 9% of all RASS sources featuring more than 15 counts are in fact listed not in the BSC, but in the FSC;

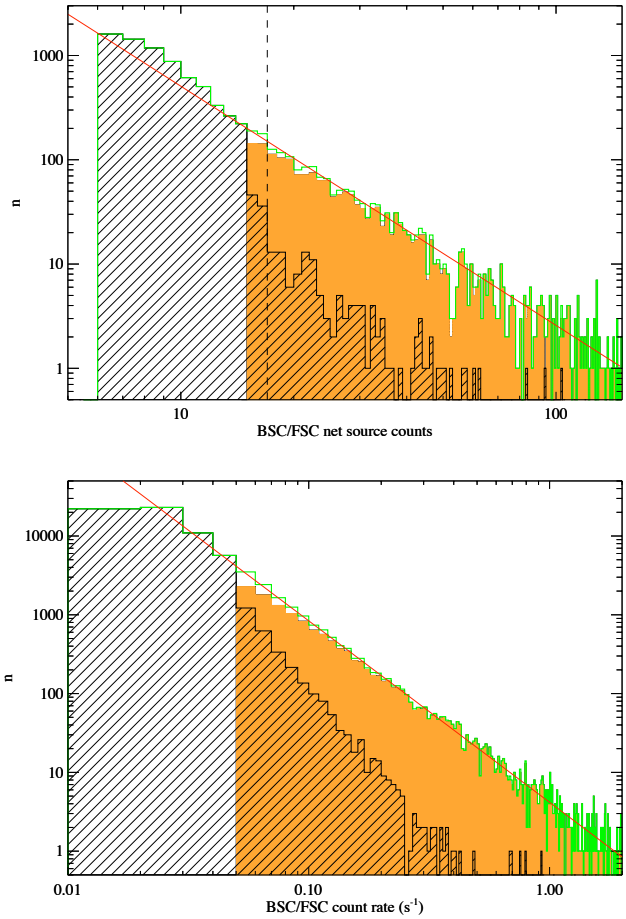

Figure A1. Differential logN-logS distributions for net counts (top) and count rates (bottom) of BSC (orange) and FSC (shaded) sources at $|b| \geq 20°$. For the count distribution (top) only sources featuring exposure times between 200 and 300 s were considered, thereby mitigating the impact of exposure time variations on the RASS detection efficiency. The source count limit of 17 photons adopted during the compilation of the MACS sample is marked by the dashed vertical line. The green histograms show the distributions that result when both catalogues are combined; best-fitting power laws are shown in red.

(ii) for sources comprising between 6 and 11 photons, the FSC catalogue is about 20–30% "over-complete", a well known phenomenon caused by an increasing number of spurious sources (many of them multiple detections of very bright or very extended sources) as the photon statistics approach the ultimate detection limit of, roughly, 5 to 6 net counts;

(iii) when both catalogues are combined, the differential logN–logS distributions for the resulting data sets follow a power law well below the count limit of 17 adopted for MACS, and well below the count-rate limit of 0.05 s^{-1} of the BSC in general.

Figure A1 demonstrates that RASS-based surveys can be successfully extended significantly beyond the limits of the BSC, a claim that is supported by the fact that the slopes of about −2.3 of the best-fitting power laws describing the merged FSC/BSC data sets are in excellent agreement with the near-Euclidean value found for galaxy clusters and extragalactic RASS sources in general (Ebeling et al. 1998; Voges et al. 1999).

The conclusion that the RASS continues to hold great promise

for *cluster* surveys may appear premature though, given that our analysis so far used *all* RASS sources in the extragalactic sky, i.e., a source population that is dominated by AGN and also includes a significant number of Galactic sources (primarily X-ray binaries and stars), all of which are X-ray point sources. Applying any insights gained from Fig. A1 to clusters would indeed be impermissible if we aimed to find additional X-ray-faint systems at low redshift[14], where even galaxy groups exhibit significant angular extent in the RASS. *At $z > 0.4$, however, galaxy clusters appear almost pointlike at the angular resolution of the RASS* (Fig. A2). As a result, the background in the standard RASS detect cell is negligible for sources comprising at least 10 net photons, except for the deepest part of the RASS near the ecliptic poles where integration times approaching, and over a small solid angle in fact exceeding, 1000 s are reached, resulting in increased background counts and thus a higher effective detection threshold in terms of net source counts (Voges et al. 2001).

Although the efficiency of the RASS detection algorithm near the detection limit has to be carefully tested as a function of RASS exposure time, the potential rewards make this effort very worthwhile. We show, in Fig. A3, the differential log$N$-log$S$ distributions in terms of energy flux[15] when two different source count thresholds are applied: the top panel illustrates the impact of the FSC for sources with net counts in excess of 17 photons, the limit adopted for MACS. Not surprisingly, little can be gained above the MACS flux limit of 1×10^{-12} erg cm^{-2} s^{-1}, but at fluxes down to 5×10^{-13} erg cm^{-2} s^{-1} the inclusion of the FSC improves upon the MACS sample size by 66%. If the count limit is lowered to 12 (bottom panel of Fig. A3), easily achievable as shown in Fig. A1, the combined FSC/BSC data set increases the survey's effective solid angle noticeably already within the MACS regime (i.e., at $f_X > 1 \times 10^{-12}$ erg cm^{-2} s^{-1}), and allows the compilation of a sample of *more than twice the size of MACS* at $f_X > 5 \times 10^{-13}$ erg cm^{-2} s^{-1}.

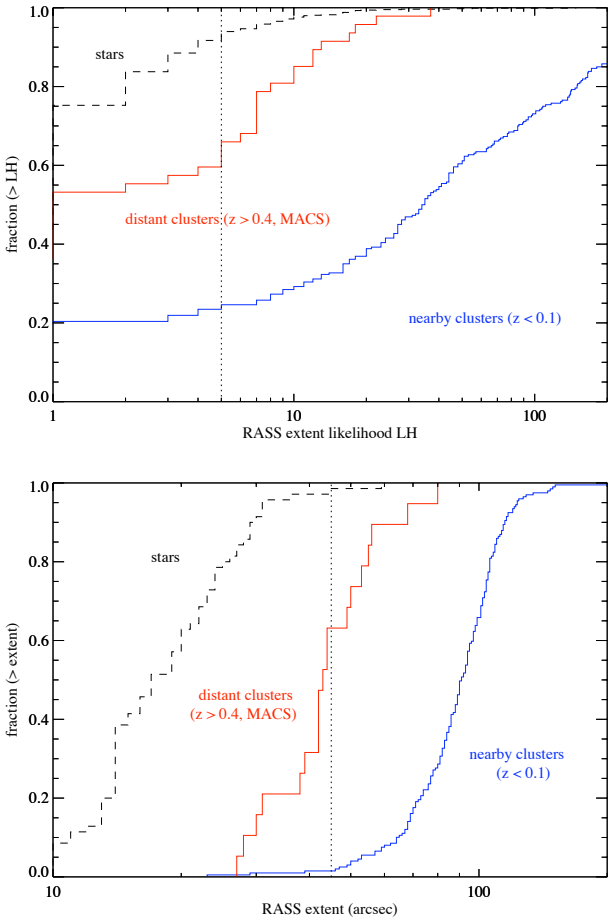

Figure A2. *(Top)* Cumulative distribution of source extent likelihood in the RASS for three classes of objects: stars (as a reference for point sources), nearby clusters, and distant clusters. The extent likelihood distribution for stars illustrates that values below 5 (dotted vertical line) are not significant and often spurious. Note how over 60% of all distant clusters are classified as point sources. *(Bottom)* Cumulative distribution of source extent for the same three object classes as shown on top, but using only sources with extent likelihood values of at least 5. The dotted vertical line marks the FWHM of the RASS point-spread function, which is also the pixel size of the RASS. Even for the minority of all distant clusters classified as extended (left panel) the assigned angular extent exceeds 1 pixel only for fewer than 40%.

A2 Optical screening

Our strategy for the identification of distant galaxy clusters from these data sets is brute force: we select all X-ray sources listed in the RASS BSC and FSC that fall within our study area and above the thresholds in X-ray flux and spectral hardness ratio, and then examine PS1 images in the g, r, i, and z bands in a 5×5 arcmin^2 region around the X-ray source position. Our goal, however, is not the identification of every X-ray source in the BSC and FSC; far from it. For each RASS source, we merely seek to answer the much simpler question: "Based on the colour images provided by PS1, could the optical counterpart of this source conceivably be a massive, distant cluster?" In essence this entails the visual identification of candidate clusters at $z \gtrsim 0.3$ as overdensities of faint, red galaxies, a simple approach that is motivated by the success of MACS, which demonstrated that distant RASS-detected clusters are readily discernible in relatively shallow optical images. As illustrated by Fig. A4, which shows eMACSJ1756.8 ($z = 0.574$) as viewed by PS1 in the 3π survey (see also Section 5.4.8), this strategy remains successful for the population of X-ray fainter clusters probed by eMACS.

At the highest redshifts probed by eMACS, however, the Balmer/4000Å break in cluster galaxies is getting close to moving out of the optical window. Care must thus be taken not to reject a RASS source based on the absence of an obvious galaxy overdensity in a *gri* PS1 image; unless the presence of a bright star, a QSO candidate, or some other, known celestial object[16] suggest a non-cluster ID, a "blank field" in a PS1/3π image is kept in our list of candidates and assigned high priority for follow-up observation. Although the associated follow-up observations resulted, in most cases, in the rejection of such sources, several discoveries vindicate our conservative approach, as is illustrated by Fig. A5 which shows an apparently blank field at the location of a RASS source. Owing to the lack of a plausible non-cluster ID we nonetheless included this source in our

[14] and thus also of low X-ray luminosity

[15] For the conversion from count rate to flux we assumed a spectrum typical of very X-ray luminous clusters at moderately high redshift, characterized by $z = 0.2$, k$T = 8$ keV, $Z = 0.2$, and the Galactic n_H column density in the direction of the source. Modifying these assumptions does not affect any of our conclusions noticeably.

[16] In order to aid the identification of non-cluster sources, we also query NASA's Extragalactic Database (NED) for known celestial objects within 2 arcmin radius of the respective X-ray source.

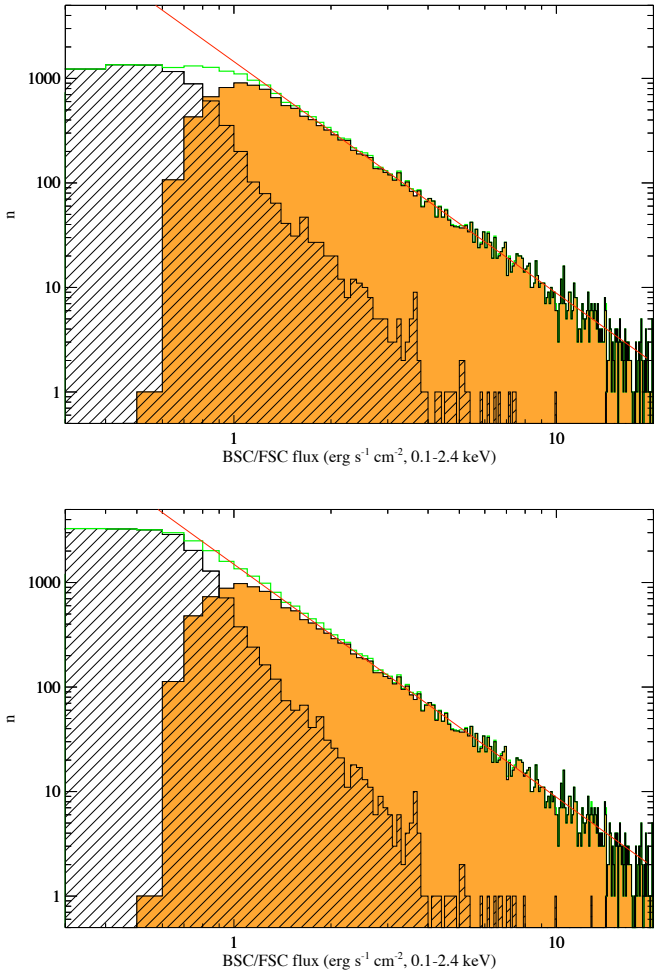

Figure A3. Differential logN-logS distributions for BSC (orange) and FSC (shaded) sources at $|b| \geq 20°$. The plot on top uses only sources comprising at least 17 net photons (the threshold used by the MACS project and marked in Fig. 4); for the botttom plot this limit is lowered to 12 photons. Green histograms and red power-law models refer to the distributions resulting when the FSC and BSC catalogues are merged.

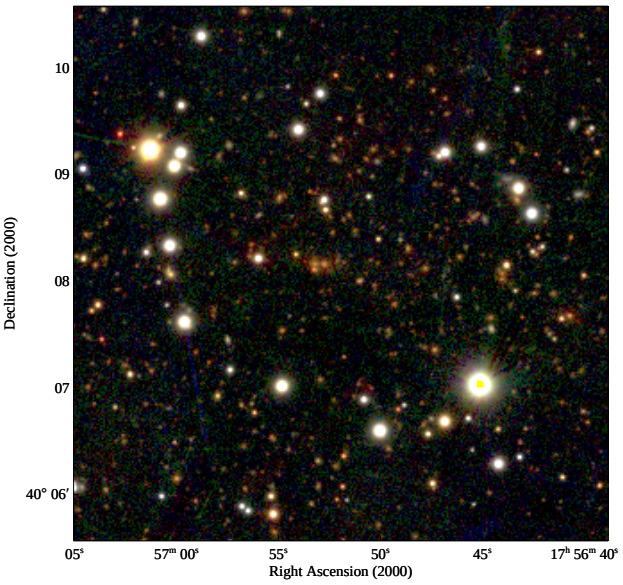

Figure A4. PS1/3π image (gri) of a 5×5 arcmin^{-2} region centred on the RASS source 1RXS J175651.8+400802. An overdensity of red galaxies near the image centre is immediately visible, as is a second apparent cluster core about 2′ to the west.

list of eMACS cluster candidates, a decision that led to the discovery of eMACSJ0324.0 ($z = 0.90$) (see Section 5.4.1).

APPENDIX B: EMACS ONE BY ONE

We here provide an overview of the data available for all eMACS clusters mentioned in this paper.

Specifically, we show colour images of the cluster core generated from *HST* data (where observations were performed in at least two passbands). Contours (in light grey) of the adaptively smoothed X-ray emission are overlaid for all eMACS clusters observed with *CXO* (see also Fig. 11), while the critical lines for strong gravitational lensing of an object at $z = 2$ are shown in yellow for systems for which a lens model is available (see Table 2). We mark multiple-image systems that are used to constrain these lens models and highlight strong-lensing features and (occasionally) cluster galaxies of special interest in insets placed around the main image.

We also show the redshift histogram in the vicinity of each cluster's systemic redshift and the velocity dispersion derived from it. The spatial distribution of all galaxies with spectroscopic redshifts measured in each field is also presented, where larger symbols mark cluster members (defined as featuring redshifts that fall within 3σ of the systemic cluster redshift in the radial-velocity histogram); in these plots, the area covered by the shown *HST* data is outlined by an orange polygon. In both the radial-velocity histograms and the maps showing the location of galaxies with spectroscopic redshifts we highlight in red the BCG (heavy line) and the second-brightest cluster galaxy (light line).

Finally, we list all galaxies with spectroscopic redshifts (whether they are cluster members or not) and mark the BCG (B), any X-ray point sources detected in *CXO* follow-up observations (X), and candidates for ram-pressure stripping (R). For the remainder of the sample, i.e., for all eMACS clusters that are listed in Table 1 but are not highlighted elsewhere in this paper, the same data summary is provided in an online-only extension of this appendix.

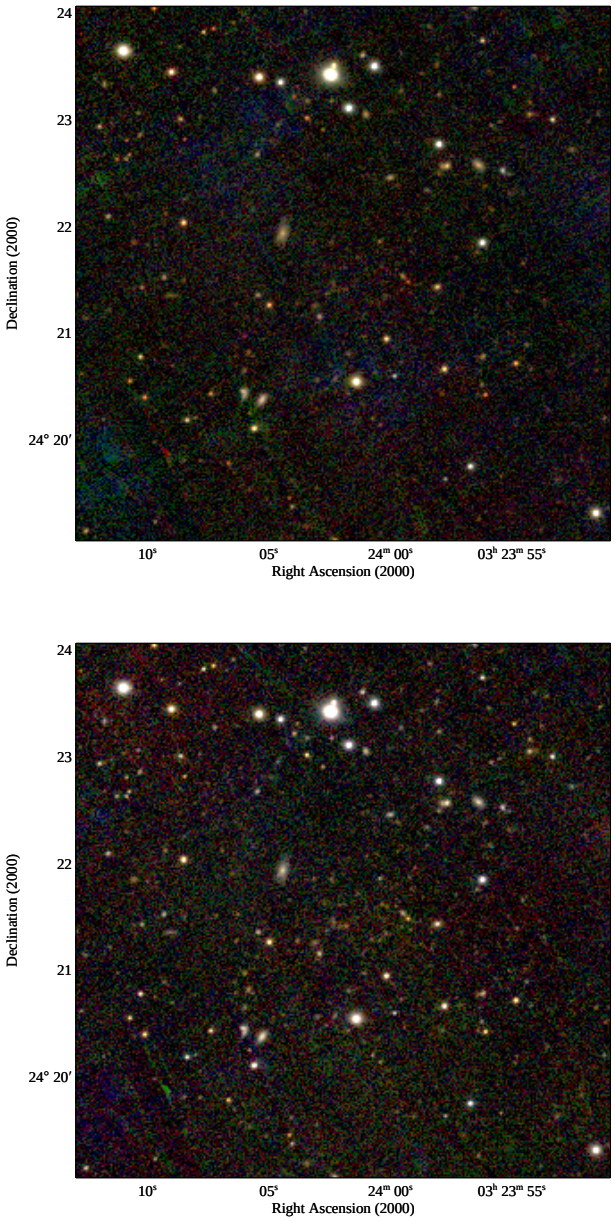

Figure A5. PS1/3π image of a 5×5 arcmin^{-2} region centred on the RASS source 1RXS J032401.8+242131. Requiring cluster candidates to show a pronounced galaxy overdensity in a gri image (top) would have led to the elimination of this source; even in the riz image (bottom) the cluster galaxies are barely visible. Follow-up observations unambiguously established the presence of a massive galaxy cluster at $z = 0.9$, the most distant cluster discovered to date in the RASS.

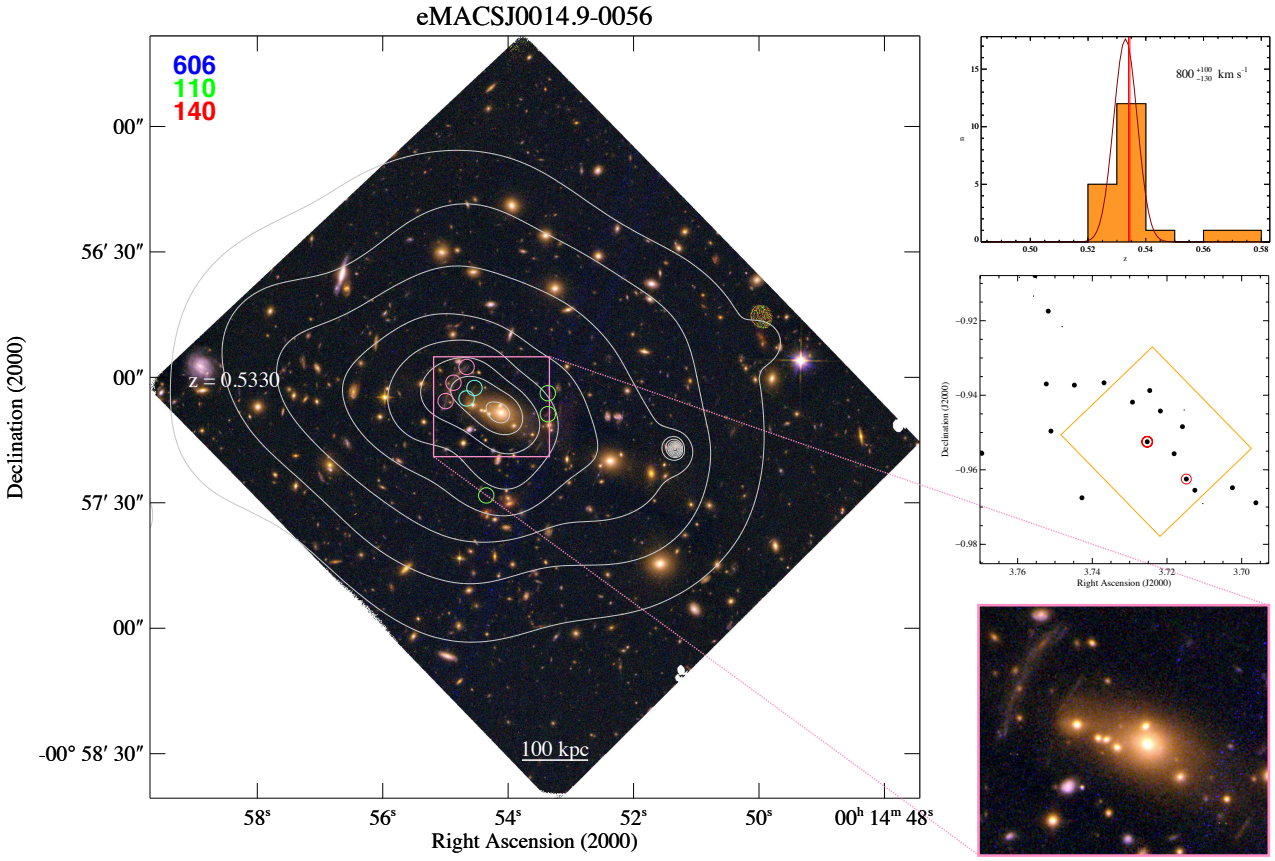

Figure B1. eMACSJ0014.9−0056 is an exceptionally X-ray luminous cluster (see Table 3) with a largely relaxed X-ray morphology. The modest number of radial velocities measured for cluster members to date precludes a more robust determination of the cluster velocity dispersion and an assessment of line-of-sight substructure. While strong-lensing features are clearly visible in the cluster core, their faintness makes follow-up spectroscopy challenging; as a result, we currently have no lens model for this system.

Coordinates (J2000) and spectroscopic redshifts of galaxies in the field of eMACSJ0014.9-0056.

	R.A. (deg)	Dec (deg)	z
	3.6932	−0.9852	0.6368
	3.6962	−0.9689	0.5351
	3.7025	−0.9648	0.5283
	3.7104	−0.9691	0.4674
	3.7125	−0.9655	0.5276
	3.7148	−0.9625	0.5340
	3.7154	−0.9440	0.2769
	3.7159	−0.9484	0.5278
	3.7181	−0.9557	0.5349
	3.7218	−0.9442	0.5358
	3.7246	−0.9387	0.5321
B	3.7253	−0.9525	0.5345
	3.7292	−0.9418	0.5372
	3.7369	−0.9367	0.5404
	3.7428	−0.9675	0.5293
	3.7448	−0.9373	0.5320
	3.7481	−0.9216	0.5707
	3.7511	−0.9496	0.5373
	3.7518	−0.9174	0.5278
	3.7523	−0.9370	0.5302
	3.7553	−0.9079	0.5330
	3.7557	−0.9134	0.5680
	3.7595	−0.9084	0.3697
	3.7696	−0.9556	0.5363

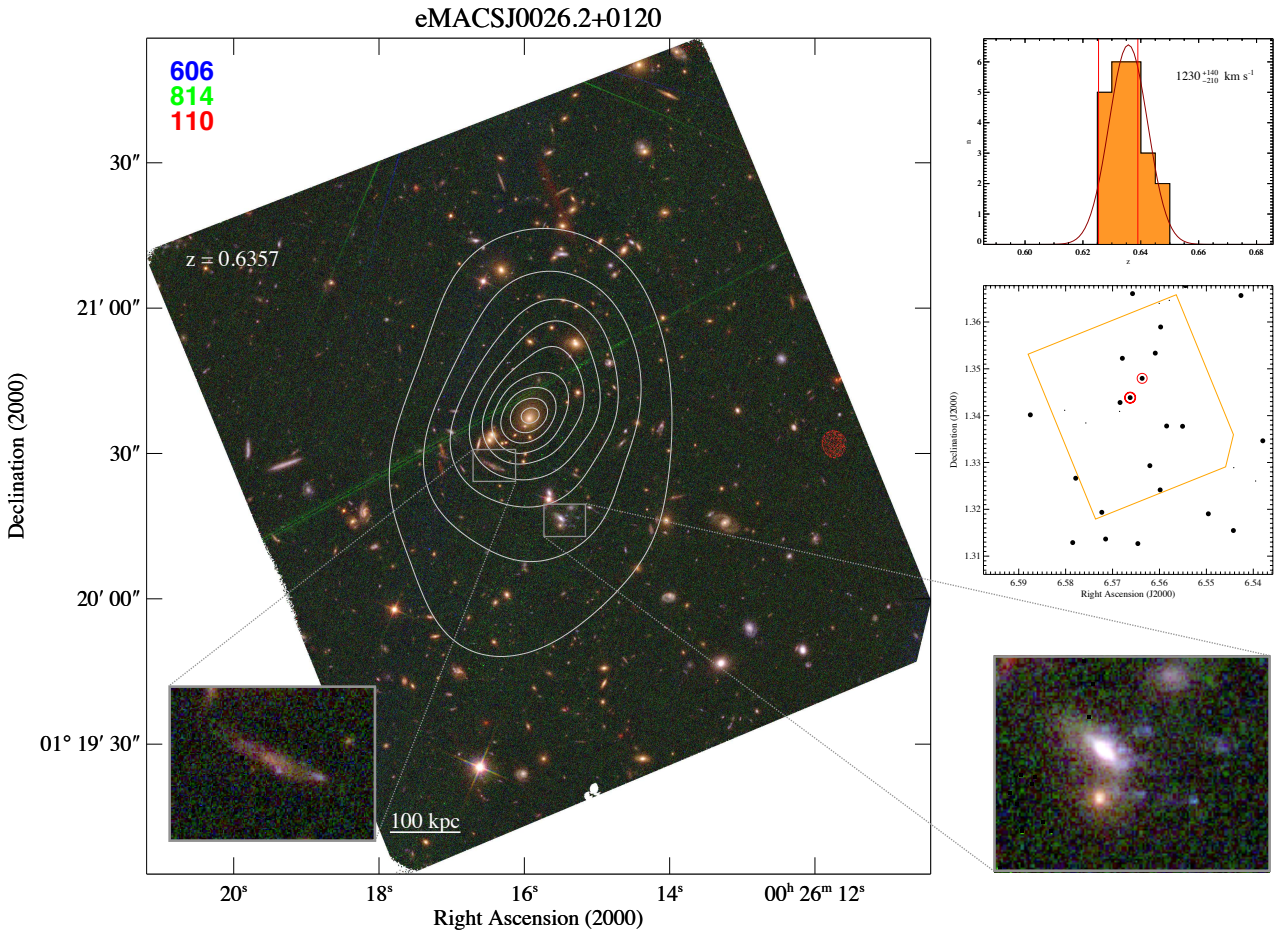

Figure B2. eMACSJ0026.2+0120 was observed with *CXO*/ACIS-S and is thus not included in the X-ray analysis performed for this work (Table 3. We nonetheless note the system's relaxed X-ray morphology and highlight a candidate for ram-pressure stripping and one of several strong-lensing features. The latter have so far not been targeted in our spectroscopic follow-up observations since

Coordinates (J2000) and spectroscopic redshifts of galaxies in the field of eMACSJ0026.2+0120.

	R.A. (deg)	Dec (deg)	z	R.A. (deg)	Dec (deg)	z
	6.5380	1.3346	0.6378	6.5779	1.3266	0.6254
	6.5395	1.3260	0.1771	6.5785	1.3129	0.6373
	6.5426	1.3657	0.6348	6.5802	1.3411	0.2386
	6.5442	1.3289	0.7497	6.5875	1.3402	0.6290
	6.5442	1.3155	0.6472	6.5954	1.3061	0.6929
	6.5496	1.3190	0.6347			
	6.5545	1.3678	0.6337			
	6.5551	1.3377	0.6325			
	6.5579	1.3646	0.7838			
	6.5585	1.3378	0.6373			
	6.5598	1.3589	0.6408			
	6.5599	1.3241	0.6479			
	6.5601	1.3640	0.6923			
	6.5609	1.3534	0.6288			
	6.5621	1.3293	0.6417			
	6.5637	1.3480	0.6254			
	6.5646	1.3127	0.6380			
	6.5657	1.3661	0.6338			
B	6.5662	1.3438	0.6390			
	6.5679	1.3522	0.6320			
	6.5684	1.3428	0.6438			
	6.5685	1.3409	1.1325			
	6.5715	1.3137	0.6391			
	6.5723	1.3194	0.6283			
	6.5757	1.3384	0.9172			

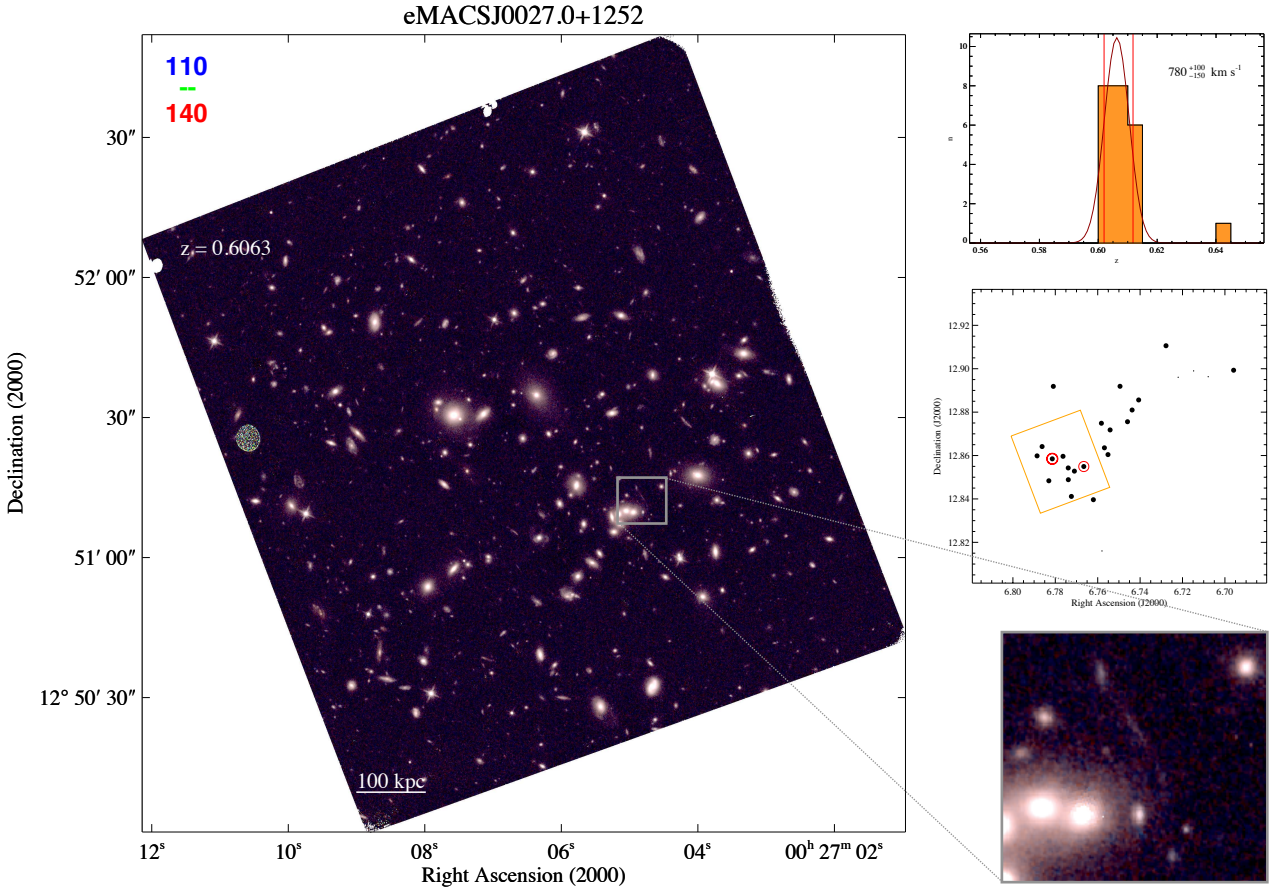

Figure B3. The only *HST* images of eMACSJ0027.0+1252 available to date were taken with WFC3 and are thus ill-suited for the identification of strong-lensing features (which are predominantly blue). We highlight one plausible multiple-image system. Without *CXO* data and at least a tentative lens model we are currently unable to characterize the physical properties and evolutionary state of this cluster.

Coordinates (J2000) and spectroscopic redshifts of galaxies in the field of eMACSJ0027.0+1252.

	R.A. (deg)	Dec (deg)	z	R.A. (deg)	Dec (deg)	z
	6.6959	12.8993	0.6107	6.7862	12.8641	0.6105
	6.7079	12.8963	0.4896	6.7886	12.8598	0.6062
	6.7148	12.8990	0.4886	6.8035	12.8012	0.7355
	6.7220	12.8961	0.4909			
	6.7278	12.9106	0.6082			
	6.7407	12.8856	0.6045			
	6.7425	12.9366	0.4912			
	6.7438	12.8810	0.6110			
	6.7459	12.8756	0.6058			
	6.7495	12.8919	0.6014			
	6.7541	12.8718	0.6064			
	6.7551	12.8604	0.6004			
	6.7568	12.8636	0.6036			
	6.7580	12.8160	0.6426			
	6.7583	12.8749	0.6052			
	6.7620	12.8396	0.6147			
	6.7666	12.8549	0.6118			
	6.7710	12.8528	0.6058			
	6.7724	12.8412	0.6132			
	6.7739	12.8489	0.6046			
	6.7739	12.8543	0.6064			
	6.7764	12.8596	0.6053			
	6.7809	12.8919	0.6025			
B	6.7814	12.8585	0.6020			
	6.7831	12.8484	0.6019			

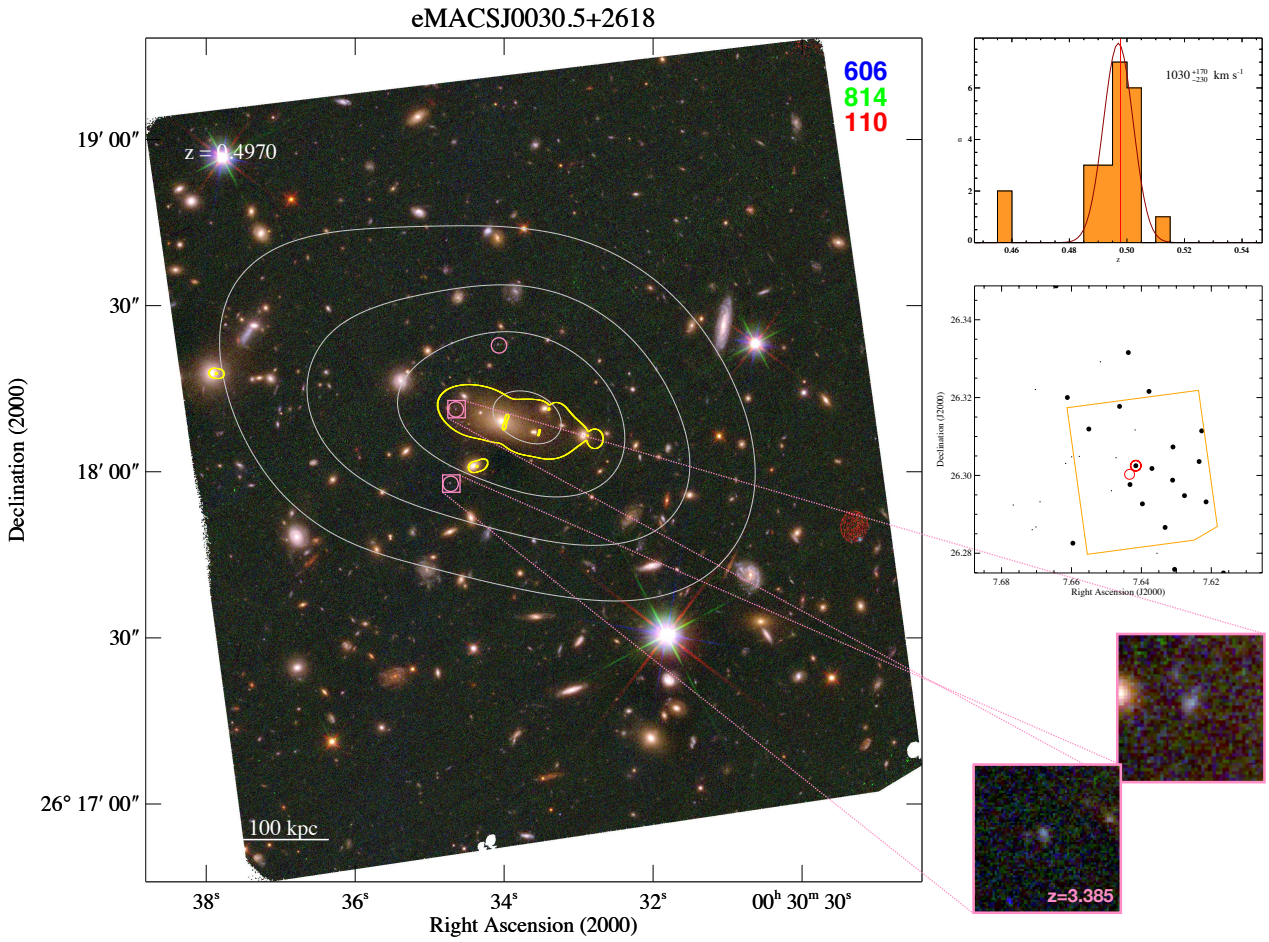

Figure B4. In spite of its high velocity dispersion, eMACSJ0030.5+2618 was found to be the least X-ray luminous eMACS cluster of the subset for which *CXO* data are available (see Table 3); consistent with this finding, it features the smallest Einstein radius of the subsample with existing lens models (Table 2). The current lens model is, however, constrained only by a single multiple-image system, whose high redshift introduces systematic uncertainties in the Einstein radius for a background source at $z = 2$ (cf. Section 5.2.2).

Coordinates (J2000) and spectroscopic redshifts of galaxies in the field of eMACSJ0030.5+2618.

	R.A. (deg)	Dec (deg)	z	R.A. (deg)	Dec (deg)	z
	7.6165	26.2749	0.4963	7.6578	26.3049	0.2664
	7.6215	26.2932	0.4943	7.6596	26.2826	0.5003
	7.6227	26.3114	0.4885	7.6599	26.3048	0.2703
	7.6235	26.3036	0.4964	7.6612	26.3200	0.5023
	7.6277	26.2948	0.4968	7.6617	26.3031	0.2703
	7.6305	26.2758	0.4954	7.6644	26.3487	0.4931
	7.6310	26.3073	0.4976	7.6690	26.2932	0.2692
	7.6311	26.2988	0.5021	7.6702	26.2868	0.2684
	7.6332	26.2866	0.4939	7.6703	26.3221	0.4577
	7.6355	26.2800	0.4579	7.6712	26.2860	0.2663
	7.6370	26.3018	0.4976	7.6767	26.2924	0.2677
	7.6378	26.3216	0.5008			
	7.6397	26.2927	0.4898			
B	7.6416	26.3025	0.4978			
	7.6418	26.3064	3.3880			
	7.6418	26.3117	0.7143			
	7.6433	26.2977	0.5010			
	7.6437	26.3316	0.4892			
	7.6442	26.3031	3.3880			
	7.6445	26.2994	3.3880			
	7.6462	26.3177	0.5002			
	7.6472	26.3046	0.2686			
	7.6485	26.2961	0.7136			
	7.6517	26.3292	0.5629			
	7.6550	26.3119	0.5103			

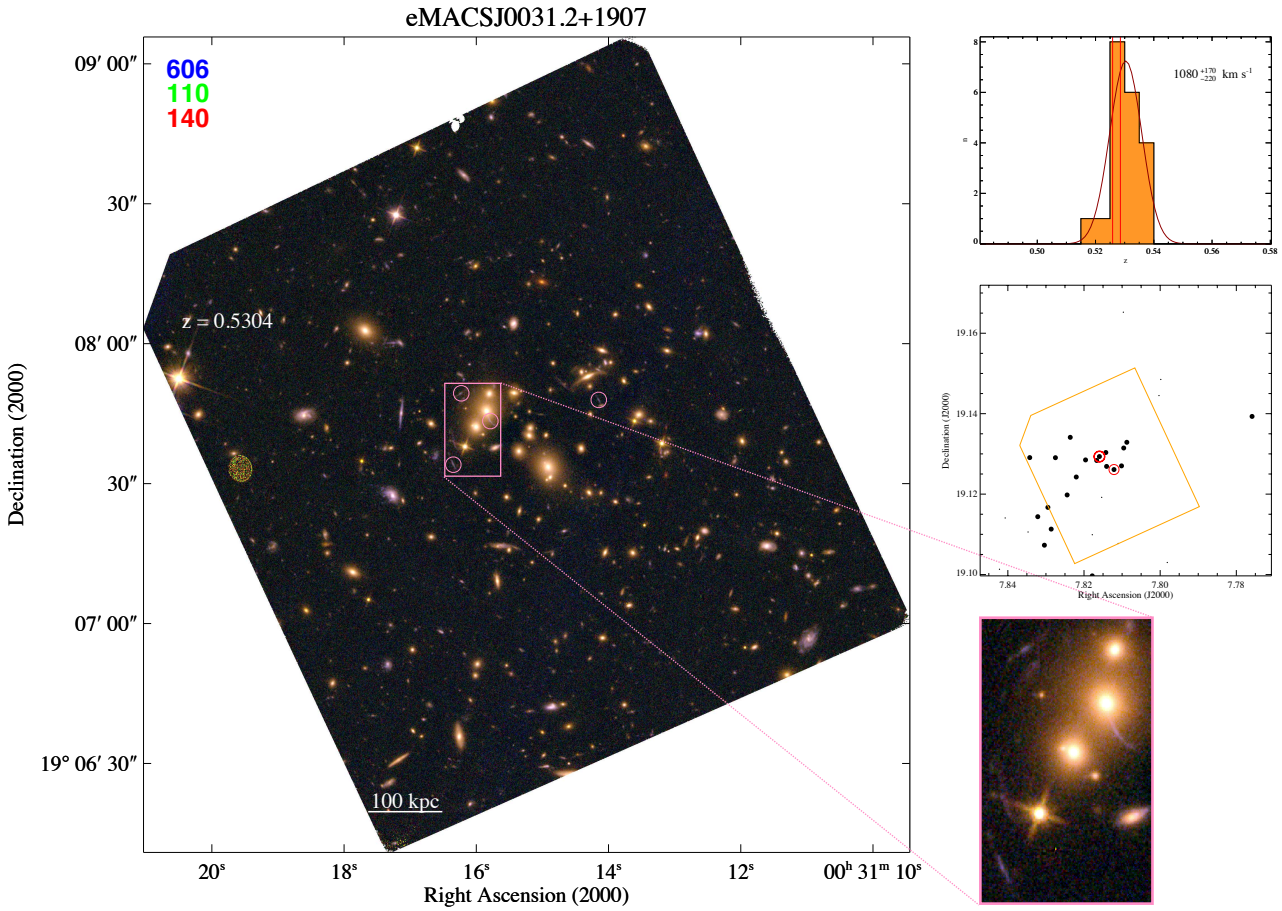

Figure B5. eMACSJ0031.2+1907 features a complex core with two galaxies vying for BCG status. Although the system's galaxy distribution and high velocity dispersion suggest recent merger activity, this hypothesis remains untested in the absence of *CXO* data and spectroscopic confirmation of the few and faint strong-lensing features.

Coordinates (J2000) and spectroscopic redshifts of galaxies in the field of eMACSJ0031.2+1907.

	R.A. (deg)	Dec (deg)	z	R.A. (deg)	Dec (deg)	z
	7.7759	19.1393	0.5268	7.8321	19.1144	0.5375
	7.7981	19.1030	0.4508	7.8343	19.1291	0.5331
	7.7998	19.1485	0.4776	7.8347	19.1106	0.4338
	7.8003	19.1445	0.5857	7.8404	19.1719	0.4509
	7.8088	19.1329	0.5271	7.8407	19.1141	0.4337
	7.8096	19.1315	0.5279	7.8422	19.1013	0.4768
	7.8097	19.1652	0.3840			
	7.8101	19.1270	0.5237			
	7.8110	19.1077	0.3503			
	7.8121	19.1261	0.5259			
	7.8141	19.1269	0.5334			
	7.8143	19.1303	0.5398			
	7.8154	19.1192	0.4504			
B	7.8160	19.1293	0.5285			
	7.8167	19.1284	0.5183			
	7.8178	19.1099	0.4789			
	7.8178	19.0997	0.5356			
	7.8196	19.1285	0.5264			
	7.8220	19.1243	0.5296			
	7.8236	19.1341	0.5301			
	7.8244	19.1198	0.5345			
	7.8275	19.1291	0.5318			
	7.8286	19.1113	0.5273			
	7.8295	19.1167	0.5310			
	7.8304	19.1073	0.5381			

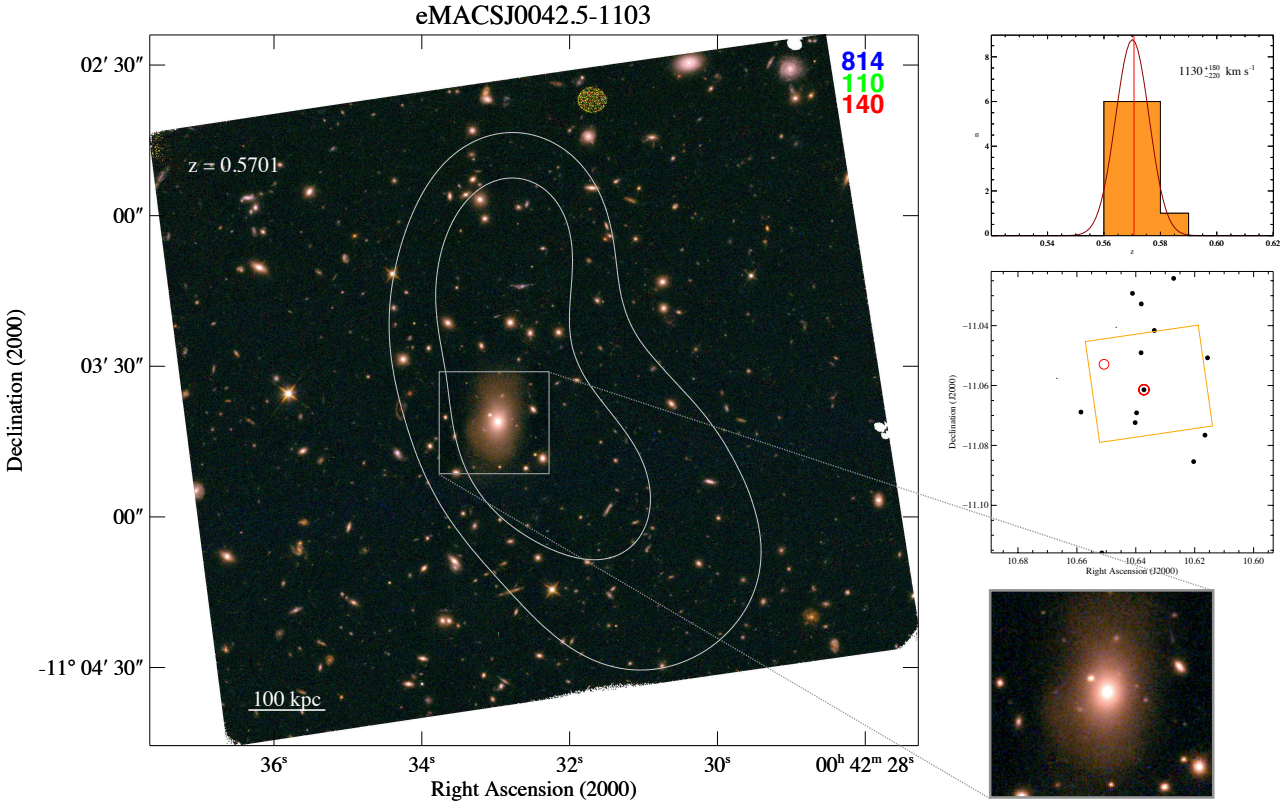

Figure B6. eMACSJ0042.5−1103 exhibits a curious combination of X-ray characteristics: a strongly disturbed ICM morphology and a high gas temperature, but also a very low X-ray surface brightness and a (by eMACS standards) only modest X-ray luminosity (Table 3). Although the X-ray surface-brightness contours are clearly not aligned with the extremely luminous, single BCG, no other galaxy concentrations are apparent within the *HST* field of view that could shed light on the origin and nature of the system's irregular appearance at X-ray wavelengths. Lacking F606W coverage of this cluster, we are currently also unable to identify multiple-image systems that could be used to directly probe the mass distribution near the cluster core.

Coordinates (J2000) and spectroscopic redshifts of galaxies in the field of eMACSJ0042.5-1103.

	R.A. (deg)	Dec (deg)	z
	10.6156	−11.0507	0.5623
	10.6165	−11.0766	0.5730
	10.6204	−11.0854	0.5656
	10.6272	−11.0242	0.5648
	10.6337	−11.0416	0.5664
B	10.6372	−11.0614	0.5706
	10.6381	−11.0327	0.5680
	10.6382	−11.0491	0.5805
	10.6397	−11.0691	0.5763
	10.6402	−11.0724	0.5720
	10.6411	−11.0292	0.5750
	10.6467	−11.0406	0.7312
	10.6500	−11.0219	0.4806
	10.6515	−11.1159	0.5638
	10.6586	−11.0689	0.5740
	10.6668	−11.0576	0.4709

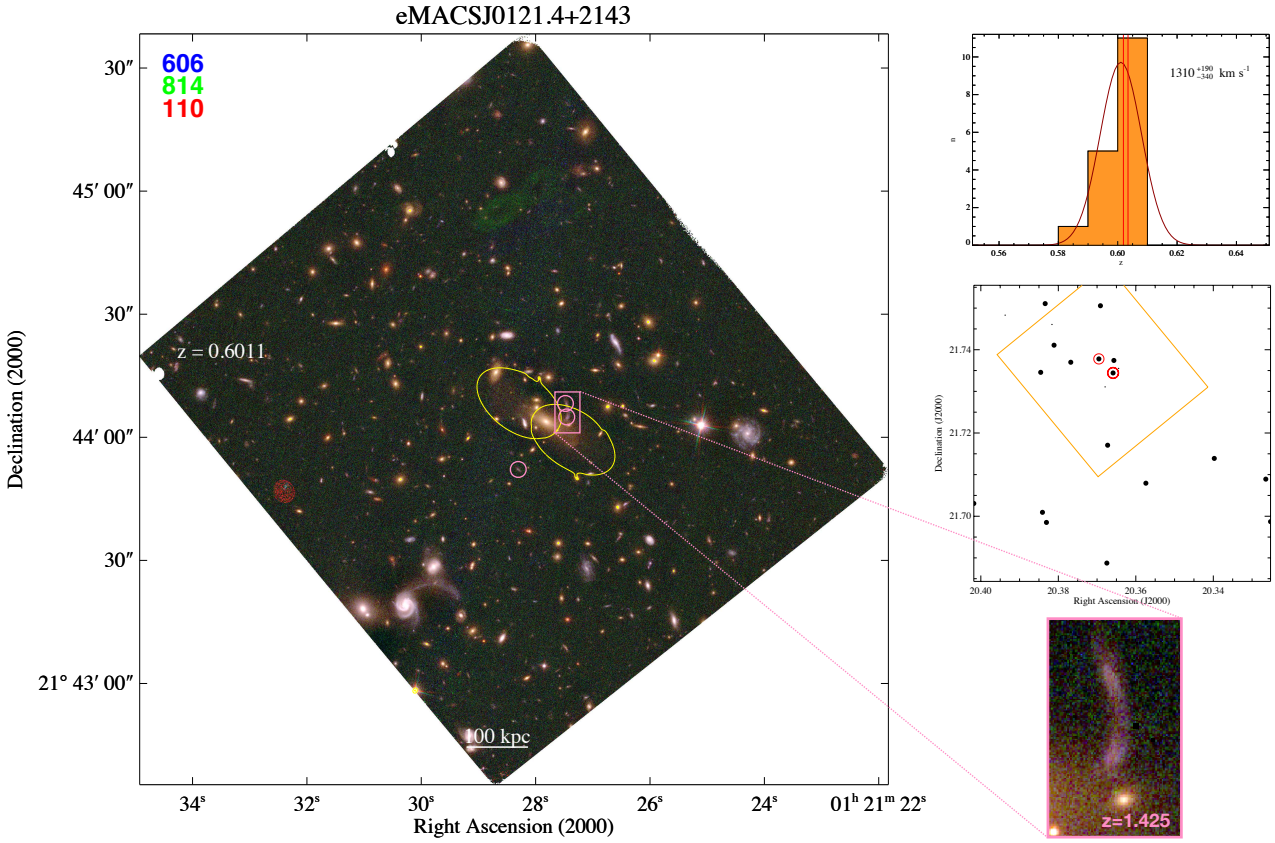

Figure B7. eMACSJ0121.4+2143 is an optically relatively unimpressive cluster whose high velocity dispersion is also highly uncertain. A prominent fold arc constrains our tentative lens model, according to which this system is also characterized by only modest lensing strength.

Coordinates (J2000) and spectroscopic redshifts of galaxies in the field of eMACSJ0121.4+2143.

	R.A. (deg)	Dec (deg)	z
	20.3252	21.6987	0.5996
	20.3265	21.7089	0.6086
	20.3398	21.7139	0.6058
	20.3574	21.7079	0.6019
	20.3644	21.7355	1.4245
	20.3657	21.7374	0.6033
B	20.3659	21.7344	0.6019
	20.3673	21.7171	0.5958
	20.3675	21.6887	0.6003
	20.3679	21.7311	1.4245
	20.3691	21.7506	0.5916
	20.3695	21.7378	0.6035
	20.3768	21.7370	0.6087
	20.3811	21.7411	0.6096
	20.3816	21.7461	0.4816
	20.3831	21.6985	0.5901
	20.3834	21.7511	0.5871
	20.3841	21.7009	0.6039
	20.3845	21.7346	0.5953
	20.3937	21.7483	0.7136
	20.4018	21.7031	0.6041

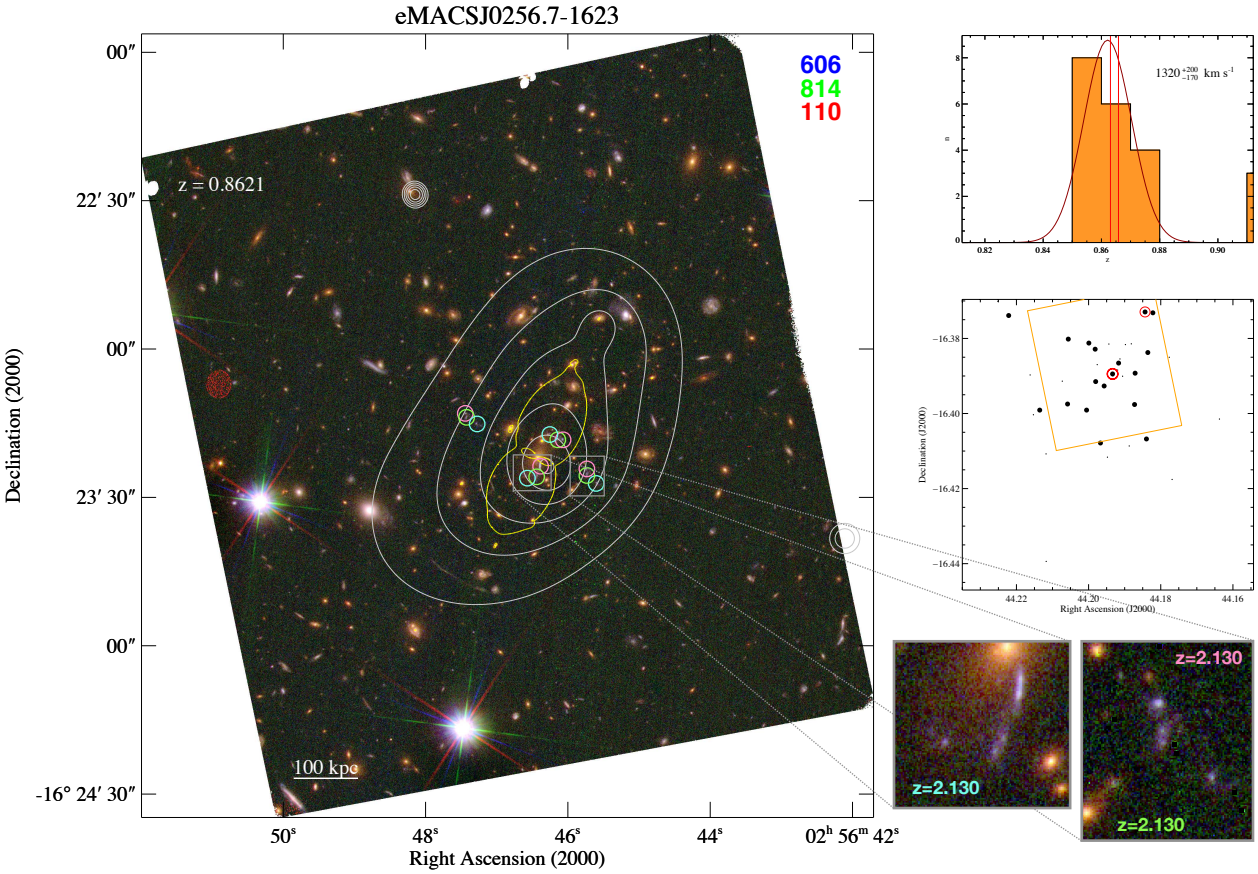

Figure B8. eMACSJ0256.7−1623 is the NW component of what was deemed to be a (wide separation) double cluster, until *CXO* observations found its SE neighbor (see Fig. B9) to be entirely devoid of ICM emission. By contrast, this system is characterized by a high and well constrained velocity dispersion and an equally well constrained lens model of the cluster core, anchored by three spectroscopically confirmed multiple-image systems. While not exceptionally powerful as a gravitational lens, eMACSJ0256.7 is highly X-ray luminous ($L_{X,CXO} = (1.2 \pm 0.2) \times 10^{45}$ erg s^{-1}; Table 3), possibly partly due a recent minor merger.

Coordinates (J2000) and spectroscopic redshifts of galaxies in the field of eMACSJ0256.7-1623.

	R.A. (deg)	Dec (deg)	z	R.A. (deg)	Dec (deg)	z
	44.1543	−16.3988	0.2587	44.1982	−16.3829	0.8662
	44.1637	−16.4015	0.6766	44.1999	−16.3812	0.8548
	44.1769	−16.4176	0.1798	44.2006	−16.3991	0.8639
	44.1776	−16.3850	0.5896	44.2056	−16.3802	0.8685
	44.1822	−16.3732	0.8592	44.2058	−16.3975	0.8570
	44.1836	−16.3838	0.8722	44.2073	−16.3914	0.4511
	44.1840	−16.4068	0.8545	44.2117	−16.4394	0.5336
	44.1843	−16.3729	0.8631	44.2118	−16.4108	0.3129
	44.1871	−16.3893	0.8744	44.2135	−16.3991	0.8532
	44.1873	−16.3976	0.8543	44.2153	−16.4003	0.7586
	44.1882	−16.3814	0.2082	44.2162	−16.3897	0.6697
	44.1887	−16.4086	0.5325	44.2221	−16.3739	0.8629
	44.1898	−16.3816	0.9140	44.2251	−16.3701	0.3962
	44.1906	−16.3901	2.1297	44.2350	−16.4465	0.5355
	44.1913	−16.3855	0.9151			
	44.1917	−16.3866	0.8747			
	44.1920	−16.3884	2.1297			
	44.1933	−16.3899	2.1296			
B	44.1934	−16.3895	0.8659			
	44.1944	−16.3815	0.9161			
	44.1948	−16.4116	0.5899			
	44.1957	−16.3927	0.8701			
	44.1967	−16.4079	0.8539			
	44.1976	−16.3870	2.1297			
	44.1980	−16.3915	0.8512			

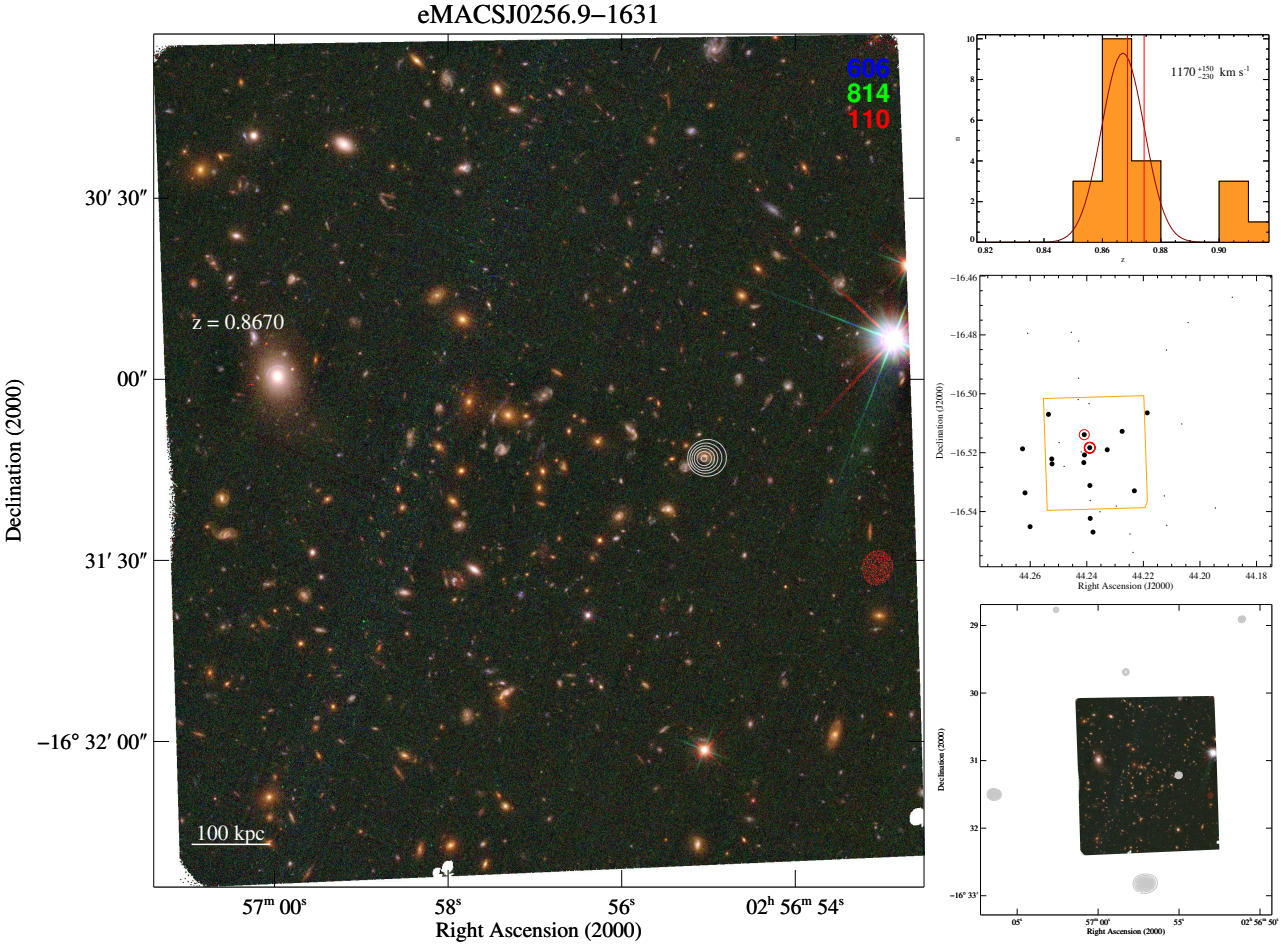

Figure B9. eMACSJ0256.9−1631. No extended emission from a diffuse ICM is detected, revealing eMACSJ0256.9 to be a filamentary structure, rather than a gravitationally collapsed cluster. Several bright X-ray point sources in the vicinity (apparent in a wider view of the same field; bottom right) are, in aggregate, the likely source of the X-ray emission detected in the RASS at this location. We note that the brightest X-ray point source in the field, south of the area observed with *HST*, is a QSO at $z = 0.8562$ and thus a member of eMACSJ0256.9.

Coordinates (J2000) and spectroscopic redshifts of galaxies in the field of eMACSJ0256.9-1631.

	R.A. (deg)	Dec (deg)	z		R.A. (deg)	Dec (deg)	z
	44.1756	−16.4703	0.4687		44.2408	−16.5208	0.8653
	44.1770	−16.4598	0.3602		44.2409	−16.5139	0.8686
	44.1886	−16.4672	0.9059		44.2411	−16.5234	0.8675
	44.1945	−16.5388	0.5795		44.2420	−16.5198	0.9177
X	44.2042	−16.4759	0.3845		44.2429	−16.4821	0.5801
	44.2064	−16.5103	0.6558	X	44.2429	−16.4947	1.7932
	44.2117	−16.5447	0.7004		44.2430	−16.5020	0.7318
	44.2118	−16.4852	0.5371		44.2455	−16.4791	0.5816
	44.2126	−16.5347	0.5446		44.2480	−16.5246	0.3267
	44.2186	−16.5065	0.8778		44.2498	−16.5166	0.3271
	44.2205	−16.5587	0.5730		44.2523	−16.5238	0.8679
	44.2232	−16.5330	0.8560		44.2524	−16.5221	0.8698
	44.2236	−16.5539	0.9070		44.2535	−16.5070	0.8608
	44.2247	−16.5476	0.3626		44.2600	−16.5451	0.8686
	44.2275	−16.5128	0.8741	X	44.2609	−16.4794	1.0861
	44.2296	−16.5381	0.6990		44.2618	−16.5336	0.8602
	44.2328	−16.5190	0.8771		44.2627	−16.5187	0.8686
	44.2353	−16.5401	0.6984	X	44.2768	−16.5249	0.9052
	44.2378	−16.5470	0.8562				
	44.2388	−16.5423	0.8570				
	44.2388	−16.5362	0.6685				
	44.2389	−16.5311	0.8681				
B	44.2390	−16.5183	0.8743				
	44.2392	−16.5033	0.7045				
	44.2405	−16.5177	0.9239				

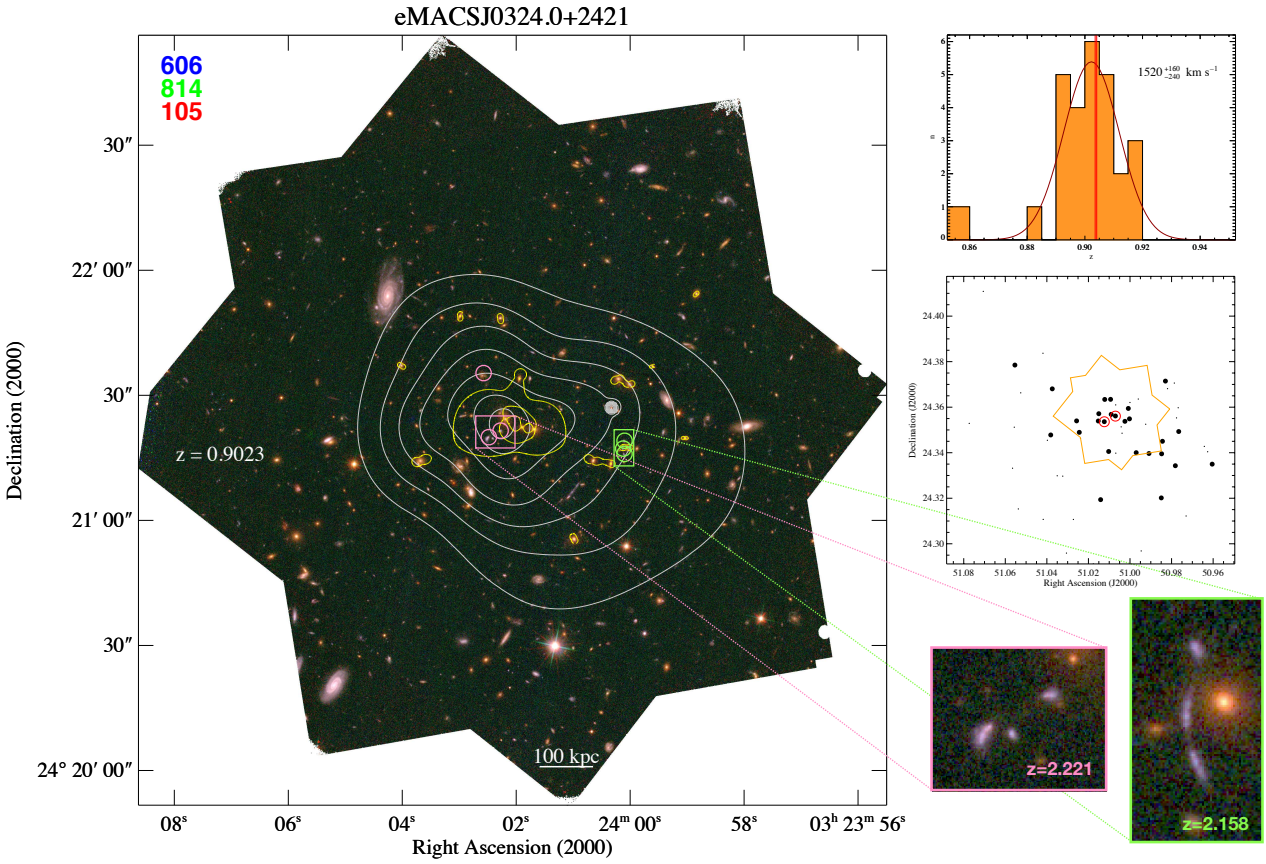

Figure B10. eMACSJ0324.0+2421 is the most distant cluster in the eMACS sample and the most distant cluster discovered in the RASS. Very compact, it is not a particularly powerful gravitational lens but features a very high velocity dispersion. As one of the most X-ray luminous clusters in the entire sample, this system is discussed in more detail in Section 5.4.

Coordinates (J2000) and spectroscopic redshifts of galaxies in the field of eMACSJ0324.0+2421.

	R.A. (deg)	Dec (deg)	z		R.A. (deg)	Dec (deg)	z		R.A. (deg)	Dec (deg)	z
	50.9605	24.3350	0.9057		51.0042	24.3514	2.1580		51.0419	24.3837	0.3555
	50.9626	24.3404	0.8551		51.0068	24.3398	0.2680	X	51.0526	24.3663	2.0716
	50.9642	24.3428	0.8109		51.0069	24.3610	2.2225		51.0537	24.3153	1.0595
	50.9730	24.3122	0.8518	B	51.0070	24.3561	0.9036		51.0554	24.3785	0.8935
	50.9766	24.3493	0.8996		51.0091	24.3568	0.9041		51.0557	24.3512	0.6582
	50.9768	24.3597	0.4027		51.0092	24.3558	2.2225		51.0565	24.3332	0.4988
	50.9776	24.3553	0.2950		51.0093	24.3634	0.8848	X	51.0666	24.4175	2.1119
	50.9782	24.3343	0.9001		51.0103	24.3405	0.9075	X	51.0706	24.4109	0.4250
	50.9787	24.3706	1.0603		51.0122	24.3634	0.9062	X	51.0774	24.3529	1.4443
	50.9819	24.3681	0.7294		51.0124	24.3536	0.9178				
	50.9830	24.3715	0.9045		51.0141	24.3194	0.8951				
	50.9844	24.3450	0.8937		51.0150	24.3571	0.9172				
	50.9848	24.3395	0.8915		51.0153	24.3539	0.9131				
	50.9849	24.3201	0.9065	X	51.0176	24.2911	2.0610				
	50.9909	24.3397	0.8902		51.0238	24.3463	0.6118				
	50.9924	24.3525	1.0708		51.0244	24.3490	0.9185				
X	50.9946	24.2969	2.0520		51.0257	24.3540	0.9073				
	50.9960	24.3636	0.6043		51.0272	24.3107	0.4466				
	50.9970	24.3400	0.8985	X	51.0306	24.2959	0.9698				
	51.0000	24.3621	1.9733		51.0324	24.3297	0.7892				
	51.0002	24.3542	2.3643		51.0350	24.3299	0.4808				
	51.0002	24.3549	0.8959		51.0374	24.3681	0.9146				
	51.0008	24.3594	0.8910		51.0381	24.3478	0.9003				
	51.0024	24.3538	0.9022		51.0397	24.3455	0.9762				
	51.0038	24.3486	1.0583		51.0418	24.3107	0.9765				

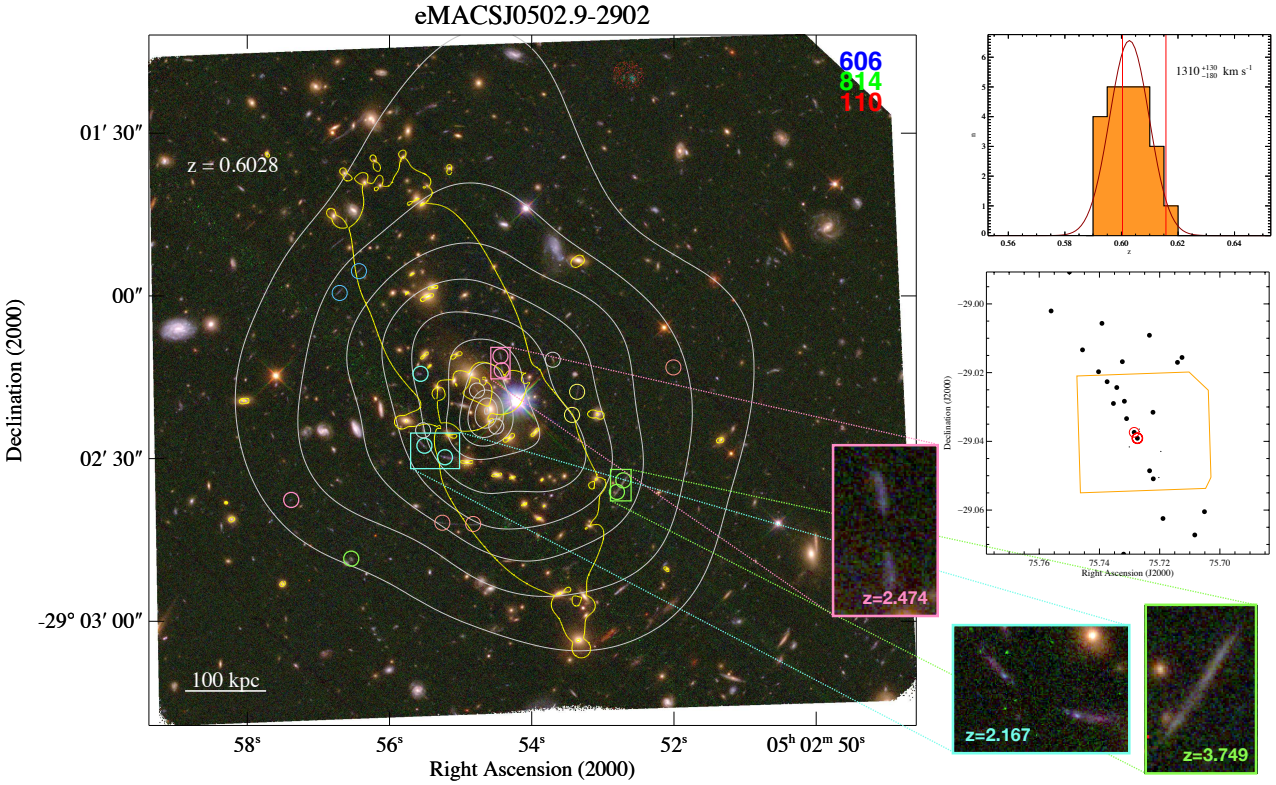

Figure B11. eMACSJ0502.9−2902 is a massive merger, characterized by several very luminous ellipticals, widely separated along a highly elongated galaxy distribution that most likely delineates the merger axis in projection on the sky. Although the system's appearance in the optical thus suggests an active, head-on collision of at least two, and possibly several, components, the evidence from our follow-up observations all but rules out an early-stage or ongoing merger. Rather, both the gaseous ICM and the (mostly dark) non-collisional matter (as derived from a strong-lensing analysis constrained by the seven multiple-image systems highlighted above) are described by single halos, albeit with different centroids relative to the locations of the two most prominent BCG candidates. Since the ICM temperature of (8 ± 1) keV is inconsistent with wide-spread, merger-induced shock heating, we propose that eMACSJ0502.9 is a post-collision merger of two or more subclusters of unequal mass, the most massive of which dominates the X-ray appearance of the system. In this scenario, the highly elongated mass distribution revealed by our strong-lensing analysis could be interpreted as evidence of an extended core of a dense filament that traces the axis of matter infall and is oriented at a large angle with respect to our line of sight, but possibly still contributes to some extent to the high velocity dispersion of (1300 ± 150) km s^{-1} of the system.

Coordinates (J2000) and spectroscopic redshifts of galaxies in the field of eMACSJ0502.9-2902.

	R.A. (deg)	Dec (deg)	z	R.A. (deg)	Dec (deg)	z
	75.7051	−29.0605	0.6052	75.7456	−29.0134	0.5930
	75.7083	−29.0672	0.5936	75.7500	−28.9907	0.5961
	75.7126	−29.0156	0.6046	75.7561	−29.0021	0.6101
	75.7141	−29.0170	0.5991			
	75.7189	−29.0625	0.6086			
	75.7196	−29.0429	3.7494			
	75.7203	−29.0505	1.6615			
	75.7221	−29.0509	0.5997			
	75.7222	−29.0315	0.5987			
	75.7234	−29.0486	0.6028			
	75.7234	−29.0091	0.6111			
	75.7267	−29.0372	2.4746			
	75.7268	−29.0364	2.4742			
B	75.7274	−29.0391	0.6004			
	75.7285	−29.0374	0.6157			
	75.7301	−29.0416	2.1667			
	75.7310	−29.0334	0.5931			
	75.7317	−29.0283	0.6128			
	75.7320	−29.0728	0.6050			
	75.7324	−29.0168	0.5943			
	75.7343	−29.0243	0.6076			
	75.7354	−29.0290	0.5979			
	75.7375	−29.0226	0.6076			
	75.7392	−29.0057	0.6050			
	75.7403	−29.0197	0.6042			

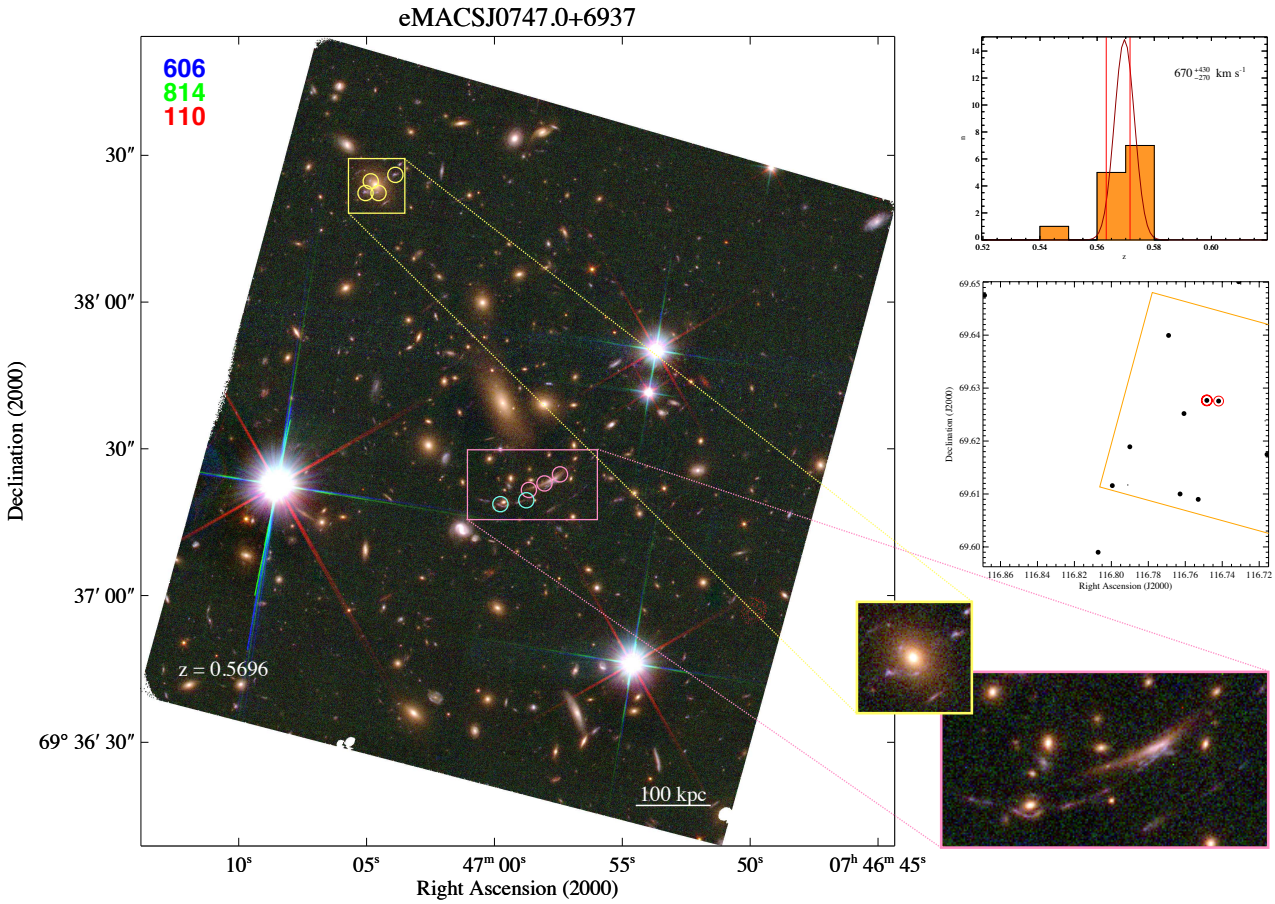

Figure B12. eMACSJ0747.0+6937 appears close to relaxed, given the optical dominance of the BCG and the absence of obvious substructure. A quantitative characterization of the physical properties of the system will require radial velocities of additional cluster members, *CXO* data, and redshifts for the strong-lensing features highlighted in this figure.

Coordinates (J2000) and spectroscopic redshifts of galaxies in the field of eMACSJ0747.0+6937.

	R.A. (deg)	Dec (deg)	z
	116.7158	69.6175	0.5683
	116.7168	69.6238	0.3134
	116.7311	69.6501	0.5664
	116.7420	69.6276	0.5632
B	116.7483	69.6277	0.5715
	116.7530	69.6090	0.5794
	116.7607	69.6252	0.5709
	116.7628	69.6100	0.5685
	116.7690	69.6399	0.5687
	116.7900	69.6189	0.5705
	116.7906	69.5963	0.5452
	116.7911	69.6117	0.5062
	116.7995	69.6116	0.5702
	116.8072	69.5990	0.5703
	116.8686	69.6475	0.5730

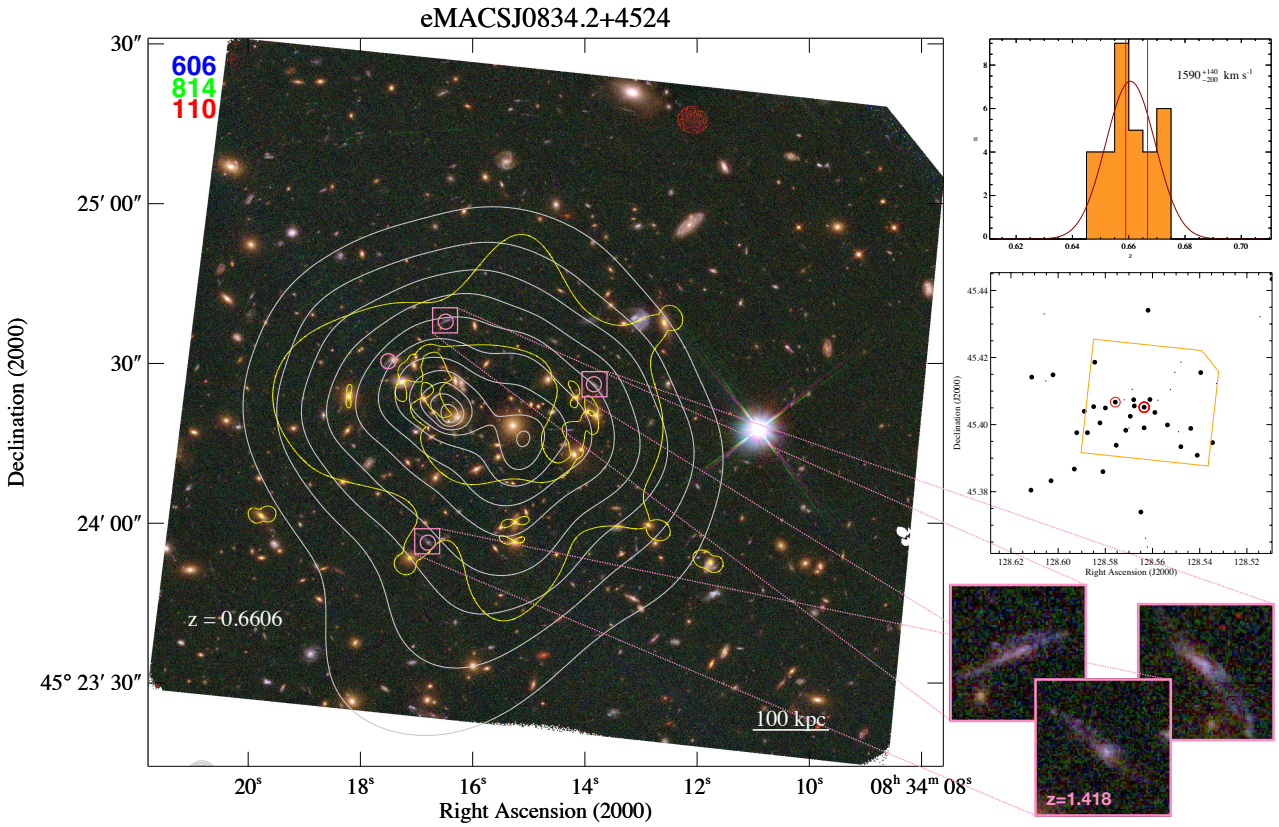

Figure B13. As one of the ten most X-ray luminous clusters in the eMACS subset observed with *CXO* to date, eMACSJ0834.2+4524 is discussed in more detail in Section 5.4. The distribution of radial velocities of cluster members shown in the top right strongly suggests the presence of substructure along the line of sight (Section 5.5.1), complementing the disturbed appearance of the system in the plane of the sky. We highlight the spectroscopically confirmed multiple-image system that anchors our lens model.

Coordinates (J2000) and spectroscopic redshifts of galaxies in the field of eMACSJ0834.2+4524.

R.A. (deg)	Dec (deg)	z	R.A. (deg)	Dec (deg)	z
128.5093	45.4434	0.6671	128.5686	45.4105	1.4182
128.5097	45.4089	0.5206	128.5694	45.4025	0.6538
128.5145	45.4322	0.9454	128.5700	45.3990	1.4182
128.5329	45.4123	0.5200	128.5713	45.3983	0.6720
128.5346	45.3946	0.6593	128.5719	45.4074	0.3613
128.5396	45.4155	0.6645	128.5754	45.3939	0.6578
128.5410	45.3909	0.6499	128.5758	45.4067	0.6589
128.5438	45.3989	0.6536	128.5800	45.4050	0.6490
128.5480	45.4186	0.5141	128.5810	45.3860	0.6617
128.5480	45.3934	0.6721	128.5823	45.4005	0.6743
128.5490	45.3979	0.5205	128.5845	45.4186	0.6488
128.5505	45.4156	0.5196	128.5849	45.4054	0.6635
128.5524	45.4105	0.5135	128.5876	45.3976	0.6592
128.5537	45.3999	0.6616	128.5889	45.4040	0.6748
128.5577	45.4073	1.4182	128.5921	45.3976	0.6511
128.5590	45.4036	0.6750	128.5931	45.3868	0.6675
128.5611	45.4075	0.6549	128.6022	45.4148	0.6635
128.5619	45.4341	0.6551	128.6030	45.3833	0.6554
128.5622	45.3635	0.5179	128.6053	45.4130	0.5142
128.5629	45.3661	0.5206	128.6059	45.4330	0.5663
B 128.5635	45.4052	0.6667	128.6112	45.4142	0.6564
128.5636	45.3991	0.6653	128.6115	45.3805	0.6581
128.5649	45.3739	0.6566	128.6286	45.4330	0.5818
128.5677	45.4056	0.6484			
128.5680	45.4074	0.6742			

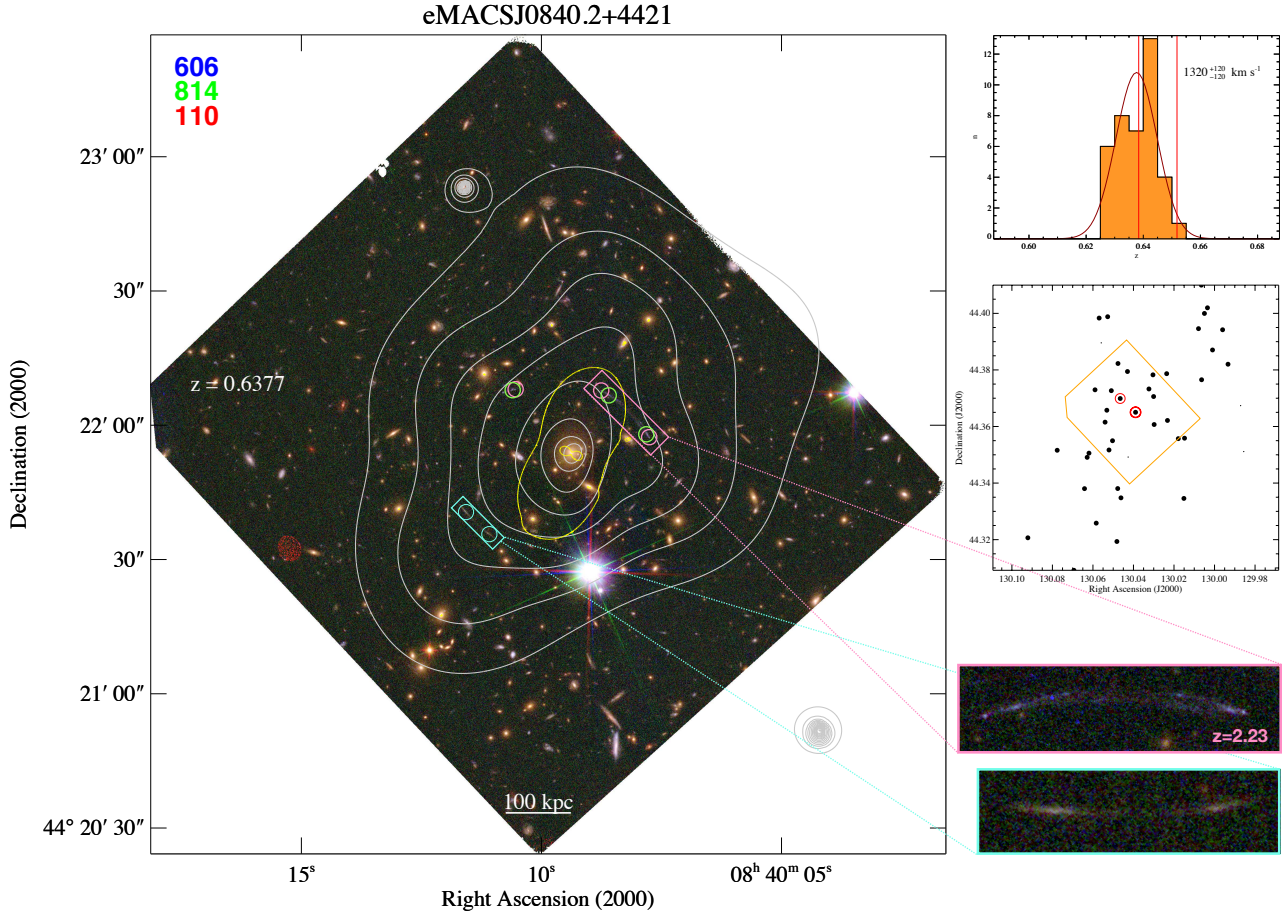

Figure B14. Originally discovered in the eMACS pilot study (Ebeling et al. 2013), eMACSJ0840.2+4421 is one of very few eMACS clusters in the (unrepresentative) subsample with *CXO* data that appear largely relaxed. Highly X-ray luminous, it is discussed in more detail in Section 5.4. Marked above are the strong-lensing features on which our current lens model is based; we also show an additional multiple-image system that has so far proven resilient to several attempts of ours to secure its redshift. This cluster was originally discovered in the eMACS pilot project (Ebeling et al. 2013).

Coordinates (J2000) and spectroscopic redshifts of galaxies in the field of eMACSJ0840.2+4421.

R.A. (deg)	Dec (deg)	z	R.A. (deg)	Dec (deg)	z
129.9856	44.3511	0.5677	130.0476	44.3823	0.6330
129.9871	44.3674	0.3533	130.0478	44.3381	0.6305
129.9933	44.3820	0.6250	130.0482	44.3193	0.6490
129.9960	44.3942	0.6416	130.0503	44.3550	0.6351
130.0010	44.3871	0.6424	130.0509	44.3727	0.6318
130.0035	44.4020	0.6282	130.0521	44.3517	0.6303
130.0050	44.4000	0.6285	130.0527	44.3988	0.6317
130.0064	44.3765	0.6448	130.0531	44.3658	0.6358
130.0065	44.4100	0.6416	130.0540	44.3615	0.6459
130.0079	44.3946	0.6423	130.0559	44.3896	0.4498
130.0148	44.3559	0.6393	130.0569	44.3983	0.6322
130.0151	44.3346	0.6388	130.0584	44.3258	0.6402
130.0179	44.3557	0.6310	130.0590	44.3730	0.6279
130.0232	44.3621	0.6283	130.0620	44.3506	0.6359
130.0236	44.3787	0.6476	130.0628	44.3491	0.6416
130.0298	44.3607	0.6286	130.0642	44.3380	0.6432
130.0301	44.3706	0.6408	130.0694	44.3092	0.6410
130.0304	44.3783	0.6333	130.0776	44.3516	0.6406
130.0323	44.3659	2.2300	130.0921	44.3207	0.6485
130.0324	44.3733	0.6370			
B 130.0390	44.3650	0.6384			
130.0426	44.3492	0.8382			
130.0430	44.3794	0.6430			
130.0462	44.3348	0.6427			
130.0465	44.3699	0.6518			

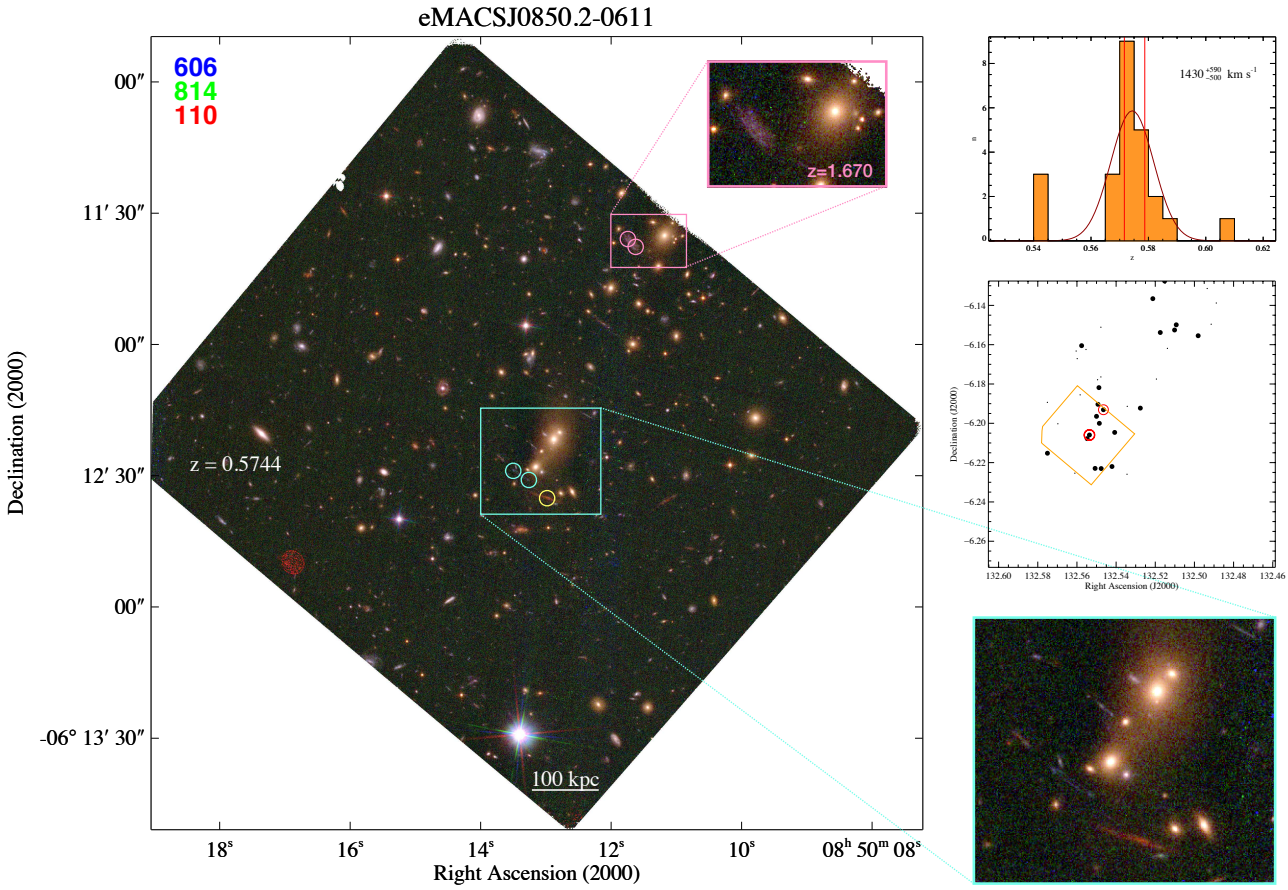

Figure B15. eMACSJ0850.2−0611 appears to be a wide-separation merger; an assessment of the progress of this process (pre- or post-collision) will be possible only once X-ray follow-up observations have been performed. Similarly, a lens model of the cluster mass distribution awaits additional follow-up spectroscopy of the strong-lensing features identified in the SE component; the sole available constraint in the NW cluster core is insufficient to derive a lens model for the cluster as a whole.

Coordinates (J2000) and spectroscopic redshifts of galaxies in the field of eMACSJ0850.2-0611.

R.A. (deg)	Dec (deg)	z	R.A. (deg)	Dec (deg)	z
132.4888	−6.1388	0.5449	132.5507	−6.2229	0.5652
132.4914	−6.1496	0.5448	B 132.5536	−6.2059	0.5716
132.4935	−6.1314	0.5440	132.5548	−6.2078	0.5684
132.4981	−6.1554	0.5704	132.5554	−6.1624	0.4543
132.5093	−6.1499	0.5713	132.5576	−6.1605	0.5725
132.5101	−6.1525	0.5730	132.5584	−6.1855	0.2612
132.5138	−6.1619	0.4535	132.5599	−6.1671	0.4534
132.5152	−6.1276	0.5712	132.5604	−6.1632	0.2602
132.5174	−6.1538	0.5728	132.5611	−6.2254	0.4418
132.5194	−6.1775	0.4138	132.5697	−6.2002	0.3959
132.5212	−6.1366	0.5800	132.5698	−6.2733	0.6419
132.5276	−6.1923	0.5733	132.5751	−6.2152	0.5804
132.5343	−6.1914	0.2599	132.5751	−6.1893	0.3295
132.5344	−6.2259	0.6091			
132.5407	−6.2046	0.5801			
132.5421	−6.2220	0.5776			
132.5465	−6.1931	0.5787			
132.5476	−6.2230	0.5698			
132.5478	−6.1511	0.1891			
132.5478	−6.1764	0.3353			
132.5486	−6.2000	0.5783			
132.5488	−6.1818	0.5873			
132.5493	−6.1903	0.5791			
132.5495	−6.1778	0.3351			
132.5500	−6.1965	0.5701			

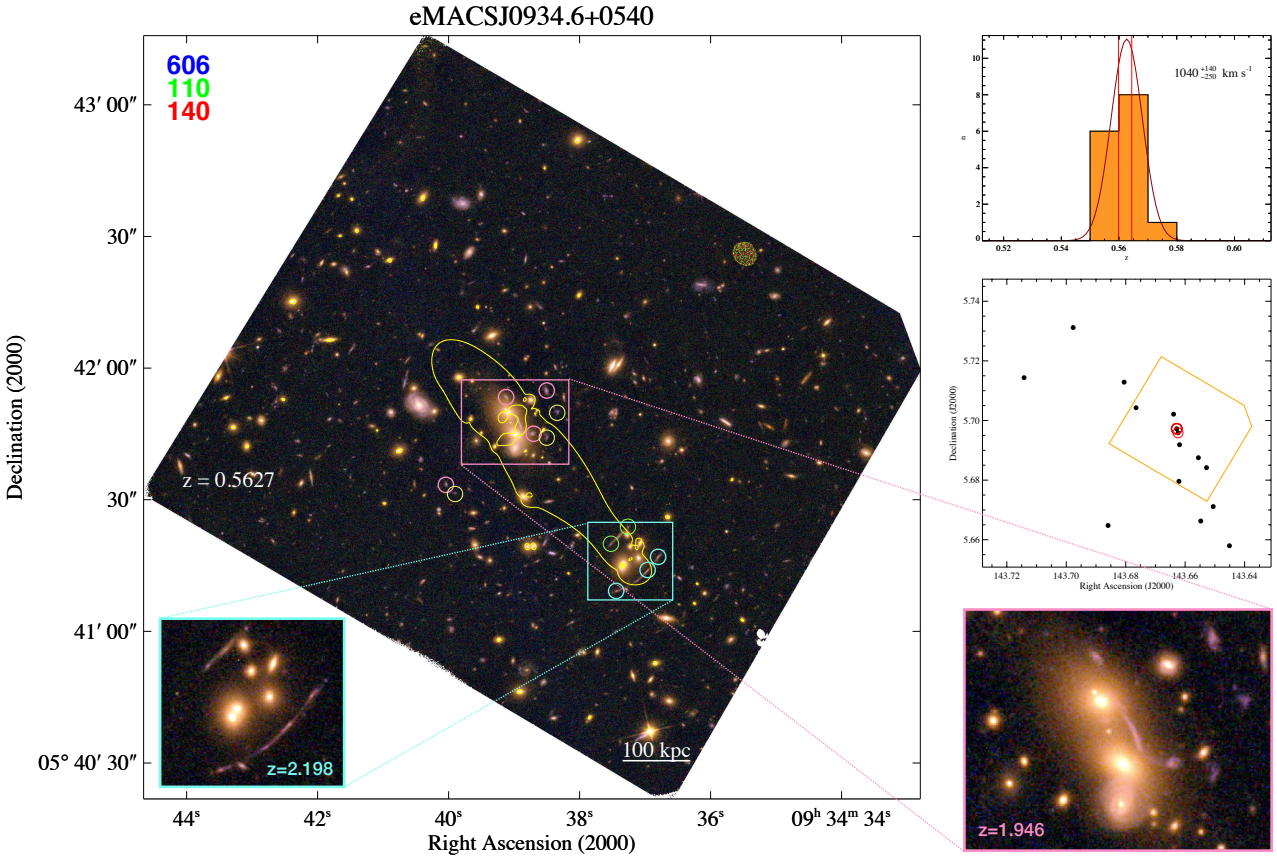

Figure B16. eMACSJ0934.6+0540 features a highly elongated mass distribution, suggestive of an ongoing merging event, according to our LENSTOOL model which is well constrained by two spectroscopically confirmed multiple-image systems. Additional redshifts of cluster members are needed for a more robust determination of the cluster velocity dispersion as well as insights into potential line-of-sight substructure.

Coordinates (J2000) and spectroscopic redshifts of galaxies in the field of eMACSJ0934.6+0540.

	R.A. (deg)	Dec (deg)	z
	143.6451	5.6580	0.5624
	143.6506	5.6711	0.5598
	143.6528	5.6842	0.5549
	143.6548	5.6663	0.5632
	143.6556	5.6875	0.5600
	143.6603	5.6508	0.6256
	143.6619	5.6919	0.5630
	143.6621	5.6796	0.5674
	143.6624	5.6959	0.5644
B	143.6628	5.6972	0.5598
	143.6639	5.7021	0.5702
	143.6765	5.7043	0.5591
	143.6768	5.7474	0.3448
	143.6805	5.7129	0.5688
	143.6859	5.6648	0.5525
	143.6977	5.7312	0.5626
	143.7142	5.7144	0.5689

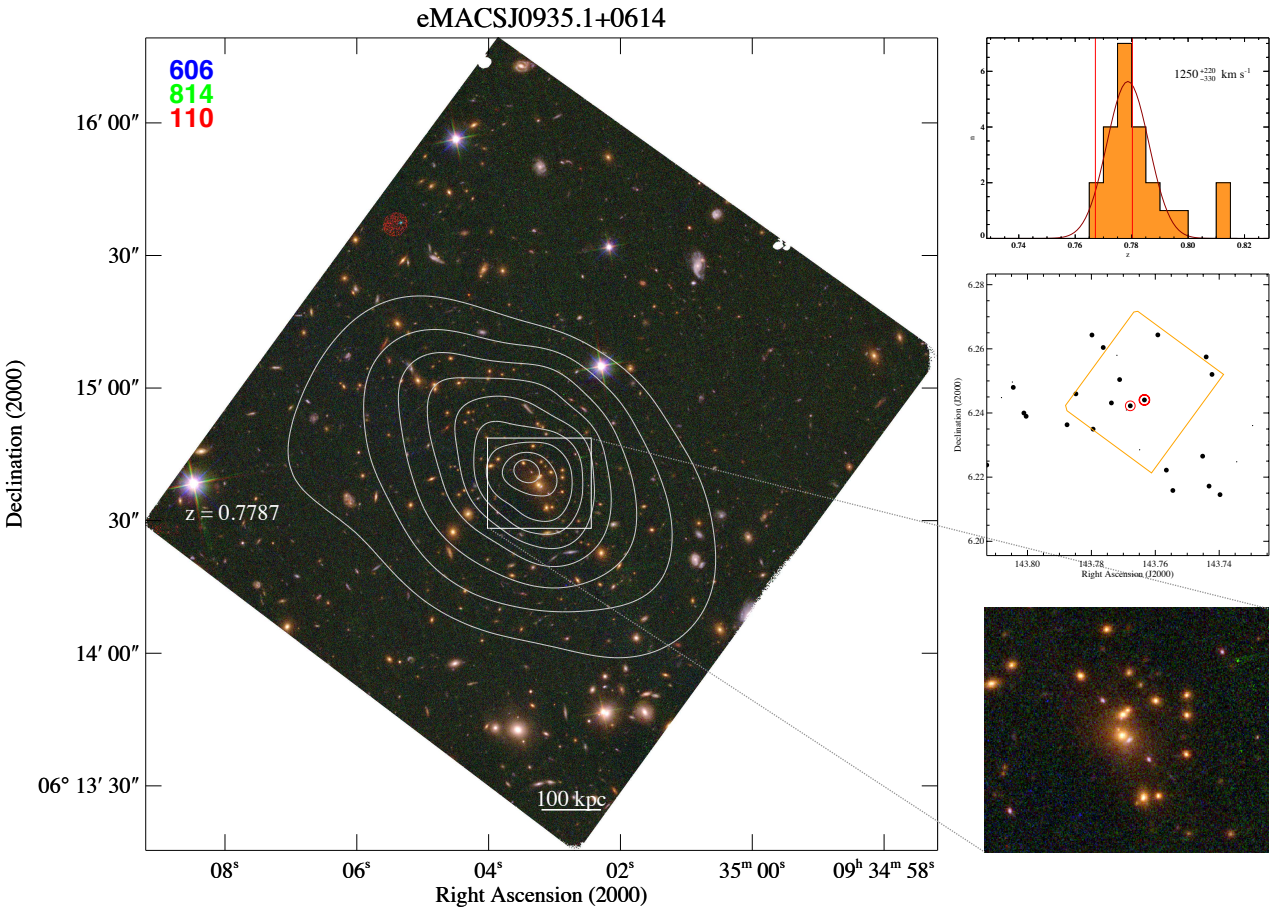

Figure B17. Having found no convincing strong-lensing features in the cluster core (a zoomed-in view is shown on the bottom right), we are unable to derive a lens model for the mass distribution in eMACSJ0935.1+0614, one of the ten most X-ray luminous clusters in the subset observed with *CXO* to date (see Section 5.4).

Coordinates (J2000) and spectroscopic redshifts of galaxies in the field of eMACSJ0935.1+0614.

R.A. (deg)	Dec (deg)	z	R.A. (deg)	Dec (deg)	z
143.7244	6.2312	0.5443	143.8044	6.2480	0.7853
143.7295	6.2361	0.7227	143.8047	6.2496	0.5664
143.7345	6.2248	0.7233	143.8081	6.2448	0.3710
143.7397	6.2145	0.7822	143.8127	6.2238	0.7747
143.7423	6.2520	0.7841			
143.7432	6.2172	0.7728			
143.7441	6.2575	0.7890			
143.7452	6.2265	0.7795			
143.7545	6.2158	0.7694			
143.7565	6.2222	0.7752			
143.7592	6.2643	0.7782			
B 143.7634	6.2441	0.7803			
143.7649	6.2285	0.3964			
143.7678	6.2422	0.7671			
143.7690	6.2409	0.8139			
143.7712	6.2504	0.7934			
143.7720	6.2580	0.8126			
143.7737	6.2431	0.7965			
143.7763	6.2604	0.7747			
143.7795	6.2350	0.7794			
143.7798	6.2643	0.7835			
143.7849	6.2460	0.7757			
143.7876	6.2363	0.7732			
143.8004	6.2390	0.7774			
143.8011	6.2400	0.7772			

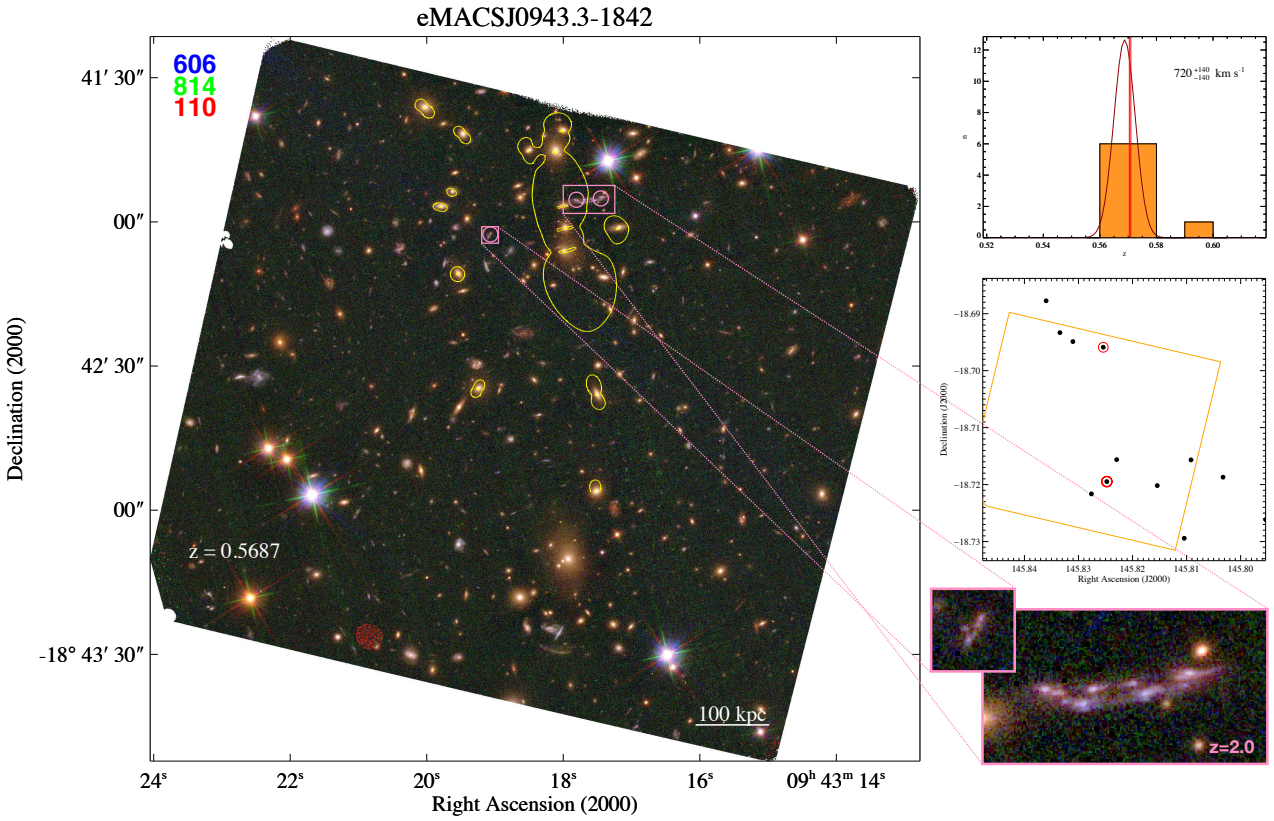

Figure B18. eMACSJ0943.3−1842. A spectroscopically confirmed multiple-image system constrains the mass distribution of the northern component of this complex system. However, lacking redshifts of other strong-lensing features, we are currently unable to incorporate the presumably dominant, southern mass component around the BCG. In light of the small number of redshifts available at present in this field, the listed cluster velocity dispersion should be considered tentative.

Coordinates (J2000) and spectroscopic redshifts of galaxies in the field of eMACSJ0943.3-1842.

	R.A. (deg)	Dec (deg)	z
	145.7954	−18.7261	0.5687
	145.8033	−18.7187	0.5657
	145.8092	−18.7157	0.5656
	145.8104	−18.7294	0.5639
	145.8154	−18.7202	0.5634
	145.8229	−18.7156	0.5726
B	145.8248	−18.7195	0.5709
	145.8254	−18.6959	0.5704
	145.8276	−18.7216	0.5738
	145.8310	−18.6949	0.5670
	145.8334	−18.6933	0.5717
	145.8360	−18.6877	0.5707
	145.8477	−18.6981	0.5966

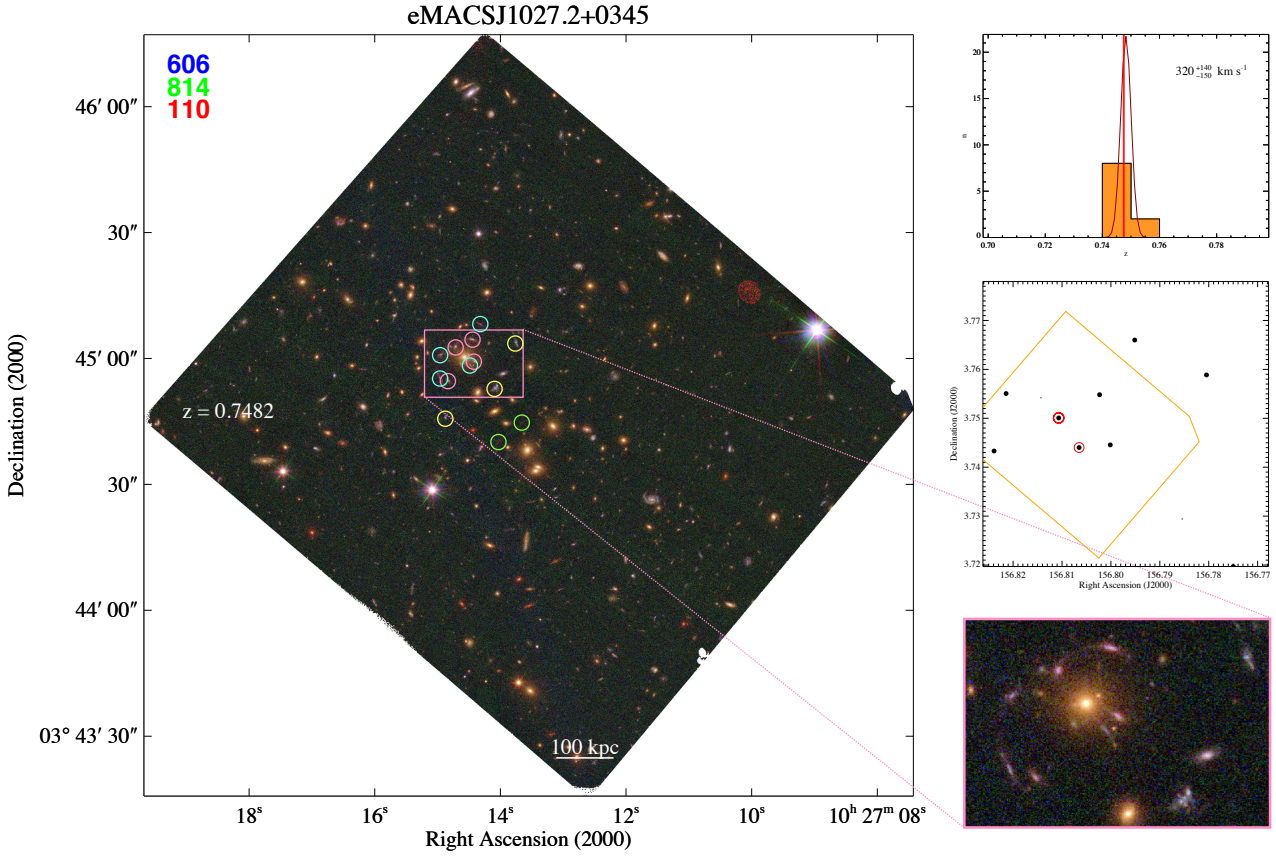

Figure B19. eMACSJ1027.2+0345 exhibits a plethora of impressive strong-lensing features; alas, none of them have redshifts at this point, preventing us from constructing a lens model. In addition, the listed cluster velocity dispersion is highly uncertain, being based on only 10 concordant redshifts.

Coordinates (J2000) and spectroscopic redshifts of galaxies in the field of eMACSJ1027.2+0345.

	R.A. (deg)	Dec (deg)	z
	156.7701	3.7780	0.3434
	156.7750	3.7197	0.7468
	156.7805	3.7589	0.7486
	156.7854	3.7294	0.6043
	156.7951	3.7660	0.7470
	156.8001	3.7446	0.7509
	156.8023	3.7548	0.7481
	156.8065	3.7440	0.7476
B	156.8107	3.7501	0.7473
	156.8143	3.7542	0.7540
	156.8214	3.7551	0.7491
	156.8239	3.7433	0.7492

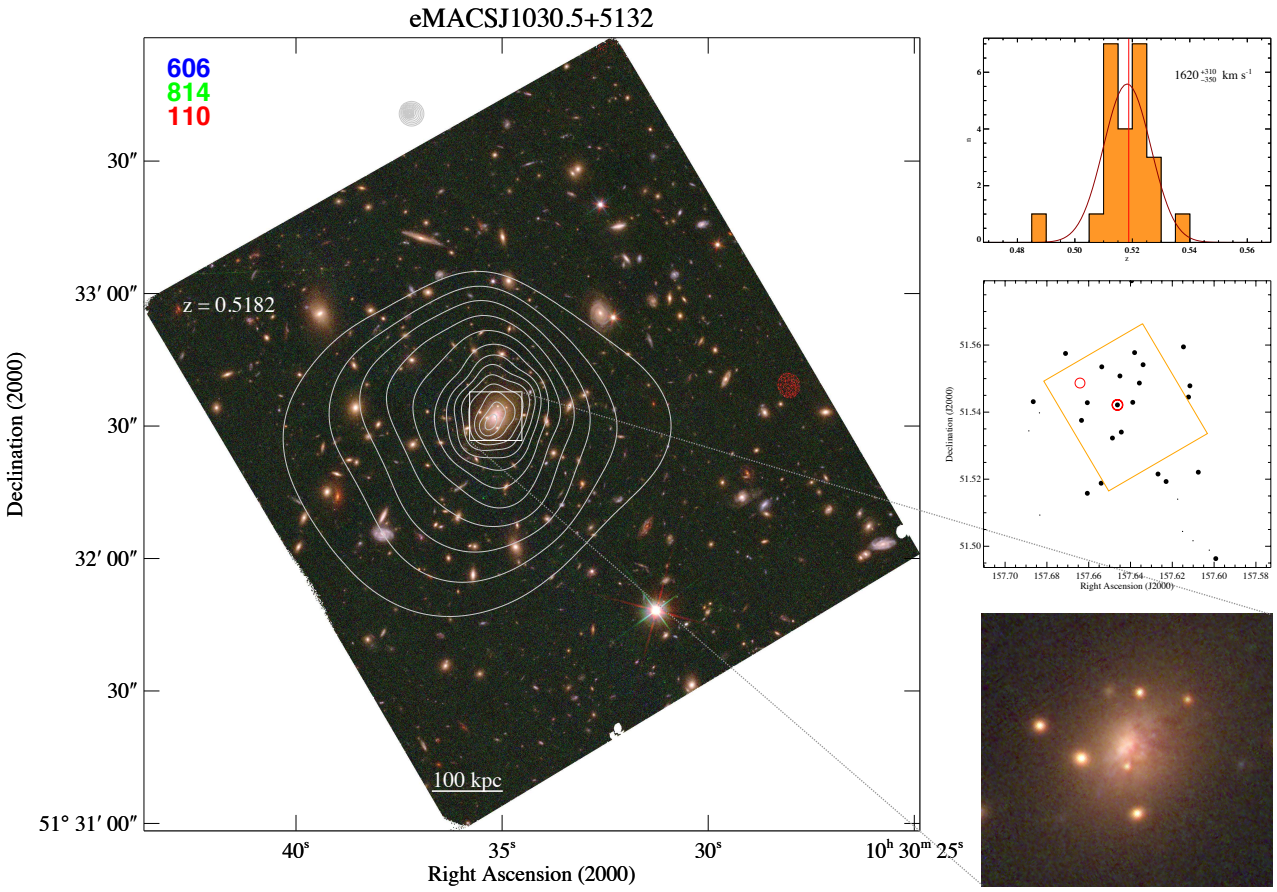

Figure B20. The BCG of eMACSJ1030.5+5132 is the brightest radio source in all eMACS clusters observed so far with the VLA at 5 GHz (Sections 3.5 and 5.5.3); it actively forms stars and, in the process, dust, as can be seen in the zoomed-in view shown on the bottom right. Extremely X-ray luminous and featuring an exceptionally high velocity dispersion, eMACSJ1030.5 is one of very few fully relaxed clusters in the eMACS subset with *CXO* data (Table 3).

Coordinates (J2000) and spectroscopic redshifts of galaxies in the field of eMACSJ1030.5+5132.

R.A. (deg)	Dec (deg)	z	R.A. (deg)	Dec (deg)	z
157.5945	51.4937	0.3569	157.6634	51.5375	0.5154
157.5992	51.4963	0.5369	157.6711	51.5575	0.5252
157.6023	51.4988	0.3940	157.6834	51.5093	0.4189
157.6076	51.5221	0.5131	157.6836	51.5398	0.4128
157.6101	51.5016	0.3560	157.6865	51.5431	0.5255
157.6116	51.5478	0.5103	157.6886	51.5344	0.4864
157.6122	51.5445	0.5204			
157.6147	51.5595	0.5150			
157.6151	51.5044	0.3568			
157.6174	51.5140	0.5832			
157.6230	51.5193	0.5247			
157.6268	51.5215	0.5261			
157.6340	51.5541	0.5119			
157.6358	51.5487	0.5214			
157.6380	51.5578	0.5238			
157.6389	51.5429	0.5228			
157.6395	51.5792	0.5169			
157.6444	51.5340	0.5076			
157.6451	51.5508	0.5202			
B 157.6462	51.5421	0.5188			
157.6486	51.5323	0.5144			
157.6538	51.5535	0.5106			
157.6540	51.5188	0.5128			
157.6607	51.5158	0.5101			
157.6607	51.5428	0.5230			

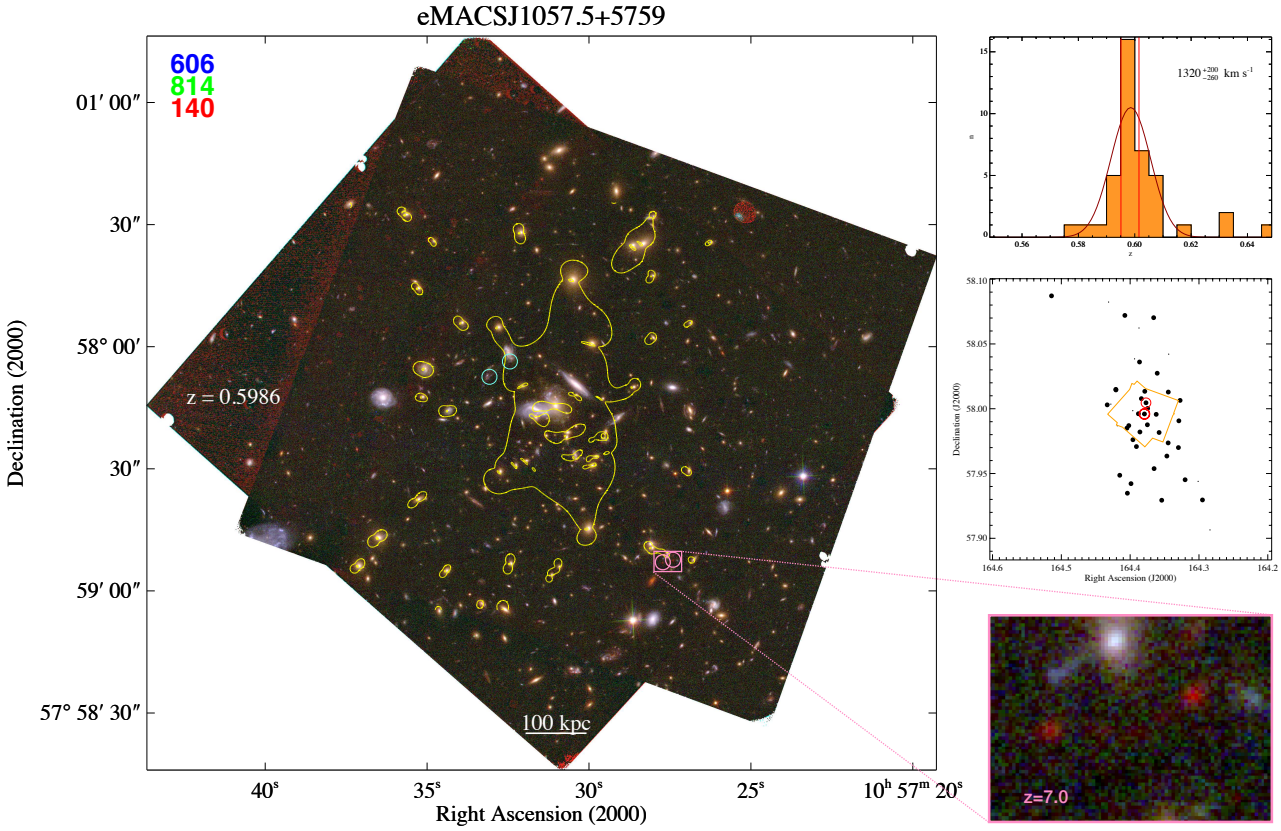

Figure B21. eMACSJ1057.5+5759 is a powerful gravitational lens; the LENSTOOL model is constrained by two multiple-image systems, one of which is spectroscopically confirmed to be at $z = 7.0$, the so far highest redshift of any background galaxy lensed by a foreground eMACS cluster. The system was originally discovered in the eMACS pilot project (Ebeling et al. 2013).

Coordinates (J2000) and spectroscopic redshifts of galaxies in the field of eMACSJ1057.5+5759.

R.A. (deg)	Dec (deg)	z	R.A. (deg)	Dec (deg)	z
164.2840	57.9065	0.7634	164.3858	57.9821	0.5965
164.2949	57.9296	0.5961	164.3864	58.0361	0.6035
164.3012	57.9439	0.6328	164.3872	58.0623	0.7464
164.3201	57.9452	0.5994	164.3880	57.9961	0.5847
164.3274	58.0064	0.6084	164.3909	57.9708	0.5927
164.3292	57.9907	0.5914	164.3936	58.0385	0.6328
164.3299	57.9700	0.5998	164.3960	57.9761	0.5952
164.3440	58.0421	0.7453	164.3962	57.9985	0.6197
164.3446	58.0129	0.6076	164.3988	57.9422	0.5967
164.3448	57.9736	0.5954	164.4020	57.9870	0.5899
164.3467	57.9635	0.5918	164.4040	57.9348	0.5973
164.3541	57.9294	0.5969	164.4047	57.9850	0.6099
164.3579	57.9817	0.5988	164.4077	58.0720	0.6018
164.3607	58.0274	0.6047	164.4151	57.9486	0.5987
164.3621	57.9957	0.6034	164.4187	57.9869	0.0466
164.3652	57.9538	0.5958	164.4207	58.0145	0.6028
164.3659	58.0703	0.6023	164.4208	58.0149	0.6050
164.3708	57.8833	0.5756	164.4280	58.0035	0.7673
164.3746	58.0002	0.5928	164.4313	58.0823	0.6465
164.3750	57.9876	0.5920	164.4333	58.0030	0.6092
164.3770	58.0046	0.5951	164.4834	58.1003	0.6527
164.3787	58.0134	0.5975	164.5143	58.0871	0.5991
B 164.3792	57.9960	0.6015			
164.3819	57.9957	0.1333			
164.3837	58.0078	0.5960			

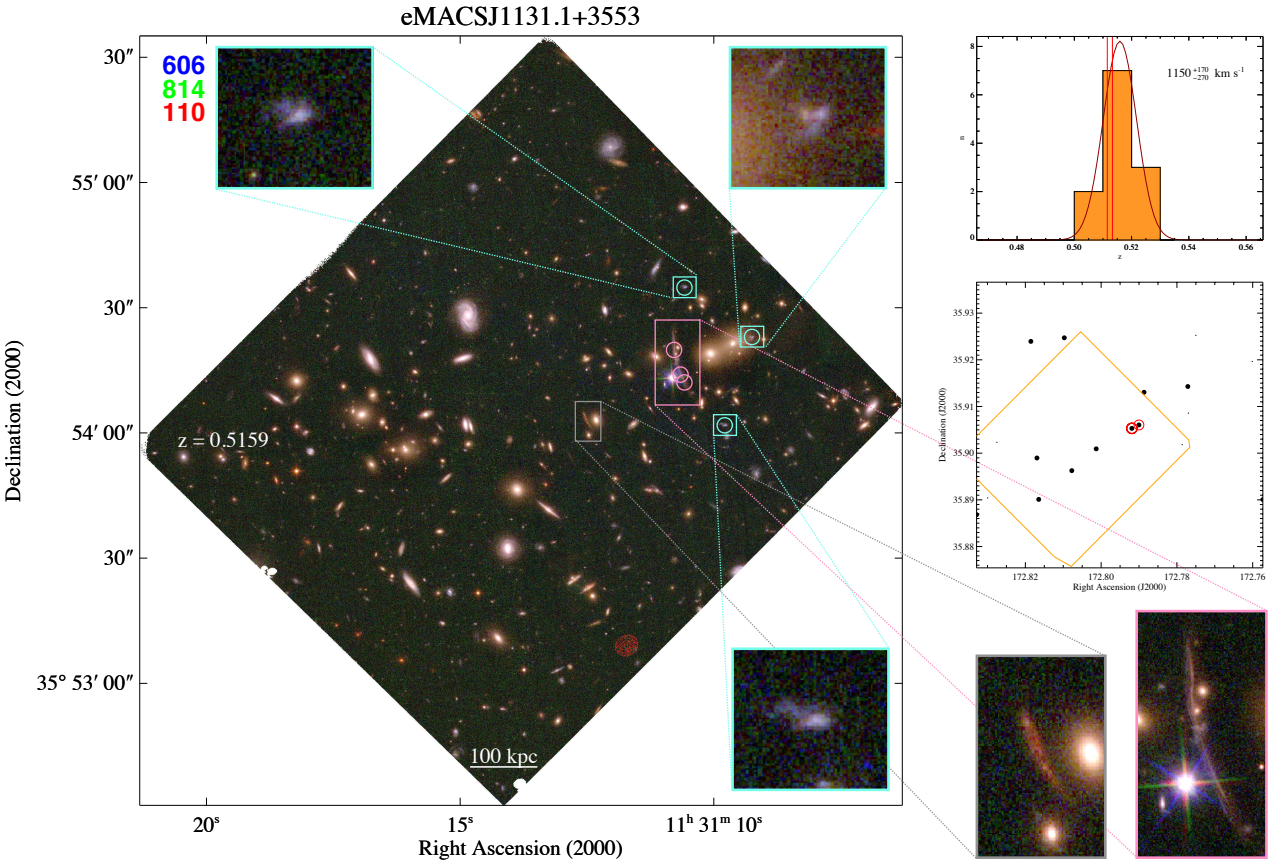

Figure B22. eMACSJ1131.1+3553 exhibits a complex (projected) galaxy distribution which is currently poorly sampled by the small number of spectroscopically confirmed cluster members. Redshifts are also unavailable for the strong-lensing features visible in the cluster core region. Consequently, little can at present be said about the system's physical properties.

Coordinates (J2000) and spectroscopic redshifts of galaxies in the field of eMACSJ1131.1+3553.

	R.A. (deg)	Dec (deg)	z
	172.7573	35.8901	0.5143
	172.7601	35.9196	0.2076
	172.7750	35.9252	0.2385
	172.7770	35.9086	0.2111
	172.7771	35.9143	0.5180
	172.7786	35.9018	0.2106
	172.7887	35.9130	0.5058
	172.7900	35.9060	0.5115
B	172.7919	35.9053	0.5133
	172.8013	35.9009	0.5210
	172.8077	35.8963	0.5238
	172.8097	35.9247	0.5192
	172.8165	35.8901	0.5216
	172.8169	35.8990	0.5155
	172.8185	35.9239	0.5163
	172.8275	35.9023	0.2112
	172.8299	35.8904	0.2215
	172.8329	35.8868	0.5083

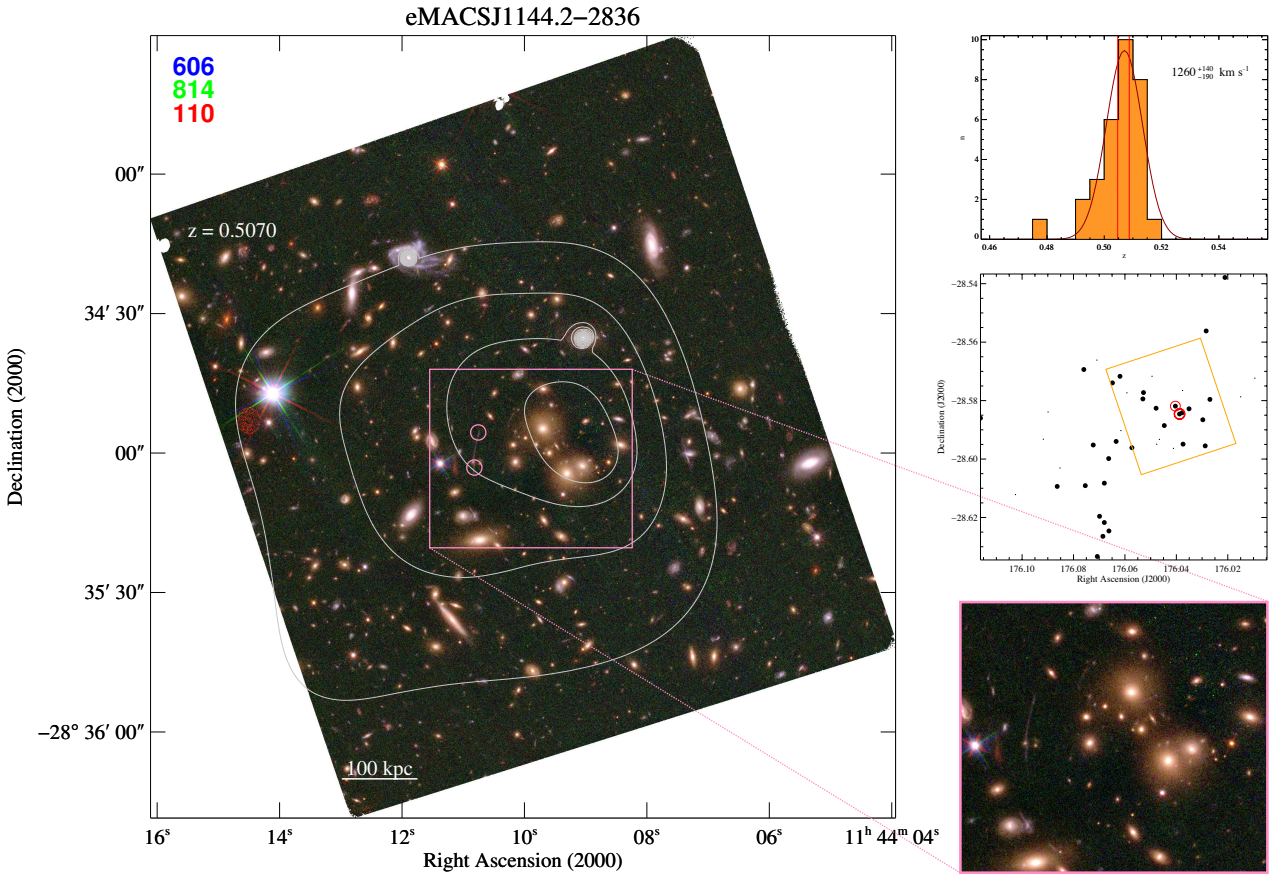

Figure B23. eMACSJ1144.2−2836. The X-ray luminosity of eMACSJ1144.2 as measured from *CXO* data is only one sixth of that recorded in the RASS. Although two X-ray point sources are detected close to the cluster core, their fluxes are far too low (at the time of the *CXO* observation) to account for the discrepancy. Featuring a high velocity dispersion and two faint, but unambiguous gravitational arcs, the system may be a cluster of modest mass connected to a filament that is partly aligned with our line of sight, thus boosting the projected, but not the three-dimensionally collapsed mass.

Coordinates (J2000) and spectroscopic redshifts of galaxies in the field of eMACSJ1144.2-2836.

R.A. (deg)	Dec (deg)	z	R.A. (deg)	Dec (deg)	z
176.0047	−28.5824	0.4752	176.0619	−28.5717	0.5087
176.0095	−28.5723	0.3909	176.0634	−28.5940	0.5149
176.0150	−28.5787	0.4116	176.0649	−28.5739	0.5094
176.0211	−28.5379	0.5134	176.0662	−28.6246	0.4995
176.0269	−28.5796	0.5068	176.0663	−28.5998	0.5030
176.0284	−28.5562	0.5075	176.0680	−28.6083	0.5033
176.0288	−28.5955	0.5135	176.0680	−28.6217	0.5130
176.0297	−28.5866	0.4932	176.0686	−28.6264	0.5025
176.0351	−28.5828	0.4939	176.0699	−28.6196	0.5104
176.0374	−28.5949	0.5144	176.0707	−28.6333	0.5125
176.0376	−28.5765	0.2127	176.0709	−28.5661	0.3296
176.0377	−28.5841	0.5010	176.0723	−28.5952	0.5092
B 176.0388	−28.5846	0.5047	176.0754	−28.6091	0.5092
176.0404	−28.5819	0.5087	176.0760	−28.5694	0.5055
176.0411	−28.5964	0.7286	176.0853	−28.6031	0.4196
176.0447	−28.5885	0.5166	176.0863	−28.6094	0.5069
176.0466	−28.5933	0.3886	176.0899	−28.5839	0.4498
176.0477	−28.5949	0.7315	176.0917	−28.5932	0.4196
176.0479	−28.5826	0.5113	176.1026	−28.6121	0.4488
176.0495	−28.5717	0.2116	176.1162	−28.5860	0.4973
176.0528	−28.5773	0.5047			
176.0530	−28.5794	0.5063			
176.0573	−28.5961	0.4991			
176.0592	−28.5773	0.4203			
176.0616	−28.5903	0.5647			

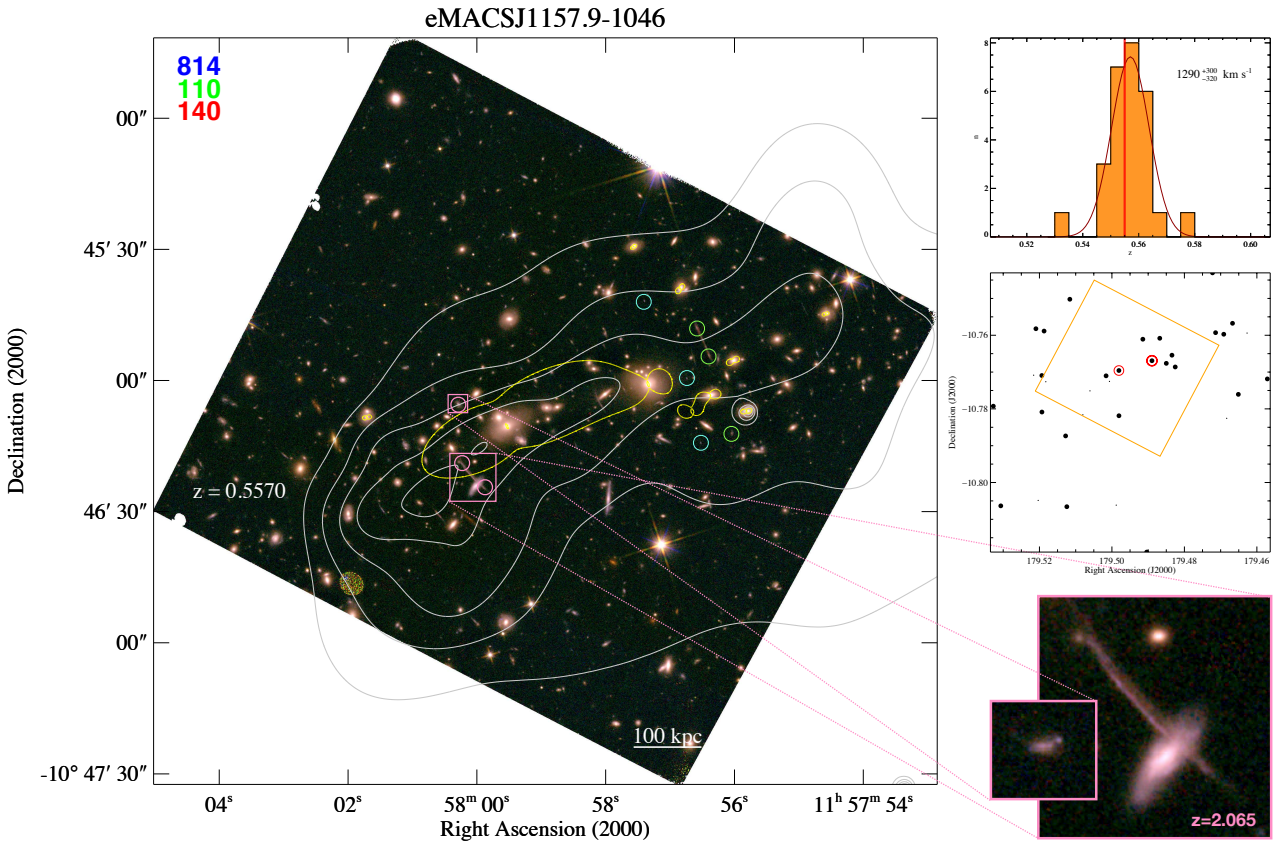

Figure B24. eMACSJ1157.9−1046. In addition to the highlighted multiple-image system constraining the mass distribution in the vicinity of the eastern BCG of this obvious merger, two multiple-image systems were identified farther west and are marked here. However, lacking redshifts, they currently do not provide usable constraints on the mass of the western subcluster. The combination of a high X-ray luminosity with a modest ICM temperature (Table 3) suggests that we observe the system well after shocks from the initial collision have dissipated.

Coordinates (J2000) and spectroscopic redshifts of galaxies in the field of eMACSJ1157.9-1046.

R.A. (deg)	Dec (deg)	z	R.A. (deg)	Dec (deg)	z
179.4571	−10.7719	0.5544	179.5182	−10.7726	1.1923
179.4627	−10.7594	0.5786	179.5187	−10.7589	0.5615
179.4651	−10.7761	0.5500	179.5193	−10.7809	0.5630
179.4667	−10.7568	0.5566	179.5193	−10.7709	0.5611
179.4683	−10.7826	0.5301	179.5203	−10.8049	0.6905
179.4691	−10.7597	0.5462	179.5210	−10.7582	0.5596
179.4714	−10.7593	0.5544	179.5216	−10.7709	0.7081
179.4722	−10.7431	0.5540	179.5307	−10.8063	0.5585
X 179.4825	−10.7686	0.5641	179.5327	−10.7793	0.5655
179.4834	−10.7654	0.5546			
179.4850	−10.7676	0.5477			
179.4868	−10.7608	0.5509			
B 179.4889	−10.7669	0.5551			
179.4904	−10.8189	0.5582			
179.4915	−10.7611	0.5562			
179.4981	−10.7819	0.5621			
179.4981	−10.7696	0.5548			
179.4988	−10.8062	0.7939			
179.5007	−10.7725	2.0651			
179.5016	−10.7710	0.5524			
179.5061	−10.7751	3.5664			
179.5080	−10.7816	0.6780			
179.5116	−10.7502	0.5629			
179.5124	−10.8066	0.5558			
179.5128	−10.7873	0.5600			

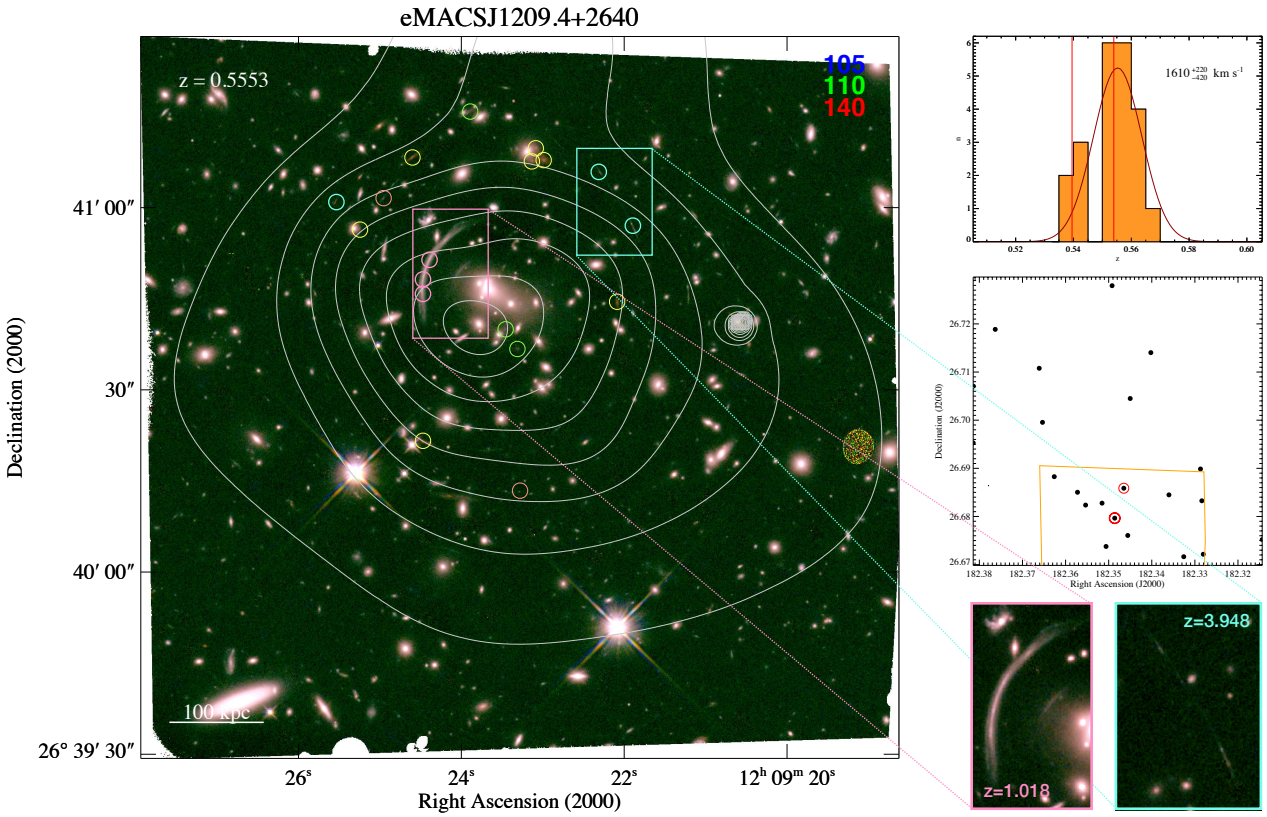

Figure B25. eMACSJ1209.4+2640 was independently discovered in the SDSS Giant Arc Survey and analyzed by Sharon et al. (2020); redshifts for the highlighted gravitational arcs were measured by Ofek et al. (2008) and Bayliss et al. (2011). In spite of the regular X-ray contours, the observed offset of the X-ray centroid from the location of the BCG and a very high velocity dispersion suggest that this highly X-ray luminous system is actively growing.

Coordinates (J2000) and spectroscopic redshifts of galaxies in the field of eMACSJ1209.4+2640.

	R.A. (deg)	Dec (deg)	z
	182.3144	26.6752	0.5573
	182.3281	26.6721	0.5548
	182.3284	26.6833	0.5446
	182.3287	26.6899	0.5637
	182.3326	26.6716	0.5569
	182.3360	26.6845	0.5673
	182.3402	26.7140	0.5411
	182.3450	26.7045	0.5436
	182.3456	26.6760	0.5625
	182.3465	26.6859	0.5540
B	182.3486	26.6797	0.5395
	182.3492	26.7279	0.5587
	182.3506	26.6738	0.5532
R	182.3515	26.6828	0.5398
	182.3554	26.6824	0.5582
	182.3572	26.6850	0.5556
	182.3626	26.6883	0.5531
	182.3654	26.6996	0.5601
	182.3661	26.7108	0.5542
	182.3763	26.7189	0.5545
	182.3779	26.6864	0.6509
	182.3814	26.7071	0.5595
	182.3814	26.6953	0.5631

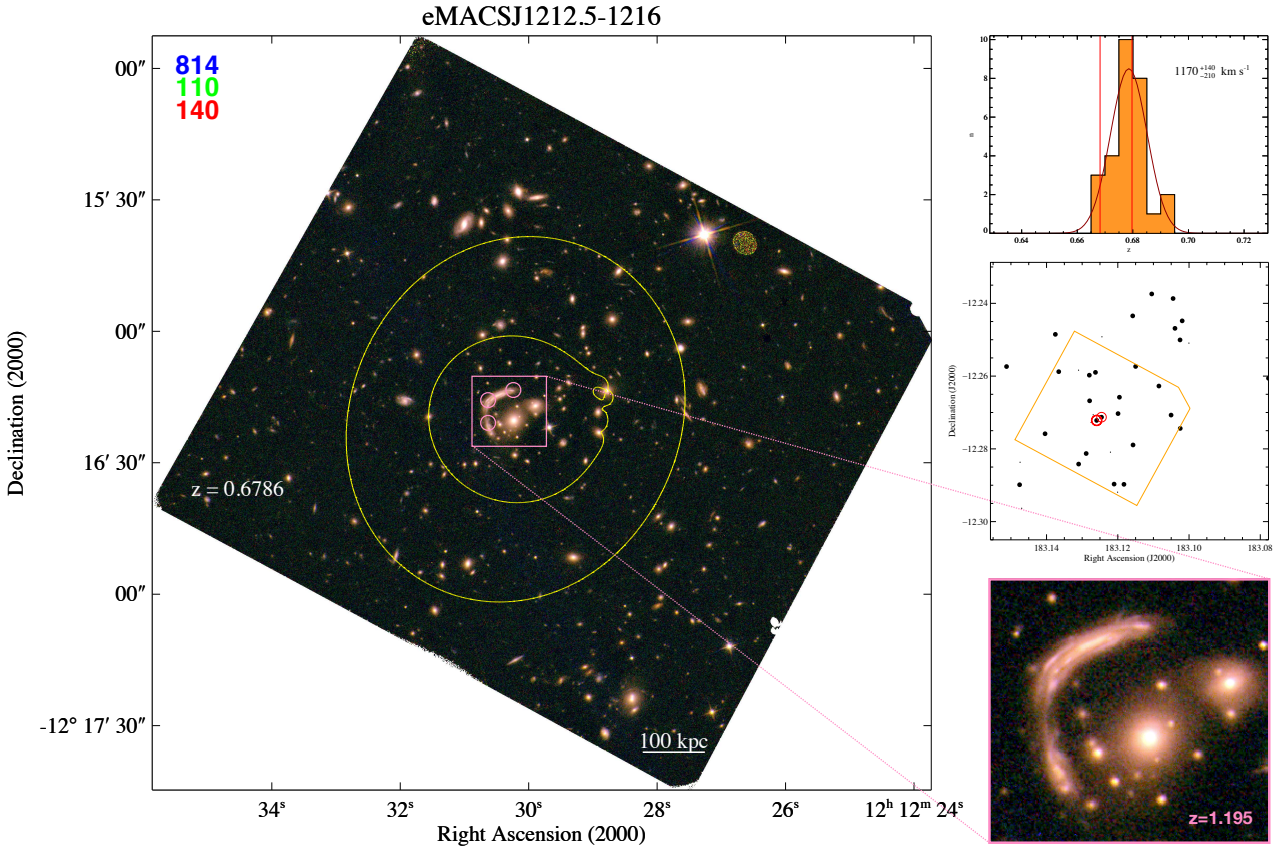

Figure B26. eMACSJ1212.5−1216 hosts one of the most spectacular multiple-image systems in any eMACS cluster; the deduced very large Einstein radius (Table 2) is, however, subject to substantial systematic uncertainties as discussed in Section 5.2.2 (see also Fig. 8). The high gravitational amplification and shear of this strong-lensing feature offer a valuable opportunity for spatially resolved high-resolution spectroscopy of an intrinsically faint galaxy at $z = 1.2$.

Coordinates (J2000) and spectroscopic redshifts of galaxies in the field of eMACSJ1212.5-1216.

R.A. (deg)	Dec (deg)	z	R.A. (deg)	Dec (deg)	z
183.0777	−12.2606	0.6785	183.1279	−12.2668	0.6687
183.1000	−12.2509	0.4524	183.1280	−12.2597	0.6728
183.1019	−12.2448	0.6814	183.1289	−12.2813	0.6798
183.1025	−12.2744	0.6784	183.1310	−12.2842	0.6763
183.1025	−12.2501	0.6815	183.1310	−12.2584	0.3641
183.1039	−12.2469	0.6763	183.1366	−12.2588	0.6735
183.1045	−12.2387	0.6795	183.1375	−12.2485	0.6842
183.1050	−12.2707	0.6898	183.1404	−12.2758	0.6848
183.1085	−12.2627	0.6803	183.1470	−12.2963	0.3646
183.1105	−12.2374	0.6706	183.1474	−12.2837	0.1718
183.1150	−12.2573	0.6780	183.1476	−12.2899	0.6766
183.1157	−12.2789	0.6733	183.1512	−12.2574	0.6824
183.1158	−12.2434	0.6804	183.1557	−12.2884	0.2563
183.1183	−12.2898	0.6841			
183.1195	−12.2658	0.6752			
183.1199	−12.2703	0.6675			
183.1201	−12.2919	0.7673			
183.1210	−12.2897	0.6905			
183.1221	−12.2809	0.8086			
183.1245	−12.2492	0.8371			
183.1246	−12.2713	0.6682			
B 183.1259	−12.2722	0.6797			
183.1263	−12.2590	0.6910			
183.1269	−12.2706	1.1954			
183.1275	−12.2727	1.1952			

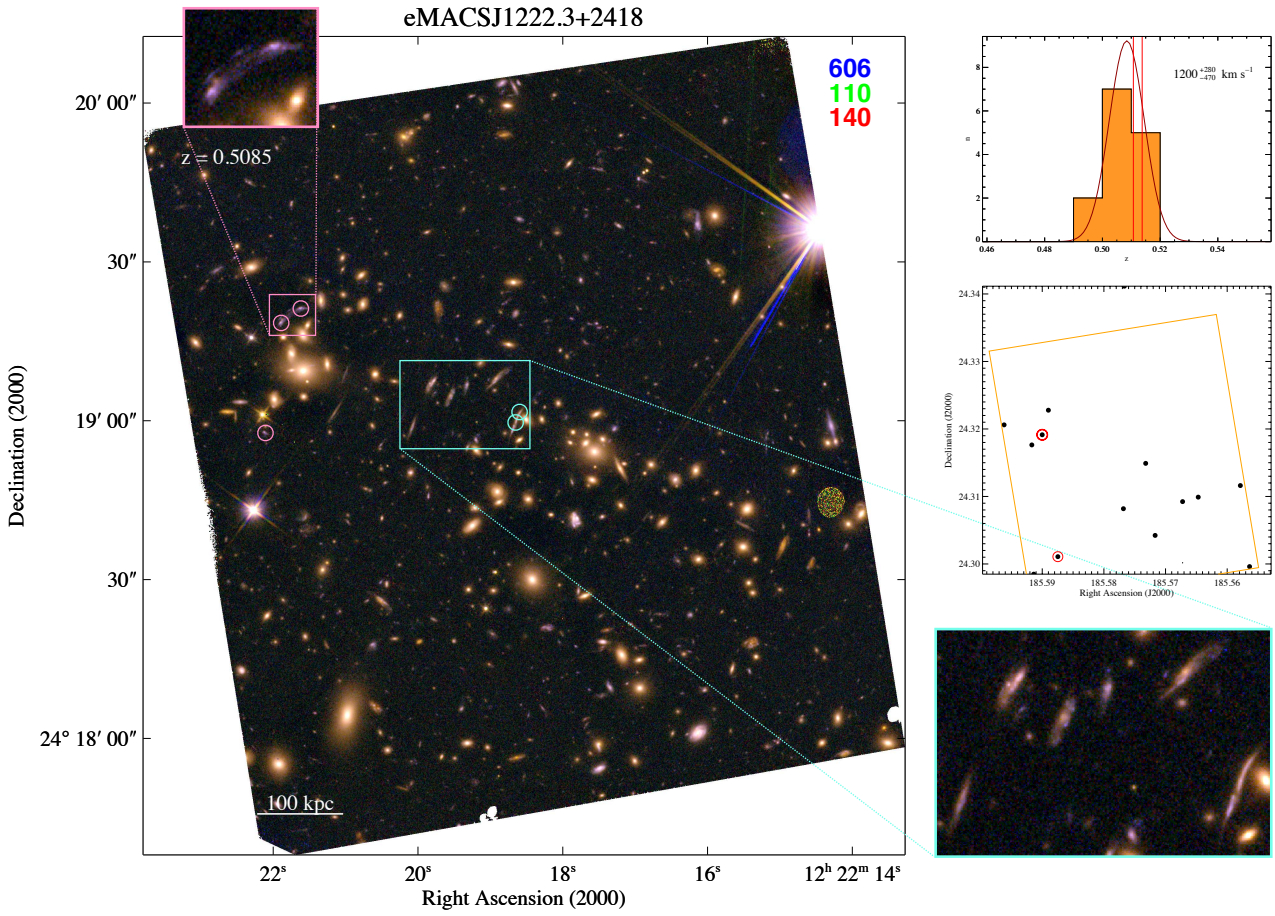

Figure B27. eMACSJ1222.3+2418 is an optically complex system that potentially contains multiple cores. Although several obvious strong-lensing features are present, none has a spectroscopic redshift at this point, preventing us from attempting to map the mass distribution in this system.

Coordinates (J2000) and spectroscopic redshifts of galaxies in the field of eMACSJ1222.3+2418.

R.A. (deg)	Dec (deg)	z
185.5564	24.2996	0.5092
185.5579	24.3116	0.5090
185.5647	24.3099	0.5084
185.5672	24.3092	0.5052
185.5672	24.3002	0.3922
185.5717	24.3042	0.5129
185.5732	24.3149	0.5055
185.5767	24.3411	0.4989
185.5768	24.3082	0.4923
185.5875	24.3011	0.5107
185.5890	24.3228	0.5100
B 185.5900	24.3191	0.5138
185.5914	24.2985	0.5024
185.5917	24.3176	0.5155
185.5962	24.3206	0.5105

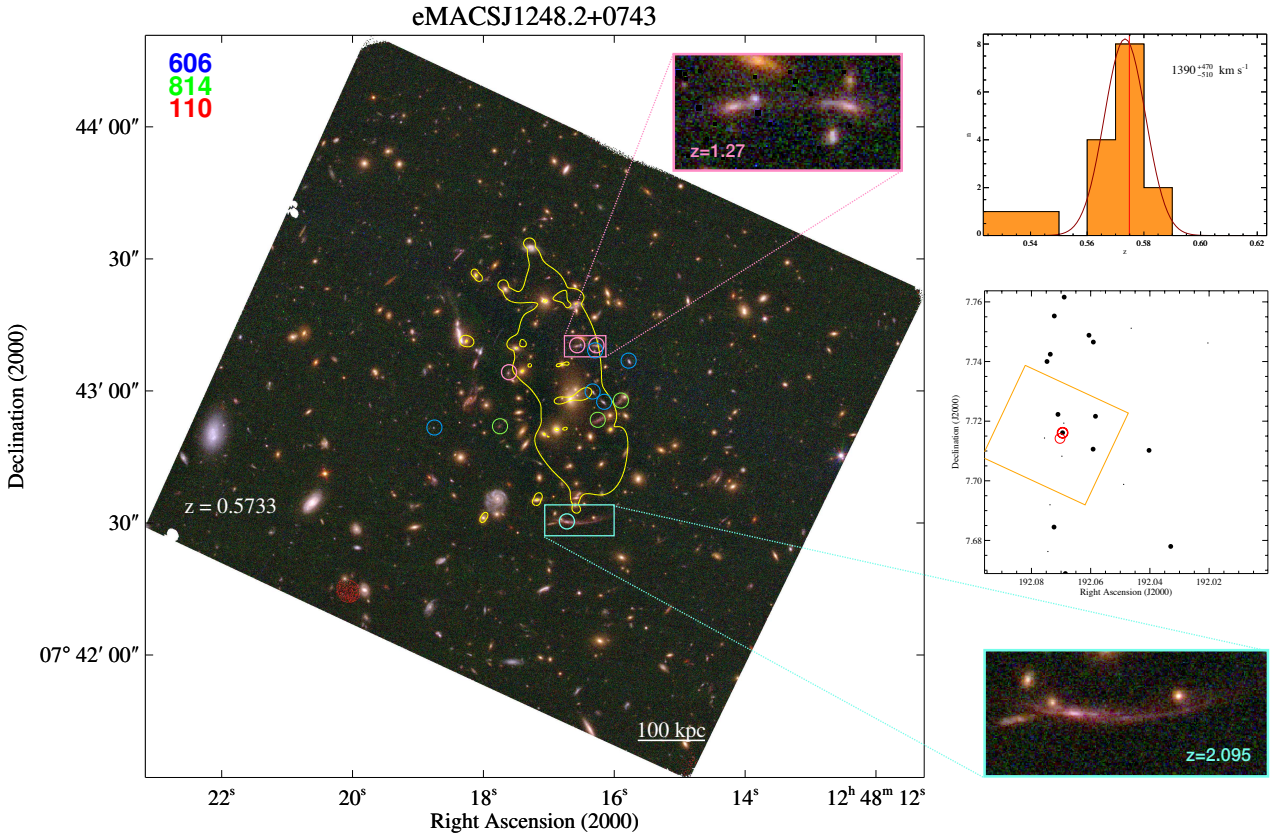

Figure B28. A well constrained LENSTOOL model shows eMACSJ1248.2+0743 to be a powerful gravitational lens. A rare hyperbolic umbilical lensing configuration is discovered west of the cluster core (Section 5.2) but has yet to be spectroscopically confirmed. Additional follow-up observations (specifically at X-ray wavelengths) will be needed to assess the dynamical state of this cluster.

Coordinates (J2000) and spectroscopic redshifts of galaxies in the field of eMACSJ1248.2+0743.

	R.A. (deg)	Dec (deg)	z
	192.0204	7.7462	0.5483
	192.0330	7.6780	0.5680
	192.0403	7.7102	0.5866
	192.0463	7.7512	0.5292
	192.0489	7.6988	0.6389
	192.0566	7.7637	0.5305
	192.0584	7.7216	0.5828
	192.0591	7.7465	0.5661
	192.0592	7.7106	0.5712
	192.0606	7.7488	0.5752
	192.0685	7.6689	0.5682
	192.0690	7.7616	0.5734
	192.0691	7.7193	1.2713
B	192.0695	7.7161	0.5749
	192.0697	7.7082	2.0949
	192.0710	7.7223	0.5799
	192.0723	7.7553	0.5746
	192.0724	7.6845	0.5731
	192.0736	7.7424	0.5681
	192.0737	7.6920	0.6410
	192.0745	7.6763	0.6404
	192.0748	7.7400	0.5718
	192.0756	7.7143	1.6167

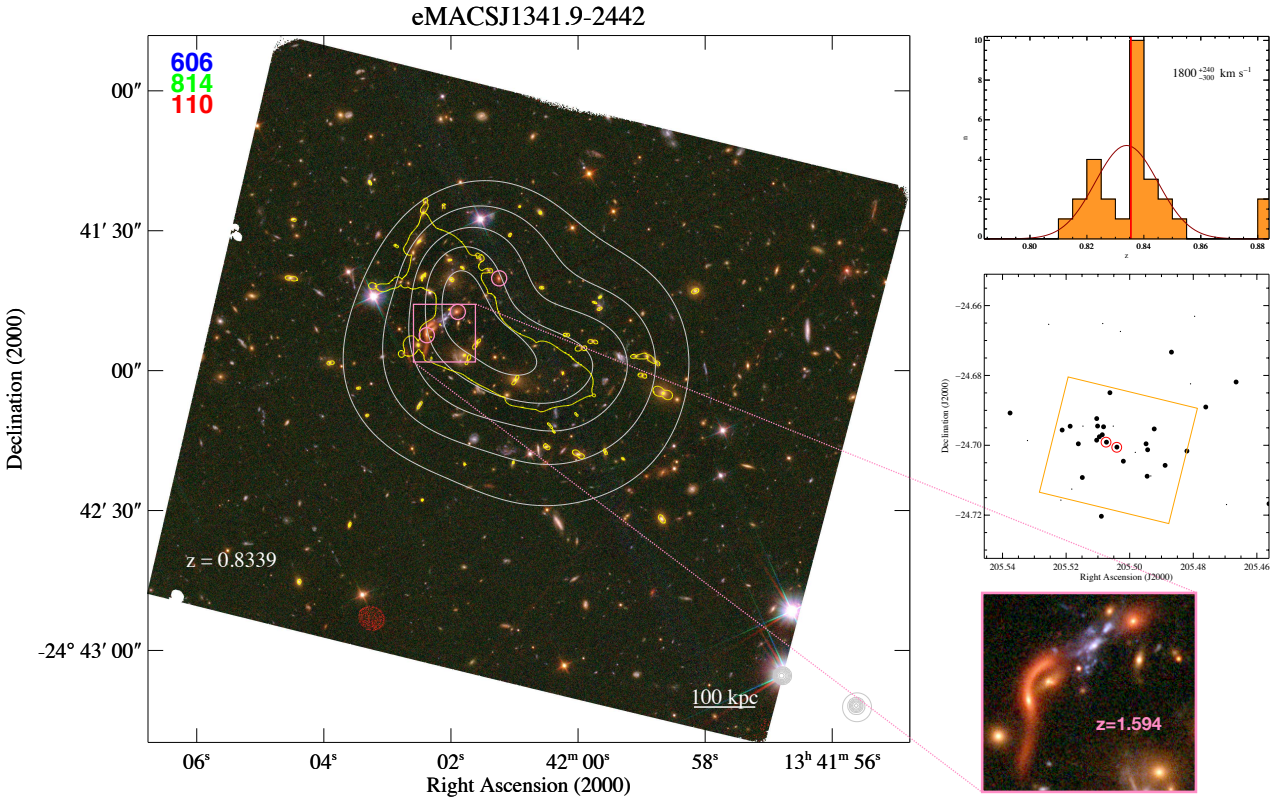

Figure B29. eMACSJ1341.9−2442. The highlighted highly magnified multiple-image system of a quiescent background galaxy at $z = 1.594$ is discussed in detail in Ebeling et al. (2018); the shown critical line for lensing of a background source at $z = 2$ is based on constraints from numerous additional strong-lensing constraints obtained from deep follow-up observations with MUSE and analyzed by Man et al. (in preparation). Non-concentric X-ray surface-brightness contours and a strongly bimodel redshift distribution identify eMACSJ1341.9 as an actively growing system.

Coordinates (J2000) and spectroscopic redshifts of galaxies in the field of eMACSJ1341.9-2442.

R.A. (deg)	Dec (deg)	z	R.A. (deg)	Dec (deg)	z
205.4562	−24.7167	0.8535	205.5095	−24.6976	0.8491
205.4665	−24.6819	0.8379	205.5099	−24.6978	1.5960
205.4696	−24.7170	0.3179	205.5101	−24.6945	0.8124
205.4761	−24.6890	0.8396	205.5104	−24.6924	0.8360
205.4796	−24.6631	0.8840	205.5104	−24.6985	0.8341
205.4809	−24.6824	0.7174	205.5147	−24.6945	1.8358
205.4820	−24.7017	0.8365	205.5149	−24.7092	0.8355
205.4869	−24.6733	0.8417	205.5162	−24.6996	0.8376
205.4889	−24.7058	0.8281	205.5182	−24.7125	0.7229
205.4923	−24.6953	0.8460	205.5187	−24.6945	0.8443
205.4934	−24.7088	3.2600	205.5212	−24.6956	0.8227
205.4944	−24.7013	0.8275	205.5216	−24.7157	0.7237
205.4945	−24.7089	0.8372	205.5255	−24.6654	0.5566
205.4949	−24.6996	0.8225	205.5322	−24.6986	0.8854
205.4982	−24.7020	1.2162	205.5376	−24.6908	0.8419
205.5020	−24.7046	0.8186	205.5457	−24.7101	0.8838
205.5029	−24.6674	0.4268			
205.5040	−24.7005	0.8353			
205.5052	−24.6945	1.5960			
205.5062	−24.6849	0.8220			
B 205.5073	−24.6991	0.8356			
205.5082	−24.6947	0.8157			
205.5085	−24.6651	0.6218			
205.5086	−24.6970	0.8222			
205.5089	−24.7203	0.8390			

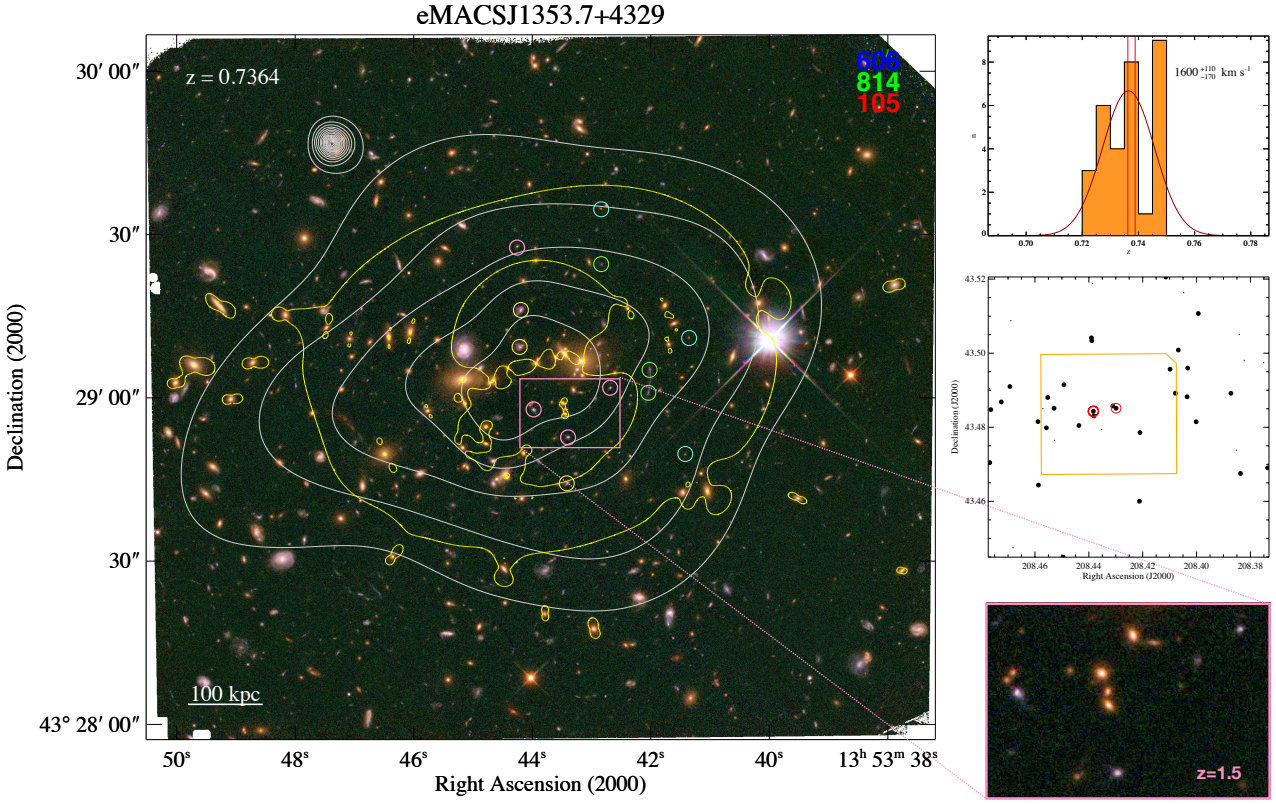

Figure B30. eMACSJ1353.7+4329 is not only one of the most X-ray luminous eMACS clusters (Table 3) but, considering the uncertainty surrounding eMACSJ1212.5 (Fig. 8), also the most powerful gravitational lens among those analysed to date (Table 2). Our current understanding of the system, complex both in projection on the plane of the sky and along our line of sight, is discussed in more detail in Section 5.4.

Coordinates (J2000) and spectroscopic redshifts of galaxies in the field of eMACSJ1353.7+4329.

R.A. (deg)	Dec (deg)	z	R.A. (deg)	Dec (deg)	z
208.3736	43.4690	0.7332	208.4390	43.5041	0.7360
208.3751	43.4974	0.5710	208.4437	43.4805	0.7408
208.3823	43.4981	0.5738	208.4493	43.4915	0.7236
208.3837	43.4675	0.7354	208.4495	43.4449	0.7464
208.3841	43.5051	0.6484	208.4527	43.4765	0.8130
208.3852	43.4738	0.6502	208.4529	43.4851	0.7494
208.3872	43.4892	0.7396	208.4553	43.4880	0.7489
208.3993	43.5107	0.7308	208.4558	43.4798	0.7480
208.4002	43.4815	0.7264	208.4571	43.4850	0.6503
208.4033	43.4960	0.7226	208.4587	43.4644	0.7292
208.4035	43.4882	0.7294	208.4589	43.4815	0.7465
208.4048	43.5163	0.5094	208.4681	43.4475	1.0138
208.4068	43.5009	0.7299	208.4689	43.5088	0.6577
208.4079	43.4892	0.7485	208.4693	43.4910	0.7480
208.4098	43.4957	0.7290	208.4725	43.4868	0.7361
208.4114	43.5206	0.7252	208.4764	43.4848	0.7453
208.4210	43.4786	0.7335	208.4768	43.4705	0.7378
208.4212	43.4600	0.7305	208.4769	43.4904	0.8116
208.4299	43.4851	0.7362			
208.4311	43.4858	0.7486			
208.4352	43.4794	0.6589			
208.4381	43.4831	0.7357			
B 208.4383	43.4843	0.7388			
208.4386	43.5188	0.9264			
208.4389	43.5034	0.7229			

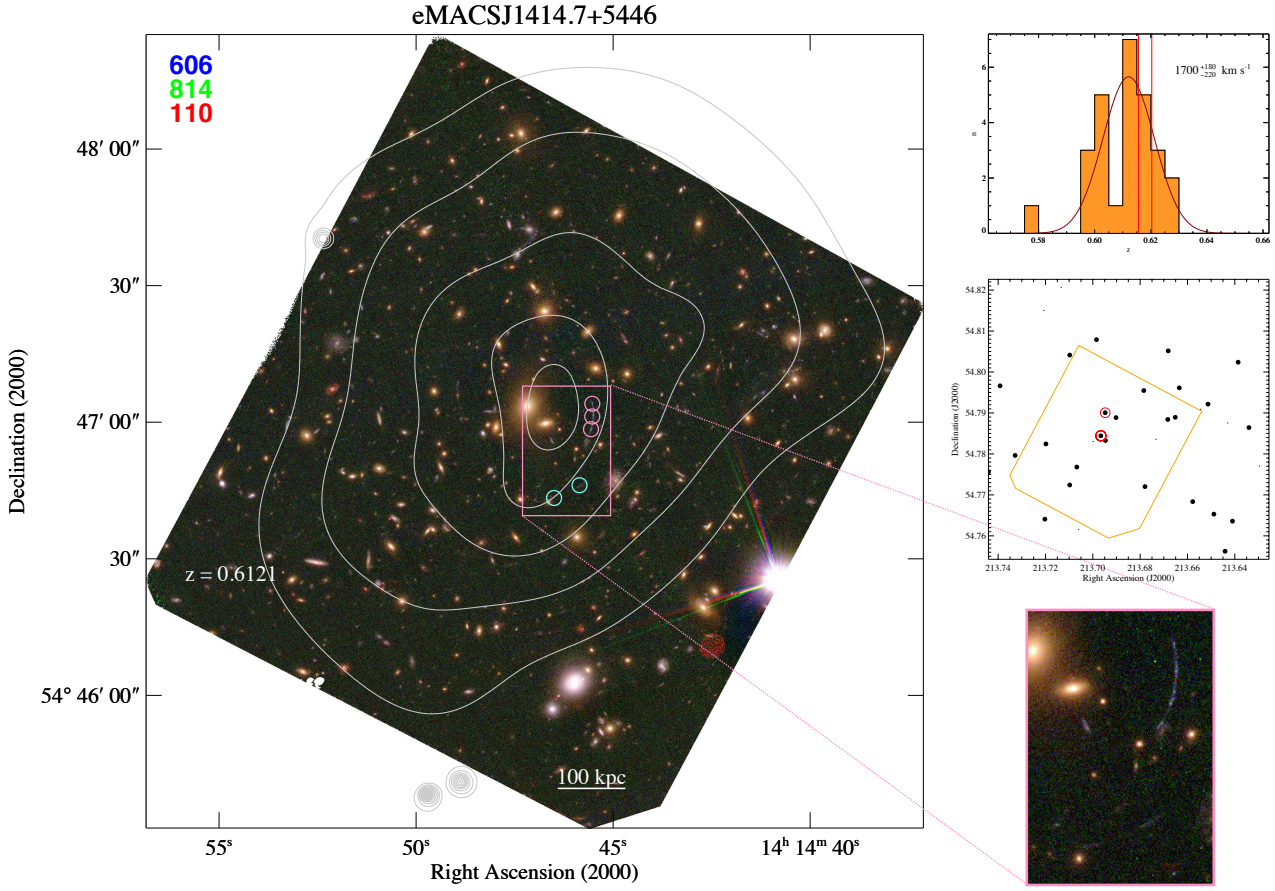

Figure B31. Although several (faint) strong-lensing features are readily discernible in the cluster core of eMACSJ1414.7+5446 (a zoomed-in view is shown on the bottom right), we currently have no redshifts for them and are at present unable to derive a lens model for the mass distribution in this extremely X-ray luminous system. Our assessemnt of the available data is summarized in Section 5.4.

.

Coordinates (J2000) and spectroscopic redshifts of galaxies in the field of eMACSJ1414.7+5446.

R.A. (deg)	Dec (deg)	z	R.A. (deg)	Dec (deg)	z
213.6256	54.7924	0.2191	213.7068	54.7768	0.5979
213.6296	54.7771	0.7356	213.7098	54.7724	0.6153
213.6341	54.7864	0.6236	213.7098	54.8041	0.6049
213.6386	54.8024	0.6121	213.7134	54.8207	0.5785
213.6410	54.7636	0.6255	213.7198	54.7824	0.6129
213.6430	54.7876	0.3828	213.7203	54.7641	0.6132
213.6441	54.7562	0.6027	213.7207	54.8150	0.3819
213.6488	54.7653	0.6089	213.7328	54.7796	0.6128
213.6513	54.7921	0.6048	213.7392	54.7966	0.6171
213.6545	54.7909	0.3844	213.7441	54.7756	0.6132
213.6578	54.7684	0.6014			
213.6635	54.7961	0.6023			
213.6652	54.7889	0.5969			
213.6681	54.8052	0.6134			
213.6683	54.7884	0.5970			
213.6733	54.7836	0.8486			
213.6780	54.7720	0.6179			
213.6784	54.7955	0.6231			
213.6902	54.7889	0.6182			
213.6946	54.7833	0.6132			
213.6948	54.7901	0.6204			
B 213.6966	54.7844	0.6156			
213.6985	54.8079	0.6261			
213.6999	54.7830	0.8493			
213.7060	54.7616	0.5189			

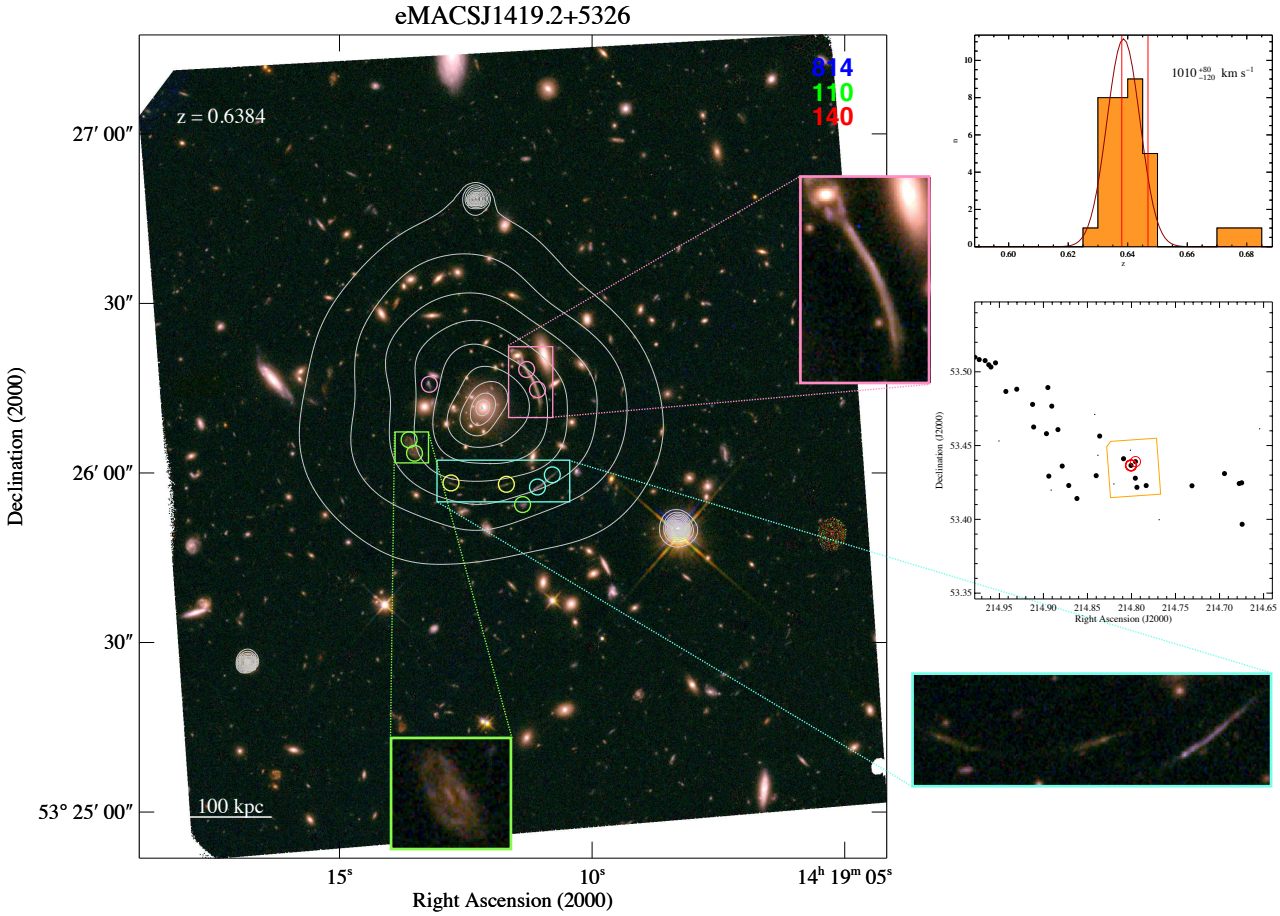

Figure B32. eMACSJ1419.2+5326, originally discovered in the eMACS pilot project (Ebeling et al. 2013), is one of very few eMACS clusters in the subset observed with *CXO* to date that appears to be fully relaxed. The X-ray surface-brightness contours above are based on an observation with ACIS-S and shown only for illustrative purposes – for the sake of uniformity, we have not included the underlying data in the X-ray analysis presented in this paper. Several multiple-image systems could be used to constrain a future lens model for this cluster.

Coordinates (J2000) and spectroscopic redshifts of galaxies in the field of eMACSJ1419.2+5326.

R.A. (deg)	Dec (deg)	z	R.A. (deg)	Dec (deg)	z
214.6400	53.3835	0.4673	214.8912	53.4198	0.6779
214.6545	53.4614	0.6808	214.8939	53.4293	0.6319
214.6743	53.3967	0.6411	214.8949	53.4893	0.6308
214.6749	53.4248	0.6451	214.8966	53.4581	0.6361
214.6777	53.4243	0.6455	214.9111	53.4626	0.6374
214.6944	53.4310	0.6409	214.9123	53.4779	0.6415
214.7313	53.4228	0.6408	214.9303	53.4882	0.6410
214.7685	53.3998	0.5743	214.9426	53.4867	0.6348
214.7833	53.4229	0.6462	214.9505	53.4531	0.6746
214.7938	53.4217	0.6391	214.9544	53.5060	0.6278
214.7955	53.4391	0.6468	214.9596	53.5032	0.6310
214.7956	53.4279	0.6411	214.9621	53.5048	0.6326
B 214.8005	53.4365	0.6380	214.9662	53.5076	0.6349
X 214.8011	53.4468	2.0027	214.9729	53.5083	0.6426
214.8090	53.4411	0.6440	214.9780	53.5099	0.6389
X 214.8200	53.4240	1.0907			
X 214.8361	53.4564	0.6303			
214.8381	53.4434	0.7220			
214.8401	53.4296	0.6430			
214.8416	53.4711	0.5571			
214.8619	53.4141	0.6377			
214.8712	53.4229	0.6351			
214.8787	53.4361	0.6347			
214.8835	53.4608	0.6359			
214.8905	53.4767	0.6450			

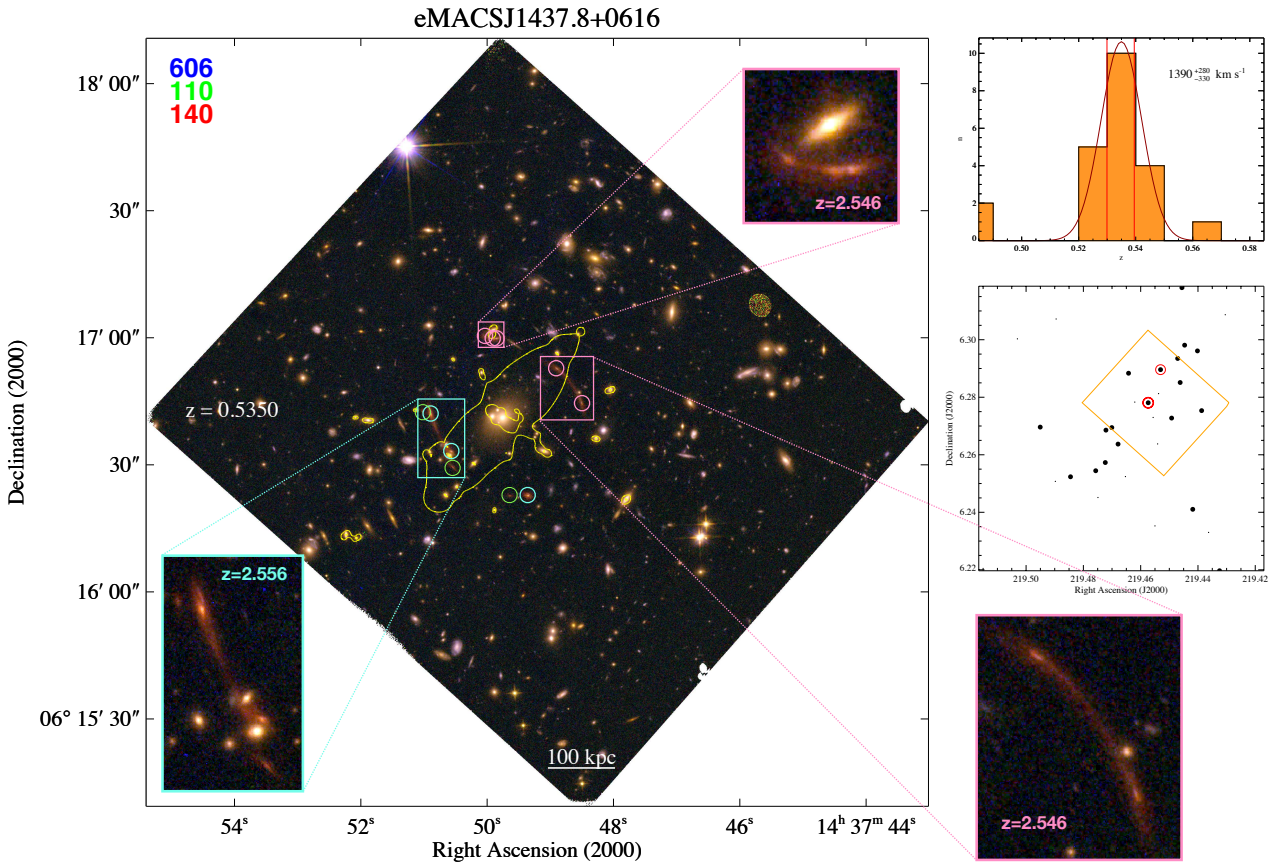

Figure B33. The lens model for eMACSJ1437.8+0616 is well constrained by three multiple-image systems, two of which are spectroscopically confirmed to be at the same redshift, making this cluster the (so far) only one in the eMACS sample to lens an identifiable background structure (see also Fig. 5). The large ellipticity of the single mass halo of the lens model, in conjunction with the high observed cluster velocity dispersion, suggests that eMACSJ1437.8 is a post-collision merger, well on its way to relaxation.

Coordinates (J2000) and spectroscopic redshifts of galaxies in the field of eMACSJ1437.8+0616.

R.A. (deg)	Dec (deg)	z	R.A. (deg)	Dec (deg)	z
219.4305	6.3087	0.5635	219.4749	6.2451	0.4061
219.4325	6.2197	0.5436	219.4757	6.2544	0.5329
219.4363	6.2330	0.4294	219.4845	6.2523	0.5364
219.4387	6.2753	0.5279	219.4895	6.3072	0.4845
219.4402	6.2961	0.5342	219.4898	6.2507	0.4057
219.4418	6.2410	0.5331	219.4951	6.2696	0.5313
219.4447	6.2981	0.5341	219.5030	6.3003	0.4841
219.4456	6.3181	0.5410			
219.4462	6.2851	0.5443			
219.4471	6.2935	0.5298			
219.4492	6.2728	0.5387			
219.4531	6.2896	0.5299			
219.4538	6.2813	2.5460			
219.4541	6.2638	0.4201			
219.4550	6.2353	0.4525			
219.4556	6.2730	2.5560			
B 219.4574	6.2781	0.5395			
219.4621	6.2783	2.5560			
219.4642	6.2883	0.5401			
219.4653	6.2524	0.4059			
219.4679	6.2637	0.5250			
219.4690	6.3186	0.4202			
219.4701	6.2695	0.5363			
219.4721	6.2686	0.5253			
219.4723	6.2573	0.5394			

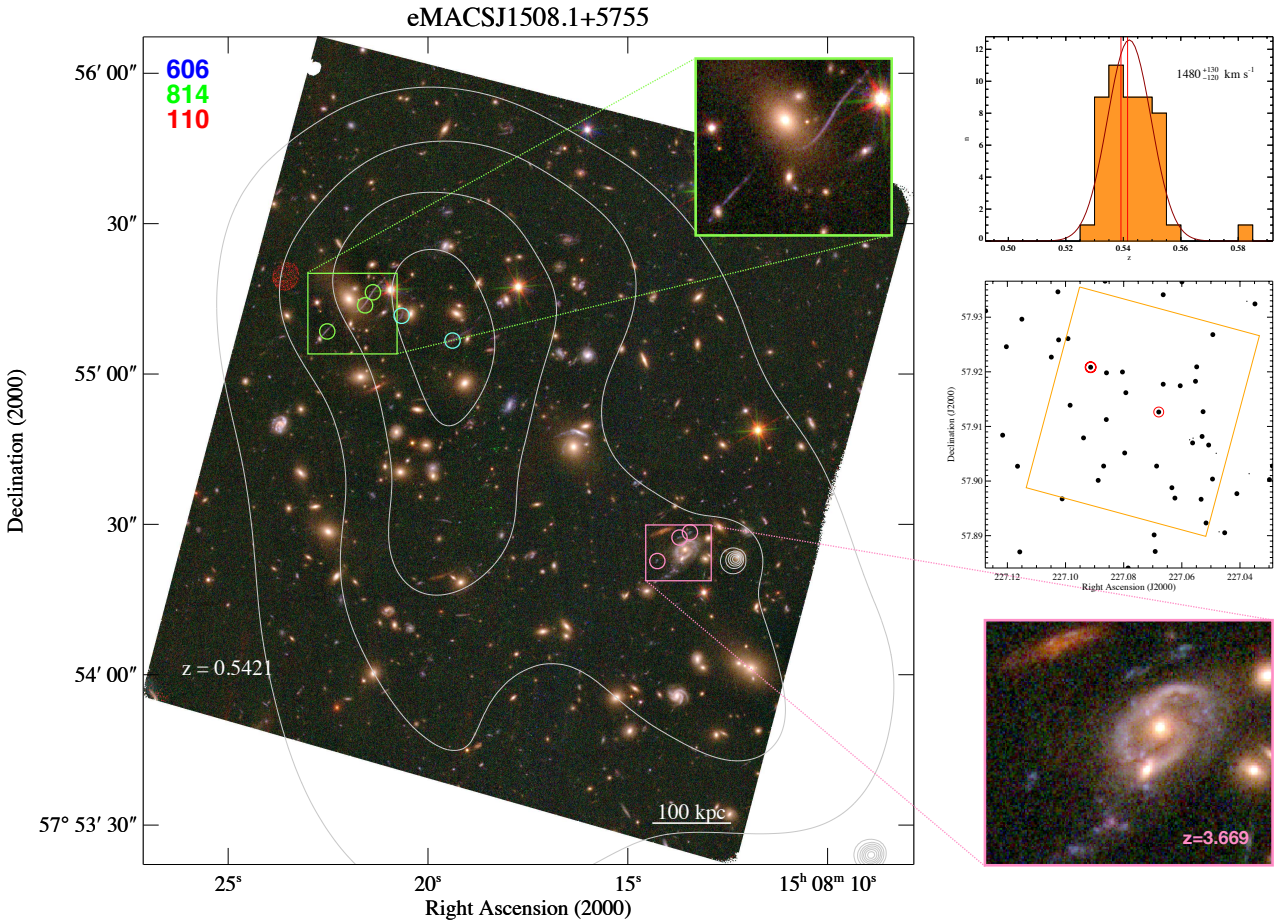

Figure B34. One of the most morphologically disturbed systems in the eMACS sample, eMACSJ1508.1+5755 features multiple optical cores and a highly irregular X-ray surface-brightness distribution whose peaks do not align with any of the galaxy concentrations. A high X-ray luminosity and high ICM temperature (Table 3), as well as a very high cluster velocity dispersion, all support the notion that eMACSJ1508.1 is observed during a major merger event. Although one multiple-image system has been spectroscopically confirmed, it provides insufficient constraints for a credible mass model until redshifts can be secured for the marked strong-lensing features in the NW component of this system.

Coordinates (J2000) and spectroscopic redshifts of galaxies in the field of eMACSJ1508.1+5755.

R.A. (deg)	Dec (deg)	z	R.A. (deg)	Dec (deg)	z	R.A. (deg)	Dec (deg)	z
227.0288	57.9027	0.5487	227.0664	57.9341	0.5363	227.1165	57.9027	0.5348
227.0299	57.9003	0.5263	R 227.0664	57.9177	0.5328	227.1204	57.9246	0.5470
227.0349	57.9324	0.5525	227.0679	57.9126	0.5415	227.1216	57.9084	0.5341
227.0368	57.9013	1.6722	227.0687	57.9027	0.5410	227.1275	57.9312	0.5471
227.0376	57.9329	0.5828	227.0692	57.8871	0.5423			
227.0411	57.8977	0.5372	227.0695	57.8901	0.5408			
227.0453	57.8905	0.5476	227.0785	57.8841	0.5381			
227.0472	57.8907	0.4197	227.0793	57.9162	0.5380			
227.0482	57.9051	2.1840	227.0797	57.9051	0.5546			
227.0493	57.9268	0.5538	227.0804	57.9200	0.5466			
227.0494	57.9004	0.5391	227.0859	57.9198	0.5425			
X 227.0508	57.9066	0.5520	227.0860	57.9113	0.5332			
227.0517	57.8923	0.5329	227.0864	57.9366	0.5382			
227.0527	57.9127	0.5452	227.0869	57.9027	0.5450			
227.0530	57.9082	0.5422	227.0888	57.9001	0.5354			
227.0534	57.8967	0.5493	B 227.0914	57.9208	0.5392			
227.0549	57.9209	0.5534	227.0938	57.9079	0.5381			
227.0553	57.9183	0.5470	R 227.0984	57.9139	0.5504			
227.0561	57.9079	3.6680	227.0992	57.9261	0.5419			
R 227.0563	57.9070	0.5548	227.1012	57.8967	0.5345			
227.0573	57.9076	3.6690	227.1024	57.9258	0.5505			
227.0600	57.9365	0.5347	227.1026	57.9346	0.5405			
227.0605	57.9174	0.5552	227.1049	57.9227	0.5364			
227.0624	57.8969	0.5338	227.1150	57.9296	0.5480			
227.0634	57.8988	0.5373	227.1157	57.8870	0.5332			

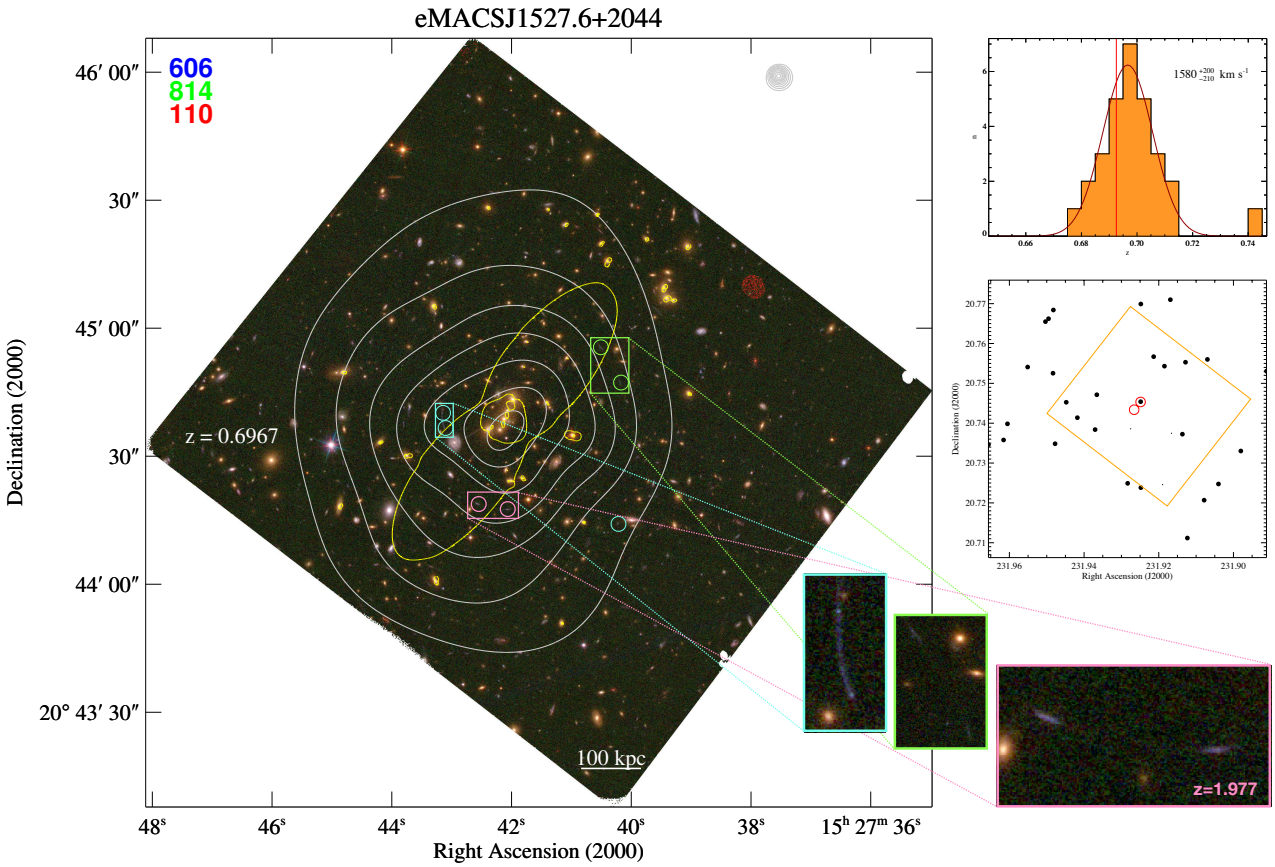

Figure B35. eMACSJ1527.6+2044 is one of the ten most X-ray luminous clusters in the subset of eMACS clusters observed with *CXO* today and, as such, discussed in more detail in Section 5.4. Although several multiple-image systems are readily identified, their faintness has so far stymied our attempts to secure a spectroscopic redshift for all but one of them.

Coordinates (J2000) and spectroscopic redshifts of galaxies in the field of eMACSJ1527.6+2044.

R.A. (deg)	Dec (deg)	z	R.A. (deg)	Dec (deg)	z
231.8912	20.7531	0.6912	231.9495	20.7662	0.7019
231.8980	20.7330	0.6981	231.9503	20.7655	0.7062
231.9040	20.7248	0.7053	231.9551	20.7541	0.7027
231.9070	20.7560	0.6849	231.9605	20.7398	0.7044
231.9078	20.7207	0.7088	231.9616	20.7358	0.6999
231.9123	20.7112	0.7110	231.9656	20.7346	0.6943
231.9128	20.7553	0.6913			
231.9137	20.7372	0.6841			
231.9166	20.7375	0.4828			
231.9169	20.7710	0.6939			
231.9185	20.7543	0.6950			
231.9190	20.7246	0.7400			
231.9214	20.7567	0.6952			
231.9248	20.7699	0.6951			
231.9248	20.7238	0.6983			
B 231.9249	20.7454	0.6926			
231.9275	20.7386	1.9770			
231.9283	20.7249	0.6874			
231.9366	20.7471	0.6755			
231.9370	20.7384	0.6856			
231.9418	20.7414	0.6958			
231.9448	20.7453	0.7110			
231.9478	20.7348	0.7012			
231.9482	20.7684	0.7026			
231.9483	20.7525	0.6880			

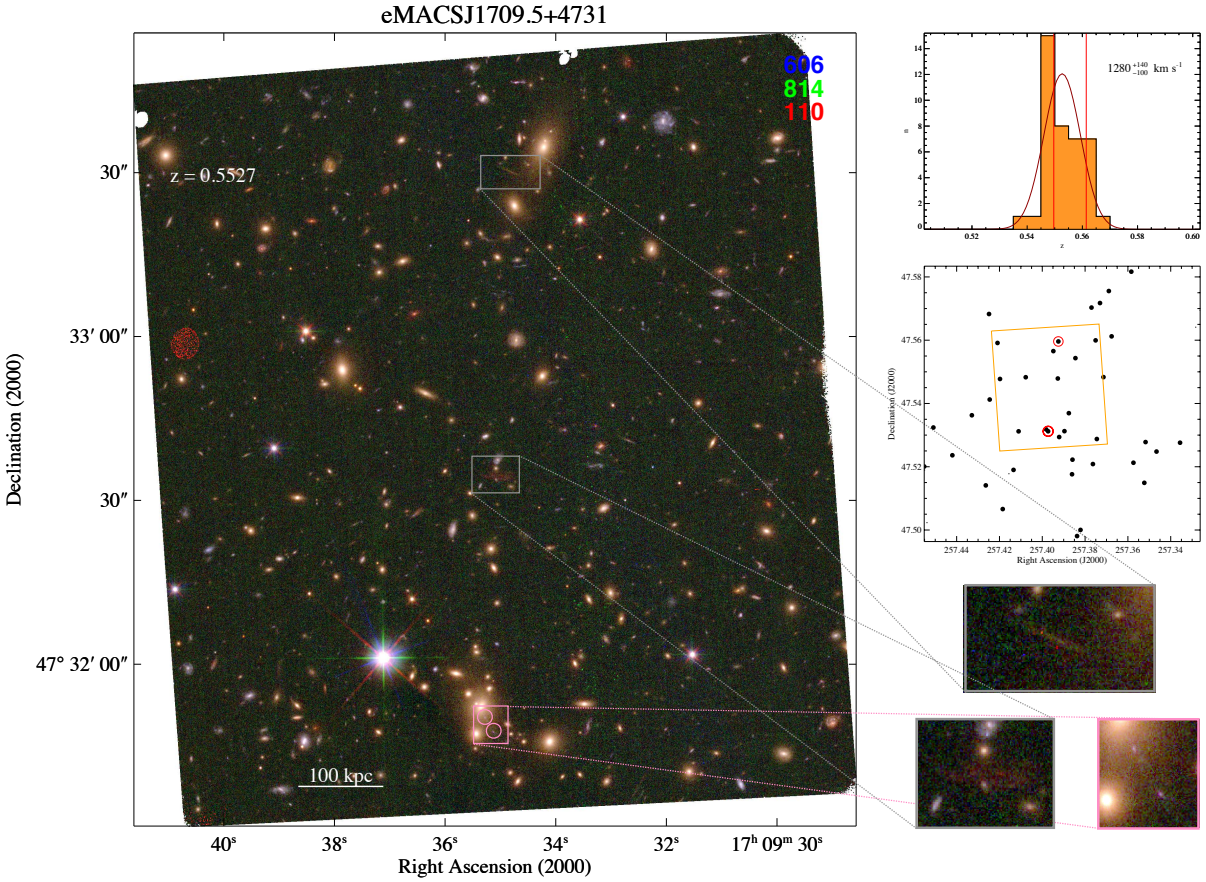

Figure B36. eMACSJ1709.5+4731 is an obvious double cluster and most likely observed in the pre-collision phase of a major merger. Little else can be said in the absence of *CXO* data and of spectroscopically confirmed strong-lensing features that would allow the construction of a lens model of the cluster mass distribution.

Coordinates (J2000) and spectroscopic redshifts of galaxies in the field of eMACSJ1709.5+4731.

R.A. (deg)	Dec (deg)	z	R.A. (deg)	Dec (deg)	z
257.3262	47.5694	0.4665	257.3927	47.5479	0.5618
257.3283	47.5641	0.4808	257.3948	47.5565	0.5566
257.3356	47.5276	0.5514	B 257.3973	47.5312	0.5497
257.3466	47.5248	0.5492	257.3982	47.5318	0.5510
257.3518	47.5278	0.5610	257.4077	47.5483	0.5616
257.3523	47.5149	0.5451	257.4111	47.5312	0.5457
257.3574	47.5213	0.5499	257.4134	47.5190	0.5590
257.3584	47.5817	0.5489	257.4156	47.5178	0.4955
257.3676	47.5612	0.5519	257.4185	47.5066	0.5508
257.3689	47.5755	0.5471	257.4198	47.5477	0.5554
257.3714	47.5483	0.5653	257.4209	47.5591	0.5549
257.3730	47.5717	0.5605	257.4246	47.5412	0.5492
257.3745	47.5288	0.5608	257.4249	47.5683	0.5461
257.3751	47.5599	0.5598	257.4264	47.5141	0.5515
257.3763	47.5208	0.5481	257.4329	47.5363	0.5465
257.3770	47.5703	0.5607	257.4420	47.5236	0.5390
257.3821	47.5000	0.5486	257.4509	47.5324	0.5515
257.3837	47.4981	0.5510	257.4539	47.5023	0.4246
257.3845	47.5543	0.5570	257.4550	47.5190	0.4806
257.3859	47.5222	0.5482	257.4552	47.5201	0.5596
257.3861	47.5176	0.5443			
257.3876	47.5369	0.5577			
257.3896	47.5312	0.5489			
257.3921	47.5294	0.5450			
257.3925	47.5596	0.5614			

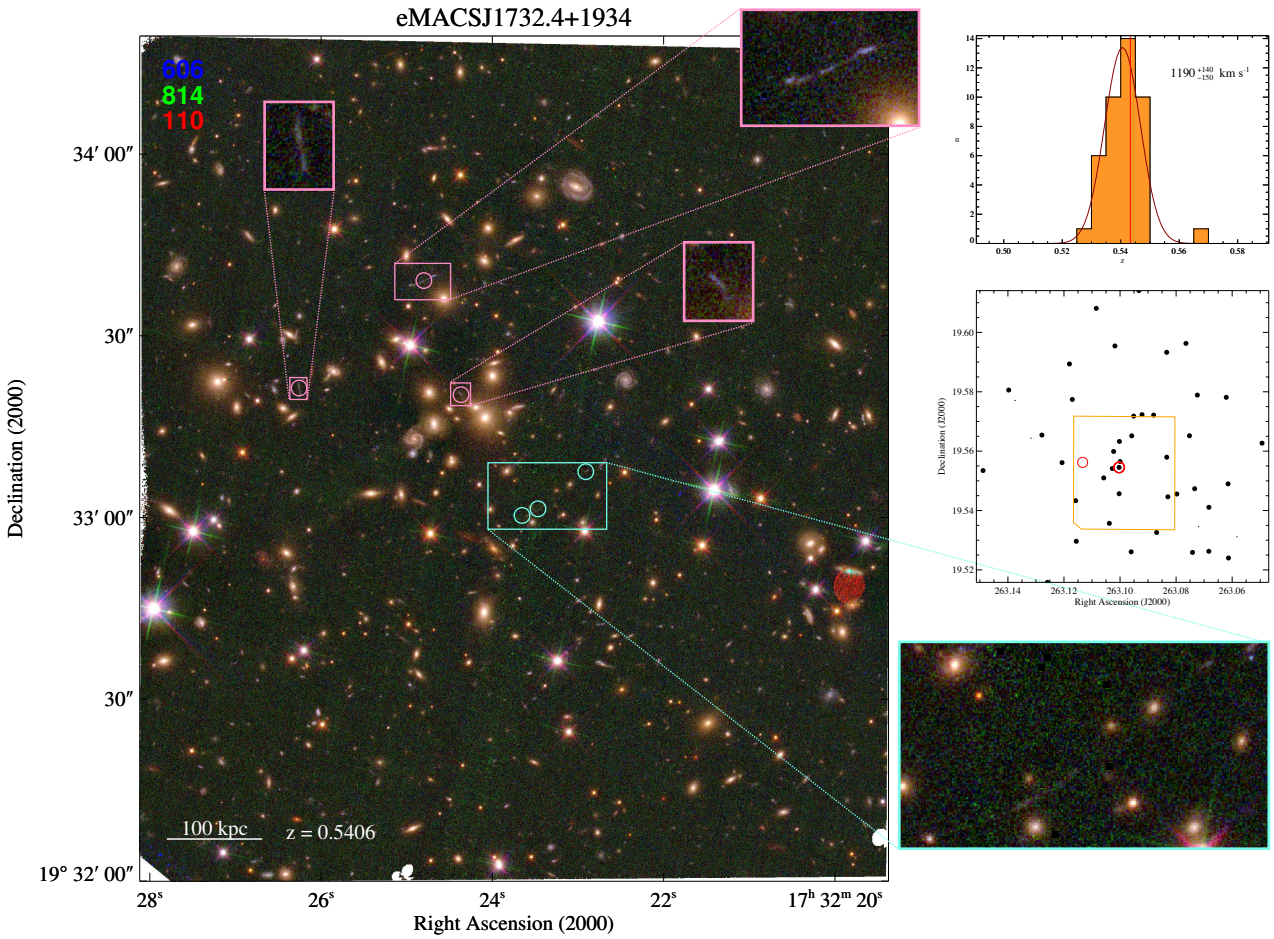

Figure B37. Lacking *CXO* data and redshifts for any of the numerous strong-lensing fetures highlighted above, we can base our assessment of eMACSJ1732.4+1934 on little more than its optical appearance which suggests an extremely extended system in a period of active growth that likely involves several groups and clusters of galaxies.

Coordinates (J2000) and spectroscopic redshifts of galaxies in the field of eMACSJ1732.4+1934.

R.A. (deg)	Dec (deg)	z	R.A. (deg)	Dec (deg)	z
263.0493	19.5627	0.5400	263.1002	19.5633	0.5368
263.0583	19.5311	0.4807	263.1003	19.5457	0.5486
263.0613	19.5240	0.5449	B 263.1003	19.5545	0.5433
263.0615	19.5490	0.5393	263.1018	19.5954	0.5470
263.0621	19.5781	0.5428	263.1023	19.5599	0.5333
263.0683	19.5411	0.5404	263.1028	19.5541	0.5293
263.0683	19.5263	0.5486	263.1038	19.5357	0.5419
263.0720	19.5345	0.5674	263.1058	19.5510	0.5367
263.0724	19.5789	0.5354	263.1085	19.6081	0.5472
263.0734	19.5473	0.5432	263.1156	19.5296	0.5469
263.0741	19.5259	0.5473	263.1158	19.5433	0.5419
263.0752	19.5652	0.5404	263.1170	19.5774	0.5358
263.0765	19.5963	0.5430	263.1181	19.5894	0.5425
263.0797	19.5456	0.5475	263.1207	19.5561	0.5349
263.0829	19.5446	0.5358	263.1259	19.5158	0.5386
263.0833	19.5580	0.5305	263.1279	19.5654	0.5362
263.0834	19.5933	0.5401	263.1317	19.5644	0.6384
263.0869	19.5326	0.5470	263.1374	19.5771	0.6425
263.0880	19.5721	0.5402	263.1397	19.5806	0.5418
263.0922	19.5723	0.5468	263.1489	19.5535	0.5321
263.0933	19.6141	0.5457			
263.0951	19.5718	0.5431			
263.0958	19.5652	0.5311			
263.0960	19.5261	0.5318			
263.1000	19.5565	0.5392			

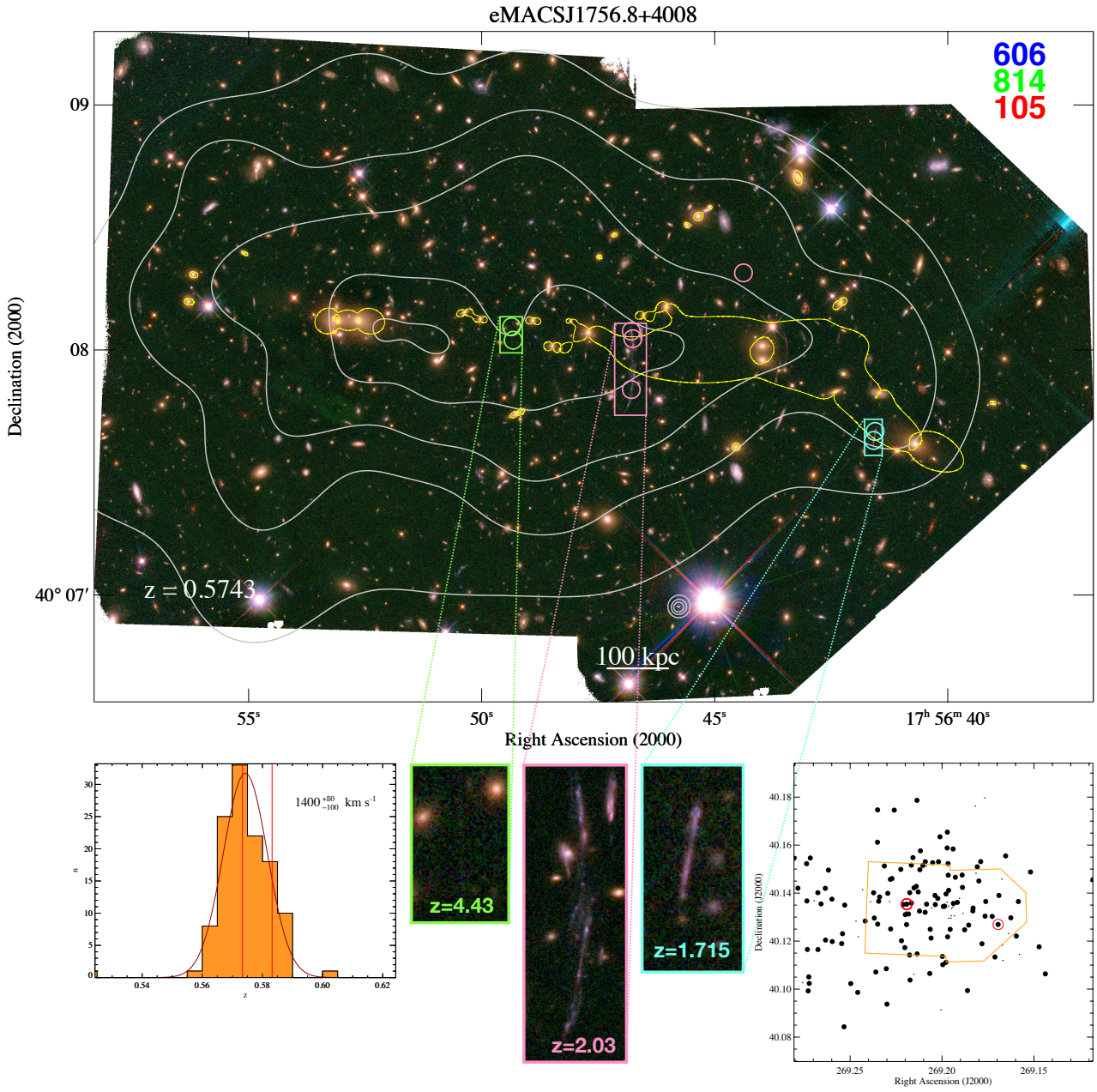

Figure B38. eMACSJ1756.8+4008 is the most extended actively merging cluster in the eMACS sample (to date) and the fourth-most X-ray luminous of the subset observed with *COX* (see Section 5.4 for a more in-depth discussion). Our lens model remains incomplete pending the identification of strong-lensing features in the East that could constrain what is likely to be the dominant mass component of this extreme merger.

Coordinates (J2000) and spectroscopic redshifts of galaxies in the field of eMACSJ1756.8+4008.

R.A. (deg)	Dec (deg)	z	R.A. (deg)	Dec (deg)	z	R.A. (deg)	Dec (deg)	z	R.A. (deg)	Dec (deg)	z	R.A. (deg)	Dec (deg)	z	R.A. (deg)
X 269.1179	40.1456	0.5862	269.1819	40.1763	0.7043	269.1970	40.1218	0.5802	269.2104	40.1515	0.5756	269.2224	40.1499	0.5689	269.2529
269.1438	40.1064	0.5671	269.1831	40.1338	0.5721	269.1971	40.1654	0.5858	269.2117	40.1576	0.5691	269.2260	40.1746	0.5742	269.2533
269.1472	40.1176	0.5843	269.1832	40.1326	0.5722	269.1972	40.1588	0.5661	269.2120	40.1498	0.5735	269.2272	40.1461	0.5695	269.2541
269.1519	40.1488	0.5848	269.1855	40.1267	0.5727	269.1973	40.1362	1.5500	269.2123	40.1325	0.5821	269.2280	40.1250	0.5670	269.2546
269.1579	40.1144	0.3719	269.1861	40.0994	0.5848	269.1978	40.1396	0.5676	269.2130	40.1405	0.5674	269.2281	40.1457	0.5864	269.2597
269.1585	40.1365	0.5712	269.1877	40.1247	0.5728	269.1979	40.1111	0.5628	269.2135	40.1147	0.5777	269.2285	40.1365	0.8939	269.2599
269.1596	40.1221	0.5702	269.1885	40.1315	1.0082	269.1986	40.1346	0.5679	269.2136	40.1786	0.5724	269.2295	40.1399	0.5782	269.2618
269.1626	40.1297	0.5646	269.1889	40.1424	0.5694	269.1993	40.1344	0.5687	269.2140	40.1428	0.5870	269.2300	40.0937	0.5799	269.2634
269.1639	40.1231	2.0558	269.1891	40.1475	0.5803	269.1996	40.1102	0.5759	269.2152	40.1422	0.5741	269.2303	40.1085	0.5742	269.2635
269.1654	40.1555	0.5631	269.1905	40.1378	0.4610	269.1998	40.1136	0.5734	269.2153	40.1061	0.6864	269.2314	40.1513	0.5692	269.2658
269.1669	40.1119	0.4145	269.1917	40.1361	0.5695	269.2005	40.0913	0.6359	269.2158	40.1548	0.5871	269.2339	40.1384	0.5766	269.2675
269.1672	40.1184	0.4244	269.1928	40.1466	0.5898	269.2011	40.1635	0.5630	269.2163	40.1366	0.9029	269.2345	40.1366	0.5783	269.2675
269.1675	40.1458	0.0923	269.1932	40.1306	0.8364	269.2019	40.1530	0.5821	269.2167	40.1358	0.5767	269.2350	40.1271	0.5861	269.2696
269.1690	40.1390	0.5682	269.1938	40.1357	0.5716	269.2023	40.1378	0.5679	269.2167	40.1517	0.5587	269.2351	40.1747	0.5736	269.2717
269.1695	40.1269	0.5832	269.1940	40.1584	0.5788	269.2037	40.1352	0.5824	269.2174	40.1038	0.5783	269.2351	40.1612	0.5603	269.2722
269.1712	40.1134	0.5818	269.1941	40.1342	1.3370	269.2038	40.1390	0.5866	269.2176	40.1402	0.5828	X 269.2360	40.1071	0.5752	269.2725
269.1727	40.1303	0.5661	269.1947	40.1336	1.3377	269.2051	40.1526	0.5739	269.2177	40.1142	0.5822	269.2369	40.1296	0.5859	269.2728
269.1762	40.1365	0.5750	269.1950	40.1306	1.3170	269.2056	40.1338	4.4326	269.2183	40.1313	0.5744	269.2382	40.1681	0.5783	269.2733
269.1766	40.1304	0.5658	269.1951	40.1295	2.0364	269.2060	40.1213	0.5737	B 269.2192	40.1354	0.5734	269.2389	40.1364	3.2670	269.2735
269.1768	40.1797	0.7163	269.1956	40.1249	0.5852	269.2064	40.1249	0.5705	269.2193	40.1269	0.5678	269.2418	40.1284	0.5657	269.2737
269.1783	40.1189	0.5701	269.1964	40.1346	1.1048	269.2067	40.1065	0.5674	269.2195	40.1322	0.8652	269.2432	40.1414	0.6905	269.2758

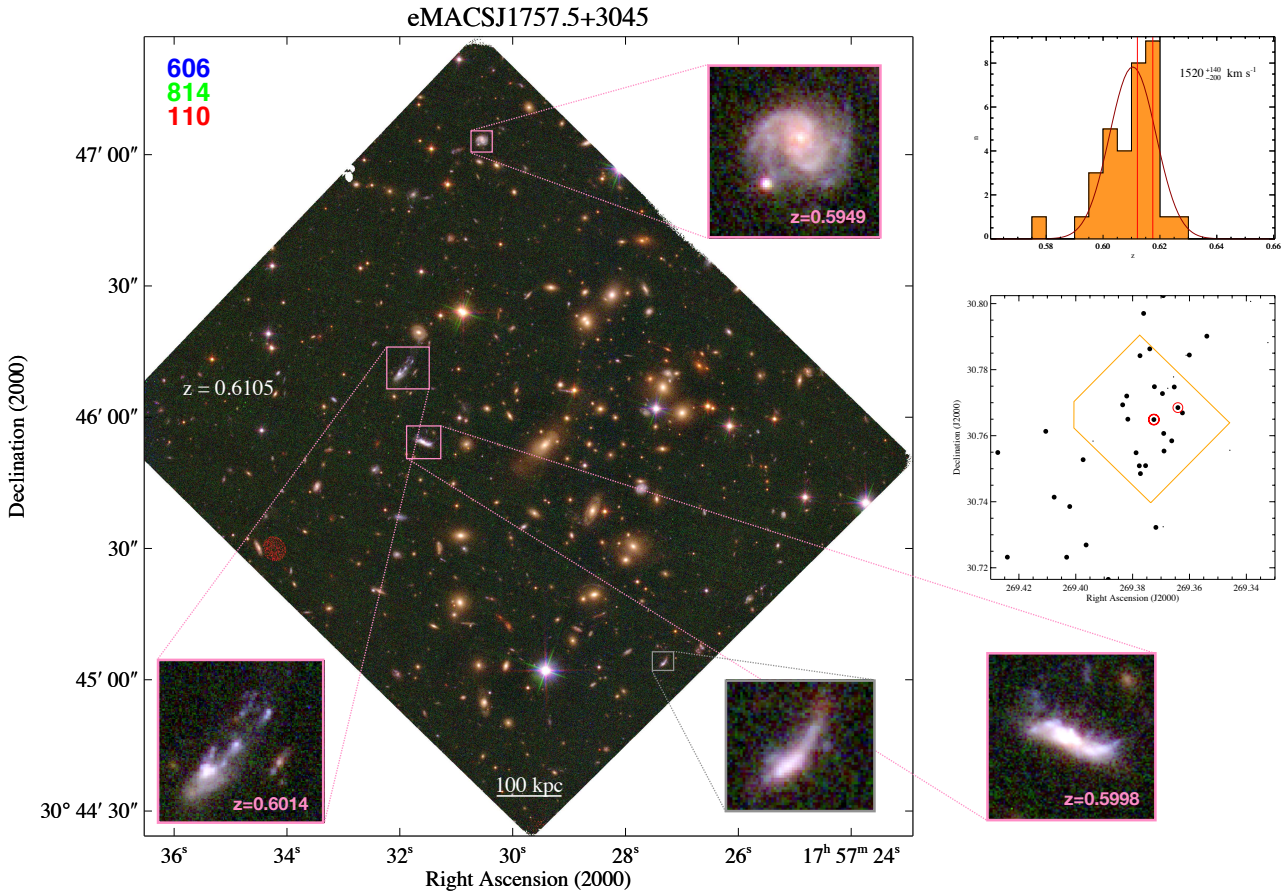

Figure B39. Another clearly unrelaxed cluster, eMACSJ1757.5+3045 currently has no *CXO* data or constraints on a lens model from multiple-image systems that could help shed light on the dynamics and geometry of the cluster's growth process. However, the morphology of several plausible candidates for galaxies undergoing ram-pressure stripping (Section 5.5.4), highlighted in insets above, point to a NW-to-SE direction of motion of galaxies relative to the ICM.

Coordinates (J2000) and spectroscopic redshifts of galaxies in the field of eMACSJ1757.5+3045.

R.A. (deg)	Dec (deg)	z	R.A. (deg)	Dec (deg)	z
269.3324	30.7882	0.4431	269.3776	30.7509	0.6113
269.3385	30.8007	0.3449	269.3788	30.7548	0.6258
269.3458	30.7556	0.4304	R 269.3817	30.7650	0.5998
269.3539	30.7901	0.6101	269.3821	30.7720	0.5957
269.3601	30.7844	0.6098	R 269.3835	30.7693	0.6014
269.3612	30.7844	0.4286	269.3886	30.7165	0.6156
269.3625	30.7669	0.6083	269.3939	30.7584	0.5773
269.3641	30.7685	0.6175	269.3964	30.7269	0.6028
269.3654	30.7748	0.5989	269.3974	30.7527	0.6192
269.3656	30.7778	1.0693	269.4021	30.7386	0.6127
269.3662	30.7584	0.6173	269.4032	30.7232	0.6154
269.3676	30.7744	0.4300	269.4076	30.7414	0.6054
269.3690	30.7554	0.6168	269.4106	30.7613	0.6025
269.3691	30.7607	0.6011	269.4241	30.7232	0.6135
269.3692	30.8024	0.6176	269.4274	30.7549	0.6046
269.3693	30.7324	0.7397			
269.3695	30.7728	0.6217			
269.3718	30.7322	0.6101			
269.3723	30.7748	0.6080			
B 269.3725	30.7649	0.6121			
269.3740	30.7863	0.6119			
269.3754	30.7509	0.6170			
269.3761	30.7970	0.6108			
269.3773	30.7485	0.6197			
R 269.3774	30.7842	0.5949			

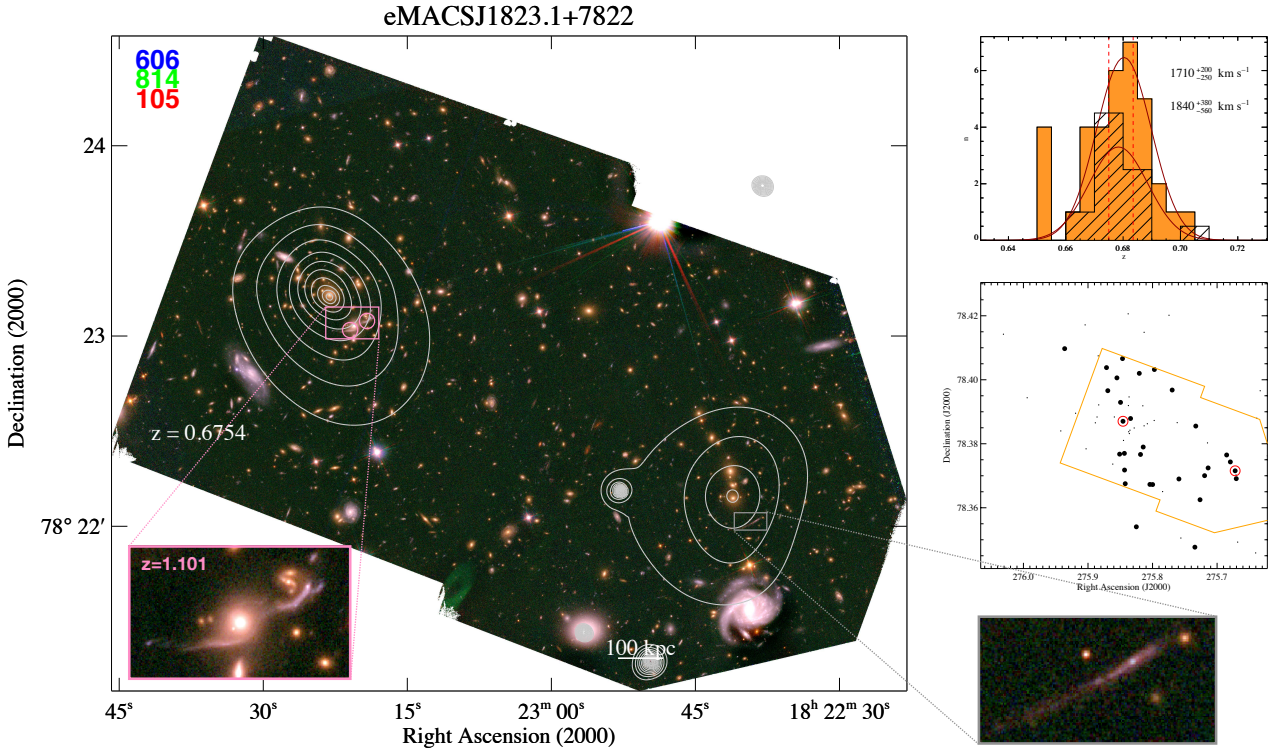

Figure B40. As is apparent from the relaxed X-ray morphologies of the (sub)clusters shown above, eMACSJ1823.1+7822 is a pre-collision merger (see also Section 5.5.2); the only one in the subset of eMACS clusters observed with *CXO*/ACIS-I to date. We therefore assign the galaxies with spectroscopic redshifts in this field to either cluster by using the perpendicular bisector of the line connecting the BCGs as a divider (solid and cross-hatched histograms above). Although a multiple-image system in the more X-ray luminous NW component has been spectroscopically confirmed , the strong impact of individual galaxies on its morphology renders it unsuitable to constrain the mass distribution of the cluster-scale mass halo. Both clusters are obviously collapsed entities (rather than projections effects); however, the combination of relatively low ICM tenperatures and high velocity dispersions suggests that both subclusters are only moderately massive and that the observed velocity dispersions are inflated by significant bulk motions along the line of sight.

Coordinates (J2000) and spectroscopic redshifts of galaxies in the field of eMACSJ1823.1+7822.

R.A. (deg)	Dec (deg)	z	R.A. (deg)	Dec (deg)	z	R.A. (deg)	Dec (deg)	z
275.6222	78.3762	0.6896	275.8041	78.3673	0.6782	275.8552	78.4006	0.6814
275.6332	78.3966	0.5659	275.8081	78.3863	0.6644	275.8592	78.3884	0.6883
275.6385	78.3880	0.5655	275.8130	78.4148	0.3690	275.8616	78.3736	0.6885
275.6402	78.3459	0.6874	275.8131	78.3856	0.6884	275.8693	78.3966	0.6786
275.6681	78.3493	0.6634	275.8145	78.3790	0.6747	275.8713	78.4038	0.6831
275.6703	78.3691	0.6733	275.8151	78.3919	0.6912	275.8834	78.3921	1.4202
275.6706	78.3703	0.6623	275.8186	78.3767	0.6696	275.8842	78.4075	0.4152
275.6720	78.3715	0.6750	275.8205	78.4020	0.6730	275.8860	78.3884	0.7034
275.6795	78.3743	0.6765	275.8251	78.3540	0.6671	275.8886	78.3865	0.6543
275.6852	78.3765	0.6711	275.8284	78.3849	1.1012	275.9030	78.3784	0.6542
275.7139	78.3724	0.6786	275.8341	78.3879	0.6762	275.9044	78.4172	0.6875
275.7149	78.3803	0.6865	275.8350	78.3842	0.4116	275.9192	78.3895	0.6659
X 275.7194	78.3700	0.6757	275.8359	78.3832	0.4103	275.9361	78.4097	0.6710
275.7264	78.3625	0.6760	275.8364	78.3946	0.6965	275.9421	78.3840	0.6518
275.7330	78.3855	0.6764	275.8369	78.3838	1.1013	275.9942	78.3944	0.6549
275.7344	78.3477	0.6752	275.8374	78.3919	0.5663	276.0310	78.4142	0.6177
275.7561	78.3505	0.6895	275.8377	78.4206	0.6923	276.0662	78.4255	0.4730
275.7592	78.3690	0.6841	275.8423	78.3675	0.6838			
275.7618	78.3866	0.4117	275.8434	78.3718	0.6791			
275.7696	78.3968	0.6670	275.8436	78.3770	0.6776			
275.7745	78.4202	0.5035	275.8450	78.3810	0.6866			
275.7844	78.3651	0.7033	B 275.8458	78.3870	0.6835			
275.7972	78.4032	0.6783	275.8465	78.4066	0.6722			
275.7975	78.3873	0.4131	275.8496	78.3929	0.6840			
275.7999	78.3673	0.6827	275.8510	78.3768	0.6813			

This paper has been typeset from a TEX/LATEX file prepared by the author.

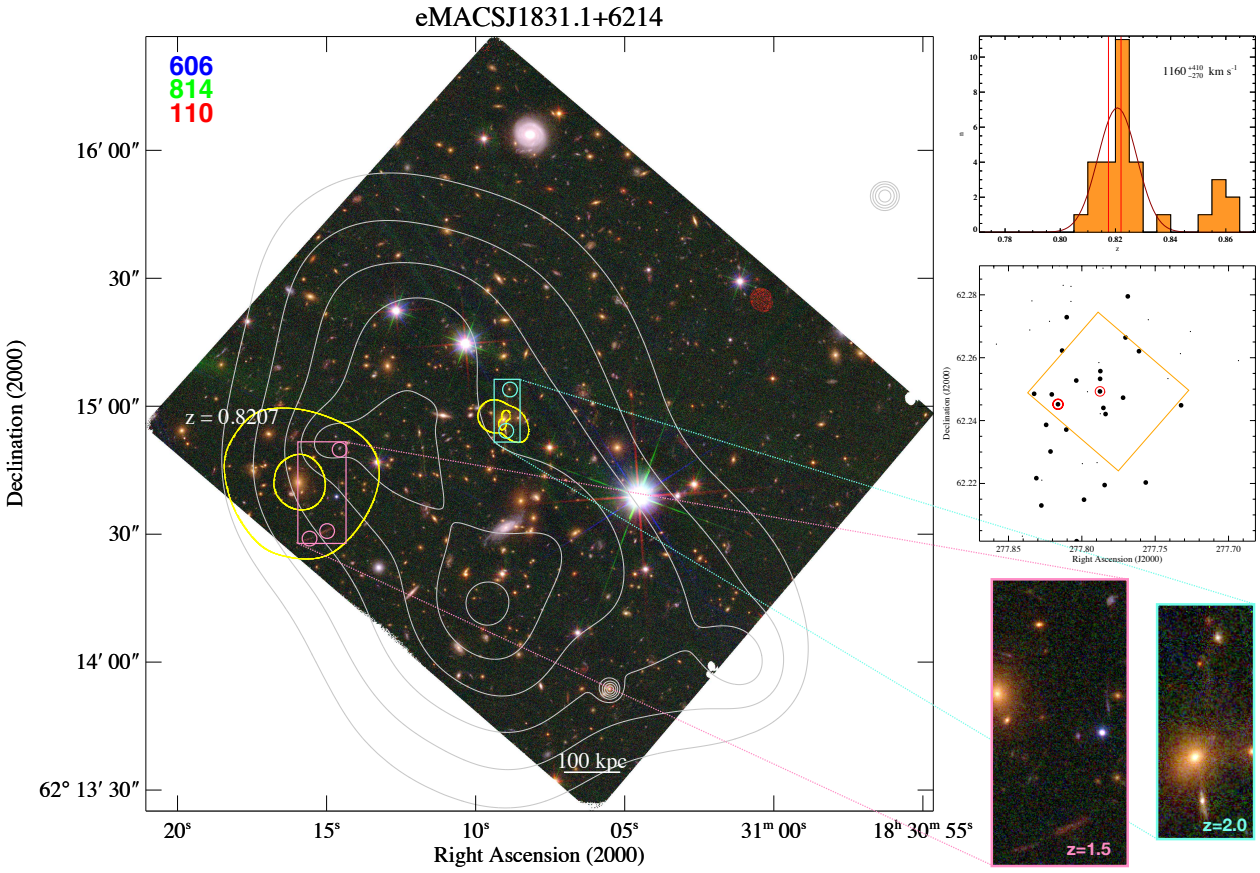

Figure B41. At $z = 0.82$, eMACSJ1831.1+6214 is one of the most distant eMACS clusters, extremely X-ray luminous, and a merger of at least two systems, as evidenced by the system's disturbed X-ray morphology and very high ICM temperature (Table 3). Although some strong-lensing constraints are available, the resulting tentative lens model clearly misses a significant part of the mass distribution in this complex merger. Note the presence of another structure in the background, visible in the radial-velocity histogram shown in the top right of this figure.

Coordinates (J2000) and spectroscopic redshifts of galaxies in the field of eMACSJ1831.1+6214.

R.A. (deg)	Dec (deg)	z	R.A. (deg)	Dec (deg)	z
277.6932	62.2591	0.6054	277.8036	62.2016	0.8229
277.7260	62.2683	0.5542	277.8038	62.2527	0.8105
277.7323	62.2449	0.8267	277.8074	62.2827	0.8522
277.7328	62.2613	0.7494	277.8074	62.2779	0.2206
277.7413	62.2534	0.6873	277.8103	62.2729	0.8139
277.7547	62.2721	0.6593	277.8106	62.2371	0.8087
277.7564	62.2203	0.8213	277.8127	62.2830	0.8580
277.7610	62.2621	0.8232	277.8134	62.2623	0.8125
277.7687	62.2795	0.8219	277.8154	62.2892	0.8605
277.7702	62.2664	0.8227	B 277.8163	62.2452	0.8175
277.7719	62.2473	0.8243	277.8205	62.2483	0.8238
277.7838	62.2421	0.8162	277.8214	62.2302	0.8185
277.7844	62.2491	2.1192	277.8220	62.2716	0.1565
277.7845	62.2195	0.8244	277.8243	62.2386	0.8293
277.7853	62.2440	0.8252	277.8273	62.2210	0.6577
277.7856	62.2885	0.8591	277.8276	62.2130	0.8113
277.7874	62.2557	0.8154	277.8310	62.2217	0.8257
277.7874	62.2422	0.2187	277.8325	62.2485	0.8201
277.7876	62.2533	0.8355	277.8340	62.2781	0.8619
277.7877	62.2493	0.8220	277.8355	62.2688	0.8562
277.7884	62.2585	0.6719	277.8405	62.2032	0.1032
277.7896	62.2266	0.6532	277.8582	62.2643	0.7060
277.7962	62.2492	0.4067			
277.7985	62.2148	0.8225			
277.7996	62.2263	0.5117			

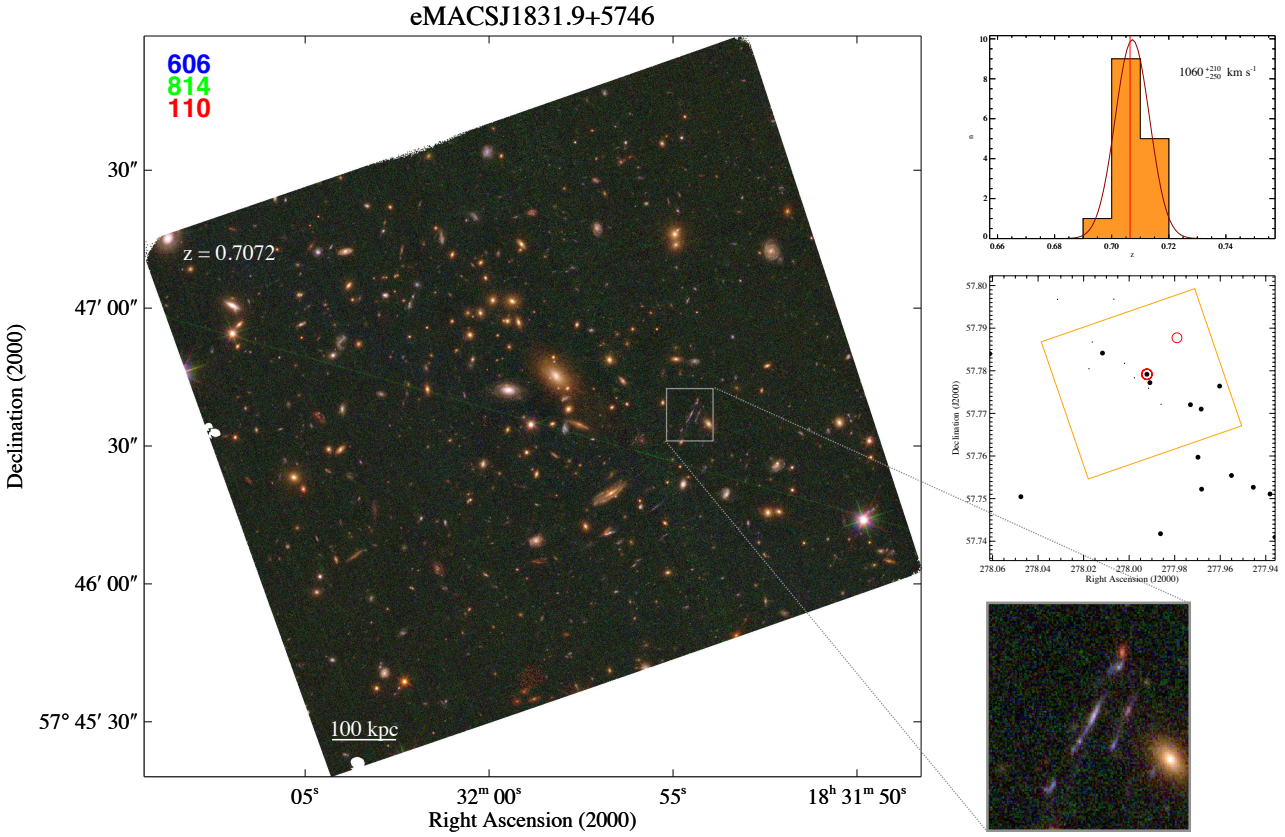

Figure B42. eMACSJ1831.9+5746. We currently have neither *CXO* data nor a lens model to characterize the physical properties of this system. A high velocity dispersion, single dominant BCG, and the presence of a prominent gravitational arc (highlighted above) suggest a massive, relatively relaxed cluster.

Coordinates (J2000) and spectroscopic redshifts of galaxies in the field of eMACSJ1831.9+5746.

R.A. (deg)	Dec (deg)	z
277.9359	57.7409	0.7099
277.9381	57.7511	0.7126
277.9455	57.7527	0.7040
277.9551	57.7554	0.7035
277.9603	57.7764	0.7160
277.9682	57.7522	0.7122
277.9684	57.7710	0.7078
277.9698	57.7597	0.7040
277.9731	57.7720	0.6930
277.9860	57.7721	0.8370
277.9862	57.7418	0.7120
277.9909	57.7772	0.7014
277.9915	57.7759	0.3541
B 277.9922	57.7792	0.7064
277.9977	57.7784	0.3530
278.0021	57.7818	0.5502
278.0067	57.7968	0.5569
278.0117	57.7842	0.7010
278.0162	57.7868	0.6096
278.0176	57.7805	0.3081
278.0315	57.7968	0.1862
278.0476	57.7505	0.7105
278.0612	57.7840	0.7086

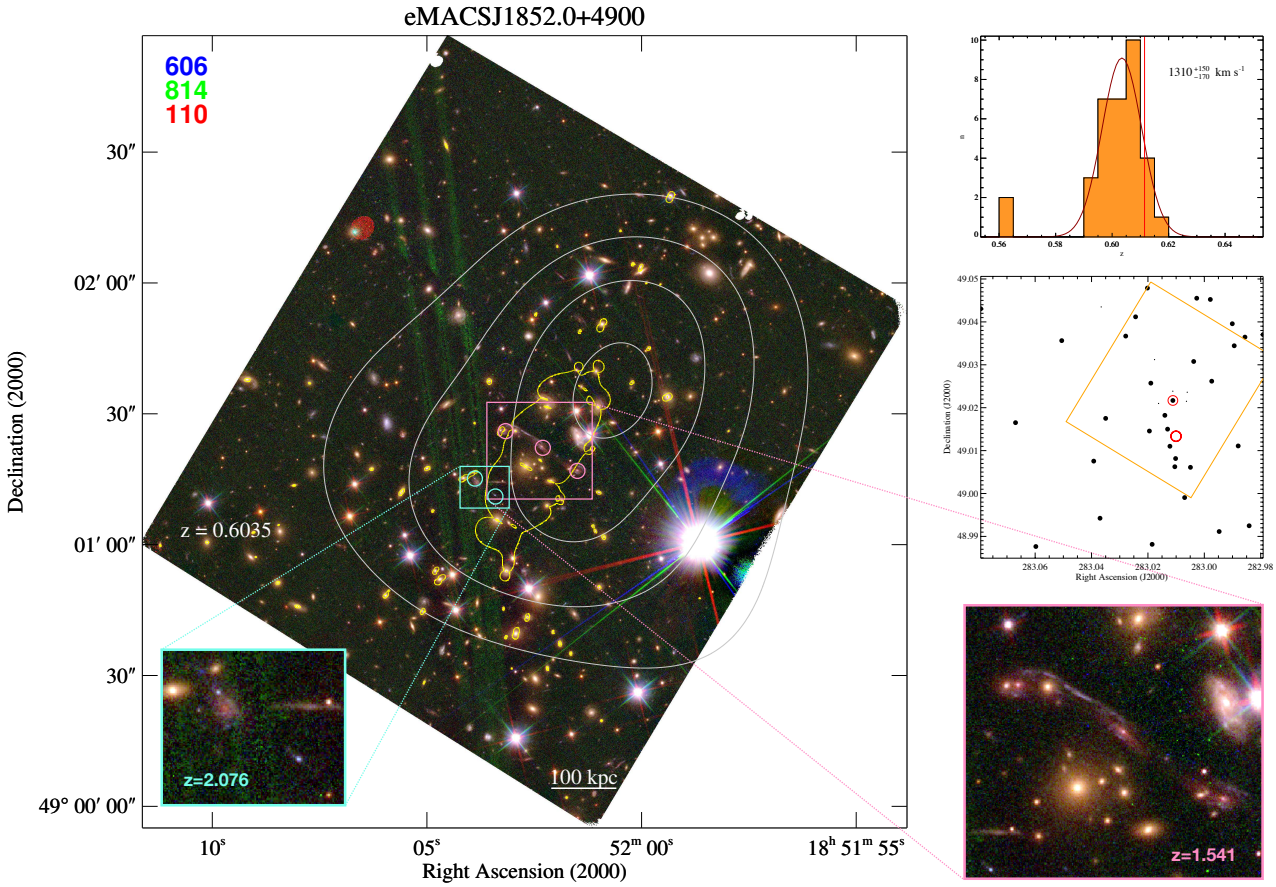

Figure B43. eMACSJ1852.0+4900 is a powerful gravitational lens (we highlight a spectacular fold arc), highly X-ray luminous, and obviously an actively growing system. The relatively modest ICM temperature recorded by *CXO* (see Table 3) suggests that we observe this cluster well past the first core passage, i.e, at a time when shocks driven by the initial collision have largely dissipated.

Coordinates (J2000) and spectroscopic redshifts of galaxies in the field of eMACSJ1852.0+4900.

R.A. (deg)	Dec (deg)	z	R.A. (deg)	Dec (deg)	z
282.9791	49.0370	0.6056	283.0185	48.9882	0.6044
282.9794	49.0288	0.6734	283.0190	49.0257	0.5959
282.9841	48.9925	0.5900	283.0195	49.0146	0.6117
282.9856	49.0365	0.6017	283.0202	49.0479	0.6041
282.9880	49.0111	0.5933	283.0244	49.0412	0.6023
282.9894	49.0344	0.6109	283.0279	49.0367	0.6054
282.9901	49.0396	0.6047	283.0350	49.0175	0.6079
282.9947	48.9911	0.6077	283.0366	49.0435	0.5607
282.9974	49.0262	0.6199	283.0370	48.9942	0.6056
282.9979	49.0452	0.6038	283.0392	49.0076	0.5972
283.0027	49.0455	0.5954	283.0506	49.0356	0.6026
283.0038	49.0308	0.6093	283.0598	48.9876	0.6072
283.0049	49.0061	0.5987	283.0670	49.0165	0.6106
283.0061	49.0236	0.3831	283.0793	49.0431	0.5972
283.0063	49.0215	1.5411			
283.0070	48.9991	0.6098			
283.0102	49.0082	0.5952			
283.0105	49.0062	0.6062			
283.0112	49.0217	0.6115			
283.0112	49.0238	1.5411			
283.0122	49.0110	0.5953			
283.0130	49.0150	0.5925			
283.0140	49.0182	0.6064			
283.0162	49.0210	2.0760			
283.0177	49.0312	0.5612			

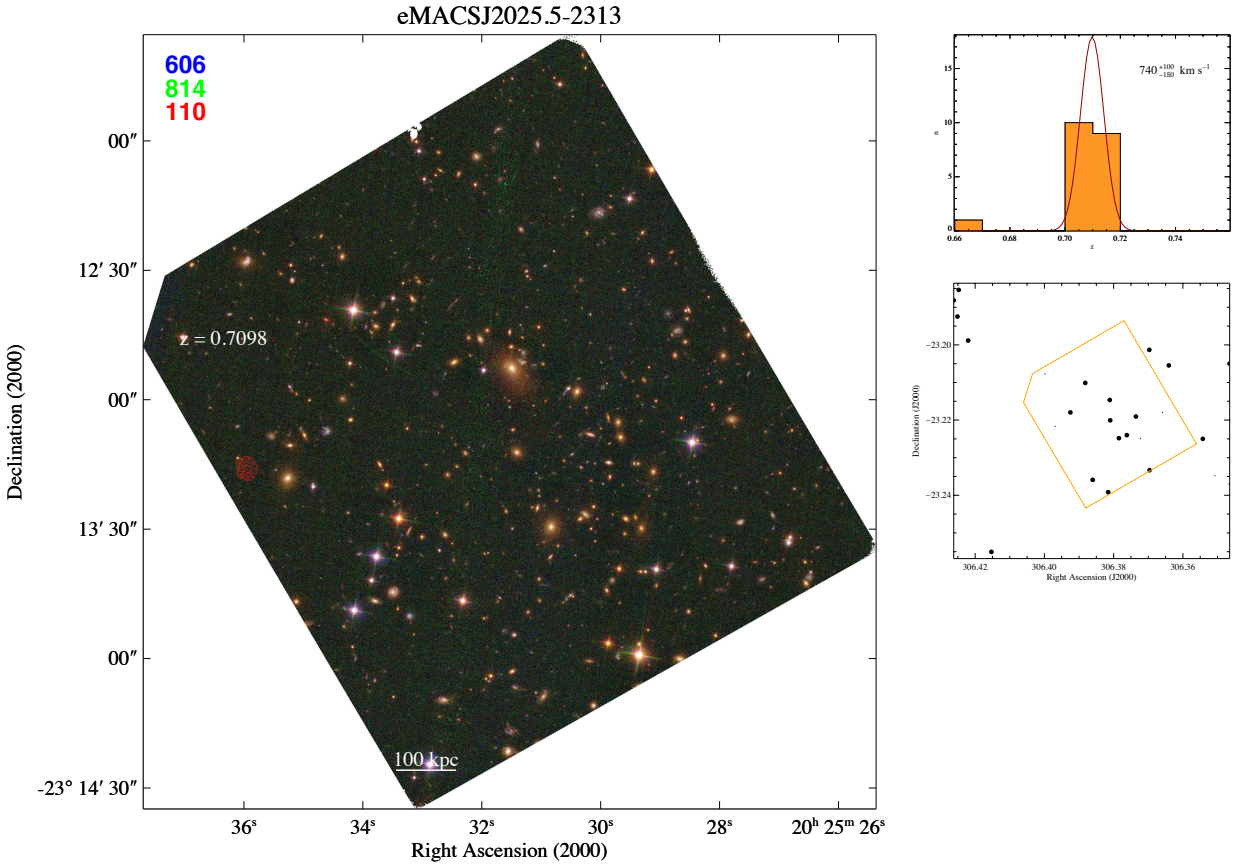

Figure B44. With little follow-up work performed on eMACSJ2025.5−2313, this cluster is currently poorly understood. Its low velocity dispersion (which, however, is based on only 19 redshifts) and lack of strong-lensing features make it an unlikely candidate for a 10^{15} $M_{\odot}$ cluster and might be indicative of point sources contributing to the very high X-ray luminosity recorded in the RASS (see Fig. 12).

Coordinates (J2000) and spectroscopic redshifts of galaxies in the field of eMACSJ2025.5-2313.

R.A. (deg)	Dec (deg)	z
306.3465	−23.2050	0.7158
306.3467	−23.2370	0.6625
306.3508	−23.2348	0.3717
306.3543	−23.2250	0.7132
306.3641	−23.2055	0.7088
306.3659	−23.2180	0.7969
306.3696	−23.2333	0.7026
306.3697	−23.2013	0.7129
306.3723	−23.2249	0.8006
306.3736	−23.2190	0.7129
306.3762	−23.2240	0.7015
306.3785	−23.2248	0.7017
306.3810	−23.2201	0.7124
B 306.3811	−23.2146	0.7117
306.3816	−23.2392	0.7085
306.3861	−23.2359	0.7069
306.3882	−23.2101	0.7137
306.3925	−23.2180	0.7102
306.3969	−23.2217	0.6198
306.3998	−23.2077	0.6455
306.4153	−23.2551	0.7094
306.4220	−23.1988	0.7094
306.4248	−23.1854	0.7086
306.4251	−23.1925	0.7114
306.4262	−23.1882	0.7072

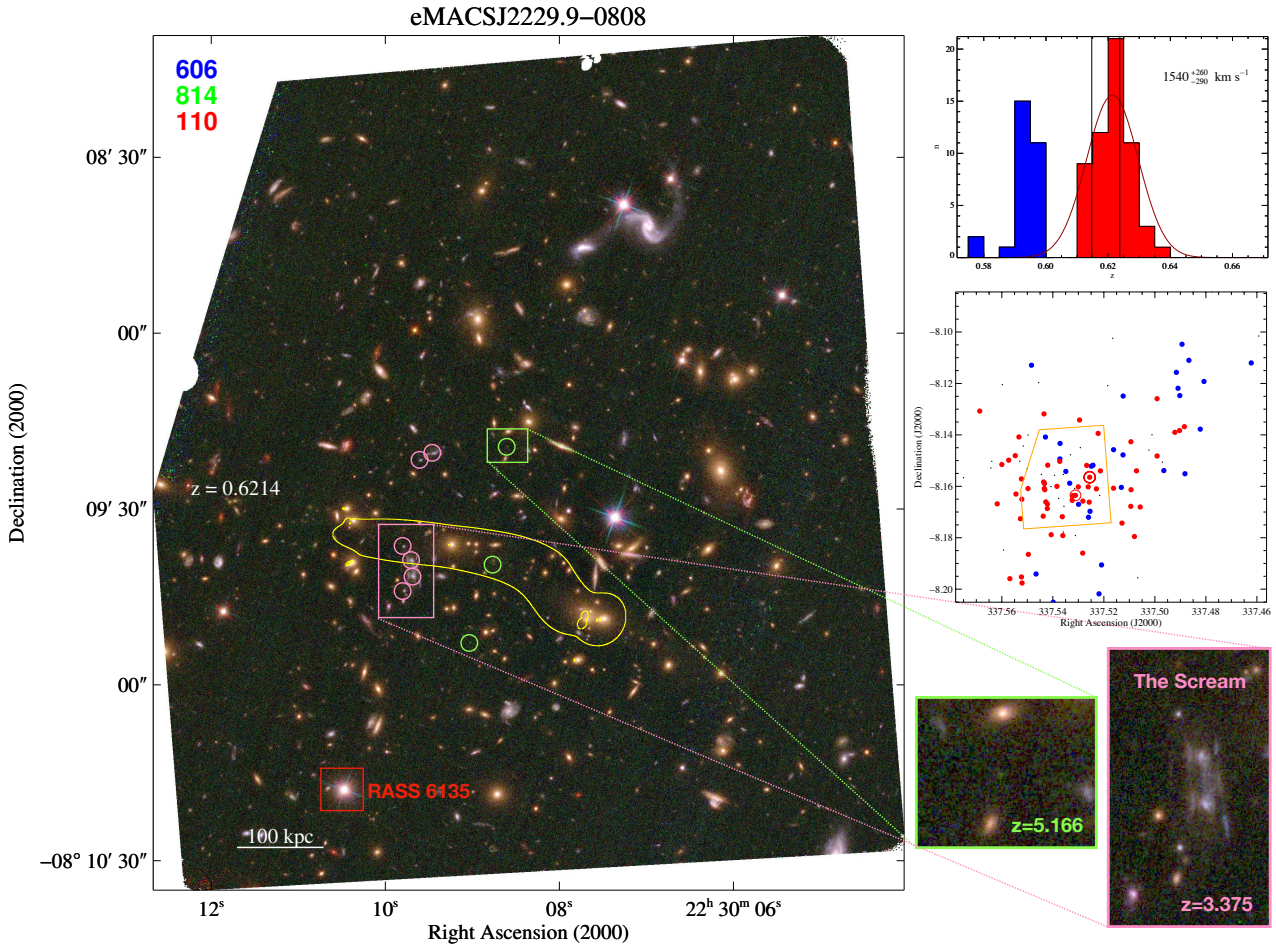

Figure B45. eMACSJ2229.9−0808. The two multiple-image systems that constrain our (partial) lens model are marked in the image and highlighted in inserts. The graphs shown on the right use colour coding to distinguish the spatial and radial-velocity distributions of the galaxy populations of two clusters at $z = 0.595$ (blue) and $z = 0.625$ (red). The bright stellar source south-east of the cluster core is RASS 6135, a luminous QSO that is a member of the more distant component of eMACSJ2229.9. A strong-lensing analysis of this system by Griffiths et al. (2021) correctly identifies the most prominent multiple-image system as a fold arc but suffers from several incorrect assumptions. Most importantly these authors assign an erroneous redshift of $z = 0.82$ to the mentioned fold arc (the correct redshift is $z = 3.375$) which causes them to overestimate the lensing mass by a factor of 3.

Coordinates (J2000) and spectroscopic redshifts of galaxies in the field of eMACSJ2229.9-0808.

R.A. (deg)	Dec (deg)	z	R.A. (deg)	Dec (deg)	z	R.A. (deg)	Dec (deg)	z	R.A. (deg)	Dec (deg)	z	R.A. (deg)	Dec (deg)	z
337.4593	−8.1016	0.5474	337.5094	−8.1427	0.6140	337.5283	−8.1860	0.6201	337.5406	−8.1788	0.6196	337.5523	−8.1571	0.6247
337.4622	−8.1120	0.5916	337.5094	−8.1678	0.6178	337.5292	−8.1450	0.1648	337.5408	−8.1601	3.3750	337.5527	−8.1726	0.6184
337.4776	−8.0844	0.3162	337.5124	−8.1249	0.5942	337.5295	−8.1342	0.6285	337.5420	−8.1518	0.6275	337.5530	−8.1503	0.7980
337.4807	−8.1192	0.5910	337.5125	−8.1478	0.5954	337.5299	−8.1670	0.5985	337.5421	−8.1669	0.6256	337.5533	−8.1408	0.6302
337.4822	−8.1378	0.5912	337.5129	−8.1743	0.6194	337.5300	−8.1602	0.6273	337.5422	−8.1686	0.6223	337.5545	−8.1630	0.6229
337.4867	−8.1110	0.5929	337.5131	−8.1604	0.5978	337.5311	−8.1635	0.6237	337.5428	−8.1661	0.6221	337.5547	−8.1481	0.6250
337.4882	−8.1551	0.5781	337.5162	−8.1458	0.5915	337.5311	−8.1792	0.4839	337.5429	−8.1408	0.5896	337.5568	−8.1959	0.6206
337.4884	−8.1368	0.6128	337.5162	−8.1608	0.6215	337.5315	−8.1609	0.5396	337.5432	−8.1613	0.6220	337.5573	−8.1498	0.6259
337.4894	−8.1048	0.5916	337.5165	−8.1024	0.7097	337.5321	−8.1636	0.6224	337.5433	−8.1589	0.6356	337.5593	−8.1848	0.4724
337.4902	−8.1247	0.5910	337.5185	−8.1209	0.4200	337.5324	−8.1655	0.6149	337.5433	−8.1609	0.6219	337.5598	−8.1205	0.3237
337.4903	−8.1383	0.6115	337.5209	−8.1906	0.5993	337.5331	−8.1477	0.7914	337.5435	−8.1318	0.6242	337.5600	−8.1515	0.6309
337.4909	−8.1219	0.5902	337.5214	−8.1540	0.6142	337.5334	−8.1588	0.5954	337.5436	−8.1583	0.6220	337.5618	−8.1668	0.6248
337.4916	−8.1157	0.5914	337.5217	−8.1635	0.5347	337.5349	−8.1542	0.5955	337.5438	−8.1716	0.6190	337.5639	−8.1503	0.5083
337.4922	−8.1390	0.6118	337.5219	−8.2018	0.5935	337.5356	−8.1678	0.4836	337.5445	−8.1554	0.3466	337.5643	−8.1529	0.2520
337.4965	−8.1539	0.5799	337.5222	−8.1394	0.6269	337.5359	−8.1778	0.3038	337.5456	−8.1197	0.5211	337.5687	−8.1308	0.6296
337.4970	−8.1506	0.4229	337.5229	−8.1610	0.6160	337.5359	−8.1554	5.1661	337.5466	−8.1941	0.5975	337.5750	−8.1567	0.7936
337.4991	−8.1482	0.6148	337.5243	−8.1518	0.5914	337.5361	−8.1792	0.6166	337.5484	−8.1129	0.5916			
337.4991	−8.1259	0.6171	337.5249	−8.1522	0.5937	337.5363	−8.1718	0.6167	337.5496	−8.1865	0.6322			
337.5011	−8.1400	0.3447	337.5254	−8.1697	0.5981	337.5372	−8.1433	0.5963	337.5497	−8.1400	0.2146			
337.5023	−8.1459	0.5405	B 337.5256	−8.1565	0.6147	337.5372	−8.1493	0.5906	337.5497	−8.1609	0.6163			
337.5057	−8.1680	0.6246	337.5257	−8.1662	0.6263	337.5373	−8.1503	0.6190	337.5501	−8.1531	0.5395			
337.5067	−8.1956	0.4113	337.5260	−8.1720	0.5969	337.5377	−8.1647	5.1661	337.5516	−8.1443	0.3453			
337.5072	−8.1540	0.6193	337.5261	−8.1602	0.6231	337.5384	−8.1600	0.6242	337.5521	−8.1976	0.6247			
337.5080	−8.1795	0.6278	337.5267	−8.1519	0.6127	337.5393	−8.1557	3.3750	337.5522	−8.1650	0.6207			
337.5093	−8.1613	0.6262	337.5282	−8.1658	0.6231	337.5399	−8.2051	0.5985	337.5523	−8.1953	0.6258			

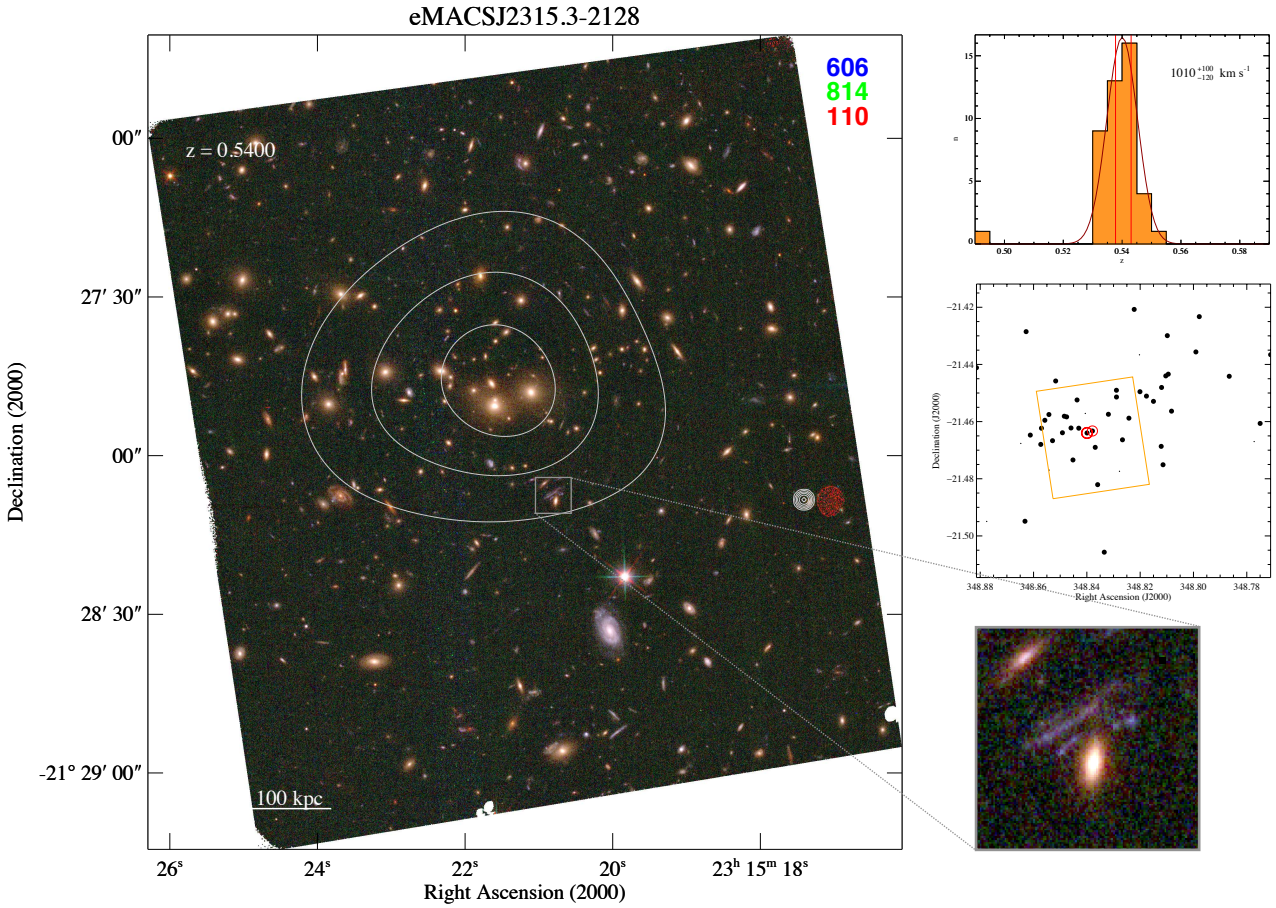

Figure B46. The X-ray luminosity of eMACSJ2315.3−2128 as measured from *CXO* data falls short of that recorded in the RASS by a factor of seven. The only X-ray point sources detected close to the cluster core is not nearly bright enough (at the time of the *CXO* observation) to account for the discrepancy. Given the low X-ray luminosity and modest strong lensing features, we tentatively interpret the high velocity dispersion and large extent of the galaxy distribution to the presence of a composite large-scale structure that combines sheetlike and filamentary components.

Coordinates (J2000) and spectroscopic redshifts of galaxies in the field of eMACSJ2315.3-2128.

R.A. (deg)	Dec (deg)	z	R.A. (deg)	Dec (deg)	z
348.7711	−21.4366	0.5383	348.8360	−21.4821	0.5428
348.7750	−21.4606	0.5424	348.8369	−21.4690	0.5457
348.7772	−21.4670	0.6050	348.8379	−21.4633	0.5430
348.7866	−21.4441	0.5441	B 348.8399	−21.4640	0.5378
348.7978	−21.4233	0.5360	348.8406	−21.4571	0.9293
348.7991	−21.4356	0.5395	348.8430	−21.4623	0.5367
348.8082	−21.4563	0.5445	348.8437	−21.4524	0.5396
348.8095	−21.4434	0.5394	348.8452	−21.4734	0.5344
348.8098	−21.4299	0.5447	348.8459	−21.4622	0.5404
348.8104	−21.4440	0.5336	348.8476	−21.4583	0.5402
X 348.8114	−21.4751	0.5424	348.8485	−21.4581	0.5435
348.8120	−21.4481	0.5302	348.8492	−21.4639	0.5343
348.8121	−21.4687	0.5431	348.8517	−21.4458	0.5341
348.8150	−21.4529	0.5419	348.8529	−21.4667	0.5370
348.8176	−21.4511	0.5430	348.8542	−21.4770	0.4846
348.8201	−21.4495	0.5309	348.8542	−21.4575	0.5343
348.8203	−21.4366	0.6551	348.8558	−21.4595	0.5466
348.8222	−21.4207	0.5537	348.8570	−21.4623	0.5465
348.8242	−21.4588	0.5323	348.8573	−21.4680	0.5392
348.8266	−21.4664	0.5396	348.8612	−21.4647	0.5320
348.8278	−21.4774	0.4922	348.8628	−21.4285	0.5399
348.8289	−21.4514	0.5355	X 348.8632	−21.4949	0.5487
348.8289	−21.4490	0.5390	348.8648	−21.4676	1.2882
348.8319	−21.4574	0.5448	348.8776	−21.4949	0.6130
348.8335	−21.5057	0.5436	348.8814	−21.4411	0.5426

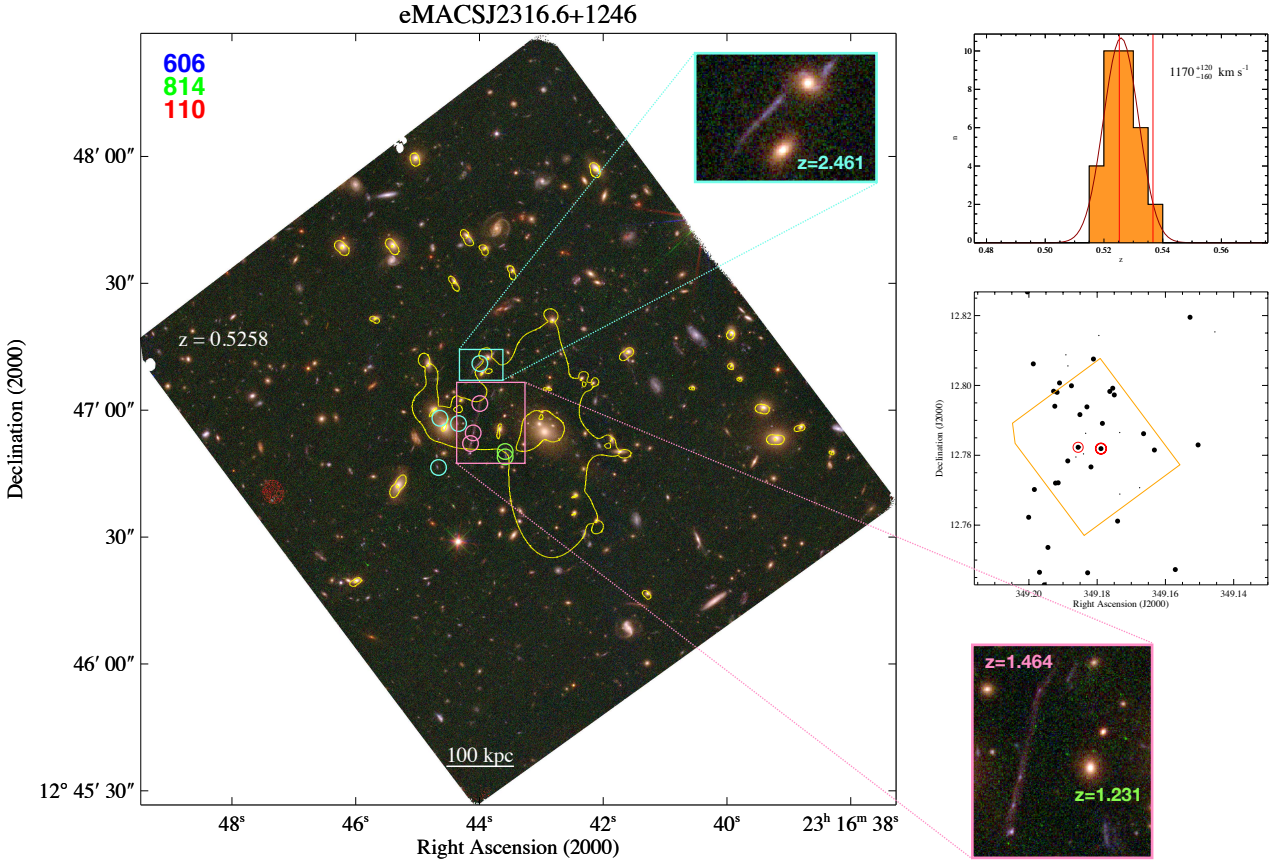

Figure B47. eMACSJ2316.6+1246 is a powerful gravitational lens with a complex morphology, even in the absence of *CXO* data to map the ICM distribution. Our lens model is well constrained by three spectroscopically confirmed multiple-image systems.

Coordinates (J2000) and spectroscopic redshifts of galaxies in the field of eMACSJ2316.6+1246.

R.A. (deg)	Dec (deg)	z	R.A. (deg)	Dec (deg)	z
349.1455	12.8153	0.4331	349.1862	12.7795	2.4597
349.1504	12.7830	0.5335	349.1875	12.7999	0.5242
349.1528	12.8195	0.5317	349.1886	12.8056	0.4615
349.1571	12.7473	0.5223	349.1886	12.7784	0.5260
349.1632	12.7815	0.5311	349.1892	12.8088	0.4628
349.1664	12.7862	0.5275	349.1910	12.8007	0.5254
349.1676	12.7707	0.3032	349.1914	12.7721	0.5258
349.1734	12.7689	0.4331	349.1917	12.7980	0.5188
349.1734	12.7865	1.4606	349.1922	12.7720	0.5310
349.1740	12.7612	0.5295	349.1924	12.7940	0.5274
349.1750	12.7973	0.5238	349.1928	12.7983	0.5347
349.1754	12.7992	0.5157	349.1944	12.7536	0.5220
349.1763	12.7983	0.5293	349.1955	12.7429	0.5211
349.1785	12.7891	0.5325	349.1969	12.7465	0.5214
B 349.1789	12.7819	0.5252	349.1984	12.7702	0.5192
349.1795	12.8143	0.6511	349.1987	12.8062	0.5216
349.1811	12.8076	0.5175	349.2001	12.7622	0.5274
349.1818	12.7767	0.5281	349.2005	12.8268	0.5233
349.1828	12.7464	0.5212			
349.1830	12.7939	0.5202			
349.1834	12.7863	2.4597			
349.1840	12.7804	1.4640			
349.1849	12.7824	2.4597			
349.1851	12.7916	0.5389			
349.1856	12.7823	0.5367			

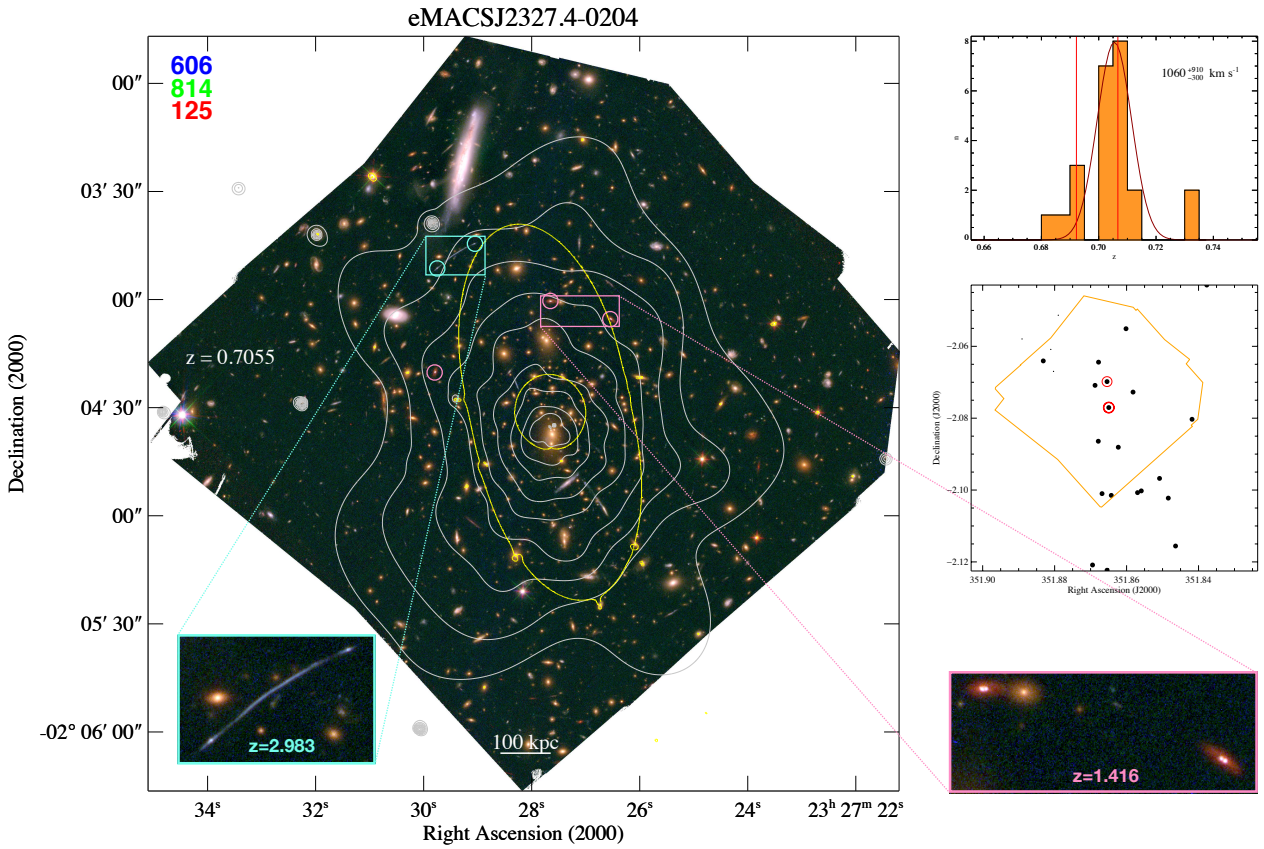

Figure B48. eMACSJ2327.4−0204, previously discovered as RCS2 J232727.6−020437 in the RCS2 cluster survey (Gilbank et al. 2011), is the most X-ray luminous cluster in the eMACS subset observed with *CXO* to date and highlighted in Section 5.4. We here show a lens model based on two multiple-image systems presented in a more detailed analysis by Sharon et al. (2015).

Coordinates (J2000) and spectroscopic redshifts of galaxies in the field of eMACSJ2327.4-0204.

	R.A. (deg)	Dec (deg)	z
	351.8377	−2.0429	0.6933
	351.8418	−2.0803	0.7097
	351.8464	−2.1156	0.7104
	351.8484	−2.1022	0.7074
	351.8508	−2.0968	0.7074
	351.8539	−2.1225	0.4633
	351.8559	−2.1002	0.7039
	351.8570	−2.1007	0.7066
	351.8582	−2.0727	0.7104
	351.8602	−2.0551	0.7039
	351.8623	−2.0881	0.7051
	351.8643	−2.1015	0.7082
B	351.8649	−2.0770	0.6922
	351.8654	−2.1223	0.7034
	351.8654	−2.0698	0.7067
	351.8668	−2.1010	0.7074
	351.8678	−2.0644	0.7024
	351.8679	−2.0864	0.6946
	351.8688	−2.0709	0.7029
	351.8695	−2.1209	0.7046
	351.8790	−2.0513	0.6822
	351.8803	−2.0670	0.7319
	351.8811	−2.0609	0.7308
	351.8832	−2.0641	0.7036
X	351.8891	−2.0579	0.6867